PROSPECTS FOR TESTING ELECTROWEAK SCALE STERILE NEUTRINOS AT FUTURE COLLIDERS

Inauguraldissertation
zur
Erlangung der Würde eines Doktors der Philosophie
vorgelegt der
Philosophisch-Naturwissenschaftlichen Fakultät
der Universität Basel

von

Eros Cazzato

aus Italien

2019

Genehmigt von der Philosophisch-Naturwissenschaftlichen Fakultät auf Antrag von Prof. Dr. Stefan Antusch und Prof. Dr. Nicola Serra.

Basel, den 13.11.2018

Prof. Dr. Martin Spiess
Dekan

Dedication:

Dedico questa tesi a Samuele.

ABSTRACT

The extension of the Standard Model of particle physics by sterile neutrinos can naturally explain the smallness of neutrino masses as observed by neutrino oscillation and nuclear beta decay experiments. These hypothetical particles, also referred to as heavy neutrinos in the mass eigenbasis, can give rise to a testable phenomenology when they have masses around the electroweak scale. Hence they are actively searched for at, for instance, colliders such as the Large Hadron Collider. The proposed future colliders, which are currently in the design phase, will be more powerful than the operated colliders to date. The new possibilities which they provide to search for sterile neutrinos and to test the neutrino mass mechanism in the not too far future have therefore to be assessed.

In this thesis, various aspects of the sterile neutrino phenomenology as well as various searches for sterile neutrinos at colliders are investigated. In particular, we study the contributions from sterile neutrinos to the Higgs boson production mechanism at colliders, the implications of long-lived heavy neutrinos that lead to displaced vertex events, lepton-number violation as the manifestation of heavy neutrino-antineutrino oscillations, lepton-flavour violation as the consequence of leptonic mixing, the possibilities to resolve heavy neutrino-antineutrino oscillations, how to test the viable leptogenesis parameter space, and their implications to collider searches. These collider studies are investigated in the context of low scale seesaw scenarios featuring $n_s = 2$ sterile neutrinos with masses in the range of $\mathcal{O}(1\ \text{GeV})$ and $\mathcal{O}(1\ \text{TeV})$, which constitutes the benchmark scenario. Within the benchmark scenario, analytical calculations, and analyses of Monte Carlo generated event samples are performed.

The investigated collider studies demonstrate promising avenues to test sterile neutrinos at future colliders. This contains novel possible search strategies by the search for Higgs bosons produced from heavy neutrinos and by probing the effects from heavy neutrino-antineutrino oscillations via the displaced vertex search. The assessed capabilities of the future colliders with respect to the sterile neutrino searches contribute to the physics case of the future colliders.

PUBLICATIONS

This thesis is based on research that lead to various publications [1–7] to which the author contributed during his PhD studies conducted under the supervision of Prof. Dr. Stefan Antusch at the Department of Physics of the University of Basel from December 2014 to October 2018. This thesis entails figures and tables that are taken from these publications as well as arguments that are inspired by the respective arguments in these publications.

[1] Stefan Antusch, Eros Cazzato, and Oliver Fischer. "Higgs production from sterile neutrinos at future lepton colliders." In: *JHEP* 04 (2016), p. 189. DOI: 10.1007/JHEP04(2016)189. arXiv: 1512.06035 [hep-ph].

[2] Stefan Antusch, Eros Cazzato, and Oliver Fischer. "Displaced vertex searches for sterile neutrinos at future lepton colliders." In: *JHEP* 12 (2016), p. 007. DOI: 10.1007/JHEP12(2016)007. arXiv: 1604.02420 [hep-ph].

[3] Stefan Antusch, Eros Cazzato, and Oliver Fischer. "Sterile neutrino searches at future e^-e^+, pp, and e^-p colliders." In: *Int. J. Mod. Phys.* A32.14 (2017), p. 1750078. DOI: 10.1142/S0217751X17500786. arXiv: 1612.02728 [hep-ph].

[4] Stefan Antusch, Eros Cazzato, and Oliver Fischer. "Sterile neutrino searches via displaced vertices at LHCb." In: *Phys. Lett.* B774 (2017), pp. 114–118. DOI: 10.1016/j.physletb.2017.09.057. arXiv: 1706.05990 [hep-ph].

[5] Stefan Antusch, Eros Cazzato, and Oliver Fischer. "Resolvable heavy neutrino-antineutrino oscillations at colliders." In: *Mod. Phys. Lett.* A34. 07n08 (2019), p. 1950061. DOI: 10.1142/S0217732319500615. arXiv: 1709.03797 [hep-ph].

[6] Stefan Antusch, Eros Cazzato, Marco Drewes, Oliver Fischer, Bjorn Garbrecht, Dario Gueter, and Juraj Klaric. "Probing Leptogenesis at Future Colliders." In: *JHEP* 09 (2018), p. 124. DOI: 10.1007/JHEP09(2018)124. arXiv: 1710.03744 [hep-ph].

[7] Stefan Antusch, Eros Cazzato, Oliver Fischer, A. Hammad, and Kechen Wang. "Lepton Flavor Violating Dilepton Dijet Signatures from Sterile Neutrinos at Proton Colliders." In: (2018). arXiv: 1805.11400 [hep-ph].

ACKNOWLEDGEMENTS

First and foremost, I want to express my gratitude to my supervisor Stefan Antusch and to Oliver Fischer. Your support, advice and guidance have been invaluable to me during my Ph.D. I learned a lot from the both of you. Not only did a learn and profit from your knowledge in physics but I also learned from your way of working. I very much enjoyed working with you, especially the many hours of discussions. I am also grateful for the provided opportunities to present our research on conferences and to visit schools.

I want to thank Prof. Dr. Nicola Serra for agreeing to be the co-referee.

I express my sincere thanks to Marco Drewes, Björn Garbrecht, Dario Gueter, Ahmed Hammad and Kechen Wang for the very pleasant collaboration and fruitful discussions.

I thank the current and former members of the Particles and Cosmology group as well as the former Astrophysics group for the pleasant and enjoyable environment.

I would like to thank Francesco Cefala, Oliver Fischer, Christiane Scherb, Kenneth Marshall, Christian Hohl, Ahmed Hammad for proofreading parts of my thesis.

Special thanks go to Molli, Holli and France for being great colleagues and for the great time spent during our studies.

Thanks go to Michi, Günni, David, Silvan and Max for the many fun games, laughing and theorycrafting.

I would like to express my thanks to Jan Riemek for being a great friend.

Last but not least, I express my deepest and sincerest gratitude to my family and to Anita for your patience and support. Especially to my parents for their continuous support and giving me the opportunity to study. For everything that you have done, thank you.

CONTENTS

Part I

INTRODUCTION

1 INTRODUCTION

1.1 MOTIVATION AND GOALS

Neutrinos in the Standard Model of particle physics (SM) come in three flavours. The flavours of the active neutrinos [1] are defined by the flavours of the associated charged lepton in the charged weak current interaction. Hence, electron-neutrinos ν_e are created or annihilated alongside electrons, as well as muon-neutrinos ν_μ and tau-neutrinos ν_τ alongside muons and taus, respectively.

Neutrinos played an important role in our understanding of astrophysics, especially in the understanding of the underlying nuclear fusion processes as the main energy generator of the Sun, which takes place inside its core. In the standard solar model, the Sun produces electron-neutrinos as a byproduct of the nuclear fusion reaction, which fuses hydrogen nuclei to a helium nucleus via the proton-proton chain reaction [8]. The flux of these so-called solar neutrinos was first measured by the Homestake experiment in the 1970s [9]. Although it demonstrated that the Sun performs nuclear fusion it observed a deficit in the solar neutrino flux of roughly 1/3 compared to the predicted flux from the standard solar model [10]. This observed deficit in the solar neutrino flux is known as the solar neutrino problem.

The theory of neutrino flavour oscillations as a possible solution to the solar neutrino problem was already known by that time [11], namely the conversion of the neutrino flavour during the propagation from the Sun to the Earth. It took many decades to experimentally observe that neutrinos do oscillate, the discovery came from Super-Kamiokande in 1998 [12] by observing the oscillation effect in atmospheric neutrinos [2]. However, they dealt with atmospheric neutrinos and not solar neutrinos, which are additionally subject to dense matter inside the Sun. As such the predicted Mikheyev–Smirnov–Wolfenstein effect [13–15], which modifies the oscillation effects in objects of dense matter, had also to be experimentally confirmed. The resolution to the long-standing solar neutrino problem was finally obtained by the Sudbury Neutrino Observatory in 2002 [16], which confirmed the oscillation of solar neutrinos. The Nobel price in physics was awarded for the discovery of neutrino oscillations to T. Kajita and A. B. McDonald in 2015, the directors of the Super-Kamiokande and Sudbury Neutrino Observatory during the discoveries, respectively.

Further experiments that were conducted over the past decades have confirmed that neutrinos can convert their flavour via neutrino oscillations [17]. These phenomena can only be explained when neutrinos have masses and leptons mix. The next goal in neutrino physics is therefore to understand the origin of neutrinos masses, i.e. the mass generating mechanism, and with it their mass spectrum [3] and the nature of the neutrinos [4]. Neither neutrino masses nor lepton mixing can be accounted for only with the left-handed neutrinos of the SM in a renormalisable way. Therefore, neutrino oscillations

[1] The SM neutrinos participate in the weak interaction and are therefore sometimes referred to as active neutrinos.

[2] Neutrinos that are produced as a byproduct of cosmic ray interactions with the atmosphere.

[3] Only their mass squared differences are known, not their absolute scale.

[4] Whether neutrinos are Dirac or Majorana particles.

are undoubtedly new phenomena for physics beyond the SM (BSM). This motivates the introduction of new degrees of freedom to the SM. The most straightforward and minimalistic way to introduce renormalisable terms for neutrino masses is by introducing right-handed neutrinos. These particles are gauge singlets under the SM gauge symmetry and thus referred to as sterile neutrinos. They can have a Yukawa term as well as a Majorana mass term. The Yukawa term couples the sterile neutrinos to active neutrinos and to the Higgs doublet of the SM via neutrino Yukawa couplings. The Majorana mass term involves only the sterile neutrinos. Non-zero neutrino masses can be generated via the well known type-I seesaw mechanism [18–22]. This mechanism implies a mixing of active and sterile neutrinos to mass eigenstates, and it results in so-called light and heavy neutrino mass eigenstates, which are admixtures of the interaction fields. The light neutrino mass eigenstates can acquire a mass which is then responsible for neutrino oscillations. The heavy neutrinos mass eigenstates are mostly sterile, such that their mass is mostly determined by the Majorana mass term. Their admixture of active neutrinos allows them to interact with the weak gauge bosons and the Higgs boson with a coupling strength that is proportional to the neutrino Yukawa coupling. The neutrino Yukawa couplings as well as the masses of the heavy neutrinos constitute additional parameters to the SM.

There is however a large freedom in choosing the mass scale of the heavy neutrinos since it is quite unconstrained and spans over many orders of magnitude. For instance, values for the mass scale of the heavy neutrinos can be motivated from the eV range up to way above the Grand Unification scale ($\mathcal{O}(10^{16}$ GeV)). Sterile neutrinos can therefore have implications on many different domains such as cosmology, astrophysics and particle physics. In the cosmological domain, the sterile neutrinos can be responsible for the observed baryon asymmetry of the universe (BAU) [23]. In the astrophysical domain, they can, for instance, constitute the dark matter (DM) particle and be responsible for the structure formation in the universe [24]. In the particle physics domain, they can, for instance, be responsible for the violation of the total lepton number [5] and respective lepton flavour numbers [6] giving rise to lepton-number and to lepton-flavour violating processes in particle physics experiments. These implications have triggered many theoretical and experimental studies that have researched the phenomenology of sterile neutrinos in these contexts [25–27]. From a theoretical and experimental point of view heavy neutrinos with masses around the electroweak (EW) scale (roughly below the GeV scale and up to the TeV scale) are tantalising. On the theoretical side, it is minimalistic and avoids a hierarchy problem. On the experimental side, the new degrees of freedom (or the particles) become kinematically accessible at particle accelerators such as the Large Hadron Collider (LHC). Especially in so-called low scale seesaw scenarios of the type-I seesaw mechanism, the masses for the light neutrinos are controlled by a symmetry which allows for unsuppressed neutrino Yukawa couplings and hence large couplings of the heavy neutrino to the SM particles. EW scale sterile neutrinos can therefore lead to testable predictions in particle physics experiments.

Currently most of the collider studies in high-energy physics focus on the LHC but testing these predictions is especially interesting for the various proposed future particle colliders with their envisaged high energies and high

[5] The violation of the total lepton number can occur when sterile neutrinos are of Majorana nature.

[6] The violation of the lepton flavour numbers can occur due to the non-vanishing leptonic mixing.

intensities. These future colliders are currently being designed and could be built by the 2030s and 2040s, about when the LHC reaches the end of its intended operation. There are several future colliders that are being proposed from different organisations with the prime goal to test the SM and to search for BSM physics. The proposed future colliders in high-energy physics can be subdivided into three collider types:

- The future electron-positron (e^+e^-) colliders are high-intensity machines that could offer integrated luminosities of order $\mathcal{O}(100\ \text{ab}^{-1})$ for the Z pole run compared to the Large Electron-Positron Collider (LEP) with $\mathcal{O}(1\ \text{fb}^{-1})$. They aim for high precision measurements of, for instance, the electroweak observables and Higgs boson properties which allow to test sterile neutrinos. The proposed future e^+e^- colliders comprise the Circular Electron Positron Collider (CEPC), Future Circular Collider in the e^+e^- mode (FCC-ee), International Linear Collider (ILC) and Compact Linear Collider (CLIC).

- The future hadron (pp) colliders are high-energy machines that are envisaged to run at center-of-mass energies of 100 TeV and above. They provide much higher collision energies and can kinematically probe heavy neutrinos (and BSM physics in general) with much larger masses than e^+e^- colliders but their precision in measuring the Higgs boson properties, etc., is more limited due to the challenging hadronic background. They comprise the Future Circular Collider in the hadron mode (FCC-hh), Super proton-proton Collider (SppC).

- The electron-proton (e^-p) colliders provide an electron beam that is brought into collision with a hadron beam. These colliders can be regarded as hybrids between the e^+e^- and pp colliders since they allow for higher center-of-mass energies than e^+e^- colliders and for a cleaner experimental environment than pp colliders. The e^-p colliders comprise the Large Hadron electron Collider (LHeC) and Future Circular Collider in the e^-p mode (FCC-eh).

The possibilities and potential of the proposed future colliders to test the phenomenology of EW scale sterile have therefore to be investigated. Our goal is to study various aspects of the sterile neutrino phenomenology at future colliders. We investigate these aspects in the context of a benchmark scenario which allows us to develop novel search strategies for sterile neutrino signatures, as well as to assess the capabilities of the various proposed future colliders. This results in estimates for the expected sensitivities of the various investigated search strategies for sterile neutrinos.

1.2 OUTLINE

This thesis is organised as follows:

Part II discusses the extension of the SM by sterile neutrinos. We first discuss the origin of neutrino masses and mixing in the presence of sterile neutrinos, and the mass generating mechanism given by the type-I seesaw mechanism in chapter 2. We briefly review the experimental status of neutrino physics with the focus on neutrino flavour oscillation data in chapter 3. We

therefore discuss neutrino flavour oscillations in vacuum. In chapter 4, sterile neutrinos with masses of roughly the order of the electroweak scale are introduced. Subsequently, the low scale seesaw scenarios featuring two EW scale sterile neutrinos are discussed and the benchmark scenario for the study of the phenomenology at colliders is specified.

Part III is concerned with the electroweak scale sterile neutrino phenomenology and searches at future colliders. We first give a small overview of the experimental search strategies and constraints for sterile neutrinos in chapter 5. In chapter 6, we discuss the status of the proposed future colliders, followed by the main production mechanisms of the heavy neutrinos, the ensuing final states and their properties for the different collider types. In chapter 7, a novel contribution to the Higgs boson production mechanism at colliders, given by the decays of the heavy neutrinos, is investigated. This production mechanism is analysed for e^+e^- colliders by which sensitivities for various physics runs are derived. Chapter 8 covers the displaced vertex signature from long-lived heavy neutrinos for e^+e^-, pp and e^-p colliders. The ensuing sensitivity of the future colliders as well as possible limits for LHCb are derived. Chapter 9 is concerned with lepton number violation that is caused by the presence of sterile neutrinos at colliders. Therein we assess the relevance of lepton number violating processes in the context of low scale seesaw scenarios at colliders. In chapter 10, the sensitivity of lepton flavour violation at future pp and e^-p colliders is investigated. In chapter 11, we investigate possible applications of the displaced vertex search to probe lepton number violation as well as leptogenesis as the explanation for the baryon asymmetry of the universe. Finally in chapter 12, we summarise and conclude.

Part II

BEYOND THE STANDARD MODEL - STERILE NEUTRINOS

2 INTRODUCTION TO NEUTRINO MASS AND MIXING

This chapter is aimed at providing an introduction to neutrino mass and mixing. Thereby, we focus on the addition of right-handed (sterile) neutrinos in order to explain the neutrino masses. We discuss Dirac neutrinos as well as Majorana neutrinos in section 2.1, before the type-I seesaw mechanism is introduced as the mechanism for generating all of the neutrino masses in section 2.2. Therein, we discuss the diagonalisation procedure for the neutrino mass matrix of the type-I seesaw mechanism. For this rather pedagogical introduction, we follow ref. [28–30].

2.1 INTRODUCTION TO NEUTRINO MASS AND MIXING

The Standard Model of particle physics (SM), that is defined by its particle content and the imposed $SU(3)_C \times SU(2)_L \times U(1)_Y$ gauge symmetry, generates successfully the mass terms for the charged leptons, quarks, and gauge bosons via spontaneous symmetry breaking of the electroweak symmetry. However, it cannot account for non-zero neutrino masses [7] in its current implementation. There are many possibilities how the SM can be extended in order to accommodate for massive neutrinos. It is therefore our duty to test such models in order to determine the generating mass mechanism, which nature has chosen for the neutrinos.

[7] At least not in a renormalisable manner.

Neutrino oscillation experiments have not only brought the evidence for the existence of neutrino masses, they also measured that some neutrino masses are non-zero as well as non-degenerate [8], and that there are non-vanishing leptonic mixing angles [9]. The experiments have furthermore shown that neutrino masses are tiny compared to the charged fermions, and that mixing in the lepton sector is stronger compared to the quark sector. To substantiate the last two points:

[8] At least two masses are non-zero and are not exactly the same. The mass scale itself is not known only the mass squared differences.

[9] We give a brief overview of the experimental findings in chapter 3.

- The masses of the charged fermions are all different and, depending on charged leptons, up-type or down-type quarks, they range over three to five orders of magnitude. Despite this, they all "live" in the same space that ranges from $\mathcal{O}(100)$ MeV to $\mathcal{O}(100)$ GeV. Neutrino masses, however, range below $\mathcal{O}(1)$ eV.
- The, from the SM known, Cabibbo-Kobayashi-Maskawa (CKM) matrix [31, 32], V_{CKM}, is a parametrisation for the weak charged current interactions of quarks, and in the SM it is responsible for quark mixing. The Pontecorvo–Maki–Nakagawa–Sakata (PMNS) matrix [33–35], U_{PMNS}, on the other hand, is an equivalent parametrisation but for the leptons instead, and it is responsible for lepton mixing [10]. Both matrices contain information on the strength of the flavour mixing which can be determined from experiments. A comparison of the flavour mixing matrix elements, such as $|V_{us}| \approx 0.22$ vs. $|U_{e2}| \approx 0.54$, $|V_{ub}| \approx 0.004$ vs.

[10] Note that the PMNS matrix is not part of the SM since masses for the neutrinos are missing.

$|U_{e3}| \approx 0.15$ and $|V_{cb}| \approx 0.04$ vs $|U_{\mu 3}| \approx 0.7$ [17], shows that the flavour mixing in the leptonic sector is much stronger.

Overall, at least 7 parameters have to be added to the SM in order to explain the observations [11].

[11] 3 parameters for the neutrino masses, as well as 3 mixing angles and one complex phase for the PMNS parameters.

These finding can be seen as the starting point for neutrino model building with the goal of providing a mechanism that explains not only the smallness of neutrinos masses when compared to the charged leptons, but also the large mixing in the leptonic sector when compared to the quark sector. A large number of contributions can be found in the literature toward this goal with the status that no model has been established by experiments so far. The contributions can be roughly subdivided into their focus on neutrino masses or leptonic mixing.

Theories that focus on a natural explanation of tiny neutrino masses are referred to as neutrino mass models. They usually achieve this feat by a mechanism that suppresses the masses of the neutrinos, and thus explains the hierarchy of the neutrinos and the charged leptons. Reviews on this topic can be found in, e.g, ref. [30, 36]. These models often cannot give a prediction for the mass scale of the neutrinos, and do not predict the values for the leptonic mixing, which are rather set by experiments.

Theories that focus on the prediction of the leptonic mixing parameters are usually derived in the context of the flavour puzzle [12], and are thus referred to as flavour models[13].

[12] The flavour puzzle is the problem of understanding the origin of the 3 families of quarks and leptons, and of their mass and mixing pattern.

[13] Flavour models usually extend the SM symmetry by new family or flavour symmetries. Reviews on this topic can be found in, e.g., ref. [37–39].

We are mainly interested in neutrino mass models, i.e. a mass generating mechanism that provides non-zero neutrino masses but should also explain the smallness of the neutrinos masses[14]. Since with the particle content of the SM no gauge invariant and renormalisable terms for neutrino masses are possible, new particles can be added to the SM from a model building perspective. Some of the different approaches in neutrino mass models for introducing new particles to the SM are [30]:

[14] Again, the problem here is not that the mass scale of the neutrinos is small per se but that the mass scale is at least 9 orders of magnitude smaller (compared the mass of the τ lepton with the mass of the heaviest possible neutrino) compared to the charged fermions.

- To allow only the minimal Higgs sector of the SM as the only source for giving mass to elementary particles. This is the simplest approach since masses for the neutrinos can be generated in analogy to generating fermion masses after electroweak symmetry breaking (EWSB) in the SM once right-handed neutrinos N_R, the counterpart of the (left-handed) neutrino ν, are introduced. Right-handed neutrinos are gauge singlet fermions, thus also referred to as sterile neutrinos [11]. They are only allowed to interact by Yukawa couplings to the neutrinos (since EWSB is the only source of giving mass to particles):

$$\mathscr{L}_{\nu,\text{Yukawa}} = -y_\nu \overline{N_R} \tilde{\phi}^\dagger L + \text{H.c.}\,, \tag{2.1}$$

  where y_ν is the neutrino Yukawa coupling, L the $SU(2)_L$ lepton doublet, $\tilde{\phi}$ is the transformed Higgs doublet $i\sigma_2\phi^*$, with ϕ being the Higgs doublet. After EWSB, the left-handed neutrinos ν in L and the right-handed neutrinos N_R form a Dirac-type mass term with mass $m_D = y_\nu v_{EW}/\sqrt{2}$, where v_{EW} is the vacuum expectation value (vev) of the Higgs [15]. In this case, the left-handed and right-handed neutrino combine to form a Dirac neutrino. In order to get the correct mass hierarchy, the neutrino Yukawa couplings need to be tiny [16]. This approach, how-

[15] The neutral component of ϕ.

[16] Dirac neutrino masses $m_D \sim 1$ eV translate into neutrino Yukawa couplings $y_\nu \sim 10^{-11}$ compared to the electron Yukawa $y_e \sim 10^{-6}$.

ever, only shifts the problem from tiny neutrino masses to tiny neutrino Yukawa couplings.

- To allow an extended Higgs sector with additional sources of EWSB. It is then possible to introduce a new Higgs boson field with a non-zero vacuum expectation value that only generates mass terms for the neutrinos. For instance the type-II seesaw mechanism [22, 40–43] induces Majorana masses for the neutrinos, see below, by introducing a $SU(2)_L$ scalar triplet whose neutral component acquires a vev after EWSB [17], a review can be found in e.g. ref. [44].

- Or to allow an entirely new source of mass, one that is independent of EWSB. One can add again right-handed (sterile) neutrinos to the SM as in the first approach. We note that without the restriction of EWSB as the only source for giving mass, the right-handed neutrinos are allowed to have a so-called Majorana-type mass term[18]:

$$\mathscr{L}_{N_R,\text{mass}} = -\frac{1}{2} M_R \overline{N_R} N_R^c + \text{H.c.}\,, \tag{2.2}$$

where M_R is the Majorana mass and c denotes the charge conjugation operation. Together with eq. (2.1), a Majorana-type mass term for the neutrinos can be generated after EWSB. The resulting Majorana masses for the neutrinos are approximately given by m_D^2/M_R. In order to get the correct mass hierarchy, either the Yukawa couplings need to be tiny or the mass of the corresponding sterile neutrinos need to be large [19]. The suppression of the neutrino mass scale is naturally embedded for very large M_R. This is the well-known type-I seesaw mechanism [18–22] which is discussed below in section 2.2. This approach is also easily adopted to triplet fermions instead, which is referred to as the type-III seesaw mechanism[20], cf. ref. [45].

The last two approaches can give a natural solution to the origin of the smallness of neutrino masses. We only briefly sketched different approaches and named popular examples, but many more mass models can be found in the literature, cf. for instance in the review ref. [36] [21]. Regardless of the underlying model that generates neutrino masses, neutrinos have either a Dirac-type mass or a Majorana-type mass term. It is therefore important to understand the implications that come with Dirac or Majorana neutrinos.

We anticipate the main implication of Dirac or Majorana neutrinos which is the conservation or violation of the total lepton number, respectively. This can be seen from the fact that eq. (2.1) and eq. (2.2) are not simultaneously conserved under a global lepton number symmetry[22]. The origin that leads to Dirac or Majorana neutrinos in the case of extending the SM by sterile neutrinos, namely the first and third approach, is eq. (2.2). If M_R is zero, then the generated neutrino mass term is Dirac-type with the mass $m_D = y_\nu v_{EW}/\sqrt{2}$. Conversely, when M_R is non-zero, the resulting mass term for the neutrinos is Majorana-type. But let us discuss the implications for Dirac and Majorana neutrinos a bit more detailed by following ref. [28, 29].

[17] In order to get the correct mass hierarchy either tiny couplings or a tiny triplet vev are required. The suppression of the neutrino mass scale is a natural consequence once the triplet vev is suppressed by a large triplet mass.

[18] Since right-handed neutrinos are singlets under the SM symmetry

[19] A Majorana neutrino mass of $m_D^2/M_R \sim 1$ eV with an assumed value for $m_D \sim 100$ GeV, which corresponds to a neutrino Yukawa coupling of $y^\nu \sim 1$, translates into $M_R \sim 10^{13}$ GeV.

[20] Instead of introducing singlet fermions, one can introduce $SU(2)_L$ triplet fermions with zero hypercharge instead. Replacing those fields with the right-handed neutrino fields in eq. (2.1) and eq. (2.2) yields the same phenomenology for neutrinos as with the type-I seesaw mechanism. However, the type-III seesaw mechanism also postulates new charged fermions.

[21] We only mention a few here: left-right symmetric models [46], models based on grand unification [47], radiative mass models [48–50], R-parity violating supersymmetry [51], string theory [52, 53] and models based on extra dimensions [54].

[22] For instance choose a lepton number for L as $+1$ and N_R as -1 then eq. (2.1) is invariant while eq. (2.2) is not.

2.1.1 *Dirac neutrinos*

The consequence of the first approach is, as we sketched above, that the SM can be extended by a Dirac mass term for the neutrinos, in analogy to the SM quarks and charged leptons, once sterile neutrinos are added. That is why, for the moment, we choose to discuss the case of $n_S = 3$ sterile neutrinos. If EWSB is the only mechanism that gives mass to particles then sterile neutrinos only interact with neutrinos by their Yukawa interaction. Therefore, the SM Yukawa interactions are extended by the neutrino Yukawa interaction, which has the analogue structure of the up-type quarks:

$$\mathscr{L}_{\text{lep.,Yuk.}} = -(y'_\ell)_{\alpha\beta}\overline{L'_\alpha}\phi\ell'_{\beta R} - (y'_\nu)_{\alpha\beta}\overline{L'_\alpha}\tilde{\phi}N'^{\beta}_R + \text{H.c.}\,, \tag{2.3}$$

where $(y'_\ell)_{\alpha\beta}$ and $(y'_\nu)_{\alpha\beta}$ are the charged lepton and neutrino Yukawa couplings, N'^{β}_R are the sterile neutrinos with $\beta = 1, 2$ and 3, L'_α are the $SU(2)_L$ lepton doublets with $\alpha = e, \mu$ and τ, ℓ'^{β}_R are the right-handed charged leptons with $\beta = e, \mu$ and τ. The matrices y'_ℓ and y'_ν are complex 3×3 matrices in the family space in the case of 3 sterile neutrinos [23]. Since the matrices y'_ℓ and y'_ν are in general non-diagonal, the involved fields have not definite masses, i.e they are not mass eigenstates, thus they are labelled by a prime. The Yukawa matrices have to be diagonalised first, before the fields can be interpreted as fields with definite masses, i.e. as mass eigenstates. They can be diagonalised by the following bi-unitary transformations

[23] More generally y'_ν is complex $3 \times n_S$ matrix.

$$U^{\ell\dagger}_L y'_\ell U^\ell_R = y_\ell\,, \qquad\qquad U^{\nu\dagger}_L y'_\nu U^\nu_R = y_\nu\,, \tag{2.4}$$

where y_ℓ and y_ν are diagonal, real and positive. With the mass eigenstates defined as

$$\begin{aligned} \ell_L &= U^{\ell\dagger}_L \ell'_L = (e_L, \mu_L, \tau_L)^T\,, \qquad \nu = U^{\nu\dagger}_L \nu'_L = (\nu_1, \nu_2, \nu_3)^T\,, \\ \ell_R &= U^{\ell\dagger}_R \ell'_R = (e_R, \mu_R, \tau_R)^T\,, \qquad N = U^{\nu\dagger}_R N'_R = (N_1, N_2, N_3)^T\,, \end{aligned} \tag{2.5}$$

the mass terms are obtained from the diagonalised Lagrangian in eq. (2.3) after EWSB[24]

[24] $\phi \to \frac{1}{\sqrt{2}}\begin{pmatrix} 0 \\ v_{EW} + h \end{pmatrix}$ with h the Higgs field.

$$\mathscr{L}_{\text{lep.,Yuk.}} = -\frac{v_{EW} + h}{\sqrt{2}}\left(\sum_{\alpha=e,\mu,\tau}(y_\ell)_{\alpha\alpha}\overline{\ell_{\alpha L}}\ell_{\alpha R} + \sum_{k=1,2,3}(y_\nu)_{kk}\overline{\nu_k}N_k + \text{H.c.}\right). \tag{2.6}$$

Hence, the Dirac neutrino masses read

$$(m_D)_{kk} = (y_\nu)_{kk} v_{EW}/\sqrt{2}\,, \quad k = 1, 2, 3, \tag{2.7}$$

and the mass eigenstates of the right- and left-handed neutrino fields combine into a Dirac spinor[25], defined as

[25] For the charged leptons the Dirac spinors read $\ell_\alpha = \ell_{\alpha L} + \ell_{\alpha R}$.

$$n_k = \nu_k + N_k\,, \quad k = 1, 2, 3. \tag{2.8}$$

The mass term for the neutrinos can then be written as the usual Dirac mass term

$$\mathscr{L}^{\text{Dirac}}_{\text{mass}} = -\sum_{k=1,2,3}(m_D)_{kk}\overline{n_k}n_k\,. \tag{2.9}$$

We emphasize that in order to get the correct mass hierarchy, neutrino masses have to be much smaller than the charged lepton and quark masses. This can only be achieved by choosing comparatively tiny Yukawa couplings [26]. Therefore, it fails to explain as to why neutrino Yukawa couplings are comparatively so small [27].

The leptonic mixing can be derived in analogy to the SM quarks. The charged weak current for the leptons [28] can be rewritten in terms of the mass eigenstates as

$$J^{\mu}_{W} = \frac{g_2}{\sqrt{2}}\overline{\nu'_L}\gamma^{\mu}\ell'_L = \frac{g_2}{\sqrt{2}}\overline{\nu}\gamma^{\mu}U^{\nu\dagger}_L U^{\ell}_L \ell_L \,. \tag{2.10}$$

It depends on the matrix product

$$U_{PMNS} = U^{\ell\dagger}_L U^{\nu}_L \,, \tag{2.11}$$

which defines the PMNS leptonic mixing matrix. Defining the left-handed neutrino flavour fields by their interaction with the mass eigenstates of the charged leptons as

$$\begin{aligned} &\nu_L = \left(\nu_{eL}, \nu_{\mu L}, \nu_{\tau L}\right)^T := U^{\ell\dagger}_L \nu'_L = U_{PMNS}\,\nu \,, \text{ or equivalently} \\ &\nu_{\alpha L} = (U_{PMNS})_{\alpha k}\,\nu_k \,, \end{aligned} \tag{2.12}$$

relates the mass eigenstates with the flavour eigenstates by the PMNS matrix. The charged weak current for the leptons can then be rewritten in either the neutrino flavour eigenbasis $\nu_{\alpha L}$ or the neutrino mass eigenbasis ν_k as

$$J^{\mu}_{W} = \frac{g_2}{\sqrt{2}}\overline{\nu_{\alpha L}}\gamma^{\mu}\ell_{\alpha L} \quad \text{or} \quad J^{\mu}_{W} = \frac{g_2}{\sqrt{2}}\overline{\nu_k}\gamma^{\mu}(U^{\dagger}_{PMNS})_{k\beta}\ell_{\beta L} \,, \tag{2.13}$$

respectively. We want to note that the flavour eigenbasis coincides with the mass eigenbasis for the charged leptons. Furthermore, the neutrino flavour fields $\nu_{\alpha L}$ indeed correspond to the neutrino fields of the SM in the massless limit which are also referred to as active neutrinos. Also, note that the right-handed component of the Dirac neutrino fields N_k do not participate in the weak interactions, since the active and sterile neutrino are not mixing.

The leptonic mixing matrix U^{D}_{PMNS} for Dirac neutrino masses can be parametrised, as in the quark sector, by 3 mixing angles $\theta_{12}, \theta_{23}, \theta_{12}$ and one complex Dirac phase δ [29] [17]:

$$U^{D}_{PMNS} = \begin{pmatrix} c_{12}c_{13} & s_{12}c_{13} & s_{13}e^{-i\delta} \\ -s_{12}c_{23} - c_{12}s_{23}s_{13}e^{i\delta} & c_{12}c_{23} - s_{12}s_{23}s_{13}e^{i\delta} & s_{23}c_{13} \\ s_{12}s_{23} - c_{12}c_{23}s_{13}e^{i\delta} & -s_{23}c_{12} - c_{23}s_{13}s_{12}e^{i\delta} & c_{23}c_{13} \end{pmatrix} . \tag{2.14}$$

The labels c_{ij} and s_{ij} denote $\cos\theta_{ij}$ and $\sin\theta_{ij}$, respectively. The values for the mixing angles and the Dirac phase range from 0 to $\pi/2$ and 0 to 2π, respectively.

We note that there is CP violation in the leptonic mixing sector when the Dirac phase δ is non-zero.

The consequence of a non-diagonal PMNS matrix is that each of the flavour lepton numbers $\mathbb{L}_e, \mathbb{L}_\mu$ and $\mathbb{L}_\tau$ are not conserved [30], i.e. the corresponding

[26] Since the obtained masses for the neutrinos as well as for the charged leptons and quarks are proportional to Yukawa coupling times the vev of the Higgs.

[27] In fact all the values of the Yukawa couplings are a completely open question, a problem that flavour models try to address.

[28] The Lagrangian density for the charged weak current interaction for the leptons reads $-J^{\mu}_{W}W_{\mu} + \text{H.c.}$ where $J^{\mu}_{W} = \frac{g_2}{\sqrt{2}}\overline{\nu'_{\alpha L}}\gamma^{\mu}P_L\ell'_{\alpha}$ with $P_L = \frac{1-\gamma^5}{2}$.

[29] Usually also referred to Dirac CP violating phase.

[30] A lepton number $\mathbb{L}_\alpha$ for each lepton family which transform the leptons as $\ell_\alpha \to e^{i\phi_\alpha}\ell_\alpha, \quad \nu_{\alpha L} \to e^{i\phi_\alpha}\nu_{\alpha L}$.

transformations are not a global symmetry of the Lagrangian density [31]. It is this non-conservation that allows for neutrino flavour oscillations.

The total lepton number $\mathbb{L} = \mathbb{L}_e + \mathbb{L}_\mu + \mathbb{L}_\tau$, however, is a conserved quantity. The corresponding global symmetry transformations leave the Lagrangian density invariant [32]. Indeed, the Dirac fermion character implies that neutrinos and antineutrinos are different. They can be distinguished by their lepton number.

[31] In fact, the reason is the Dirac mass term for the neutrinos in eq. (2.6). No transformation for the N_k fields can be found which leave the Dirac mass term and the kinetic terms simultaneously invariant.

[32] $\ell_\alpha \to e^{i\phi}\ell_\alpha, \quad \nu_k \to e^{i\phi}\nu_k$

2.1.2 *Majorana neutrinos*

The consequence of the second and third approach when generating neutrino masses is that neutrinos are Majorana fermions, i.e. they have a Majorana mass term. In order to understand the difference to the Dirac case, let us first emphasise that in the Dirac case an independent component is introduced, namely the right-handed neutrino field. Together, with the left-handed neutrino field they form a massive Dirac spinor. Generally speaking, a left and right-handed component of a Dirac spinor $\psi = \psi_L + \psi_R$ fulfil the Dirac equation

$$(i\gamma^\mu \partial_\mu - m)\psi = 0 \quad \Longleftrightarrow \quad \begin{array}{l} i\gamma^\mu \partial_\mu \psi_L = m\psi_R \\ i\gamma^\mu \partial_\mu \psi_R = m\psi_L \end{array} . \tag{2.15}$$

But two independent components are not necessary in order to describe massive particles. They can indeed by related to each other, which has shown Ettore Majorana [55], and the resulting solution is therefore named the Majorana particle. The idea is that the two separate equations in (2.15) can be written to represent the same equation but with one independent field only. Let us consider the charge conjugation operator that transforms a spinor ψ according to

$$\psi \longrightarrow \psi^c = \eta C \overline{\psi}^T = -\eta \gamma^0 C \psi^* , \tag{2.16}$$

where C denotes the charge conjugation matrix[33] and η denotes an arbitrary phase[34] with $|\eta|^2 = 1$. Notice that acting with the charge conjugation operator on ψ_L gives $\psi_L^c = (P_L\psi)^c = P_R\psi^c = (\psi^c)_R$ a right-handed field. Thus writing the spinor as

$$\psi = \psi_L + \psi_L^c , \tag{2.17}$$

both equations underlying the Dirac equation (2.15) can then be rewritten as

$$i\gamma^\mu \partial_\mu \psi_L = m\psi_L^c . \tag{2.18}$$

The spinor in eq. (2.17) is referred to as Majorana spinor and it satisfies the Majorana condition

$$\psi = \psi^c . \tag{2.19}$$

The Majorana condition implies that the particle is identical to its antiparticle, i.e. a Majorana fermion is its own antiparticle. Thus Majorana fermions require to be neutral. Since a Majorana fermion is described by only one independent field ψ_L (or equivalently ψ_R), the degrees of freedom are halved compared to a Dirac fermion.

[33] That fulfils these three operations:
$C\gamma_\mu^T C^{-1} = -\gamma_\mu$
$C^\dagger = C^{-1}$,
$C^T = -C$.

[34] Since acting C twice on ψ must be the identity operator: $(\psi^c)^c = |\eta|^2\psi$. And since η has no further consequences it can be chosen to 1 [56, 57].

At the level of the Lagrangian density, also a mass term for a Majorana fermion has to obey Lorentz invariance and therefore not vanish due to chirality. This means a mass term has to connect a spinor and an adjoint spinor of different chiralities[35]. It can be shown that ψ_L^c transforms as ψ_L under Lorentz transformations, and $\overline{\psi_L^c}$ as $\overline{\psi_L}$, respectively[28] . Thus a valid Lagrangian density can be constructed as

$$\begin{aligned}\mathscr{L}^{\text{Majorana}} &= \frac{1}{2}\left(\overline{\psi_L} i\gamma^\mu \partial_\mu \psi_L + \overline{\psi_L^c} i\gamma^\mu \partial_\mu \psi_L^c - m\overline{\psi_L^c}\psi_L - m\overline{\psi_L}\psi_L^c\right) \\ &= \overline{\psi_L} i\gamma^\mu \partial_\mu \psi_L - \frac{m}{2}\left(\overline{\psi_L^c}\psi_L + \overline{\psi_L}\psi_L^c\right) , \end{aligned} \tag{2.20}$$

[35] For Dirac fermions, the mass term is given by the combination $\overline{\psi_R}\psi_L + \overline{\psi_L}\psi_R$.

[36] where the factor $1/2$ takes care of the double counting of the degrees of freedom. As stated above, Majorana fermions are required to be neutral, this fact can explicitly be seen when examining the mass term. For the phase transformation $\psi_L \to e^{i\phi}\psi_L$, the field ψ_L^c transforms as $e^{-i\phi}\psi_L^c$, hence $\overline{\psi_L^c}\psi_L \to e^{i2\phi}\overline{\psi_L^c}\psi_L$ is not invariant under phase rotations. As a consequence the total lepton number $\mathbb{L}$ is not a conserved quantity. The mass term therefore violates lepton number by two units.

[36] And further refined to $\frac{1}{2}\overline{\psi}\left(i\gamma^\mu\partial_\mu - m\right)\psi$ with $\psi = \psi_L + \psi_L^c$.

Returning to neutrinos in the SM: As we have seen, only the left-chiral component is needed to construct a Majorana mass term. However in the SM, the combination $\overline{\nu_L^c}\nu_L$ is not allowed by the SM gauge symmetry. Hence such a term cannot be obtained from EWSB with the SM content at the renormalisable level. A Majorana mass term can be constructed at the non-renormalisable level with the SM content by

$$\mathscr{L}_{\text{dim }5} = -\kappa_{\alpha\beta}\left(\overline{L_\alpha^c} i\sigma_2 \phi\right)\left(L_\beta i\sigma_2 \phi\right) + \text{H.c.} , \tag{2.21}$$

where $\mathscr{L}_{\text{dim }5}$ contains a product of fields with mass dimension 5 and κ is a coupling matrix with mass dimension -1. After EWSB the dimension 5 operator, also referred to as the Weinberg operator, generates the Majorana mass term

$$\mathscr{L}_{\text{dim }5} = -\frac{1}{2}\kappa_{\alpha\beta} v_{EW}^2 \overline{\nu_{\alpha L}^c}\nu_{\beta L} + \text{H.c.} . \tag{2.22}$$

We note that the SM with this additional non-renormalisable term should be considered as an effective low-energy theory. The full and renormalisable theory, which has additional degrees of freedom added to the SM, generates such a Majroana mass term for the neutrinos when these additional degrees of freedom are "integrated out" of the theory.

As in the Dirac case, the involved fields are in general not the mass eigenstates. We start from a general mass term in the case of 3 Majorana neutrinos which is given by

$$\mathscr{L}_{\text{mass}}^{\text{Majorana}} = -\frac{1}{2}(M_L)_{\alpha\beta}\overline{\nu_{\alpha L}'^c}\nu_{\beta L}' + \text{H.c.} , \tag{2.23}$$

where M_L is a complex symmetric 3×3 matrix. In order to express the neutrino fields in terms of mass eigenstates, the matrix M_L has to be diagonalised. It can be diagonalised by one unitary matrix U_L^ν with the transformation

$$(U_L^\nu)^T M_L U_L^\nu = m_\nu , \tag{2.24}$$

also referred to as Takagi decomposition, cf. for instance ref. [58], with real and positive masses m_{ν_k}. The mass eigenstates are defined by

$$\nu = U_L^{\nu\dagger}\nu'_L = (\nu_1, \nu_2, \nu_3)^T \,. \tag{2.25}$$

After diagonalisation the mass term reads

$$\mathscr{L}_{\text{mass}}^{\text{Majorana}} = -\frac{1}{2} m_{\nu_k} \overline{\nu_k^c} \nu_k + \text{H.c.}\,. \tag{2.26}$$

With the Majorana field described in eq. (2.17), the Majorana field for the neutrinos

$$n_k = \nu_k + \nu_k^c\,, \quad k = 1, 2, 3, \tag{2.27}$$

can be used to rewrite the Majorana mass term as

$$\mathscr{L}_{\text{mass}}^{\text{Majorana}} = -\frac{1}{2} \sum_{k=1,2,3} m_{\nu_k} \overline{n}_k n_k \,. \tag{2.28}$$

As in the Dirac case, the charged weak current can be written in either the neutrino flavour eigenbasis $\nu_{\alpha L} = (U_{PMNS})_{\alpha k}\, \nu_k$ or in the neutrino mass eigenbasis ν_k as

$$J_W^\mu = \frac{g_2}{\sqrt{2}} \overline{\nu_{\alpha L}} \gamma^\mu \ell_{\alpha L} \quad \text{or} \quad J_W^\mu = \frac{g_2}{\sqrt{2}} \overline{\nu_k} \gamma^\mu (U_{PMNS}^\dagger)_{k\beta} \ell_{\beta L}\,, \tag{2.29}$$

respectively. However, differently from the Dirac case, the PMNS mixing matrix has not only one CP-violating phase but three instead. The two additional phases cannot be eliminated as in the Dirac case, because the Majorana mass term is not invariant under phase rotations. The leptonic mixing matrix U_{PMNS}^M for Majorana neutrino masses is then written as the product [17]

$$U_{PMNS}^M = U_{PMNS}^D \times \text{diag}(1, e^{i\alpha_{21}/2}, e^{i\alpha_{31}/2})\,, \tag{2.30}$$

where the phases α_{21} and α_{31} are referred to as the Majorana CP violation phases.

2.2 TYPE-I SEESAW MECHANISM

The most minimalistic and straightforward extension of the SM for generating Dirac-type or Majorana-type neutrino masses is the type-I seesaw mechanism. In this section, we review the underlying mass mechanism by introducing n_S right-handed (sterile) neutrinos to the SM as is partly discussed in ref. [28, 29].

We start by emphasising that right-handed neutrinos are singlets under the SM gauge symmetries, i.e. they do not participate in the strong, weak or electromagnetic interactions, hence sterile. While the left-handed neutrinos from the SM do participate in the weak interactions, and are hence referred to as active neutrinos.

When introducing sterile neutrinos to the SM, the SM Lagrangian density is generally extended by a Yukawa interaction term of the neutrinos with the

Higgs doublet field and by a Majorana mass term for the sterile neutrinos. After EWSB, the additional terms to the Lagrangian density is given by

$$\mathscr{L}_{\text{type I}} = -m_D \overline{N'_R} \nu'_L - \frac{1}{2} \overline{N'_R} M_R N'^c_R + \text{H.c.}\,, \tag{2.31}$$

where M_R is the complex symmetric $n_S \times n_S$ sterile neutrino Majorana mass matrix, $m_D = (y'_\nu) v_{EW}/\sqrt{2}$ the complex $3 \times n_S$ Dirac mass matrix. The mass terms of the above equation can be recast into a single term, by defining the $(3+n_S)$ vector for the left-chiral fields [37]

$$n'_L = \left(\nu'_{eL}, \nu'_{\mu L}, \nu'_{\tau L}, N'^{1\,c}_R, \ldots, N'^{n_S\,c}_R\right)^T . \tag{2.32}$$

Hence, the Lagrangian density reads

$$-\frac{1}{2} \begin{pmatrix} \overline{\nu'^c_L} & \overline{N'_R} \end{pmatrix} \begin{pmatrix} 0 & m_D^T \\ m_D & M_R \end{pmatrix} \begin{pmatrix} \nu'_L \\ N'^c_R \end{pmatrix} + \text{H.c.}\,. \tag{2.33}$$

The $(3+n_S) \times (3+n_S)$ complex symmetric block matrix

$$\mathcal{M}' = \begin{pmatrix} 0 & m_D^T \\ m_D & M_R \end{pmatrix} , \tag{2.34}$$

can be diagonalised by a unitary transformation, transforming $\mathcal{M}'$ as

$$\mathcal{U}^T \mathcal{M}' \mathcal{U} = \begin{pmatrix} m_\nu & \\ & M_N \end{pmatrix} = \mathcal{M}\,, \tag{2.35}$$

with real and positive diagonal matrices m_ν and M_N. The mass eigenstates are then given by

$$n_k = \mathcal{U}^\dagger_{k\alpha} n'_{\alpha L} = \left(\nu_1, \nu_2, \nu_3, N_1, \ldots, N_{n_S}\right)^T . \tag{2.36}$$

After the diagonalisation the mass term in eq. (2.33) is described by $3+n_S$ Majorana mass terms, with Majorana masses as in eq. (2.26),

$$\mathscr{L}_{\text{type I}} = -\frac{1}{2} m_{\nu_k} \overline{\nu^c_k} \nu_k - \frac{1}{2} M_{N_i} \overline{N^c_i} N_i + \text{H.c.}\,. \tag{2.37}$$

In order to find an explanation for the smallness of neutrino masses, let us consider possible scenarios of the mass matrix $\mathcal{M}'$ by examining the relative sizes of M_R and m_D, i.e. the eigenvalues. For more details the reader is referred to ref. [25, 30] and references therein:

- $M_R = 0$, the pure Dirac case: For each active and sterile pair, the diagonalisation leads to Majorana neutrinos with degenerate masses, they can be combined into a Dirac spinor which conserves lepton number.
- $M_R \ll m_D$, the pseudo-Dirac limit: For each active and sterile pair, the Majorana neutrino mass eigenstates have nearly degenerate masses of order m_D with mass differences of order M_R. They combine into pseudo-Dirac neutrinos, which behave almost like a Dirac neutrino, see for instance ref. [59, 60].

[37] See eq. (2.16) for the definition of the charge conjugation, and recall that $\psi^c_R = (\psi_R)^c = (\psi^c)_L$ is a left-chiral field.

- $M_R \sim m_D$, the active-sterile mixed case: All mass eigenstates contain active and sterile neutrino states of roughly the same order.
- $M_R \gg m_D$, the seesaw limit: There are heavy neutrino mass eigenstates with masses of order M_R which are composed of mainly sterile states, and light neutrino mass eigenstates with masses of order $(m_D)^2/M_R$ which are composed of mainly active neutrino states. The suppression m_D/M_R yields an explanation why the observed neutrinos are much lighter than the weak scale.

The seesaw limit of the neutrino mass term described by $\mathscr{L}_{\text{type I}}$ in eq. (2.31) is referred to as type-I seesaw [18–22]. The Lagrangian $\mathscr{L}_{\text{type I}}$ together with the SM is seen as the full renormalisable theory, and in the seesaw limit, one can integrate out the heavy neutrinos and obtain the SM with neutrino masses from the Weinberg operator eq. (2.22) as the low-energy theory.

For the diagonalisation, the mass matrix $\mathcal{M}'$ can be diagonalised by a two step approach: First block-diagonalise $\mathcal{M}'$ and second diagonalise each block separately by two unitary transformations. This procedure has been investigated in, e.g., ref. [61–63]. The unitary matrix for the block-diagonalisation can be expressed as the exponential of an antihermitian matrix [61]

$$U_{BD} = \exp\begin{pmatrix} 0 & \Theta \\ -\Theta^\dagger & 0 \end{pmatrix} = \begin{pmatrix} \mathbb{1} - \frac{1}{2}\Theta\Theta^\dagger & \Theta \\ -\Theta^\dagger & \mathbb{1} - \frac{1}{2}\Theta^\dagger\Theta \end{pmatrix} + \mathcal{O}(\Theta^3)\,. \tag{2.38}$$

In the seesaw limit ($M_R \gg m_D$), the matrix Θ can be treated as a perturbation

$$\Theta \simeq m_D^\dagger M_R^{\dagger -1}\,, \tag{2.39}$$

and is referred to as the active-sterile mixing matrix. The unitary matrix for the block-diagonalisation reads in the seesaw limit as

$$U_{BD} \simeq \begin{pmatrix} \mathbb{1} - \frac{1}{2} m_D^\dagger (M_R M_R^\dagger)^{-1} m_D) & (M_R^{-1} m_D)^\dagger \\ -(M_R^{-1} m_D) & \mathbb{1} - \frac{1}{2}(M_R^{-1} m_D m_D^\dagger M_R^{\dagger -1}) \end{pmatrix}\,, \tag{2.40}$$

to order $\mathcal{O}\left(m_D^\dagger M_R^{\dagger -1}\right)$. The block-diagonal mass matrix is then given by

$$\mathcal{M}_{BD} \simeq \begin{pmatrix} -m_D^T M_R^{-1} m_D & 0 \\ 0 & M_R \end{pmatrix}\,. \tag{2.41}$$

Usually, the upper left 3×3 sub-block is referred to as the light neutrino mass matrix

$$m_\nu' = -m_D^T M_R^{-1} m_D\,. \tag{2.42}$$

The block-diagonal matrix $\mathcal{M}_{BD}$ can be diagonalised by diagonalising each block separately. The resulting unitary matrix $\mathcal{U}$ for the diagonalisation of the mass matrix $\mathcal{M}'$ is then given by

$$\mathcal{U} = U_{BD} \begin{pmatrix} U^\nu & \\ & U^N \end{pmatrix} = \begin{pmatrix} N & B \\ C & D \end{pmatrix}\,. \tag{2.43}$$

As a result of the seesaw mechanism, there are 3 so-called light neutrino mass eigenstates, which are mostly composed of the active neutrinos. Their mass matrix is given by $m'_\nu = -m_D^T M_R^{-1} m_D$ which results in masses of the order $m_\nu \sim m_D^2/M_R$. The n_S so-called heavy neutrino mass eigenstates are mostly composed of the sterile states. Their mass matrix is given to leading order by M_R.

Note that from the unitarity condition of $\mathcal{U}$ the sub-matrices fulfil, among others, the following equations

$$\mathcal{N}\mathcal{N}^\dagger + BB^\dagger = \mathbb{1} \qquad \text{and} \qquad \mathcal{N}^\dagger\mathcal{N} + C^\dagger C = \mathbb{1}\,. \tag{2.44}$$

This implies that the sub-matrix $\mathcal{N}$, which represents the 3×3 active-light mixing matrix, is not necessarily unitary. Generally speaking, the leptonic mixing matrix, i.e. the leptonic PMNS mixing matrix, is given by $U_L^{\ell\dagger}\mathcal{N}$ [38]. In the basis where the charged lepton mass matrix is diagonal the PMNS matrix is just $\mathcal{N}$. The non-unitarity is a generic feature of additional heavy particles that mix with the light neutrinos or the charged leptons, see e.g. ref. [64].

[38] Since for the charged weak current $J^\mu_W = \frac{g_2}{\sqrt{2}}\overline{\nu_k}\gamma^\mu(\mathcal{U}^\dagger)_{k\alpha}(U_L^\ell)_{\alpha\beta}\ell_{\beta\,L} = \frac{g_2}{\sqrt{2}}\overline{\nu_k}\gamma^\mu(U^\dagger)_{k\beta}\ell_{\beta\,L}$.

The neutrino flavour eigenstates are defined in analogy to the previous discussions as

$$\nu_{\alpha L} = U_{\alpha k}\nu_k\,, \quad k = 1,\ldots,n_S\,, \tag{2.45}$$

where the mixing matrix is given by the $3\times n_S$ sub-block $U = U_L^{\ell\dagger}\begin{pmatrix}\mathcal{N} & B\end{pmatrix}$ (or simply by $U = \begin{pmatrix}\mathcal{N} & B\end{pmatrix}$ in the mass basis of the charged leptons). As we see in the last equation, the flavour eigenstates are a combination of the massive light and heavy neutrino states in the Majorana case. The heavy neutrino mass eigenstates, which are composed mostly of the sterile neutrinos do participate in the weak interaction due to a non-vanishing mixing of the active and sterile neutrinos. The mixing of the active and sterile states is governed by the active-sterile mixing matrix Θ in eq. (2.39). Contrary to the Dirac case where the mass eigenstates of the active and sterile states do not mix. Note that the $3\times n_S$ mixing matrix U is also not unitary, although $UU^\dagger = \mathbb{1}$, the combination $U^\dagger U$ yields usually not the identity matrix.

3

EXPERIMENTAL NEUTRINO PHYSICS - A BRIEF OVERVIEW

In this chapter we aim at providing a brief overview on the experimental status of neutrino physics. We cover various neutrino experiments and the experimental measurements for neutrino masses and mixing. We focus on neutrino oscillation experiments, to this end, the concept of neutrino flavour oscillations is discussed. For a more comprehensive coverage see, for instance, the particle physics review ref. [17, 65], articles on neutrino physics ref. [66–68], reviews with many references [25, 26, 36] and books [28, 29]. Throughout this chapter we follow ref. [28, 29].

3.1 NEUTRINO OSCILLATIONS

Neutrino flavour oscillations were proposed by Pontecorvo [11] after the discovery of the muon neutrino in the 1960s. He suggested the $\nu_e \to \nu_\mu$ flavour transitions to be taking place for neutrinos coming from the sun, which is the main physical explanation to the solar neutrino problem, see in section 3.2 on solar neutrino experiments.

Neutrino flavour oscillations are quantum mechanical phenomena as a consequence of neutrino mixing. Oscillations occur when neutrino mass eigenstates cannot be distinguished, i.e. they are coherently produced and detected due to their tiny mass differences. The neutrino oscillation probability in vacuum can easily be derived in the plane wave approximation [69–73].

To start with, the neutrino mixing of the flavour fields, $\nu_{\alpha L} = (U_{PMNS})_{\alpha k}\nu_k$ in eq. (2.12), are a linear combination of the mass eigenstate fields weighted by the elements of the unitary mixing matrix. In terms of one-particle states, however, the created neutrino flavour state with momentum $\vec{p}$ is related by

$$|\nu_\alpha\rangle = (U^*_{PMNS})_{\alpha k}\,|\nu_k\rangle \ , \tag{3.1}$$

due to the charged weak current term $J^\mu_W = \frac{g_2}{\sqrt{2}}\overline{\nu_k}\gamma^\mu(U^\dagger_{PMNS})_{k\beta}\ell_{\beta L}$ creating a neutrino together with an antilepton when invoking the field operators, see e.g. ref. [26, 74]. With the description in ref. [74], the massive neutrino states have a definite mass $m_k \equiv m_{\nu_k}$ and definite energy $E_k = \sqrt{|\vec{p}|^2 + m_k^2}$, thus they evolve in time as

$$|\nu_k(t)\rangle = e^{-iE_k t}\,|\nu_k(t=0)\rangle = e^{-iE_k t}\,|\nu_k\rangle \tag{3.2}$$

in the plane wave approximation. For the flavour states it immediately follows that [39]

$$|\nu_\alpha(t)\rangle = \sum_k (U^*)_{\alpha k} e^{-iE_k t}\,|\nu_k\rangle = \sum_\beta \left(\sum_k (U^*)_{\alpha k}(U)_{\beta k} e^{-iE_k t}\right)|\nu_\beta\rangle \ , \tag{3.3}$$

[39] In order to save space: $U \equiv U_{PMNS}$.

where the expression in parenthesis is the transition amplitude from flavour α to β. The flavour state, initially consisting only of the flavour α at $t = 0$, becomes at times $t > 0$, in general, a superposition of the different flavour states. The probability to transition from flavour α to β is given by

$$P(\nu_\alpha \to \nu_\beta) = \left|\langle \nu_\beta | \nu_\alpha(t)\rangle\right|^2 = \sum_{k,j} (U^*)_{\alpha k}(U)_{\beta k}(U)_{\alpha j}(U^*)_{\beta j} e^{-i(E_k - E_j)t} \,. \tag{3.4}$$

[40] Since neutrino masses are tiny compared to the energy of the detectable neutrinos, $\vec{p}^2 \gg m_k^2$, they can always be considered as ultrarelativistic.

For ultrarelativistic neutrinos[40], the energy can be approximated as

$$E_k = \sqrt{|\vec{p}|^2 + m_k^2} \approx |\vec{p}| + \frac{m_k^2}{2E} \,, \tag{3.5}$$

since $|\vec{p}| \approx E$. Assuming the same momentum for all massive neutrino, the transition probability reads

$$P(\nu_\alpha \to \nu_\beta, t) = \sum_{k,j} (U^*)_{\alpha k}(U)_{\beta k}(U)_{\alpha j}(U^*)_{\beta j} \exp\left(-i\frac{\Delta m_{kj}^2}{2E} t\right) , \tag{3.6}$$

where Δm_{kj}^2 defines the mass squared differences as

$$\Delta m_{kj}^2 = m_k^2 - m_j^2 \,. \tag{3.7}$$

[41] Instead of trying to resolve the time dependent transitions, the experiments are designed to measure the transition probabilities for a known distance L from the neutrino source.

Since ultrarelativistic neutrinos propagate at almost the speed of light, the time dependence[41] can be replaced by $L \approx t$, and one obtains the standard neutrino oscillation formula

$$P(\nu_\alpha \to \nu_\beta, L) = \sum_{k,j} (U^*)_{\alpha k}(U)_{\beta k}(U)_{\alpha j}(U^*)_{\beta j} \exp\left(-i\frac{\Delta m_{kj}^2}{2E} L\right) . \tag{3.8}$$

In order for the flavour oscillations to occur, neutrinos need to have non-degenerate masses and non-vanishing leptonic flavour mixing. We note that the amplitudes are constant and fixed by the mixing matrix elements, and that the phases are fixed by the mass squared differences for a given experiment. Hence, the values for the elements of the mixing matrix as well as the mass squared differences can be inferred from neutrino oscillation experiments. However, two features cannot be accessed by neutrino oscillations, the absolute mass scale and possible CP violating Majorana phases[42].

[42] The Majorana phases cancel in the neutrino oscillation formula. Hence, neutrino flavour oscillations experiments cannot distinguish Dirac or Majorana neutrinos.

It can be convenient to split the sum of the oscillation formula into two parts a constant and an oscillatory term

$$\begin{aligned} P(\nu_\alpha \to \nu_\beta, L) = &\sum_k |(U)_{\alpha k}|^2 |(U)_{\beta k}|^2 \\ &+ 2\,\mathrm{Re}\left(\sum_{k>j} (U^*)_{\alpha k}(U)_{\beta k}(U)_{\alpha j}(U^*)_{\beta j} \exp\left(-i\,2\pi \frac{L}{L_{kj}^{osc}}\right)\right) , \end{aligned} \tag{3.9}$$

where the so-called oscillation length

$$L_{kj}^{osc} = \frac{4\pi E}{\Delta m_{kj}^2} \,, \tag{3.10}$$

has been introduced. Note that the oscillating term is present due to the interference of the massive neutrino states ν_k, and therefore dependent on their coherence[43].

The neutrino oscillation formula can be classified in 3 regimes:

- For $L \ll L^{osc}$: The initial flavour state is maintained, $P(\nu_\alpha \to \nu_\beta, L) \approx \delta_{\alpha\beta}$.
- For $L \gg L^{osc}$: Coherence can be lost, the oscillatory term is averaged and thus the oscillation pattern vanishes. Flavour transitions are still possible, the probability becomes $P(\nu_\alpha \to \nu_\beta, L) \approx \sum_k |(U)_{\alpha k}|^2 |(U)_{\beta k}|^2$.
- For $L \sim L^{osc}$: Experiments aim to operate in this regime, since the oscillation effect from Δm^2_{kj} can be measured the best.

There are two approaches that experiments can use to detect the flavour oscillations from a neutrino beam. Either by an appearance experiment, viz. searching neutrinos ν_β from a beam starting with neutrinos ν_α. This experiment measures the so-called transition probability $P(\nu_\alpha \to \nu_\beta)$. Or by a disappearance experiment, viz. searching the remaining ν_α starting from a neutrino beam with ν_α. This experiment measures the so-called survival probability $P(\nu_\alpha \to \nu_\alpha)$.

In a simplified model with two neutrinos only, the leptonic mixing matrix is parametrized by one mixing angle θ [44] and there is one mass squared difference Δm^2. In this simplified model, the transition probability results in

$$P(\nu_\alpha \to \nu_\beta, L) = 2\sin^2(2\theta)\sin^2\left(\frac{\Delta m^2}{4E}L\right), \tag{3.11}$$

while the survival probability results in

$$P(\nu_\alpha \to \nu_\alpha, L) = 1 - 2\sin^2(2\theta)\sin^2\left(\frac{\Delta m^2}{4E}L\right). \tag{3.12}$$

As stated above, experiments aim at operating in the regime $\frac{\Delta m^2}{4E}L \sim 1$, in SI units the ratio reads [29]

$$1.27\frac{\Delta m^2[eV^2]}{4E[GeV]}L[km] \sim 1. \tag{3.13}$$

The probability for neutrino oscillations in the plane wave approximation can be derived, in general, for any number of neutrinos. For the case of 3 neutrinos, the oscillation formulas can be found, for instance, in [65]. We also note that the derivation for the antineutrinos [45] can be treated analogously. The survival probability for antineutrinos remains the same as for neutrinos, $P(\nu_\alpha \to \nu_\alpha) = P(\overline{\nu}_\alpha \to \overline{\nu}_\alpha)$, which is guaranteed by the CPT theorem[46]. The transition probability $P(\overline{\nu}_\alpha \to \overline{\nu}_\beta)$, however, can be different from $P(\nu_\alpha \to \nu_\beta)$. This difference measures the amount of CP violation in the lepton sector, see e.g. ref. [65] for further information.

We comment that although the plane wave approximation is simple and gives the correct result, the underlying assumptions are wrong [76]. Consistent approaches are, the wave packet approach in quantum mechanics [77–79] or in quantum field theory [80–85]. See for instance ref. [86] which compares both approaches.

[43] The oscillation pattern vanishes if neutrinos are produced or detected incoherently, or propagate over too long distances [75]. Loss of coherence can be understood in the framework of wave packets rather than plane waves, see the comment at the end of the section.

[44] The mixing matrix reads $U = \begin{pmatrix} \cos\theta & \sin\theta \\ -\sin\theta & \cos\theta \end{pmatrix}$.

[45] It is customary to speak of neutrinos and antineutrinos also in the Majorana case, given that neutrinos in oscillation experiments are ultrarelativistic. By convention Majorana neutrinos with negative (positive) helicity are referred to as neutrinos (antineutrinos), see section 6.2.3 of ref. [28].

[46] CPT theorem implies $P(\nu_\alpha \to \nu_\beta) = P(\overline{\nu}_\beta \to \overline{\nu}_\alpha)$

3.2 OSCILLATION EXPERIMENTS

As discussed in the previous section, neutrino flavour oscillations can be detected in an appearance or disappearance experiments. The characteristics of a neutrino oscillation experiment are the average energy E of the produced neutrinos and the baseline L, i.e. the distance between the neutrino source and the detector. In order to best probe the oscillation effect and the dependency on the mass squared differences , which are defined in eq. (3.7), the condition in eq. (3.13) is satisfied for the operating regime. In the following, we give a brief overview and selection of the neutrino oscillation experiments [25, 28, 29]:

NUCLEAR REACTOR EXPERIMENTS: Production of $\overline{\nu}_e$ from β-decay of heavy nuclei. The antineutrinos have an average energy of order MeV.

- SBL[47], $L \sim \mathcal{O}(10\,\mathrm{m})$: ILL [87], Gosgen [88], Rovno [89], Krasnoyarsk [90], Bugey [91], Savannah River [92], NEOS [93].
- LBL[48], $L \sim \mathcal{O}(1\,\mathrm{km})$: CHOOZ [94], Palo Verde [95], Double CHOOZ [96], Daya Bay [97], RENO [98].
- VLBL[49], $L \sim \mathcal{O}(100\,\mathrm{km})$: KamLAND [99], JUNO [100].

[47] Short base line (SBL)

[48] Long base line (LBL)

[49] Very long base line (VLBL)

ACCELERATOR EXPERIMENTS: Accelerators can produce a high energy neutrino beam in the energy range of order 1 to 100 GeV. The neutrinos originate from the decay of pions, kaons or muons.

- SBL, $L \sim \mathcal{O}(1\,\mathrm{km})$: From pion and kaon decay: CHARM [101], BNL-E776 [102], CHORUS [103], NOMAD [104], LSND [105], NuTeV [106]. From muon decay: LSND [107], KARMEN [108]. From Beam dump : BEBC [109], CHARM [110], CDHSW [111].
- LBL, $L \sim \mathcal{O}(10^3\,\mathrm{km})$: K2K [112], MINOS [113], OPERA [114], T2K [115], NOνA [116], DUNE [117].

SOLAR NEUTRINO EXPERIMENTS: Experiments that detect the produced ν_e from thermonuclear fusion of the Sun. Neutrinos have an energy of order MeV and travel a distance of about $1.5 \cdot 10^{11}$ km to the Earth. The first solar neutrino experiment was Homestake [118] in the 1970s. It measured a solar neutrino flux much smaller as expected from the standard solar models, see for instance ref. [119, 120] and references therein. This discrepancy is referred to as the solar neutrino problem. More solar neutrino experiments have been performed since then: Kamiokande [121], Super-Kamiokande [122], GALLEX [123], SAGE [124], GNO [125], SNO [126], BOREXINO [127]. The experimental confirmation that neutrino oscillations are the underlying mechanism which explain the solar neutrino problem[50] , was obtained by SNO [16] in 2002.

[50] The Mikheyev–Smirnov–Wolfenstein effect [13–15] plays a crucial role in this regard. It is an oscillation effect occurring inside objects of dense matter, such as the Sun.

ATMOSPHERIC NEUTRINO EXPERIMENTS: Atmospheric neutrinos are produced as a byproduct of a cosmic ray interacting with the atmosphere. The cosmic rays produce a cascade of pions and kaons which decay into muons and neutrinos, the muons further decay into electrons and neutrinos which can be detected by experiments. The energy for the neutrinos ranges in the order of 1 to 100 GeV and they travel distances

of order 10 km to 10^4 km before being detected[51]. Experiments that measure atmospheric neutrinos are Kamiokande [128], IMB [129], NUSEX [130], Frejus [131], Super-Kamiokande [12], MACRO [132], Soudan-2 [133], IceCube [134]. In 1998, Super-Kamiokande delivered experimental evidence for the oscillation of atmospheric neutrinos [12]. The Nobel prize was awarded for the discovery of neutrino oscillations (Super-Kamiokande and SNO) in 2015.

[51] Large distances can be achieved when neutrinos are produced on the other side of the Earth and consequently travelling through the Earth to where the experiment is located.

In order to explain the oscillation data at least 3 light neutrinos are required. There are the flavour eigenstates ν_e, ν_μ and ν_τ, and the corresponding mass eigenstates ν_1, ν_2 and ν_3. Depending on Dirac or Majorana nature of the neutrinos, the leptonic mixing matrix, the PMNS matrix, is given by either eq. (2.14) or eq. (2.30)[52]. The mixing angles are chosen in the convention of ref. [65], see fig. 1: The so-called solar parameters[53], θ_{12} and Δm^2_{21}, drive the oscillation of ν_e into the flavour μ. The so-called atmospheric parameters[54], θ_{23} and Δm^2_{32}, drives the oscillation of ν_μ. The so-called reactor neutrino mixing angle θ_{13}, which is usually measured in reactor neutrino experiments, is then the smallest mixing angle.

[52] Although as stated in the previous section, the Majorana phases cancel out for neutrino flavour oscillation experiments.

[53] The name originates from the solar neutrino experiments.

[54] The name originates from the atmospheric neutrino experiments.

We note that neutrino oscillation experiments are only sensitive to mass squared differences and that only two of them are independent in the 3 neutrino mixing case. From the neutrino oscillation data, the value for Δm^2_{21} has been determined, while for Δm^2_{32} only the absolute value. Therefore, two patterns of neutrino mass orderings are possible depending on the sign of Δm^2_{32}:

- Normal ordering (NO) of the neutrino masses: For $\Delta m^2_{32} > 0$, the mass ordering is given by $m_1 < m_2 < m_3$.
- Inverse ordering (IO) of the neutrino masses: For $\Delta m^2_{32} < 0$, the mass ordering is given by $m_3 < m_1 < m_2$.

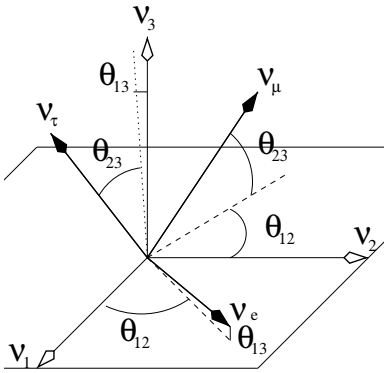

Figure 1: The flavour state basis in relation with the mass eigenstate basis in terms of the 3 mixing angles and setting the phases to 0. Reprinted with permission from ref. [37], copyright 2013 by IOP Publishing Ltd.

We give a summary in tab. 1 of the best fit values obtained in a global analysis from oscillation data in the three neutrino mixing case from ref. [135], cf. ref. [136, 137] for other recent global fits. We note that Dirac CP phase δ favours a value of $\sim 3\pi/2$, although with a rather large uncertainty and no further experimental evidence, it is still rather unclear whether CP is violated or conserved. The resulting composition of the massive states for the two different orderings are illustrated in fig. 2, taken from ref. [37]. In the figure, the left plot corresponds to the NO pattern, while the right plot corresponds to the IO pattern. The measurement of the mass squared differences reveals that at least two of the neutrinos have a non-vanishing mass. The absolute masses of the neutrinos cannot be determined in neutrino oscillation experiments, they are still unknown. The lightest neutrino could have no mass at all, it could be massless.

Despite the success of the 3 neutrino mixing framework in explaining most of the neutrino oscillation data, there exist a few experimental results that cannot be explained within. They are referred to as neutrino anomalies.

NEUTRINO ANOMALIES: A solution to these anomalies might require additional neutrinos, usually sterile neutrinos are proposed. For a review covering the anomalies see ref. [25] and references therein.

Parameter	Best fit	1σ range	Best fit	1σ range
	NO ($m_1 < m_2 < m_3$)		IO ($m_3 < m_1 < m_2$)	
$\sin^2\theta_{12}/10^{-1}$	3.06	2.94 — 3.18	3.06	2.94 — 3.18
$\sin^2\theta_{23}/10^{-1}$	4.41	4.20 — 4.68	5.87	5.63 — 6.07
$\sin^2\theta_{13}/10^{-2}$	2.166	2.091 — 2.241	2.179	2.093 — 2.255
$\delta/^\circ$	261	202 — 312	277	231 — 317
$\Delta m^2_{21}/10^{-5}$ eV^2	7.50	7.33 — 7.69	7.50	7.33 — 7.69
$\Delta m^2_{3\ell}/10^{-3}$ eV^2	2.524	2.485 — 2.563	−2.514	−2.555 — −2.476

Table 1: The best-fit values with the 1σ ranges for the parameters of 3 neutrino mixing from a global fit analysis done in ref. [135]. Note that for NO, $\Delta m^2_{3\ell} = \Delta m^2_{31} > 0$, while for IO, $\Delta m^2_{3\ell} = \Delta m^2_{32} < 0$.

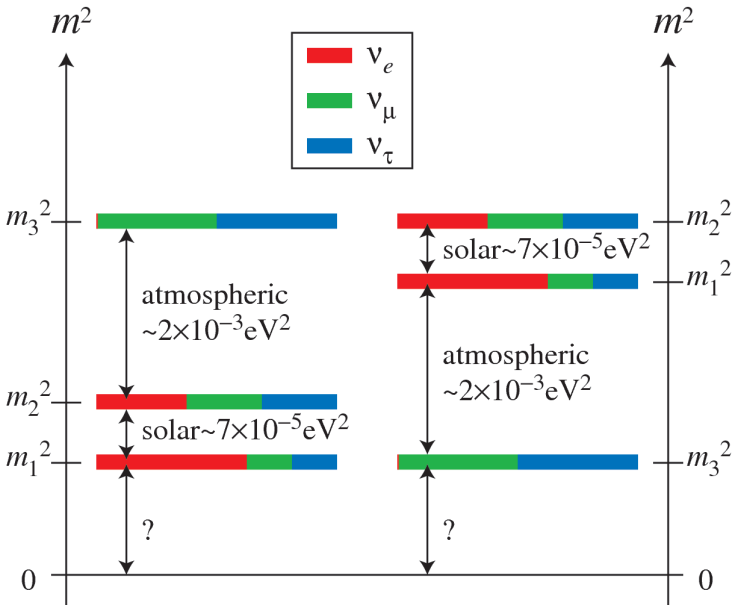

Figure 2: Shown are the two possible neutrino mass orderings. On the left NO and IO on the right. For each massive state the probability to contain the respective flavour eigenstates is shown by the colored amount. The absolute mass scale is not accessible by neutrino oscillation experiments, the mass of the lightest neutrino is unknown and represented by the question marks. Reprinted with permission from ref. [37], copyright 2013 by IOP Publishing Ltd.

- LSND anomaly: Appearance experiment observing a much larger mass squared difference [107], requiring a fourth neutrino - a sterile neutrino. The LSND result is controversial.
- MiniBooNE anomaly: The MiniBooNE experiment is designed to verify LSND's controversial result. In the early stages of the experiment, the significance of the anomaly has decreased[138–140] but was still consistent with the LSND result. The very recent MiniBooNE data has made the anomaly much more pronounced [141].

- Gallium anomaly: The GALLEX [142] and SAGE [143, 144] experiment have measured a ν_e deficit at very short baselines, possibly due to ν_e disappearance.
- Reactor antineutrino anomaly: Discrepancy of measured reactor antineutrino fluxes with expectation from theory [145].

The anomalies would be compatible with a fourth sterile neutrino that satisfies the mass squared difference $\Delta m^2_{\text{sterile}} > 1\ \text{eV}^2$.

Although, neutrino oscillation experiments provide a lot of information on leptonic mixing and mass ordering[55], they cannot provide any information on the neutrino mass scale, i.e. the mass of the of the lightest neutrino, nor on the nature of neutrino masses, i.e. if they are Dirac or Majorana. Conceptually different experiments are required in order to tackle these two short comings, which we discuss in the following sections.

[55] The mass ordering can be determined by oscillation experiments once they measure the sign of Δm^2_{32} or, equivalently, Δm^2_{31}.

3.3 DIRAC OR MAJORANA NATURE?

The Dirac or Majorana nature of neutrinos can be discerned by probing lepton number violating processes where neutrinos are involved.

NEUTRINOLESS DOUBLE BETA DECAY EXPERIMENTS: The most promising process of this kind is the so-called neutrinoless double-β decay ($0\nu\beta\beta$) of nuclei. This process takes a simple form such as $N(A,Z) \to N(A,Z+2) + 2e^-$, where no antineutrinos are emitted as in the usual double-β^- decay. The corresponding Feynmandiagram is shown in fig. 3. This process violates the total lepton number $\mathbb{L}$ by two units and is allowed if neutrinos are massive Majorana particles. Even if there are other lepton number violating processes that are the dominant contribution to $0\nu\beta\beta$, still massive Majorana neutrinos are guaranteed by the so-called black box theorem [146]. See ref. [147] for a recent review on $0\nu\beta\beta$.

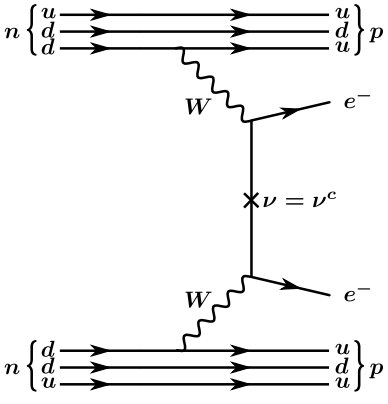

Figure 3: Feynmandiagram for $0\nu\beta\beta$ process is shown. The exchange of neutrinos is only possible when the massive neutrinos are Majorana particles.

3.4 NEUTRINO MASS SCALE EXPERIMENTS

The values for the mass squared differences imply that one neutrino should have at least a mass of $\sqrt{\Delta m^2_{31}} \sim 0.05$ eV. There are several methods used in order to extract the absolute mass scale.

BETA DECAY EXPERIMENTS: Measuring the β decay spectrum of nuclei near the endpoint, gives upper bounds on the effective neutrino mass $m^2_\beta = \sum_k |U_{ek}|^2 m^2_k$. The performed tritium β decay experiments performed by the Mainz [148] and Troitsk [149] experiments yielded the most precise measurements. The combined bound is given by $m_\beta \leqslant 1.8$ eV [150]. The KATRIN experiment is also based on the β decay of tritium and plans to be sensitive down to $m_\beta \sim 0.2$ eV [151].

NEUTRINOLESS DOUBLE BETA DECAY EXPERIMENTS: While the two charged leptons have a continuous spectrum in double-β decay, they have a monochromatic spectrum in $0\nu\nu\beta$. In $0\nu\nu\beta$ the decay rate is proportional to $m_{\beta\beta} = \left|\sum_k U^2_{ek} m_k\right|$. A list of selected experiments: IGEX

[152], HDM [153], SOLOTVINO [154], CUORICINO [155], KamLAND-Zen [156], NEMO-3 [157], GERDA [158], EXO [159], CUORE [160], MAJORANA [161].

It is also possible to derive constraints on the absolute neutrino masses from cosmological or astrophysical observations, see for instance [162].

3.5 CONSTRAINING THE STERILE NEUTRINO MASS SCALE

In section 2.2 we considered the pseudo-Dirac limit ($M_R \ll m_D$), the active-sterile mixed case ($M_R \sim m_D$), and the seesaw limit ($M_R \gg m_D$), as cases which relate the sterile neutrino mass matrix and the Dirac mass matrix. The experimental data from neutrino oscillation experiments help to constrain these cases by the non-observation of neutrino oscillations into sterile states. This is possible due to the non-vanishing active-sterile mixing of the neutrinos. Fig 4, taken from ref. [163], illustrates the allowed masses M_N for the mass eigenstates of the sterile neutrinos. The figure is subdivided in 3 regions due to the experimental constraints from neutrino oscillation data. The 3 regions roughly correspond to the above considered cases. In the pseudo-Dirac limit, masses $M_N \gtrsim 10^{-9}$ eV are constrained by neutrino oscillations data [163, 164]. The active-sterile mixed case is ruled out up to $M_N \sim 10^{-1}$ eV [164, 165]. For the seesaw limit, the scale M_N is almost unconstrained and may be as low as 1 eV.

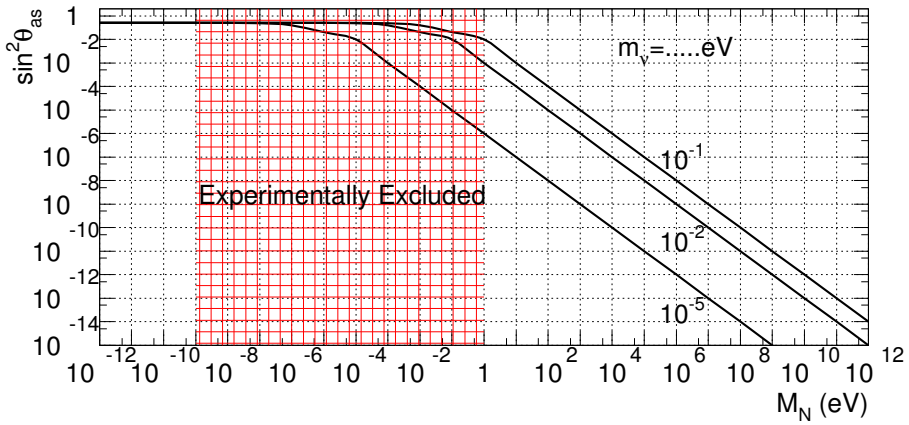

Figure 4: The figure shows the excluded and allowed values for the mass M_N of the mass eigenstates of the sterile neutrinos from neutrino oscillation experiments. Shown is also an estimate for the magnitude of the active-sterile mixing as a function of M_N, for different values of the mostly active neutrino masses. Reprinted with permission from ref. [163], copyright 2009 by American Physical Society.

4 ELECTROWEAK SCALE STERILE NEUTRINOS

In this chapter, we discuss the seesaw scenario that is employed as the benchmark scenario for the investigation of the sterile neutrino phenomenology at colliders. In section 4.1, we discuss the different motivations for sterile neutrinos at various mass scales. We focus on electroweak (EW) scale sterile neutrinos in the context of low scale seesaw scenarios and their natural explanation for the smallness of neutrino masses in section 4.2. The benchmark scenario based on the low scale seesaw scenario with $n_S = 2$ sterile neutrinos is specified in section 4.3. The implementation of the benchmark model is discussed and validated in section 4.4.

4.1 THE MOTIVATED MASSES RANGES FOR STERILE NEUTRINOS

Since the mass scale for the sterile neutrinos, i.e. the mass of the heavy neutrino, is almost unconstrained in the seesaw limit, it is useful to discuss experimentally motivated hints as well as theoretically motivated predictions for specific mass scales. Various possibilities for the heavy neutrino mass scale are considered and discussed in the literature, ref. [25, 166] review many of this possibilities.

In order to motivate some specific mass scales outside the realm of neutrino masses and mixing, we need to broaden our perspective. Starting from the SM and the present cosmological model ΛCDM [167], which is based on general relativity as the theory of gravity, as the current theoretical framework, there are several open questions that are not understood in this framework [56]. These questions are related to observed phenomena in particle physics as well as cosmology which are deemed as new physics by the community. There are 3 major open questions that are widely accepted by the community to be related to particle physics and which may also be related to sterile neutrinos. These 3 open questions are as follows:

- The smallness of neutrino masses and mixing in the lepton sector.
- The baryon asymmetry of the universe (BAU), which is the question after the origin of the baryonic matter in the early universe, confer for instance ref. [168].
- The origin and composition of dark matter (DM).

Each of these phenomena may have preferred mass scales for the sterile neutrinos, either motivated by an underlying theory or experimental observations. For instance, various theoretical frameworks of neutrino mass predict different mass scales for sterile neutrinos, see e.g. [25, 169, 170]. Or the matter-antimatter asymmetry is explained by leptogenesis and its different scenarios involving sterile neutrinos, see, e.g, ref. [166] and references therein. Furthermore, it is possible to explain some of the phenomena simultaneously by combining sterile neutrinos of different mass scales. Because the mass matrix

[56] We keep the list of open questions short by mentioning some of the keywords, it is by no means meant to be an exhaustive or complete list: Neutrino masses, baryon asymmetry of the universe, dark matter, flavour puzzle, strong CP problem, hierarchy problem, flatness and horizon problem, dark energy.

of the sterile neutrinos can have different eigenvalues M_{Ni}, which are associated to a mass scale, in different mass ranges. Ref. [166] summarises the various motivated mass scales as follows:

- $M_{Ni} \gtrsim 10^9$ GeV: Such a large mass scale gives a straightforward explanation for the smallness of neutrino masses, with neutrino Yukawa couplings similar to the other fermions [57], by the scale suppression of the standard seesaw mechanism, see section 2.2. Mass scales in this range are theoretically motivated by Grand Unified Theories (GUT) [171]. For instance, SO(10) GUT models [172] predict the same number of sterile neutrinos as families for the quarks and leptons. Moreover, the BAU can be generated via out-of-equilibrium decays of the heavy neutrinos referred to as thermal leptogenesis [173, 174], see for instance [166, 169, 175] and references therein.

- $M_{Ni} \sim$ EW scale: Around this mass scale, sterile neutrinos have the possibility to be tested in accelerator experiments . From a theoretical point of view it is minimal in the sense that there is no new physics scale. All the physics is introduced around the EW scale. This avoids a hierarchy problem that would arise when two very different scales should explain physics at one specific scale. The matter-antimatter asymmetry can be explained, for masses above the EW scale, via resonant leptogenesis [176] while for masses below the EW scale via leptogenesis from right-handed neutrino oscillations [177], cf. also, e.g., [178–181].

- $M_{Ni} \sim$ keV: In this mass range, sterile neutrinos are considered as possible viable candidates for DM [182] because they can be very long-lived due to a very small active-sterile mixing to the active neutrino. For an overview see, e.g., [25, 166, 183, 184] and references therein.

- $M_{Ni} \sim$ eV: Experimentally motivated by the observed anomalies in neutrino oscillation data, see section 3.2.

[57] Neutrino Yukawa couplings of order 1 requires a mass of the heavy neutrino of order 10^{14} GeV for a light neutrino mass of 0.1 eV.

There are well motivated specific mass ranges for sterile neutrinos. We note that different frameworks are possible that explain neutrino oscillations, BAU and DM simultaneously by involving neutrinos at different mass scales. A prominent example in this regard is the so-called neutrino minimal standard model[58] (νMSM) [185, 186].

In summary, sterile neutrinos can be basically motivated from the eV scale up to the GUT scale.

A guiding principle is that whatever the preferences for the mass scales are, they should lead to testable predictions. To this end, a driving question of this thesis is: What aspects of the sterile neutrino phenomenology could be tested with the future particle accelerators in mind? In order to investigate this question, EW sterile neutrinos are compelling due to their kinematical accessibility.

But immediately one is confronted by the following fact. By invoking the usual seesaw mechanism, in order to explain the smallness of neutrino masses, the heavy neutrino mass eigenstates would be much too weakly coupled to the SM to be produced at particle accelerators. The reason is that sterile neutrinos interact only via their Yukawa couplings to the SM, which become

[58] It posits 3 sterile neutrinos, 2 of which have degenerate masses of order 10 GeV, and 1 of which has a mass of order 1 keV. The electroweak scale sterile neutrino generate the light neutrino masses via the seesaw mechanism and at the same time they are responsible for the BAU, while the keV neutrino comprises the DM candidate.

quite small when the scale suppression of the usual seesaw mechanism is due to EW scale sterile neutrinos rather than GUT scale ones [59]. This remains a problem even for the future and far more advanced particle accelerators. However, naturally small masses from the light neutrino mass matrix, $m'_\nu = -m_D^T M_R^{-1} m_D$, are not only achieved by the usual scale suppression from the sterile neutrino mass matrix in the usual seesaw mechanism. But can also be achieved by a cancellation among the contributions to m'_ν without relying on a large mass scale nor small Yukawas. Such a cancellation, however, requires a good explanation otherwise the cancellations amount to a fine tuning problem.

Indeed an explanation for the cancellations can be arranged in terms of symmetries, which is discussed in the next section. Seesaw scenarios that rely on cancellations for a natural explanation for the smallness of neutrino masses, do not require small neutrino Yukawa couplings nor a very large mass scale for the heavy neutrinos. Therefore, they are referred to as low scale seesaw scenarios. In these scenarios sizeable production cross sections of the heavy neutrinos at particle accelerators are possible and become thus testable in experiments. They provide an attractive framework to study particle accelerator signatures for the powerful accelerators in the foreseeable future.

[59] A mass of 0.1 eV for the light neutrino requires a neutrino Yukawa coupling of order 10^{-6} for a mass of the heavy neutrino of order 100 GeV.

4.2 LOW SCALE SEESAW SCENARIOS

In this section, we discuss the low scale seesaw scenarios for sterile neutrinos with masses around the EW scale. The main idea behind small neutrino masses is a cancellation of the different contributions to the light neutrino mass matrix $m'_\nu = -m_D^T M_R^{-1} m_D$ rather than a scale suppression by large values of M_R from the usual seesaw mechanism.

Assuming the seesaw relation, $m_\nu \sim y^2 v_{EW}^2 / M_N$, the Yukawa couplings are constrained to the order of $10^{-6}\sqrt{\frac{100\,\text{GeV}}{M_N}}$ for neutrino masses of order 0.1 eV. Since sterile neutrinos interact only via the Yukawa couplings to the SM particles, heavy neutrinos can be produced only via their active-sterile mixing with the active neutrinos. Hence, the production cross section for the heavy neutrinos becomes small in the usual seesaw. If larger neutrino Yukawa couplings are allowed, for instance ones close to experimental allowed upper limit $y \lesssim 10^{-2}$, see chapter 5.2, then contributions to the light neutrino mass matrix are of order $10^7 \frac{100\,\text{GeV}}{M_N}$ eV. Hence, a cancellation between the contributions to the light neutrino mass matrix m'_ν at the order of 10^{-8} is required to accommodate masses of order 0.1 eV. Therefore, the cancellation avoids the need for small neutrino Yukawa couplings that would otherwise lead to very small production cross section of heavy neutrinos at particle accelerators.

A natural explanation to avoid such a fine tuning problem in these cancellations can be ensured by some symmetry argument.

The concept behind the symmetry is that it leads to a specific structure of the full neutrino mass matrix which ensures vanishing light neutrino masses to leading order. Non-vanishing light neutrino masses are obtained by small perturbations of this structure once the symmetry is slightly broken. Therefore, a seesaw scenario that realises viable light neutrino masses due to a

cancellation from a symmetry argument, is a viable alternative to the usual seesaw mechanism.

In the following sections, we discuss the cancellation condition required for vanishing light neutrino masses in section 4.2.1, the cancellation structure from the conservation of a lepton-number in section 4.2.2, and how non-vanishing masses for the light neutrinos are generated in section 4.2.3. The discussion focuses on the case of $n_S = 2$ sterile neutrinos. Throughout, these discussions we follow ref. [187]. Once the content is understood, we can proceed to specify the benchmark scenario, used for our investigation of the sterile neutrino phenomenology at particle accelerators.

4.2.1 *Cancellation condition*

In this section, we discuss the requirements for an exact cancellation of the contributions to the light neutrino mass matrix m_ν'[60] following ref. [187] and references therein.

[60] $m_\nu' = -m_D^T M_R^{-1} m_D$

Let us start by noting that the m_ν' can be expressed in terms of the contributions from each right-handed neutrino in the basis where M_R is diagonal:

$$(m_\nu')_{\alpha\beta} = \sum_i (m_\nu'^{(i)})_{\alpha\beta} = \sum_i -\frac{1}{M_{N_i}} (m_D^T)_{\alpha i} (m_D)_{i\beta} \,, \tag{4.1}$$

where M_{N_i} is the eigenvalue of the sterile neutrino mass matrix M_R, which is assumed to be non-singular. In general, each sterile neutrino generates a rank 1 contribution to the light neutrino mass matrix such that, with $n_S \leqslant 3$ sterile neutrinos, there can be at most n_S massive light neutrinos. The involved Dirac mass matrix m_D can be written in terms of the contributing neutrino Yukawa vectors, and in the case of $n_S = 2$ sterile neutrinos it reads

$$m_D^T = \frac{v_{EW}}{\sqrt{2}} (\vec{y}_1 \ \vec{y}_2) \,, \quad \text{with } \vec{y}_i = (y_{ei}, y_{\mu i}, y_{\tau i})^T \,. \tag{4.2}$$

The contributions to m_ν' cancel exactly when

$$m_\nu' = m_\nu'^{(1)} + m_\nu'^{(2)} = -\frac{v_{EW}^2}{2} \left(\frac{\vec{y}_1 \vec{y}_1^T}{M_{N_1}} + \frac{\vec{y}_2 \vec{y}_2^T}{M_{N_2}} \right) = 0 \,. \tag{4.3}$$

This implies $\vec{y}_1 \propto \vec{y}_2$ for the Yukawa vectors [188, 189]. Writing the complex neutrino Yukawa vectors as

$$\vec{y}_i = y_i \vec{u} \,, \tag{4.4}$$

where $\vec{u}$ is a complex vector of unit length, one obtains the following condition from eq. (4.3)

$$\frac{v_{EW}^2}{2} \left(\frac{y_1^2}{M_{N_1}} + \frac{y_2^2}{M_{N_2}} \right) = 0 \,. \tag{4.5}$$

Consequently, the light neutrinos are exactly massless when the Dirac mass matrix, m_D, is of rank 1.

These results also apply to the more general case of $n_S = 3$ sterile neutrinos [187, 190–192].

In ref. [187], the condition (4.5) and rank 1 requirement were proven to be necessary conditions and that neutrino masses vanish to all orders in the active-sterile mixing $\Theta \simeq m_D^\dagger M_R^{\dagger -1}$.

Therefore, the values of the Yukawa matrix or equivalently the active-sterile mixing matrix, are not required to be suppressed due to the standard seesaw mechanism, but they are allowed to be larger and thus testable in experiments.

4.2.2 *Exact cancellation from a lepton-number-like symmetry*

Here, we discuss how the exact cancellation of the contributions arise due to the conservation of a lepton-number in the case of $n_S = 2$ sterile neutrinos. This case has been studied in, e.g., [187–206]. Consider that for a pair of right-handed neutrinos N_R^1, N_R^2 [61] the following lepton numbers are assigned:

[61] Note that the prime has been dropped for the fields.

$$\mathbb{L}'(\nu_L) = \mathbb{L}'(N_R^1) = -\mathbb{L}'(N_R^2) = 1\,, \tag{4.6}$$

and where the lepton number $\mathbb{L}'$ is conserved. Since this is not the ordinary lepton number, we refer to this symmetry as a lepton-number-like symmetry. Although in the literature both terminologies are used interchangeably. Under the lepton-number-like symmetry the neutrino mass term reads

$$-\frac{1}{2}\begin{pmatrix}\overline{\nu_L^c} & \overline{N_R^1} & \overline{N_R^2}\end{pmatrix}\begin{pmatrix}0 & \vec{y}\frac{v_{EW}}{\sqrt{2}} & 0\\ \vec{y}^T\frac{v_{EW}}{\sqrt{2}} & 0 & M\\ 0 & M & 0\end{pmatrix}\begin{pmatrix}\nu_L\\ N_R^{1\,c}\\ N_R^{2\,c}\end{pmatrix} + \text{H.c.}\,. \tag{4.7}$$

Due to the lepton-number assignments (4.6), the active neutrinos $\nu_{\alpha L}$ couple only to the sterile neutrino field N_R^1, while the sterile fields couple to a Dirac mass term [62], $-M\,\overline{N_R^1}N_R^{2\,c} + \text{H.c.}$. Consequently the sterile neutrino fields can be combined to a Dirac spinor

[62] When two independent left and right-chiral components couple to form a Dirac type mass term.

$$N_D = N_R^1 + N_R^{2\,c} \tag{4.8}$$

with the resulting Dirac mass term $-M\overline{N_D}N_D + \text{H.c.}$

From eq. (4.7), the 2×3 Dirac mass matrix and the Majorana mass matrix have the following symmetry structure[63]

[63] Recall that the full mass matrix, discussed in eq. (2.34), is given by $\mathcal{M}' = \begin{pmatrix}0 & m_D^T\\ m_D & M_R\end{pmatrix}$,

$$m_D = \frac{v_{EW}}{\sqrt{2}}\begin{pmatrix}\vec{y}^T\\ 0\end{pmatrix}\,,\quad M_R = \begin{pmatrix}0 & M\\ M & 0\end{pmatrix}\,. \tag{4.9}$$

It can immediately be seen that m_D is of rank 1 and that the neutrino mass matrix vanishes due to the structure ,

$$m_\nu' = -m_D^T M_R^{-1} m_D = \frac{v_{EW}^2}{2}\begin{pmatrix}\vec{y} & 0\end{pmatrix}\begin{pmatrix}0 & M\\ M & 0\end{pmatrix}\begin{pmatrix}\vec{y}^T\\ 0\end{pmatrix} = 0\,. \tag{4.10}$$

In order to reconcile the symmetry structure (4.7) with the cancellations discussed in the previous subsection 4.2.1, one has to change in the basis

where the Majorana mass matrix for the right-handed neutrinos is diagonal. This is achieved by the following unitary transformation

$$R = \frac{1}{\sqrt{2}} \begin{pmatrix} \mathbb{1} & 0 & 0 \\ 0 & 1 & \pm i \\ 0 & 1 & \mp i \end{pmatrix}, \quad R^T \mathcal{M}' R = \begin{pmatrix} 0 & \vec{y} \frac{v_{EW}}{\sqrt{2}}/2 & \pm i \vec{y} \frac{v_{EW}}{\sqrt{2}}/2 \\ \vec{y}^T \frac{v_{EW}}{\sqrt{2}}/2 & M & 0 \\ \pm i \vec{y}^T \frac{v_{EW}}{\sqrt{2}}/2 & 0 & M \end{pmatrix}, \tag{4.11}$$

where $\mathcal{M}'$ is the full mass matrix in eq. (4.7). From the resulting matrix it is trivial to see that the necessary condition for the cancellation, eq. (4.5), is fulfilled. In ref. [187] it is noted that due to the symmetry, the given symmetry structure is stable under radiative corrections.

We note that after the diagonalisation of the full neutrino mass matrix, the obtained heavy neutrinos have exactly degenerate masses approximately of mass M [64]. The pair can be combined to a Dirac spinor, as described in eq. (4.8), when rotating back to the sterile basis.

[64] The sterile neutrino mass matrix M_R receives small second order corrections from the active-sterile mixing matrix Θ.

We discuss the case of 3 sterile neutrinos very briefly. We give a possible symmetry structure that realises the cancellation of the contributions to the light neutrino mass matrix due to a conservation of some lepton number, cf. for instance [187, 195],

$$m_D = \frac{v_{EW}}{\sqrt{2}} \begin{pmatrix} \vec{y}^T \\ 0 \\ 0 \end{pmatrix}, \quad M_R = \begin{pmatrix} 0 & M & 0 \\ M & 0 & 0 \\ 0 & 0 & M_3 \end{pmatrix}. \tag{4.12}$$

As in the case of 2 sterile neutrinos, the light neutrino mass matrix vanishes, and a heavy Dirac neutrino is formed by 2 of the sterile neutrinos as in eq. (4.8). The third sterile neutrino is decoupled from the other neutrinos and it can have a non-zero mass M_3 if the lepton number is assigned as $\mathbb{L}'(N_{R3}) = 0$.

[65] For the case of n sterile neutrino pairs, i.e. $n_S = 2n$, the entries M of the sub-block M_R can be replaced by $n \times n$ matrices.

Similar structures[65] that lead to a cancellation of the contributions of m'_ν can be found for a general number of neutrinos n_S in, e.g., [187, 189, 197, 204].

Instead of the conserved lepton number also other symmetries can ensure the cancellation required. For example some discrete subgroup of $U(1)$ or a discrete flavour symmetry from A_4, see for instance [187].

4.2.3 *Light neutrino masses from perturbations*

Non-vanishing light neutrino masses are obtained from small perturbations of the symmetry structure needed for the cancellations. Or in other words, small deviations from the exact symmetry limit generate light neutrino masses, i.e. they violate the "lepton-number-like" symmetry. In the $n_S = 2$ sterile neutrino case, the most general mass matrix is obtained by lifting all the zeros[66]

[66] Of course a Majorana mass term for the active neutrinos is still forbidden by the SM gauge symmetry.

of the full mass matrix in eq. (4.7), cf. e.g. ref. [187, 204]:

$$\mathcal{M}' = \begin{pmatrix} 0 & \vec{y}\frac{v_{EW}}{\sqrt{2}} & \vec{y}'\frac{v_{EW}}{\sqrt{2}} \\ \vec{y}^T\frac{v_{EW}}{\sqrt{2}} & \varepsilon_{11} & M \\ \vec{y}'^T\frac{v_{EW}}{\sqrt{2}} & M & \varepsilon_{22} \end{pmatrix}, \tag{4.13}$$

where ε_{11}, ε_{22} and $\vec{y}'$ are small parameters, i.e. the dimensionful parameters $\varepsilon_{11}, \varepsilon_{22} \ll M, v_{EW}$ while for the perturbed Yukawa couplings $\vec{y}'^\dagger\vec{y}' \ll \vec{y}^\dagger\vec{y}$.

With the perturbations present, the contributions to the light neutrino mass matrix read

$$m_\nu' = -\varepsilon_{22}\frac{v_{EW}^2}{2M^2}\vec{y}\vec{y}^T + \frac{v_{EW}^2}{2M}\left(\vec{y}'\vec{y}^T + \vec{y}\vec{y}'^T\right). \tag{4.14}$$

The light neutrino mass matrix gives rise to 2 massive and 1 massless neutrino, which is consistent with the present neutrino data.

As is noted in ref. [187, 204], only non-zero ε_{22} and $\vec{y}'$ contribute to the light neutrino mass matrix at the here considered tree-level.

The introduction of the small perturbations give rise to the violation of the total lepton number of the SM, i.e. lepton-number violating processes are possible. The reason for lepton number violation is that the heavy neutrinos combine to form a pseudo-Dirac particle rather than a Dirac particle [59, 207, 208]. This means that the perturbations give contributions to the heavy neutrino mass matrix after the diagonalisation, which results in Majorana mass terms for the heavy neutrinos with nearly, rather than exactly, degenerate masses. This reason is discussed in chapter 9 when we investigate lepton number violation at particle accelerators.

On the other hand, the amount of lepton number violation is proportional to the perturbations which are required to be small in order to explain masses of the light neutrinos. The amount of lepton number conservation is dependent on the Yukawa vector $\vec{y}$, which is unsuppressed due to the cancellations of the contributions to m_ν'.

4.2.4 *Specific cases*

When the are perturbations present, there are more than enough parameters in m_ν', see eq. (4.14), to give masses to the light neutrinos. There are more than enough parameters in m_ν' with the perturbations present, eq. (4.14), to fit the measured neutrino data. Therefore, it is useful to look at the simpler cases where only some of the perturbations are present. Only the case of $n_S = 2$ sterile neutrinos is relevant for us.

Inverse seesaw case: $\varepsilon_{22} \neq 0$; $\varepsilon_{11}, \vec{y}' = 0$

The texture of the full neutrino mass matrix reduces in the inverse seesaw case to

$$\mathcal{M}' = \begin{pmatrix} 0 & \vec{y}\frac{v_{EW}}{\sqrt{2}} & 0 \\ \vec{y}^T\frac{v_{EW}}{\sqrt{2}} & 0 & M \\ 0 & M & \varepsilon_{22} \end{pmatrix}. \tag{4.15}$$

This type of texture is referred to as inverse seesaw [193, 209–212]. For $n_S = 2$, this texture leads to two massless light neutrinos[67]. We comment that with the same texture at least 4 right-handed neutrinos are required [195, 204].

Linear seesaw case: $\vec{y}' \neq 0$; $\varepsilon_{11}, \varepsilon_{22} = 0$

The texture of the full neutrino mass matrix reduces in the linear seesaw case to

$$\mathcal{M}' = \begin{pmatrix} 0 & \vec{y}\frac{v_{EW}}{\sqrt{2}} & \vec{y}'\frac{v_{EW}}{\sqrt{2}} \\ \vec{y}^T\frac{v_{EW}}{\sqrt{2}} & 0 & M \\ \vec{y}'^T\frac{v_{EW}}{\sqrt{2}} & M & 0 \end{pmatrix} . \tag{4.16}$$

This type of texture generates masses for 2 of the light neutrinos and leaves one massless[68]. The masses of the light neutrinos are of order $\frac{v_{EW}^2}{M} y' y$. Since the mass is linear in the usual Yukawa couplings y, this type of texture is referred to as linear seesaw [213–216]. We note that the resulting light neutrino mass matrix has two physical phases[69], the Dirac CP phase and one Majorana phase.

Because there are few parameters a, simple connection can be found which allows to reconstruct the Yukawa vectors $\vec{y}$ and $\vec{y}'$ from the light neutrino masses and mixing parameters [204].

In ref. [204], the following results are derived which depend on the possible orderings for the neutrino masses:

$$\text{NO:} \quad m_1 = 0\,, \quad |m_2| = \frac{y y' v_{EW}^2}{2M}(1-\rho)\,, \quad |m_3| = \frac{y y' v_{EW}^2}{2M}(1+\rho)\,, \tag{4.17}$$

$$\text{IO:} \quad m_3 = 0\,, \quad |m_1| = \frac{y y' v_{EW}^2}{2M}(1-\rho)\,, \quad |m_2| = \frac{y y' v_{EW}^2}{2M}(1+\rho)\,. \tag{4.18}$$

Here, the parameter ρ is fixed by the ratio of the mass squared differences

$$r_{NO} = \frac{|\Delta m_{21}^2|}{|\Delta m_{32}^2|}\,, \qquad r_{IO} = \frac{|\Delta m_{21}^2|}{|\Delta m_{13}^2|}\,, \tag{4.19}$$

and is obtained by plugging in the eigenvalues of the light neutrinos in r and solving for ρ,

$$\rho_{NO} = \frac{\sqrt{1+r}-\sqrt{r}}{\sqrt{1+r}+\sqrt{r}}\,, \qquad \rho_{IO} = \frac{\sqrt{1+r}-1}{\sqrt{1+r}+1}\,. \tag{4.20}$$

The authors of ref. [204] find for the components of the reconstructed Yukawa vectors

$$y_\alpha = \frac{y}{\sqrt{2}}\left(\sqrt{1+\rho}\,U_{\alpha i}^* + \sqrt{1-\rho}\,U_{\alpha j}^*\right)\,, \tag{4.21}$$

$$y'_\alpha = \frac{y'}{\sqrt{2}}\left(\sqrt{1+\rho}\,U_{\alpha i}^* - \sqrt{1-\rho}\,U_{\alpha j}^*\right)\,, \tag{4.22}$$

with $i = 3$, $j = 2$ for NO and $i = 2$, $j = 1$ for IO.

[67] The light neutrino mass matrix, $m'_\nu = -\varepsilon_{22}\frac{v_{EW}^2}{2M^2}\vec{y}\vec{y}^T$, is of rank 1 and thus generates a mass term for only 1 of the 3 light neutrinos. Its mass is of order $\varepsilon_{22} v_{EW}^2 y^2/M^2$

[68] Since the light neutrino mass matrix, $m'_\nu = \frac{v_{EW}^2}{2M}(\vec{y}'\vec{y}^T + \vec{y}\vec{y}'^T)$, is of rank 2.

[69] The full mass matrix has seven phases, 3 phases from the Yukawa vector $\vec{y}$, 3 phases from $\vec{y}'$ and 1 phase from M. 5 phases can be absorbed by the fields ν'_{e,μ,τ_L} and $N'^{1,2}_R$.

The reconstruction works also for a non-vanishing Dirac CP phase and up to the Majorana phase that cannot be measured in neutrino oscillation experiments. As a consequence of eq. (4.21) and (4.22), the neutrino Yukawa couplings are constrained by the PMNS parameters that are measured in neutrino oscillation experiments, see chapter 3.2.

General case: $\varepsilon_{11}, \varepsilon_{22}, \vec{y}' \neq 0$

Notably, the contributions to the light neutrino mass matrix , see eq. (4.14), can be rewritten to have the same structure as in the linear seesaw case

$$m_\nu' = -\varepsilon_{22}\frac{v_{EW}^2}{2M^2}\vec{y}\vec{y}^T + \frac{v_{EW}^2}{2M}\left(\vec{y}'\vec{y}^T + \vec{y}\vec{y}'^T\right) \tag{4.23}$$

$$= \frac{v_{EW}^2}{2M}\left(\left(\vec{y}' - \frac{\varepsilon_{22}}{M}\vec{y}\right)\vec{y}^T + \vec{y}\left(\vec{y}' - \frac{\varepsilon_{22}}{M}\vec{y}\right)^T\right) . \tag{4.24}$$

Therefore, one is able to reconstruct the Yukawa vector $\vec{y}$ by the method from ref. [204]. While for the vector $\vec{y}'$ the reconstruction is not possible because there is an ambiguity due to the new free parameter.

4.3 A MINIMAL SYMMETRY PROTECTED LOW SCALE SEESAW SCENARIO

Low scale seesaw scenarios give a natural explanation for the smallness of neutrino masses by arguments of a protective symmetry that gives rise to cancellations in the light neutrino mass matrix. This allows for the neutrino Yukawa couplings to be unsuppressed and as large as $\mathcal{O}(1)$, which makes this scenario accessible at colliders when the sterile neutrinos are of order of the EW scale. The benchmark scenario that is used in order to study the phenomenology of sterile neutrinos at colliders, is based on the low scale seesaw scenario with $n_S = 2$ sterile neutrinos which have masses around the EW scale. The benchmark scenario is referred to as "symmetry protected seesaw scenario" (SPSS), which is discussed, for instance, in ref. [1, 3, 217]. The SPSS allows for additional sterile neutrinos as long as they are decoupled from the collider phenomenology. Light neutrino masses that are consistent with neutrino oscillation data [70] can either be generated when the protective symmetry is slightly broken, which allows for the small perturbations to the cancellation structure of the full neutrino mass matrix. Or alternatively, when the additional sterile neutrinos contribute to the light neutrino mass matrix. We note that the additional neutrinos might as well be responsible for the BAU or DM. The SPSS therefore captures the essential collider phenomenology of the EW scale sterile neutrinos, while it allows to be more general than specific models.

[70] Although, light neutrino masses are usually negligible for the collider phenomenology.

In the following sections, we specify the benchmark scenario in section 4.3.1, the interactions of the light and heavy mass eigenstates to the SM particles in section 4.3.2, we discuss the modifications to electroweak observables in section 4.3.2, and discuss the two-body and three-body decays of the heavy neutrinos in section 4.3.4. The following sections aim at an instructive and rather complete summary of the SPSS and can therefore be heavily inspired by the model sections in ref. [1, 3, 217].

4.3.1 *The benchmark scenario: symmetry protected seesaw scenario (SPSS)*

We consider for the benchmark scenario a pair of sterile neutrinos N_R^1 and N_R^2 with the lepton number assignments $\mathbb{L}'(\nu_L) = \mathbb{L}'(N_R^1) = -\mathbb{L}'(N_R^2) = 1$ under a "lepton-number-like" (global) $U(1)$ symmetry.

The Lagrangian density in the limit of intact symmetry, i.e. without the perturbations of the cancellation structure, is given by

$$\mathscr{L} = \mathscr{L}_{SM} - \overline{N_R^1} M N_R^{2\,c} - y_{\nu_\alpha} \overline{N_R^1} \widetilde{\phi}^\dagger L^\alpha + \text{H.c.} + \dots \,, \tag{4.25}$$

where the kinetic terms of the sterile neutrinos as well as the primes labelling the fields are omitted. $\mathscr{L}_{SM}$ is the SM Lagrangian density. The Yukawa term connects the right-handed neutrino N_R^1 to the lepton doublet L^α and to the transformed Higgs doublet $\tilde{\phi} = i\sigma_2\phi^*$ with the Higgs doublet ϕ. The coupling strength is given by the complex-valued neutrino Yukawa couplings y_{ν_α} for $\alpha = e, \mu, \tau$. The mass parameter M of the mass term can be chosen real without loss of generality[71].

[71] By absorbing the phase of M, for instance, in the redefinition of N_R^2.

As mentioned above, the benchmark scenario captures the essential collider phenomenology of low scale seesaw models with the two sterile neutrinos N_R^1 and N_R^2 but allows for additional sterile neutrinos as long as they are decoupled from the collider phenomenology which is indicated by the ellipses in eq. (4.25). The additional neutrinos require either to be comparatively heavy or to be uncharged under the "lepton-number-like" symmetry. In the limit of intact symmetry they can neither mix with N_R^1 and N_R^2 nor participate in Yukawa interactions with the lepton doublets, and thus they would be decoupled from other particles. Therefore, the relevant parameters for the collider phenomenology of sterile neutrinos are the neutrino Yukawa couplings $y_{\nu_e}, y_{\nu_\mu}, y_{\nu_\tau}$ and the mass parameter M.

After electroweak symmetry breaking, the Dirac mass matrix and the sterile neutrino mass matrix have the familiar form, discussed in eq. (4.9):

$$m_D = \frac{v_{EW}}{\sqrt{2}} \begin{pmatrix} y_{\nu_e} & y_{\nu_\mu} & y_{\nu_\tau} \\ 0 & 0 & 0 \end{pmatrix}, \quad M_R = \begin{pmatrix} 0 & M \\ M & 0 \end{pmatrix}. \tag{4.26}$$

The part of the Lagrangian density containing the full 5×5 neutrino mass matrix reads

$$-\frac{1}{2} \begin{pmatrix} \overline{\nu_{e_L}^c} \\ \overline{\nu_{\mu_L}^c} \\ \overline{\nu_{\tau_L}^c} \\ \overline{N_R^1} \\ \overline{N_R^2} \end{pmatrix}^T \begin{pmatrix} 0 & 0 & 0 & m_{\nu_e} & 0 \\ 0 & 0 & 0 & m_{\nu_\mu} & 0 \\ 0 & 0 & 0 & m_{\nu_\tau} & 0 \\ m_{\nu_e} & m_{\nu_\mu} & m_{\nu_\tau} & 0 & M \\ 0 & 0 & 0 & M & 0 \end{pmatrix} \begin{pmatrix} \nu_{e_L} \\ \nu_{\mu_L} \\ \nu_{\tau_L} \\ N_R^{1\,c} \\ N_R^{2\,c} \end{pmatrix} + \text{H.c.}\,, \tag{4.27}$$

where the Dirac masses are given by $m_{\nu_\alpha} = y_{\nu_\alpha} v_{EW}/\sqrt{2}$ with $v_{EW} = 246.22$ GeV.

We re-emphasise that in the limit of intact symmetry the sterile neutrino N_R^2 does not couple to the SM leptons via the Yukawa interaction, consequently the cancellation of the contributions to the light neutrino mass matrix is exact and the three light neutrinos are massless, see section 4.2.2.

The diagonalisation of the full neutrino mass matrix, $\mathcal{M}'$ from eq. (4.27), is performed, as described in section 2.2, by the two step diagonalisation with the leptonic mixing matrix in eq. (2.43). For the block-diagonalisation we plug the Dirac and Majorana mass matrices of eq. (4.26) into the block-diagonalisation matrix $\mathcal{U}_{BD}$ in (2.40). The 2×2 sub-block for the sterile neutrinos can then be diagonalised separately by the unitary matrix

$$U^N = \frac{1}{\sqrt{2}} \begin{pmatrix} +i & 1 \\ -i & 1 \end{pmatrix} , \tag{4.28}$$

as illustrated in eq. (2.43). With these substitutions, the full unitary leptonic mixing matrix up to second order in the neutrino Yukawa couplings y_{ν_α} is obtained [217]

$$\mathcal{U} = \begin{pmatrix} \mathcal{N}_{e1} & \mathcal{N}_{e2} & \mathcal{N}_{e3} & -\frac{i}{\sqrt{2}}\theta_e & \frac{1}{\sqrt{2}}\theta_e \\ \mathcal{N}_{\mu 1} & \mathcal{N}_{\mu 2} & \mathcal{N}_{\mu 3} & -\frac{i}{\sqrt{2}}\theta_\mu & \frac{1}{\sqrt{2}}\theta_\mu \\ \mathcal{N}_{\tau 1} & \mathcal{N}_{\tau 2} & \mathcal{N}_{\tau 3} & -\frac{i}{\sqrt{2}}\theta_\tau & \frac{1}{\sqrt{2}}\theta_\tau \\ 0 & 0 & 0 & \frac{i}{\sqrt{2}} & \frac{1}{\sqrt{2}} \\ -\theta_e^* & -\theta_\mu^* & -\theta_\tau^* & \frac{-i}{\sqrt{2}}(1-\frac{1}{2}\theta^2) & \frac{1}{\sqrt{2}}(1-\frac{1}{2}\theta^2) \end{pmatrix} , \tag{4.29}$$

where the (complex) active-sterile mixing parameters are defined as

$$\theta_\alpha = \frac{y_{\nu_\alpha}^*}{\sqrt{2}} \frac{v_{EW}}{M} , \qquad \alpha = e, \mu, \tau , \tag{4.30}$$

and the active-sterile mixing angle squared is given by

$$\theta^2 = \sum_\alpha |\theta_\alpha|^2 . \tag{4.31}$$

The 3×3 sub-block $\mathcal{N}$ of the full mixing matrix (4.29) is the effective mixing matrix of the three active neutrinos [64, 218], i.e the PMNS matrix [72]. The elements are given as

$$\mathcal{N}_{\alpha i} = (\delta_{\alpha\beta} - \frac{1}{2}\theta_\alpha\theta_\beta^*)\,(U^\nu)_{\beta i} , \tag{4.32}$$

with U^ν being a unitary 3×3 matrix, cf. ref. [61]. As anticipated in section 2.2 the PMNS matrix is non-unitary, see eq. (2.44).

[72] In the basis where the charged lepton mass matrix is diagonal.

The resulting diagonalisation yields the eigenvalues corresponding to the masses of the mass eigenstates:

$$\mathcal{U}^T \mathcal{M}' \mathcal{U} \cong \text{Diag}\,(0, 0, 0, M, M) , \tag{4.33}$$

where the small $\mathcal{O}(\theta^2)$ correction to the masses of the heavy neutrinos can be neglected.

The resulting mass eigenstates are the three light neutrinos ν_i (i = 1, 2, 3), which are massless and two heavy neutrinos N_j (j = 1, 2) with degenerate mass eigenvalues M in the limit of intact symmetry. The neutrino mass eigenstates are an admixture of the active and sterile neutrinos, as is discussed in section 2.2,

$$n_j = (\nu_1, \nu_2, \nu_3, N_1, N_2)^T = \mathcal{U}_{j\alpha}^\dagger n'_\alpha , \tag{4.34}$$

with the left-chiral active-sterile states

$$n'_\alpha = \left(\nu_{e_L}, \nu_{\mu_L}, \nu_{\tau_L}, N_R^{1\,c}, N_R^{2\,c}\right)^T . \tag{4.35}$$

We note that experiments usually constrain the mixing between the active and sterile states rather than the neutrino Yukawa couplings directly. Often, the active-sterile mixing is expressed by the elements of the full $(3+n_S)\times(3+n_S)$ mixing matrix $\mathcal{U}$ in eq. (2.43) as

$$|\mathcal{U}_{\alpha i}|^2 = |(\Theta U^N)_{\alpha i}|^2 , \quad \alpha = e,\mu,\tau, \quad i = 4,\ldots,3+n_S , \tag{4.36}$$

where the active-sterile mixing matrix is given by $\Theta \simeq m_D^\dagger M_R^{\dagger -1}$. In the case of the SPSS, the mixing matrix elements are related to the active-sterile mixing parameters as

$$|\mathcal{U}_{\alpha i}|^2 = \frac{1}{2}|\theta_\alpha|^2 . \tag{4.37}$$

Altogether, the SPSS introduces 7 additional parameters to the SM in the limit of intact symmetry: the modulus and phase of the neutrino Yukawa coupling y_{ν_α} for $\alpha = e,\,\mu,\tau$ and the mass parameter corresponding to the mass of the heavy neutrinos. Equivalently, the three active-sterile mixing angles, θ_α for $\alpha = e,\,\mu,\tau$ can be chosen instead of the neutrino Yukawa couplings, see eq. (4.30).

We note that in specific models where the "lepton-number-like" symmetry is slightly broken in order to explain the neutrino oscillation data there can be correlations among the neutrino Yukawa couplings. In the case of exactly 2 sterile neutrinos, i.e. no additional sterile neutrinos are present in the theory, there are correlations among the y_{ν_α}, see, for instance, the discussion at the end of the linear seesaw case and the general case in section 4.2.4, where the neutrino Yukawa couplings are constrained by the PMNS parameters. In the case of additional sterile neutrinos, the neutrino Yukawa couplings can be unconstrained by the PMNS matrix since the additional sterile states can cancel the contributions to the neutrino mass matrix.

In order to test such correlations among the neutrino Yukawa couplings, and not to assume them a priori, the overall strategy of the SPSS is to study how to measure the neutrino Yukawa couplings independently in collider experiments. For the study of the collider phenomenology, we consider the 4 independent parameters $|\theta_e|$, $|\theta_\mu|$, $|\theta_\tau|$ and M [73]. For simplicity, we sometimes refer to these parameters as the sterile neutrino parameters.

[73] The phases might be measurable in neutrino oscillation experiments rather than in collider experiments [3, 219, 220].

4.3.2 *Modification of the weak currents*

Due to the mixing between the active and sterile neutrinos, the heavy neutrinos, which are mostly sterile, contain a small amount of the active neutrinos as well and thus also participate in the weak interaction. Therefore, the strength of the weak interactions is suppressed by the active-sterile mixing

for the heavy neutrinos. The gauge interactions of the weak currents $j^{\pm}_{\mu}$ and j^{0}_{μ} can be expressed in the mass basis of the neutrinos, that are given by

$$j^{\pm}_{\mu} = \sum_{i=1}^{5} \sum_{\alpha=e,\mu,\tau} \frac{g}{\sqrt{2}} \bar{\ell}_{\alpha} \gamma_{\mu} P_{L} U_{\alpha i} n_{i} + \text{H.c.}\,, \tag{4.38}$$

$$j^{0}_{\mu} = \sum_{i,j=1}^{5} \sum_{\alpha=e,\mu,\tau} \frac{g}{2\,c_{W}} \overline{n_{j}}\, U^{\dagger}_{j\alpha} \gamma_{\mu} P_{L} U_{\alpha i} n_{i}\,, \tag{4.39}$$

where g is the weak coupling constant, c_W is the cosine of the weak mixing angle, P_L [74] is the left-chiral projection operator, $U_{\alpha i}$ are the elements of the leptonic mixing matrix in eq. (4.29), and n_i are the neutrino mass eigenstates defined in eq. (4.34). The weak currents involving the light and heavy neutrinos read

[74] $P_L = \frac{1}{2}(1-\gamma^5)$

$$\begin{aligned} j^{\pm}_{\mu} &= \sum_{\alpha=e,\mu,\tau} \sum_{i=1}^{3} \frac{g}{\sqrt{2}} \mathcal{N}_{\alpha i}\, \bar{\ell}_{\alpha}\, \gamma_{\mu} P_{L} \nu_{i} + \text{H.c.} \\ &\quad + \sum_{\alpha=e,\mu,\tau} \frac{g}{\sqrt{2}} \theta_{\alpha}\, \bar{\ell}_{\alpha}\, \gamma_{\mu} P_{L} \frac{1}{\sqrt{2}} \left(-i N_{1} + N_{2}\right) + \text{H.c.}\,, \end{aligned} \tag{4.40}$$

$$\begin{aligned} j^{0}_{\mu} &= \frac{g}{2\,c_{W}} \sum_{i,j=1}^{5} \vartheta_{ij} \overline{n_{i}} \gamma_{\mu} P_{L} n_{j} \\ &\supset \frac{g}{2\,c_{W}} \sum_{i,j=1}^{3} \left(\vartheta_{ij} \overline{\nu}_{i} \gamma_{\mu} \nu_{j}\right) \\ &\quad + \frac{g}{2\,c_{W}} \sum_{i=1}^{3} \left(\vartheta_{i4} \overline{\nu}_{i} \gamma_{\mu} N_{1} + \vartheta_{i5} \overline{\nu}_{i} \gamma_{\mu} N_{2}\right) + \text{H.c.}\,, \end{aligned} \tag{4.41}$$

with the definition [217]:

$$\vartheta_{ij} = \sum_{\alpha=e,\mu,\tau} U^{\dagger}_{i\alpha} U_{\alpha j}\,. \tag{4.42}$$

For $i, j \leqslant 3$ one obtains

$$\vartheta_{ij} = \sum_{\alpha=e,\mu,\tau} \mathcal{N}^{\dagger}_{i\alpha} \mathcal{N}_{\alpha j} = \left(\mathcal{N}^{\dagger} \mathcal{N}\right)_{ij}\,, \tag{4.43}$$

while for $i \leqslant 3$ and $j = 4, 5$ one gets

$$\vartheta_{i4} = \sum_{\alpha=e,\mu,\tau} (-i)\, \mathcal{N}^{*}_{i\alpha} \frac{\theta_{\alpha}}{\sqrt{2}}\,, \qquad \text{and} \qquad \vartheta_{i5} = \sum_{\alpha=e,\mu,\tau} \mathcal{N}^{*}_{i\alpha} \frac{\theta_{\alpha}}{\sqrt{2}}\,, \tag{4.44}$$

with the PMNS matrix $\mathcal{N}$ that is defined in eq. (4.32).

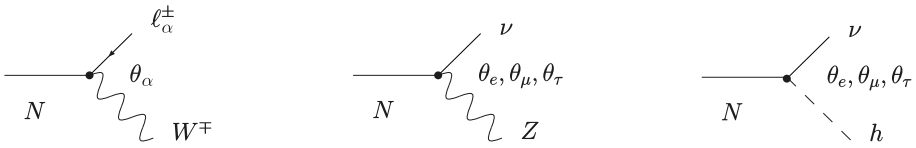

Figure 5: Feynman diagrams of the vertices involving a single heavy neutrinos in the mass basis. For Majorana neutrinos, the usual arrow indicating the flow of charge is omitted. One could introduce a fermion flow instead and derive similar Feynman rules as for Dirac fermions, cf. ref. [221]. We also omitted the explicit indices of the neutrinos. The labels θ_α, for $\alpha = e, \mu, \tau$, denote the dependence of the diagrams on the active-sterile mixing to the leading order.

Figure 6: Feynman diagrams of the vertices involving the light neutrinos only. The label $\mathcal{N}$ denotes the dependence of the diagrams on the PMNS matrix and its elements to leading order.

The Yukawa part of the Lagrangian density contains also the interaction with the Higgs boson. It can be expressed in the mass basis and to leading order in the active-sterile mixing angle it reads

$$\begin{aligned}
&\sum_{\alpha=e,\mu\tau} y_{\nu_\alpha} \overline{N_R^1} \widetilde{\phi}^\dagger L^\alpha + \text{H.c.} \\
\supset &\sum_{\alpha=e,\mu\tau} y_{\nu_\alpha} \sum_{i,j=1}^{5} \overline{n_j^c} U_{j4}^T \phi^0 U_{\alpha i} n_i + \text{ H.c.} \\
= &\frac{M}{v_{EW}} \sum_{i=1}^{3} \left(\vartheta_{i4}^* \overline{N_1^c} + \vartheta_{i5}^* \overline{N_2^c} \right) h \nu_i + \text{ H.c.}\,, \qquad (4.45)
\end{aligned}$$

where $h = \sqrt{2}\,\mathrm{Re}(\phi^0)$ is the real scalar Higgs boson. Hence, also the Higgs boson interacts with the heavy neutrinos. We note that there is no $h\nu\nu$ interaction at tree level due to the structure of the leptonic mixing matrix.

The resulting vertices of a single heavy neutrino interacting with the SM gauge and Higgs bosons are shown in fig. 5. The vertices involving only the light neutrinos are shown in fig. 6. The interactions involving the heavy neutrinos are suppressed by the active-sterile mixing angles, while the interactions of the light neutrinos are modified by the PMNS matrix $\mathcal{N}$ with respect to the SM interactions of the active neutrinos.

We note that the Z and the Higgs boson also feature couplings to two heavy neutrinos. These couplings are proportional to ϑ_{ij} with $i, j = 4, 5$, for which they satisfy

$$|\vartheta_{ij}| = \frac{1}{2}\,\theta^2\,, \qquad (4.46)$$

with the mixing angle square defined in eq. (4.31).

4.3.3 *Modification of electroweak observables*

As a consequence of the modification of the weak currents is that predictions for the electroweak observables compared to the SM are modified, confer, e. g., ref. [217, 218, 222]. This is due to the modified couplings of the light neutrinos affecting the predictions of the electroweak precision observables. The modifications manifest as non-unitarity effects from the effective PMNS matrix $\mathcal{N}$. Notably, the non-unitarity effects do not involve any exchange of the heavy neutrinos, their simple presence in the theory is already enough to cause these effects.

Let us discuss this effect by the modification of the Fermi constant G_F. In the SM, the Fermi constant is inferred from muon decays which involves the charged weak current. Due to the modification of the weak currents, the theory prediction for G_F is modified by the non-unitarity effects and therefore sensitive to the active-sterile mixing parameters. The Feynman diagram for the muon decay in the context of the SPSS is shown in fig. 7. The muon decay cross section for heavy neutrino masses $M \gg m_\mu$ is given in the SPSS by

$$\sigma_{\mu^- \to e^- \nu \bar{\nu}} = \left(\mathcal{N}\mathcal{N}^\dagger\right)_{ee} \left(\mathcal{N}\mathcal{N}^\dagger\right)_{\mu\mu} \cdot \sigma^{\text{SM}}_{\mu^- \to e^- \nu \bar{\nu}} \,, \tag{4.47}$$

where the summation over all possible final state neutrinos is implied. Since the PMNS matrix $\mathcal{N}$ is non-unitary, see eq. (4.32), the factors $\mathcal{N}\mathcal{N}^\dagger$ are not equal to unity, and thus the muon decay cross sections are different. The Fermi constant in the context of the SPSS is obtained by comparing the respective theory predictions for the muon decay cross sections. Let G_μ denote the Fermi constant extracted from muon decays, then G_μ corresponds to G_F in the SM. But in the SPSS, G_F is fixed by the relation between the cross sections in eq. (4.47) and the correspondence becomes

$$\begin{aligned} G_\mu^2 = G_F^2 \longrightarrow G_\mu^2 &= G_F^2 \cdot (\mathcal{N}\mathcal{N}^\dagger)_{ee} (\mathcal{N}\mathcal{N}^\dagger)_{\mu\mu} \\ &= G_F^2 \cdot (1 - |\theta_e|^2)(1 - |\theta_\mu|^2) \,. \end{aligned} \tag{4.48}$$

We emphasise that the modification of the Fermi constant is attributed to the non-unitarity of the PMNS matrix, hence, such modifications are referred to as non-unitarity effects.

As a consequence of the modification of G_F, the theory prediction for a number of other SM parameters are affected. Therefore, it constitutes one of the main sources for the non-unitarity effects. For instance the theory prediction for the weak mixing angle θ_W is modified which at tree level reads [222]

$$s_W^2 = \frac{1}{2}\left[1 - \sqrt{1 - \frac{2\sqrt{2}\alpha\pi}{G_\mu m_Z^2}\sqrt{(1 - |\theta_e|^2)(1 - |\theta_\mu|^2)}}\right] . \tag{4.49}$$

Consequently, also the theory prediction for the W boson mass is modified via the relation $m_Z^2 c_W^2 = m_W^2$. But also the theory prediction for the vev v_{EW} of the Higgs potential is modified by the Fermi constant in the SPSS [1]

$$v_{EW} = \frac{1}{\sqrt{\sqrt{2} G_F}} = 246.22 \left[1 - 0.25 \left(|\theta_e|^2 + |\theta_\mu|^2\right)\right] . \tag{4.50}$$

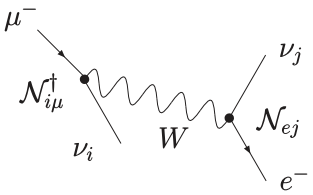

Figure 7: Feynman diagram of the muon decay processes in the SPSS. For the cross section the sum over all light neutrinos is taken.

There are further observables that are affected by the modification of the weak currents, see for instance ref. [217, 222, 223] and references therein. These modifications allow to test the active-sterile mixing via precision measurements of the SM observables, see section 5.1.2.

4.3.4 *Decay width of the heavy neutrinos*

Due to the active-sterile mixing the heavy neutrino mass eigenstates N_1 and N_2 couple to the W and Z bosons via the weak current interactions in eq. (4.40) and eq. (4.41), and the Higgs boson via the Yukawa interactions in eq. (4.40). If kinematically allowed, the heavy neutrinos can then be produced by the decays of the gauge and Higgs bosons (if $M < m_W, m_Z, m_h$) [75]. The neutrinos themselves can also decay into leptons and bosons by the 2-body decay ($M > m_W, m_Z, m_h$) or into leptons and quarks by the 3-body decay ($M < m_W, m_Z, m_h$).

[75] For the SPSS, the decay widths of the bosons to the heavy neutrinos can be found for instance in ref. [217].

We primarily discuss the decay widths of the heavy neutrinos here, since the total decay width is intimately connected to the lifetime of the heavy neutrino. As such, heavy neutrinos are unstable particles.

Two-body decays

The 2-body decays of the heavy neutrinos, N_j with $j = 1, 2$, into the weak gauge and the Higgs bosons are kinematically allowed if $M > m_W, m_Z, m_h$. They comprise the following decays:

$$N_j \to W^{\pm}\, \ell_\alpha^{\mp}\,, \qquad N_j \to Z \nu_i\,, \qquad N_j \to h \nu_i\,. \tag{4.51}$$

We discuss the tree-level partial decay widths for heavy Dirac and Majorana neutrinos. The partial decay widths of a heavy neutrino into the above decays are given by ref. [1, 217]

$$\Gamma(N_j \to W\, \ell_\alpha) = \frac{|\theta_\alpha|^2}{2} \frac{G_F\, M^3}{8\sqrt{2}\pi} \left(1 - \mu_W^2\right)^2 \left(1 + 2\mu_W^2\right)\,, \tag{4.52}$$

$$\Gamma_M(N_j \to Z\, \nu_i) = |\vartheta_{ij}|^2 \frac{G_F\, M^3}{8\sqrt{2}\pi} \left(1 - \mu_Z^2\right)^2 \left(1 + 2\mu_Z^2\right)\,, \tag{4.53}$$

$$\Gamma_M(N_j \to h\, \nu_i) = |\vartheta_{ij}|^2 \frac{M^3}{16\,\pi\, v_{EW}^2} \left(1 - \mu_h^2\right)^2\,, \tag{4.54}$$

where Γ_M stands for the width of a heavy Majorana neutrino, G_F for the Fermi constant [76], $i = 1, 2, 3$, $j = 1, 2$ and μ_X for m_X/M.

[76] $G_F = \frac{g^2}{\sqrt{2}4 m_W^2} \approx 1.166 \cdot 10^{-5}\ \text{GeV}^{-2}$

Since the light neutrinos cannot be measured experimentally (at colliders), their contribution to the partial widths can be taken together and expressed in terms of the active-sterile mixing angles

$$\Gamma(N_j \to W\, \ell_\alpha) = \frac{|\theta_\alpha|^2}{2} \frac{g^2}{64\pi} \frac{M^3}{m_w^2} \left(1 - \mu_W^2\right)^2 \left(1 + 2\mu_W^2\right)\,, \tag{4.55}$$

$$\Gamma_D(N_j \to Z\, \Sigma_i \nu_i) = \frac{|\theta|^2}{2} \frac{g^2}{128\pi} \frac{M^3}{m_w^2} \left(1 - \mu_Z^2\right)^2 \left(1 + 2\mu_Z^2\right)\,, \tag{4.56}$$

$$\Gamma_D(N_j \to h\, \Sigma_i \nu_i) = \frac{|\theta|^2}{2} \frac{g^2}{128\pi} \frac{M^3}{m_w^2} \left(1 - \mu_h^2\right)^2\,, \tag{4.57}$$

where Γ_D stands for the decay widths of a heavy Dirac neutrino. The partial decay widths are straightforward to calculate in the Dirac case and can be found in the literature [190, 224–227]. However, in the literature it is usually not immediately clear if the decay widths apply to the Dirac or Majorana case. The main difference comes into play when including the Hermitian conjugate processes:
In the Dirac case, N_j decays to $W^+\ell_\alpha^-$ and $\overline{N}_j$ to $W^-\ell_\alpha^+$. While in the Majorana case N_j has equal probability to decay into $W^+\ell^-$ or $W^-\ell^+$. For the neutral current decays, the partial widths in the Majorana case are related by a factor of 2 with respect to the Dirac case

$$\Gamma_M(N \to Z\,\Sigma_i\nu_i) = 2\Gamma_D(N \to Z\,\Sigma_i\nu_i)\,, \tag{4.58}$$
$$\Gamma_M(N \to h\,\Sigma_i\nu_i) = 2\Gamma_D(N \to h\,\Sigma_i\nu_i)\,. \tag{4.59}$$

As a consequence of the Majorana condition, the total decay width for a heavy Majorana neutrino is twice the total Dirac decay width:

$$\Gamma_D^{N,2-\text{body}} = \sum_{\alpha,i}\Gamma(N_j \to W^+\,\ell_\alpha^-) + \Gamma_D(N_j \to Z\,\nu_i) + \Gamma_D(N_j \to h\,\nu_i)\,, \tag{4.60}$$
$$\Gamma_M^{N,2-\text{body}} = \sum_{\alpha,i}\Gamma_M(N_j \to W\,\ell_\alpha) + 2\Gamma_D(N_j \to Z\,\nu_i) + 2\Gamma_D(N_j \to h\,\nu_i)\,, \tag{4.61}$$

where $\Gamma_M(N_j \to W\,\ell_\alpha) = \Gamma(N_j \to W^+\,\ell_\alpha^-) + \Gamma(N_j \to W^-\,\ell_\alpha^+)$.

The branching ratios are calculated as

$$\text{BR}_i = \frac{\Gamma_i}{\sum_i \Gamma_i} = \frac{\Gamma_i}{\Gamma^{N,\text{tot}}}\,. \tag{4.62}$$

For $M \gg m_h = 125$ GeV, the partial decay widths summed over all final state leptons or, equivalently, the corresponding branching ratios fulfil the ratio

$$\begin{aligned}&\Gamma(N \to W^+\,\ell^-) : \Gamma_D(N \to h\,\nu) : \Gamma_D(N \to hZ\,\nu)\\ =&\Gamma_M(N \to W\,\ell) : \Gamma_M(N \to Z\,\nu) : \Gamma_M(N \to h\,\nu)\\ =&2 : 1 : 1\,.\end{aligned} \tag{4.63}$$

Three-body decays

For heavy neutrino masses below the W boson mass, the previously discussed 2-body decays are kinematically not allowed, but the 3-body decays mediated by off-shell SM bosons become accessible. The heavy neutrinos decay modes for the 3-body decay are:

$$\begin{aligned}N_j &\to \nu\nu\nu && \text{invisible}\,,\\ N_j &\to \nu\ell^+\ell^- && \text{leptonic}\,,\\ N_j &\to \nu q\bar{q} && \text{hadronic}\,,\\ N_j &\to \ell^\pm q'\bar{q} && \text{semileptonic}\,.\end{aligned} \tag{4.64}$$

In the low-energy limit, $M \ll m_W$, the partial decay widths of the 3-body decay of the heavy neutrino simplify and can be calculated by the use of the

theory of Fermi interaction. For $M \gtrsim 5$ GeV, one can make further approximations by neglecting the masses of the final state fermions. We note that considering open quarks is already an approximation in and of itself. For the formulae with the decay modes into mesons cf. for instance ref. [228].

The partial decay widths for the different decay channels can be found for instance in ref. [228–230]:

$$\Gamma(N \to \ell_1^- \ell_2^+ \nu_2) = \frac{|\theta_{\ell_1}|^2}{2} \frac{G_F^2 M^5}{192\pi^3}, \quad \ell_1 \neq \ell_2, \tag{4.65a}$$

$$\Gamma(N \to \nu_1 \ell_1^+ \ell_1^-) = \frac{|\theta_{\ell_1}|^2}{2} \frac{G_F^2 M^5}{192\pi^3} \left((1 + c_L)^2 + c_R^2\right), \tag{4.65b}$$

$$\Gamma(N \to \nu_1 \ell_2^+ \ell_2^-) = \frac{|\theta_{\ell_1}|^2}{2} \frac{G_F^2 M^5}{192\pi^3} \left(c_L^2 + c_R^2\right), \quad \ell_1 \neq \ell_2, \tag{4.65c}$$

$$\Gamma(N \to \nu_1 \overline{\nu}_2 \nu_2) = \frac{|\theta_{\ell_1}|^2}{2} \frac{G_F^2 M^5}{192\pi^3} c_\nu^2, \quad \ell_1 \neq \ell_2, \tag{4.65d}$$

$$\Gamma(N \to \nu_1 \overline{\nu}_1 \nu_1) = \frac{|\theta_{\ell_1}|^2}{2} \frac{G_F^2 M^5}{192\pi^3} 2c_\nu^2, \tag{4.65e}$$

$$\Gamma(N \to \ell^- \overline{q}_d q_u) = \frac{|\theta_\ell|^2}{2} \frac{G_F^2 M^5}{192\pi^3} N_C, \tag{4.65f}$$

$$\Gamma(N \to \nu_1 \overline{q} q) = \frac{|\theta_{\ell_1}|^2}{2} \frac{G_F^2 M^5}{192\pi^3} N_C \left((c_L^q)^2 + (c_R^q)^2\right), \tag{4.65g}$$

where $\ell_{i=1,2,3} = e, \mu, \tau$, N_C is the color factor and $c_L^{(q)}, c_R^{(q)}, c_\nu$ are the left and right chiral couplings to the Z boson [77].

[77] $c_L = -\frac{1}{2} + s_W^2$, $c_R = +s_W^2$, $c_L^u = \frac{1}{2} - \frac{2}{3}s_W^2$, $c_R^u = -\frac{2}{3}s_W^2$, $c_L^d = -\frac{1}{2} + \frac{1}{3}s_W^2$, $c_R^d = +\frac{1}{3}s_W^2$, $c_\nu = \frac{1}{2}$, where $s_W^2 = \sin^2\theta_W \approx 0.23$ is the sine squared of the weak mixing angle.

Here, the decays in eq. (4.65a), (4.65f) stem from charged currents only while the ones in eq. (4.65c), (4.65d), (4.65e), (4.65g) from neutral currents only. The decays in eq. (4.65b) stem from both charged and neutral currents.

The contributions to the total decay width of the 3-body decay are obtained by summing over all the possible final states from the above partial widths. This corresponds to multiplying the partial widths with the correct multiplicity factors:

$$\Gamma(N \to \nu \ell^+ \ell^-) = \frac{|\theta|^2}{2} \frac{G_F^2 M^5}{192\pi^3} \Big(2 \cdot 2 + 2(1 + c_L^2 + c_R^2), + 2 \cdot 2(c_L^2 + c_R^2)\Big), \tag{4.66}$$

$$\Gamma(N \to \nu\nu\nu) = \frac{|\theta|^2}{2} \frac{G_F^2 M^5}{192\pi^3} (2 \cdot 2c_\nu^2 + 2 \cdot 2c_\nu^2), \tag{4.67}$$

$$\Gamma(N \to \ell jj) = \frac{|\theta|^2}{2} \frac{G_F^2 M^5}{192\pi^3} (2 \cdot 3 \cdot 2), \tag{4.68}$$

$$\Gamma(N \to \nu jj) = \frac{|\theta|^2}{2} \frac{G_F^2 M^5}{192\pi^3} \Big(2 \cdot 3 \cdot 3((c_L^d)^2 + (c_R^d)^2), + 2 \cdot 3 \cdot 2((c_L^u)^2 + (c_R^u)^2)\Big), \tag{4.69}$$

where j stands for a quark jet, it represents any of the kinematic available quarks, $j \in \{u, d, c, s, b, \overline{u}, \overline{d}, \overline{c}, \overline{s}, \overline{b}\}$. For decays into $\nu\ell^+\ell^-$, there are extra factors due to the conjugate process ($\cdot 2$), and each flavour $\ell_2 \neq \ell_1$ ($\cdot 2$). For decays into $\nu\nu\nu$, there are extra factors due to the conjugate process ($\cdot 2$), and each flavour $\ell' \neq \ell$ ($\cdot 2$). For decays into ℓjj, there are extra factors due

to the conjugate process (·2), and final state quark pairs ($\bar{d}u$) and ($\bar{s}c$) for diagonal CKM matrix (·2). For decays into νjj, there are extra factors due to the conjugate process (·2), and the number of up-type and down-type quarks in the final state u, c (·2) and d, s, b (·3), respectively.

By adding all the partial widths together, eq. (4.66) to eq. (4.69), the total width for the 3-body decays of the heavy neutrino in the low-energy limit is obtained

$$\Gamma^{N,3-\text{body}} \approx 0.129 \frac{|\theta|^2}{2} \frac{G_F^2 M^5}{\pi^3} \,. \tag{4.70}$$

The branching ratios, see eq. (4.62) for the definition, result in the following values in this approximation:

$$\left.\begin{array}{ll} \text{BR}(N \to \nu\nu\nu) & \sim 8\% \\ \text{BR}(N \to \nu\ell^+\ell^-) & \sim 23\% \end{array}\right\} \sim 31\% \,,$$
$$\left.\begin{array}{ll} \text{BR}(N \to \nu jj) & \sim 20\% \\ \text{BR}(N \to \ell jj) & \sim 49\% \end{array}\right\} \sim 69\% \,. \tag{4.71}$$

Sometimes, the decays of the first two branching ratios together are also referred to as leptonic decays of the heavy neutrino and the last two as semileptonic decays of the heavy neutrino, in contrast to the nomenclature of eq. (4.64).

4.4 THE MODEL IMPLEMENTATION

Our goal is to investigate the phenomenology of EW scale sterile neutrinos in order to assess the prospects for testing these future colliders. For the subsequent investigations, simulations of the collider phenomenology from sterile neutrinos in the framework of the SPSS are performed. To this end, we use Monte Carlo event generators as essential tools for which we need to implement the SPSS as the framework. The Monte Carlo event generators produce simulated data of particle physics processes at the parton level. In order to obtain events at the reconstructed level, the partonic events have to be reconstructed from the simulation of the detector response. This comprises the parton showering and hadronisation which is done by Pythia [231] [http://home.thep.lu.se/Pythia/]. The subsequent fast simulation of the detector response is performed by Delphes [232] [https://cp3.irmp.ucl.ac.be/projects/delphes]. This data can be used as the basis for the analysis of various signatures, for instance with Madanalysis [233–235] [https://launchpad.net/madanalysis5] or Mathematica [https://www.wolfram.com/mathematica/].
These steps, also referred to as the analysis chain, are represented schematically in fig. 8.

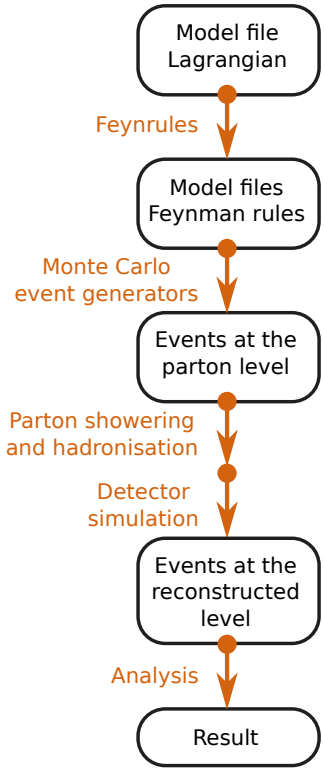

Figure 8: Employed analysis chain . For details see text.

4.4.1 *Implementation*

We implemented the SPSS in a model file for Feynrules 2.0 [236] [78]. Feynrules allows us to produce different model file outputs such as the Universal FeynRules Output [237] which can be used for the event generator MadGraph5

[78] Feynrules [http://feynrules.irmp.ucl.ac.be] is a Mathematica package that calculates the Feynman rules and produces different outputs for various MC event generators.

[238–243] [79] or WHIZARD-output [244] which can be used by the WHIZARD event generator [245, 246] [80].

[243] [231] [232]

In Feynrules, the SPSS (in the limit of intact symmetry) is implemented in the mass eigenbasis of the neutrinos, i.e. the additional accessible particles for the interactions are the 3 massless light Majorana neutrinos and the 2 heavy Majorana neutrinos with degenerate masses M. The couplings of the heavy and light neutrinos to the SM particles are implemented via the charged and neutral weak current interactions eq. (4.38) and eq. (4.39), and the Yukawa interaction (4.45). As described at the end of section 4.3.1, the relevant parameters for the phenomenology of the heavy neutrinos in the framework of the SPSS are 3 Yukawa couplings $y_{\nu_e}, y_{\nu_\mu}, y_{\nu_\tau}$ [81] and the mass parameter M. These are the 4 new input parameters which are accessible by Feynrules and the Monte Carlo event generators.

The SM input parameters are set to their default values, except the Fermi constant, where the non-unitarity effects are taken into account by the modification according to eq. (4.48). We show some values of the relevant input parameters such as the mass of the Z boson, the fine structure constant (at the Z pole), the Fermi constant from muon decays, and the mass of the Higgs boson that are used throughout this thesis:

Input parameter	m_Z [GeV]	$\alpha(m_Z)^{-1}$	G_μ [GeV^{-2}]	m_h [GeV]
Value	91.1876	127.9	1.16637×10^{-5}	125

We remark that the current implementation of the SPSS in Feynrules is limited to lepton-number conserving processes only, since we are studying the SPSS in the limit of intact symmetry. In order to study lepton-number violating effects, the protective symmetry has to be slightly broken which introduces the perturbation parameters to the neutrino mass matrix. The heavy neutrinos would form pseudo-Dirac particles, i.e. heavy Majorana neutrinos with non-degenerate masses. This would effectively introduce the mass splitting of the heavy neutrinos as a new parameter. Furthermore, the implementation is limited to unitary gauge for simplicity.

4.4.2 *Model validation*

In this section, we perform a validation of the model implementation by comparing the numerical results for the heavy neutrino partial decay widths, obtained from WHIZARD 2.4, with the analytical formulae.

For the 2-body decays of the heavy neutrino into the SM bosons, we calculated the partial widths $\Gamma_M(N_j \to W\Sigma_\alpha \ell_\alpha)$, $\Gamma_M(N_j \to Z\Sigma_i \nu_i)$, $\Gamma_M(N_j \to h\Sigma_i \nu_i)$, cf. eq. (4.52) to (4.54), for several mass points in the range of 100 GeV to 1 TeV. The comparison of the numerical values with the analytical formulae for the Majorana case is shown in fig. 9a. As can be seen in this figure, there is good agreement between both. The corresponding branching ratios are shown in fig. 9b, which fulfil the $2:1:1$ correspondence in the limit that $M \gg m_h$, cf. eq. (4.63).

For the 3-body decays of the heavy neutrino, the low-energy approximation was calculated and also compared to the numerically obtained full expression.

[79] MadGraph5_aMCNLO: https://launchpad.net/mg5amcnlo

[80] The WHIZARD Event Generator: http://whizard.hepforge.org

[81] The Yukawa couplings can also be mapped onto the active-sterile mixing parameters $\theta_e, \theta_\mu, \theta_\tau$ via eq. (4.30).

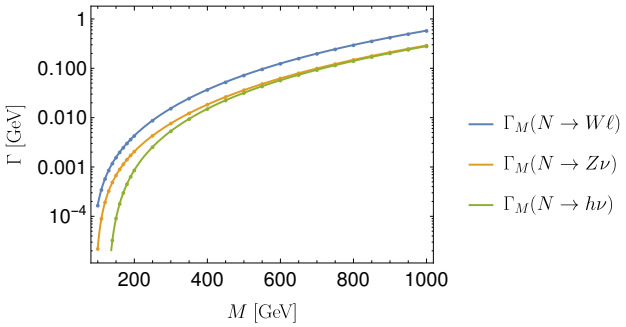

(a) Shown are the 2-body partial decay widths of a heavy Majorana neutrino for the analytical formulae and the numerical result. The partial decay widths are calculated for an active-sterile mixing angle of $\theta^2 = 0.042^2 \approx 10^{-3}$.

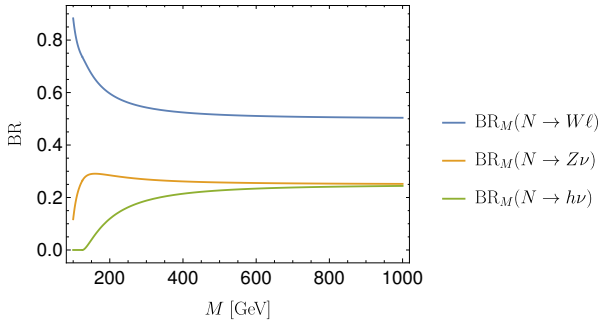

(b) Shown are the branching ratios of the 2-body partial decay widths of a heavy Majorana neutrino, summed over all possible fermions.

Figure 9: Comparison of the 2-body partial decay widths and branching ratios of a heavy Majorana neutrino into W, Z, Higgs boson, summed over all possible fermions. The solid lines represent the analytic formulae and the dots represent the numerical result obtained by WHIZARD 2.4 for the different mass points. The partial decay widths are calculated for an active-sterile mixing angle of $\theta^2 = 0.042^2$.

The low-energy approximation, $M \ll m_W$, for the 3-body decay of the heavy neutrino can be calculated in WHIZARD by the following approach. One can scale up the masses m_W, m_Z, m_h by some overall factor, which renders any higher order terms in M/m_X negligible. However, this also changes the magnitude of the decay width since the Fermi constant, which appears in the calculation of the decay width, is calculated from the W boson mass. One can remedy this by correcting the resulting magnitude by the introduced overall factor.

We compare in fig. 10 the analytical formulae for the total and partial widths of the 3-body decay in the low-energy approximation, i.e. eq. (4.66) – (4.70), to the numerically obtained results by the above described approach in WHIZARD. Also here, the agreement between the analytically and numerically obtained widths is good.

But, once the two-body decays become efficient this approximation should break down. We further compare the decay widths in the low-energy approximation to the full expression obtained by WHIZARD. The comparison is shown in fig. 11a. Therein can be seen that the corrections start to become substantial for masses $\gtrsim 40$ GeV while the approximation becomes very inaccurate once on-shell decays into W become possible.

In the full expression, not only the total width of the 3-body decays changes but also the respective branching ratios shown in eq. (4.71). The resulting branching ratios for masses up to 100 GeV are shown in fig. 11b.

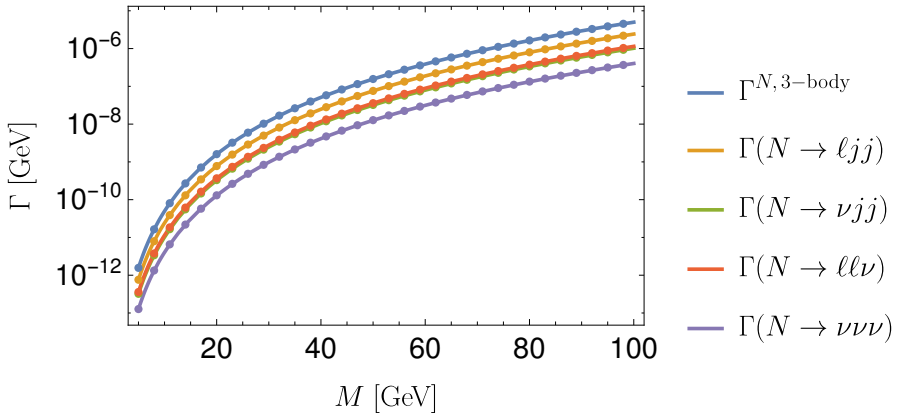

Figure 10: Comparison of the 3-body total and partial decay widths of a heavy Majorana neutrino in the low-energy approximation, $M \ll m_W$. The solid lines represent the analtic formulae (4.66) to (4.70) and the dots represent the numerical result obtained by WHIZARD for the different mass points. The partial decay widths are calculated for an active-sterile mixing angle of $\theta^2 = 0.042^2$.

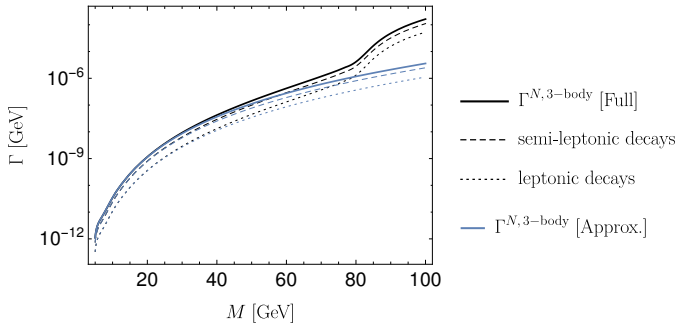

(a) Comparison of the total and partial width of the 3-body decays of a heavy Majorana neutrino in the low-energy approximation to the full expression. The solid lines represent the total decay width, while the dashed and dotted lines represent all leptonic ($(N \to \nu\nu\nu) + (N \to \nu\ell^+\ell^-)$) and semileptonic ($(N \to \nu jj) + (N \to \ell jj)$) decays, respectivley. The decay widths are calculated for an active-sterile mixing angle of $\theta^2 = 0.042^2$.

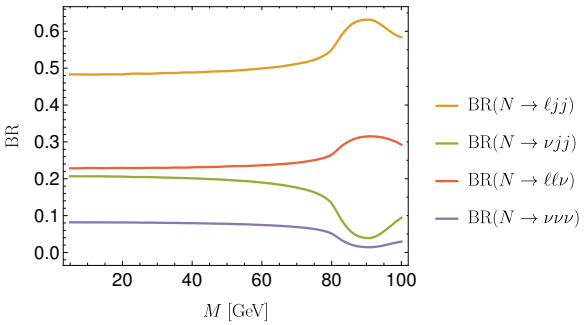

(b) Branching ratios of the 3-body decay of the heavy neutrino as a function of the heavy neutrino mass M.

Figure 11: Shown are the total decay width and the branching ratios of the 3-body decays of the heavy neutrino.

Part III

STERILE NEUTRINO PHENOMENOLOGY AND SEARCHES AT COLLIDERS

5 OVERVIEW OF SEARCH STRATEGIES

Before we dive into the sterile neutrino phenomenology and searches at future collider, it is useful to first have a small overview of the overall search strategies and present constraints for sterile neutrinos around the GeV scale.

5.1 LANDSCAPE OF STERILE NEUTRINO SEARCHES

There are several experimental searches that have put limits on the active-sterile mixing from heavy neutrino masses at the eV scale up to the TeV scale. These searches are subdivided into two categories, direct and indirect searches. In the following we, briefly summarise various direct and indirect searches that are described in ref. [27, 217, 247, 248].

To have an overall feeling for the sensitivity on the active-sterile mixing of certain searches, we show fig. 12 taken from ref. [27, 247]. The limits shown in the figure are intended rather as illustrations than hard limits on the active-sterile mixing, since many of these limits are derived in the context of one sterile neutrino and one active-sterile mixing explaining the whole phenomenology. Therefore, these limits do not always directly translate to limits in context of the SPSS. One would need to check the derivation of each limit and if necessary recast these limits in the framework of the SPSS. We refer the reader to ref. [27, 217, 247, 248] and references therein for more details such as the derivation of the limits. The present constraints in the context of the SPSS are then discussed in the next section 5.2.

In fig. 12 the limits on the active-sterile mixing, expressed by the mixing matrix elements, are shown for various direct and indirect sterile neutrino searches in the mass range of 100 MeV $\lesssim M \lesssim$ 500 GeV. The line labelled "Sessaw" corresponds to the standard seesaw relation in the 1 family case. Therein, also a disfavoured region from cosmological constraint on Big Bang Nucleosynthesis (BBN) is shown by the line labelled "BBN".

5.1.1 *Direct searches*

For direct searches, information is drawn from the direct production of new states (also especially in the case of absence of new states), i.e. the heavy neutrino is supposed to appear as a real particle. Various direct searches are summarised below:

- Peak searches in meson decays:[248] If heavy neutrinos would be produced from meson decays together with a charged lepton, then the lepton spectrum would show a peak at a characteristic energy. The search for this peak puts constraints on the active-sterile mixing. Hence, in peak searches it is not necessary to observe the decays of the heavy neutrino. Peak searches are performed in pion, kaon as well as B and τ decays, see the "$\pi \to \ell\nu$","$K \to \ell\nu$", "Belle" and "B-factory" lines in fig. 12. These searches probe the MeV $\lesssim M \lesssim$ GeV range.

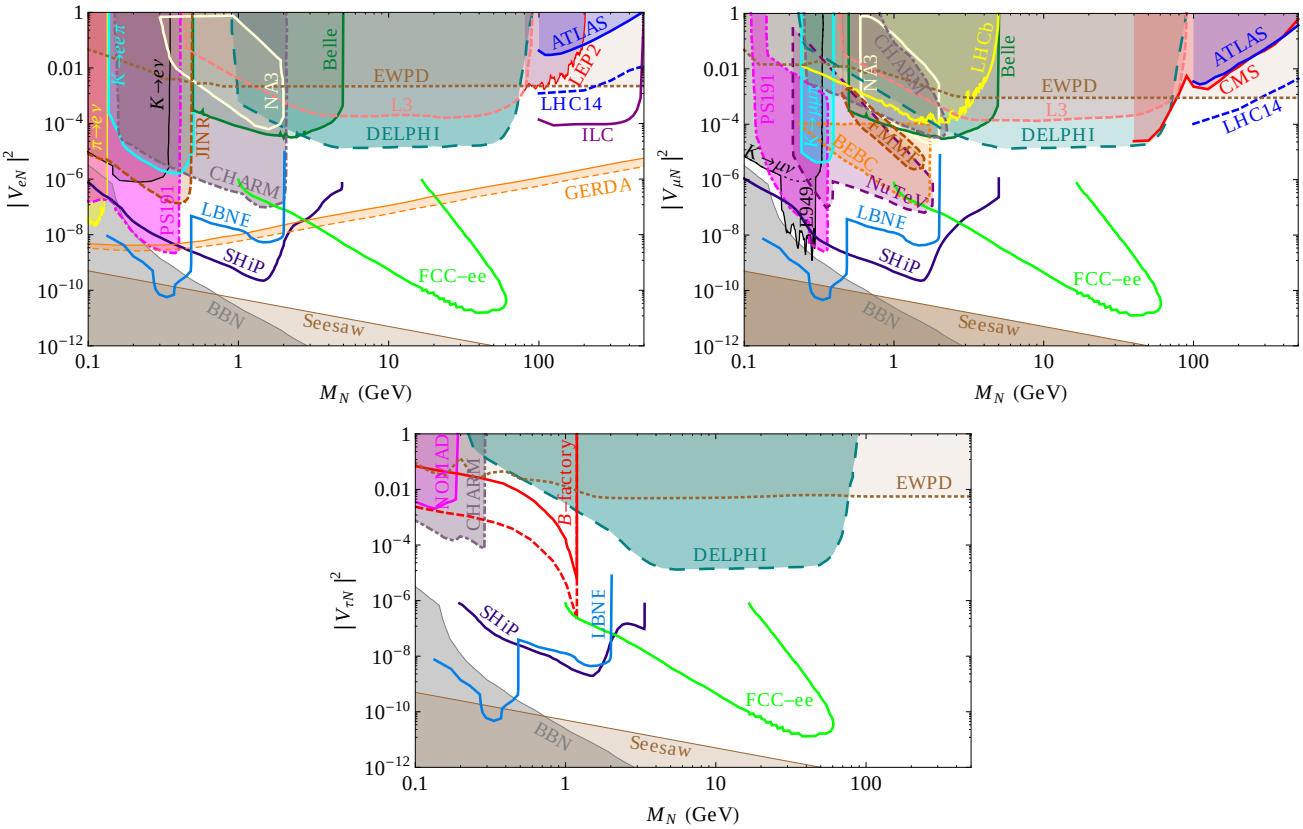

Figure 12: Limits on the mixing $|V_{eN}|^2$, $|V_{\mu N}|^2$ and $|V_{\tau N}|^2$ reprinted from [27] (copyright CC-BY 3.0). In our notation this would correspond to the mixing $|\mathcal{U}_{eN}|^2 = |\mathcal{U}_{e4}|^2 + |\mathcal{U}_{e5}|^2 = |\theta_e|^2$, $|\mathcal{U}_{\mu N}|^2 = |\theta_\mu|^2$, and $|\mathcal{U}_{\tau N}|^2 = |\theta_\tau|^2$. The limits are derived under the assumption that a single heavy neutrino mass scale M_N and a single activ-sterile neutrino mixing $V_{\alpha N}$ are relevant [27], i.e. the active-sterile mixing of other flavors $\beta \neq \alpha$ are subdominant.

- Beam dump experiments: A proton beam is dumped into a dense material (the fixed target) from which heavy neutrinos can be produced in meson decays (when kinematically allowed). Their subsequent decay can be visible (discerned from the background) if the sterile neutrino decays at some distance from the background that is produced at the fixed target. The long-lived heavy neutrino gives rise to the signature of a displaced secondary vertex [82]. Limits from beam dump experiments range from MeV $\lesssim M \lesssim$ GeV, see the limits from experiments at CERN "PS191", "NA3", "CHARM", "BEBC", "NOMAD", from experiments at Fermilab "FMMF", "NuTeV" and from experiments at IHEP "IHEP-JINR" in fig. 12.

  The proposed fixed-target experiment SHiP (Search for Hidden Particle) at CERN [249] can test long-lived heavy neutrinos to much smaller sensitivities than the above mentioned experiments, see the line labelled "SHiP" in fig. 12. The heavy neutrinos would be produced from the decays of D and B mesons and also τ leptons.

  The proposed long base line accelerator experiment Deep Underground Neutrino Experiment (DUNE) [117], formerly the Long Baseline Neu-

[82] The detector of the experiment is usually at some distance downstream the beam, i.e. behind the fixed target, where heavy neutrinos that propagate through the fixed target can decay and be detected [247]. Since the heavy neutrino is uncharged, the propagation inside the detector volume is not visible. The visible signature, once the heavy neutrino decays, is charged particles appearing from a single point which is some distance away from the production point.

trino Experiment (LBNE) [250], can also probe heavy neutrinos from D meson decays with its near detector, see the "LBNE" line in fig. 12.

- Lepton-number violating decays: Searches for lepton-number violating rare meson decays from heavy Majorana neutrinos have been performed in the $K^+ \to \ell^+\ell^+\pi^-$ channel which gives limits in the $\sim$ 100 MeV range, see the line labelled as "$K \to \ell\ell\pi$" in fig. 12.

  In analogy to the rare meson decays, there is further the possibility to search for lepton-number violating τ decays [248].

- Z boson decays at collider experiments: Heavy neutrinos can be produced from Z boson decays for neutrino masses below the Z boson mass. The subsequent decays of the heavy neutrino have been searched for at the Large Electron-Positron Collider (LEP) [83], see the limits labelled after the experiments "DELPHI" and "L3" in fig. 12.

  Specifically, the strongest upper bound stems from DELPHI on $BR(Z \to \nu N)$ which can be expressed in a upper limit on the active-sterile mixing θ^2 in the context of the SPSS [217].

  A proposed future electron-positron collider with high-luminosities at the Z pole, such as the Future Circular Collider in the electron positron mode (FCC-ee), could probe very small active-sterile mixings of long-lived heavy neutrinos via displaced vertices [2, 252], see the line labelled "FCC-ee" in fig. 12.

- Direct searches at colliders: Heavy neutrinos heavier than the Z boson can be produced on-shell at colliders. Direct searches were performed at LEP-2 for center-of-mass energies $\sqrt{s}$ around the WW production threshold of 161 GeV and beyond up to 208 GeV [84]. Mixings for heavy neutrinos masses in the 100 to 200 GeV range have been constrained for semileptonic decays, see the "LEP 2" line in fig. 12.

  Proposed future electron-positron colliders can significantly improve the sensitivity in two ways. First, higher sensitivity in the active-sterle mixing due to a much higher luminosity and, second, wider reach for the neutrino masses due to operating at much higher center-of-mass energies. See for instance the "ILC" line with $\sqrt{s} = 500$ GeV in fig. 12.

  Also hadron colliders have performed direct searches for heavy Majorana neutrinos from the lepton-number violating same-sign dilepton signature. The LHC has performed these searches for heavy neutrino masses heavier than the Z boson [85], see the "ATLAS" and "CMS" lines in fig. 12.

[83] More specifically, these searches have been performed at LEP-1. The goal of LEP-1 was to study the Z resonance, see for instance [251].

[84] The goal of LEP-2 was to study the fermion pair production cross section for center-of-mass energies above the Z boson mass and measurement of the WW production cross section, see e. g. ref. [253].

[85] Often LHC analyses consider only one sterile neutrino. In ref. [3], it is argued that in this case the standard seesaw formula, $m_\nu \approx \frac{y_\nu^2 v_F^2 w}{2M}$, is valid and the active-sterile mixing is constrained to the brown line labelled "Seesaw". Whereas in low scale seesaw scenarios, larger active-sterile mixings are consistent with neutrino masses, but the lepton-number violating effects are possibly suppressed.

5.1.2 *Indirect searches*

For indirect searches, information is drawn from observables that are affected by the sterile neutrinos indirectly, i.e. the heavy neutrino would appear as a virtual particle. Various indirect searches are summarised below.

- Neutrino oscillations: It is noted that significant mixing of the active and sterile neutrinos are required and that the heavy neutrino mass

cannot be too large [27, 248]. The eV mass range can be probed well by neutrino oscillation experiments.

- Neutrinoless double β decay: $0\nu\beta\beta$ experiments mostly constrain the 10 eV $\gtrsim M \gtrsim$ MeV range. However, it is possible to draw limits from the interpolated $0\nu\beta\beta$ half-life for arbitrary heavy neutrino masses [86], see the "GERDA" line in fig. 12.

- Electroweak precision observables: Due to the modification of the weak currents, the theory prediction of the Fermi constant is modified [87] as described in section 4.3.3. This further affects various EW parameters in the SM such as the weak mixing angle, the W boson mass, etc. By performing global fits of the electroweak precision observables limits on the active-sterile mixing can be derived [88], see the line labelled "EWPD" in fig. 12.

- Z boson decay parameters: The invisible Z boson decay width [89] is sensitive to the active-sterile mixing due to the Z boson decaying into light neutrinos and the modification of the Fermi constant G_μ.

- Higgs boson branching ratios: Due to an additional decay channel of the Higgs boson into neutrinos, the branching ratios of the Higgs boson are altered. The measurement of the branching ratios of the Higgs boson at the LHC allows to constrain the active-sterile mixing, see for instance [217].

- Lepton universality tests: The deviation of the ratio of decay rates of mesons and charged leptons of different flavour from unity gives limits on the mixing [90], see for instance ref. [217, 222].

- Rare flavour-violating charged lepton decays: Decays $\ell_\alpha \to \ell_\beta \gamma$ are possible in the presence of sterile neutrinos at the 1-loop level. Experiments put limits on the corresponding branching ratios. The most stringent limit here stems from the MEG experiment on $\mathrm{BR}(\mu \to e\gamma) < 5.7 \cdot 10^{-13}$ at 90% confidence level (C.L.) [255]. For more details on rare lepton flavour-violating decays cf. for instance [256, 257].

  It also possible to derive limits for the lepton-flavour violation 3-body decays of the charged leptons, for instance $\mathrm{BR}(\mu \to eee)$, which seem subdominant compared with the limit on $\mu \to e\gamma$ [248].

5.2 CONSTRAINTS

For the constraints on the sterile neutrino parameters, we summarise the limits derived in the context of the SPSS from ref. [217, 222]. Specifically, we discuss the constraints on the active-sterile mixing parameters for heavy neutrino masses M between 10 GeV and 200 GeV as seen in fig. 13. We note that the constraints discussed here, do not contain all observable features. Further constraints on various models with sterile neutrinos can be found, for instance, in ref. [25, 166, 208, 223, 248, 257–271].

[86] The limit from $0\nu\nu\beta$ seems severe, but this limit is derived in the case of one sterile neutrino only and the same argument applies as in side note 85. In that case the limits would be weaker.

[87] $G_\mu^2 = G_F^2 \cdot (\mathcal{N}\mathcal{N}^\dagger)_{ee}(\mathcal{N}\mathcal{N}^\dagger)_{\mu\mu}$

[88] Usually, further precision observables from the SM are taken into account, e.g. Z boson decays parameters, lepton universality test, rare flavour-violating charged lepton decays, etc., see below.

[89] The invisible Z boson decay width, Γ_{inv}, is defined as the width $\Gamma(Z \to \nu\nu)$ summed over all flavour or light neutrino states, respectively. From the measured Γ_{inv} at e^+e^- colliders such as LEP, the number of neutrino families, N_ν, is inferred. The resulting value at LEP, $N_\nu = 2.9840 \pm 0.0082$, differs about 2 standard deviations from 3 [251]. This deficit can be caused by the mixing of active and sterile neutrinos. Confer for instance ref. [254] and references therein.

[90] The ratios are given by $R^X_{\alpha\beta} = \Gamma^X_\alpha / \Gamma^X_\beta$, where α and β label the flavour of one charged leptons, and X the parent particle. An example process is $\pi \to \ell_\alpha^- \overline{\nu}_\alpha$. Lepton universality corresponds to the case of unit ratios as predicted by the SM.

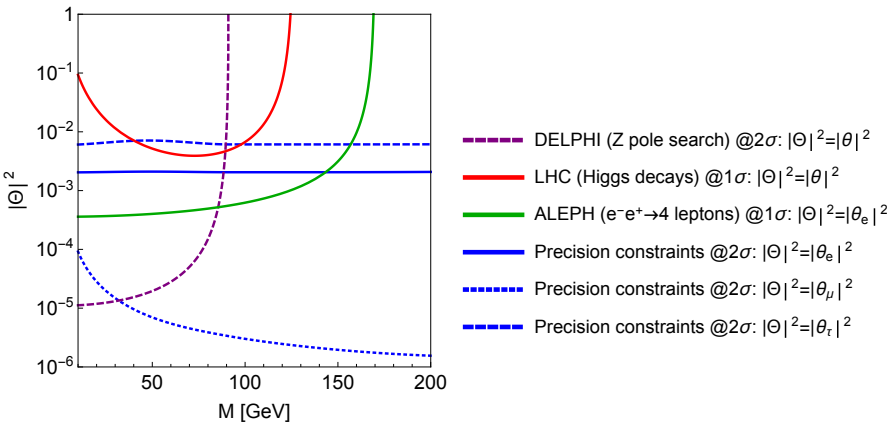

Figure 13: Shown is the summary of constraints on sterile neutrino parameters in the context of the SPSS. The figure is reprinted from [3], which contains the updated figure originally from [217]. The summary includes the upper limits on the active-sterile mixing parameters from indirect searches in electroweak precision data, searches in Higgs boson branching ratios and direct searches at LEP, all of which can be found as sections in the main text.

Indirect searches in electroweak precision data

In ref. [217, 222], present constraints from indirect searches in precision observables are obtained from a global fit of the EW precision observables, Z boson decay parameters, lepton universality observables, rare flavour violating charged lepton decays, as well as CKM unitarity tests. The resulting upper bounds at 90% C.L. from the global fit for the active-sterile mixing $|\theta_\alpha|^2$, with $\alpha = e, \mu, \tau$, are shown in fig. 13 by the blue lines labelled as "precision constraints".

For heavy neutrino masses $M \gtrsim m_Z$ the corresponding upper bounds to the moduli of active-sterile mixing angles [91] at 1σ C.L. can be approximated as [1, 222]

$$|\theta_e| = 0.042, \qquad |\theta_\mu| = 0.015\,, \qquad |\theta_\tau| = 0.065\,. \tag{5.1}$$

While for the e-μ, e-τ and μ-τ flavour combinations of the active-sterile mixing angles, the upper bounds

$$|\theta_e\theta_\mu| = 7\times10^{-6}\,, \qquad |\theta_e\theta_\tau| = 1.4\times10^{-3}\,, \qquad |\theta_\mu\theta_\tau| = 4.8\times10^{-4}\,, \tag{5.2}$$

at 1σ C.L. are obtained.

[91] Equivalently for the neutrino Yukawa couplings, $|y_{\nu\,\alpha}| = |\theta_\alpha|\frac{\sqrt{2}M}{v_{EW}}$.

Searches in Higgs boson branching ratios

The additional decay channel of the Higgs boson into a heavy neutrino modifies the Higgs boson branching ratios into the known SM particles. The branching ratio measurement of $h \to \gamma\gamma$ at ATLAS and CMS has been used in ref. [217], to put limits on the partial decay width $\Gamma(h \to \nu N)$. The result-

ing constraint on θ^2 is shown in fig. 13 by the red line labelled "LHC (Higgs decays)".

Direct searches at LEP

Direct searches for heavy neutrinos from Z bosons decays at the LEP-1 experiments DELPHI [272], OPAL [273], ALEPH [274] and L3 [275] are the most constraining collider searches. DELPHI provides the most stringent bound on $\mathrm{BR}(Z \to \nu N)$. The resulting limit on θ^2 is derived in ref. [217] and is shown in fig. 13 by the purple line labelled as "DELPHI (Z pole search)".

In direct searches at LEP-2, the *WW* production cross section was measured by analysing 4 lepton final states [92] at center-of-mass energies 183 to 208 GeV [253]. In this process also a bound on the deviation of the SM cross section was inferred at the 1σ C.L. In ref. [217] constraints on $|\theta_e|^2$ are inferred from this deviation. The corresponding limit on $|\theta_e|^2$ is shown in fig. 13 by the green line labelled as "ALEPH ($e^+e^- \to 4$ leptons)"

[92] The process is given by $e^+e^- \to WW \to (\bar{\nu}\ell^-)(\ell^+\nu)$

6 HEAVY NEUTRINOS AT FUTURE COLLIDERS

6.1 FUTURE COLLIDERS

The discovery of a Higgs bosons by ATLAS [276] and CMS [277] at the Large Hadron Collider (LHC) in 2012, that looks to be compatible with the SM Higgs boson, is a major milestone for particle physics since it would complete the SM. For the time being, the LHC and its high-luminosity upgrade, the High-Luminosity Large Hadron Collider (HL-LHC) once it is commissioned in 2026 [278], are the main avenues by which the properties of this boson are studied. However, there are open questions surrounding the Higgs boson, i.e. open questions in SM physics, that cannot be answered adequately by the LHC, especially the question about its self-interaction [93] [279]. This coupled with no convincing evidence for new physics so far at the LHC with $\sqrt{s} \sim 13$ TeV, although there must be new phenomena related to the open questions from BSM physics [94] have called upon strategies to ensure a continuation of a high-energy physics programme after the operation of the LHC until 2035 [280]. The strategies to get further answers are the next-generation accelerators that provide higher-energies and higher intensities. From the experience of LEP and the LHC, around 20 to 30 years are realistic for the conception, design and construction of such a future accelerator. Therefore, such a future accelerator has to be planned well in advance in order that it can be commissioned in the 2030s-2040s to ensure a continuation of the high-energy physics programme.

[93] The self-interaction is related to the origin of the mass of the Higgs boson itself.

[94] Such as the BAU, DM, and neutrino masses, etc.

At present, there are several future accelerators in the design process which are proposed by different organisations. The design process is roughly subdivided into 2 phases. A conceptual design phase and a technical design phase.

The aim of the conceptual design phase are amongst others: To identify the physics case and the physics goals; To formulate luminosity goals; To study different machine baselines, accelerator layouts and detector concepts; To perform an initial design of the accelerator and detector; To identify critical technical challenges that require further R&D; To explore the physics potential of the layouts; To consider the required infrastructure; To consider various operation concepts; To estimate the costs to build and operate the various accelerator designs. This information is collected and streamlined into an official document by the organisation, usually referred to as conceptual design report (CDR). The further strategy for the technical design is based on the considerations of the CDR. In the subsequent technical design phase, the accelerator project has to be brought to a technically mature stage and finalised into a technical design report (TDR) where it is ready for construction. The technical design phase comprises among other things: To address the physics goals; To validate the technical design from the R&D results, for instance, to develop, simulate, build and validate a prototype of the detector; To analyse the cost and value of the accelerator.

In the following we discuss the different accelerators that are proposed by different organisations. Depending on their underlying goals, the accelerators have different design strategies. The future accelerators are proposed to be colliders, i.e. they accelerate two beams and bring them to collision. There are mainly 3 types of machines proposed, electron-positron (e^+e^-), hadron (pp) and electron-proton (e^-p) colliders.

The proposed future colliders are:

- Future Circular Colliders (FCC) [95]: The FCC design study, hosted by CERN under a recommendation of the European Strategy for particle physics [281], entails a high-energy circular hadron collider, called the FCC-hh [282–284], a high-luminosity circular electron-positron collider, called the FCC-ee [285], as well as a proton-electron collider, called the FCC-eh [286, 287]. The circular collider is proposed to have a 100 km long circumference and to be built in the area of Geneva [288]. The FCC study is focused on the development of the FCC-hh with $\sqrt{s} \sim 100$ TeV and the FCC-ee operating at $\sqrt{s}$ between $90 - 350$ GeV as a possible first stage, similarly to LEP and the LHC. The FCC design study plans to release a CDR by the end of 2018 for the update of the European Strategy for particle physics in 2019-2020 [288]. Since the FCCs are in its conceptual design phase, the numbers are prone to changes.

- Circular Electron Positron Collider - Super proton-proton Collider (CEPC-SppC) [96]: The CEPC-SppC design study, initiated by IHEP, entails the feasibility of a circular electron positron collider, called the CEPC, and a hadron collider, called the SppC, in China. The circular collider is proposed to have a 100 km long circumference instead of the earlier planned 54 km [289], there are several possible construction sites discussed in China. The CEPC-SppC study is focused on the development of the CEPC operating at $\sqrt{s}$ between $90 - 240$ GeV with the subsequent upgrade to the SppC with $\sqrt{s} \sim 75$ GeV and with future upgrades up to $125 - 150$ TeV [290]. At the time of writing, the CEPC-SppC study group is finalising the CDR, confer ref. [290].

- International Linear Collider (ILC) [97]: The design of the ILC, which is coordinated by the Global Design Effort under a mandate from the International Committee for Future Accelerators [291], is comprised of a linear electron-positron collider. The ILC is proposed to be operating at $\sqrt{s}$ between $90 - 500$ GeV and with a subsequent upgrade up to 1000 GeV [292]. Furthermore, it offers beams with a high degree of spin polarisation. The TDR, confer ref. [292], of the ILC has been released in 2013. After its release, the TDR is being adjusted for the possibility that the ILC is hosted by Japan [293]. The specific site is located in the Kitakami highlands of Japan, where the ~31 km long collider could be built. Although the project is very mature, there is up to now no worldwide consensus to construct the ILC and an appropriate international organisation has still to be set up [293].

- Compact Linear Collider (CLIC) [98]: The design of the CLIC, which is coordinated by CERN under a mandate from the International Committee for Future Accelerators [291], is comprised of a linear electron-positron

[95] https://fcc.web.cern.ch/Pages/default.aspx

[96] http://cepc.ihep.ac.cn

[97] http://www.linearcollider.org/ILC

[98] http://clic-study.web.cern.ch

collider. The core of the study is the development of a new accelerator technology, which has the same name as the collider. CLIC would provide center-of-mass energies up to 3 TeV and offers spin polarisation for the electron beam [294]. The 11 up to 50 km long linear collider is proposed to be built on and around the CERN site. The study group released CLIC's CDR in 2012, confer ref. [294]. At present, the CLIC case is being prepared for the next update of the European Strategy for Particle Physics 2019-2020 [295].

- Large Hadron electron Collider (LHeC) [99]: An upgrade to the LHC is being designed on the possibility to install an electron beam with a high degree of spin polarisation, such that it can be brought to collision with the proton beam of the LHC, this project is referred to as the LHeC. The CDR for the LHeC has been released in 2012, confer ref. [296]. The LHeC intends to accompany the hadron physics programme of the LHC once the HL-LHC upgrade is installed.

[99] http://lhec.web.cern.ch

To the above list, we would like to note that there are also many close collaborations between these study groups where synergies are found. For instance, the Linear Collider Collaboration [100] has the aim to ensure that synergies are used as efficiently as possible between the CLIC and ILC [297].

[100] http://www.linearcollider.org

The subsequent sections are subdivided into e^+e^-, pp and e^-p colliders. Therein, the relevant physics parameters of the colliders are summarised for this thesis, being the operating center-of-mass energies, i.e. the physics runs, and their target integrated luminosities. Also the general physics goals of the collider types with an emphasis on SM measurements are addressed. Of course, there is also a strong physics case for heavy neutrinos at the proposed future colliders, which is the main part of the investigations in this thesis. Therefore, it is necessary to discuss the dominant production channels for heavy neutrinos, and the resulting signal channels after their subsequent decay for e^+e^-, pp and e^-p colliders first. The following investigation is based on work that is partly published in [3].

The heavy neutrinos can be produced from high-energy collisions of the electron and proton beams by the weak interactions or the Higgs boson, which we discussed in section 4.3.2. First, we discuss possible production channels of the heavy neutrinos, address its dependency on the active-sterile mixing angles and give the cross sections as a function of the heavy neutrino mass for the dominant production channels in section 6.2.1 for e^+e^-, 6.3.1 for pp and 6.4.1 for e^-p colliders. Second, we show the possible signal channels that are comprised of the various production and decay channels of the heavy neutrinos and discuss their dependency on the active-sterile mixing angles. These signal channels give rise to various final states in which observable effects from sterile neutrinos can be searched for. We summarise the resulting final states and their contributions from the different signal channels in section 6.2.2 for e^+e^-, 6.3.2 for pp and 6.4.2 for e^-p colliders.

6.2 FUTURE ELECTRON-POSITRON COLLIDERS

As mentioned in the previous section, there are four future electron-positron colliders in the design process at present, the two circular colliders CEPC

and FCC-ee, and the two linear colliders CLIC and ILC. Circular colliders can reach particularly high luminosities because each time a bunch of particles are brought head on to collision, the remaining particles of the bunch that have not collided can be recycled [101] and used for further head on collisions. Moreover, they can provide several interaction points [298]. However, for light particles such as electrons, the energy the electrons can take is limited by the energy loss from synchrotron radiation [102] [285]. Linear e^+e^- colliders on the other hand, can reach higher center-of-mass energies because the particles are accelerated on predominantly straight tracks, however, they are limited in their luminosity because they provide one interaction point and the accelerated particles cannot be recycled after the collision. This relation is illustrated in fig. 14, taken from [299], for the proposed future lepton colliders. The CEPC and FCC-ee achieve much higher luminosities for $\sqrt{s} \sim 240$ GeV and below, while CLIC and ILC can achieve $\sqrt{s} \sim 500$ GeV and into the TeV range as well as providing beams with spin polarisation. In the case of the ILC a beam polarisation for the electron/positron of 80%/30% are achievable [300]. While in the case of the CLIC, only a beam polarisation for the electron of 80% is planned [295].

[101] Literally, they can keep circulating.

[102] Charged particles on bent tracks emit synchrotron radiation.

Each of the proposed future e^+e^- colliders has its own intended operating range depending on their physics goals. The main physics goal of future lepton colliders is to provide high-precision measurements of the SM parameters. The SM parameters can be measured by studying the relevant processes at relevant center-of-mass energies. Some of the relevant physics goals of the e^+e^- colliders are, cf. for instance the CDRs ref. [290, 292]:

- Electroweak observables in the $e^+e^- \to Z$ process for the Z pole run ($\sqrt{s} \sim 90$ GeV).
- The W boson mass in the $e^+e^- \to WW$ process for the WW threshold run ($\sqrt{s} \sim 160$ GeV).
- Higgs boson coupling in the $e^+e^- \to Zh$ process for the SM Higgs physics run ($\sqrt{s} \sim 250$ GeV) [103].
- Top quark mass and coupling in the $e^+e^- \to \bar{t}t$ process for the top threshold scan ($\sqrt{s} \sim 350$ GeV).
- Top quark Yukawa coupling to Higgs and Higgs self-coupling for the high-energy runs ($\sqrt{s} \sim 500$ GeV and above).

[103] Although the CEPC and FCC-ee plan to have the Higgs physics run at $\sqrt{s} \sim 240$ GeV [290, 299]

In this regard, each of the lepton colliders has its unique physics program, which is defined by a target integrated luminosity for specific center-of-mass energies. The physics program for the circular colliders, the CEPC and FCC-ee, and linear colliders, the ILC and CLIC, is shown in the left and right panel of fig. 15, respectively.

Overall, the lepton colliders are considered as Z, W, Higgs, and top factories. They not only boast large luminosities, but also provides a much cleaner experimental environment than the LHC, since there is no strong interaction between the beams, thus pile up is rare [104] and triggering [105] is easier. Hence, they are very well designed to study rare Z, W, Higgs boson and top decays, which may also give insight into BSM physics such as sterile neutrinos. We refer the interested reader, for instance, to the respective CDRs and TDRs for the BSM physics case at e^+e^- colliders.

[104] pile up: multiple events per bunch crossing.

[105] A process that decides which events are recorded.

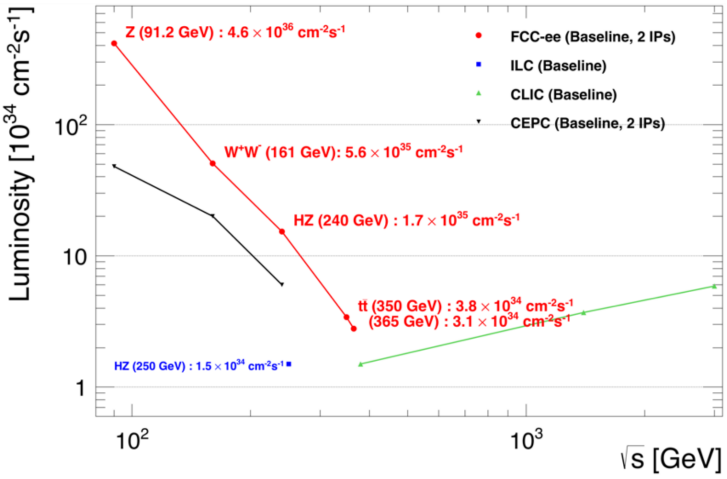

Figure 14: Shown are the expected instanteneous luminosities for the baseline of the proposed future e^+e^- colliders and their physics runs as a function of the center-of-mass energy. Reprinted from [299], copyright CC-BY 4.0 2018 CERN.

6.2.1 *Production mechanism*

In this section we discuss the dominant production processes for the heavy neutrinos at e^+e^- colliders.

There are 2 dominant productions processes. One is given by electron-positron annihilation into a heavy and light neutrino via a s channel Z boson. And the other one by a t-channel exchange of W boson. The corresponding Feynman diagrams for the production of a heavy neutrino are depicted in fig. 17. As can be seen from the figure, both production mechanisms give rise to a heavy neutrino that is accompanied by a light neutrino. The cross sections for the production processes are proportional to the active-sterile

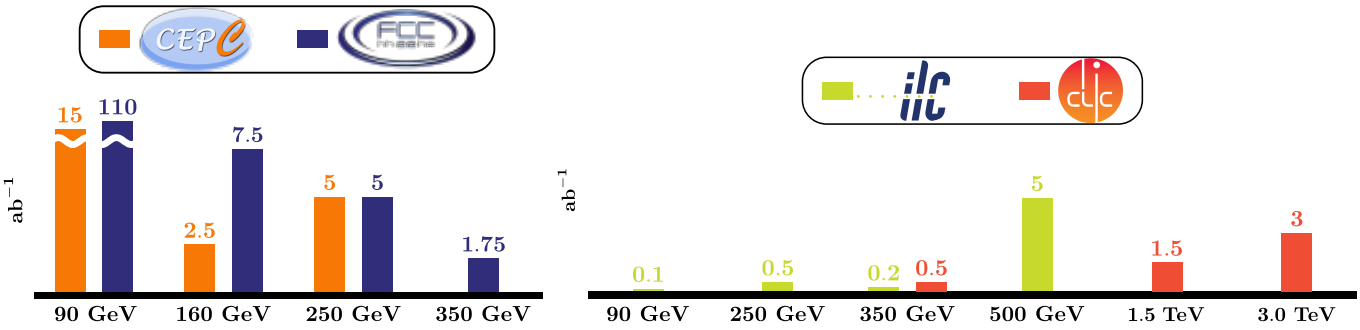

Figure 15: Shown are the physics programs for the respective future e^+e^- colliders given by the operating center-of-mass energies and envisaged integrated target luminosities in units of ab^{-1}. The circular colliders are represented on the left side. The approximate integrated luminosities for 2 interaction points at the CEPC, values taken from the CDR [290], and FCC-ee, values taken from [301] for 10 years run time, are illustrated therein. The linear colliders are represented on the right side. The integrated luminosities for the G-20 operation scenario from ref. [302] and the additional Giga-Z program [303] at the ILC as well as the physics runs for CLIC, values taken from [295], are illustrated therein.

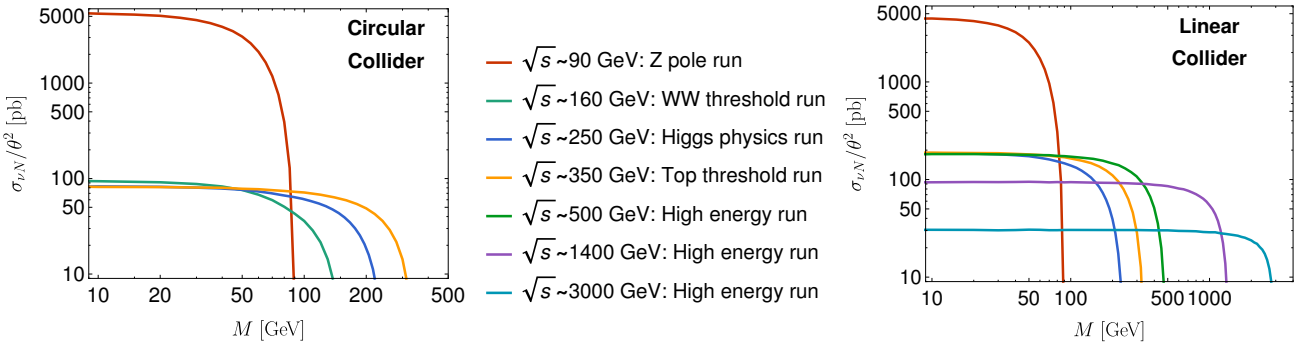

Figure 16: Shown is the heavy neutrino production cross section divided by the square of the active-sterile mixing angle as a function of the heavy neutrino mass for different center-of-mass energies. The cross sections were evaluated by WHIZARD with the inclusion of initial state radiation, i.e. emission of radiation by the incoming electron and positron beams which reduces the beam energy, and only for the linear colliders the inclusion of lepton beam polarisation. For the initial state polarisation a (L, R) beam polarisation of (80%,30%) was included. The following cuts have been applied to the cross sections: $|\cos(\theta)| \leqslant 0.99$, with θ being the angle between the heavy neutrino and the lepton beams.

mixings θ^2 and $|\theta_e|^2$, respectively, when summed over all light neutrinos. For the t-channel W exchange diagram, the active-sterile mixing angle $\theta_e^{(*)}$ is fixed due to the incident electron or positron beam. A sub-dominant channel constitutes heavy neutrinos from Higgs boson decays [106].

The heavy neutrino production cross section is given by

$$\sigma_{\nu N} = \sum_{i,j} \sigma(e^- e^+ \to N_j \nu_i)\,. \tag{6.1}$$

It contains the contributions from all the light neutrino ($i = 1,2,3$) and heavy neutrino ($j = 1,2$) mass eigenstates. The cross section is shown as a function of the heavy neutrino mass M for the different physics runs and for the different accelerator layouts in fig. 16. Assuming a mixing of $\theta^2 \sim 10^{-5}$, which is consistent with the present constraints, up to $\sim 10^4$ heavy neutrinos per ab^{-1} of integrated luminosity can be produced at the proposed future circular and linear colliders. For a total integrated luminosity of 100 ab^{-1}, 10 ab^{-1} and 0.1 ab^{-1}, $\sim 10^6$, $\sim 10^5$ and $\sim 10^3$ heavy neutrinos could be produced at the FCC-ee, CEPC, ILC, respectively. The heavy neutrino production is dominated by the s-channel Z boson contribution for $\sqrt{s} \simeq m_z$, while the t-channel W boson contribution takes over for the physics programs at the other center-of-mass energies, namely $\sqrt{s} = 160$ GeV and above [107]. Hence, the two production processes can be approximately separated by the center-of-mass energy of the physics programs.

[106] The Higgs boson is predominantly produced at e^+e^- colliders from Higgs strahlung and WW boson fusion process.

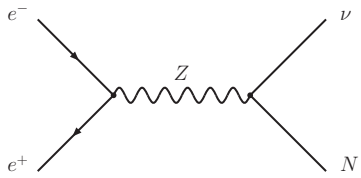

(a) Shown is the heavy neutrino from s-channel Z boson. The active-sterile mixing dependency of the cross section is θ^2 when the contributions are summed over all light neutrinos.

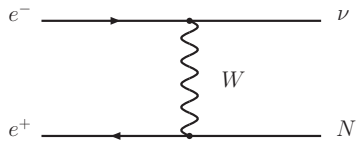

(b) Heavy neutrino from t-channel W boson. The active-sterile mixing dependency of the cross section is $|\theta_e|^2$ when the contributions are summed over all light neutrinos.

Figure 17: Depicted are the Feynman diagrams that dominate the production of heavy neutrinos at e^+e^- colliders.

[107] This is due to the t-channel process dropping at a slower rate with increasing center-of-mass energy as the s-channel process.

6.2.2 *Signal channels*

Here, we show the possible signal channels and resulting final states and discuss their dependency on the active-sterile mixing angles as well. For the here considered heavy neutrino masses, the in the electron-positron collision produced heavy neutrinos decay further into leptons and quarks (when kinematically allowed) via the decays of the W, Z and the Higgs boson. In fig. 18, the Feynman diagrams for the various signal channels via t-channel W bosons

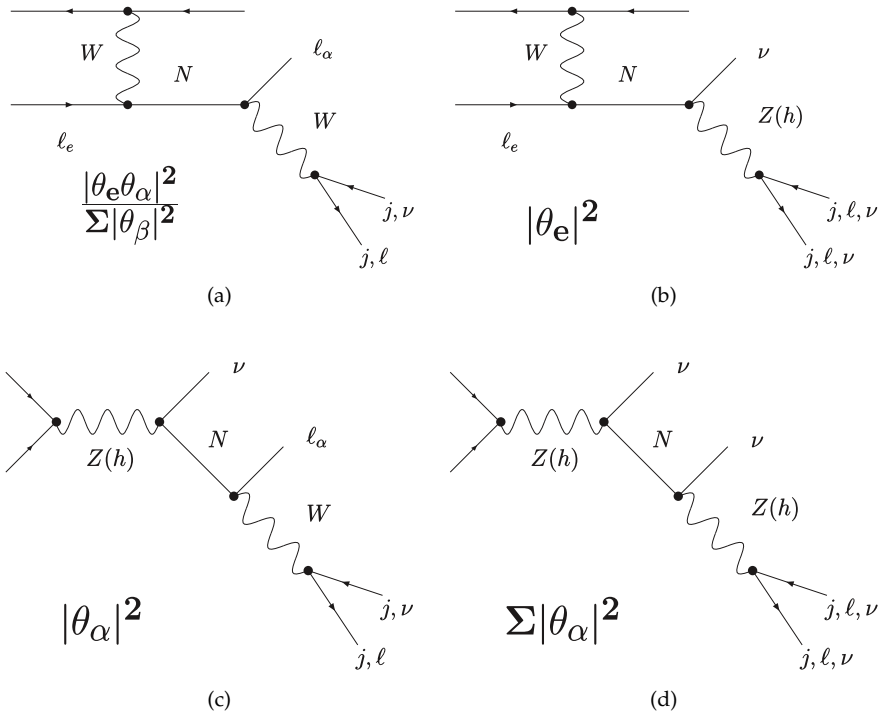

Figure 18: Shown are the Feynman diagrams for the heavy neutrino signal channels from the production processes shown in fig. 17 for e^+e^- colliders. The leading order dependence on the active-sterile mixing angles are shown for the squared amplitude in the narrow width approximation of the heavy neutrino when summed over all light neutrinos. For each occurrence of a Z boson there is a corresponding diagram with a Higgs boson instead, which is dentoed by (h). The subseqeuent decay of the heavy neutrino into SM particles are also depicted and denoted. In this regard, we note that j denotes a quark jet.

and s-channel Z bosons are shown to leading order in the active-sterile mixing angles. For each diagram with a Z boson, the corresponding diagram with a Higgs boson instead is also allowed. For each of the presented diagrams, the active-sterile mixing angle dependence of the corresponding cross section is calculated in the narrow width approximation of the heavy neutrino propagator [108]. The processes including the t-channel W boson exchange channel have always a θ_e dependency due to the production process being dependent on $|\theta_e|$ in e^+e^- collisions. This means that the physics runs above the Z pole are mainly sensitive to $|\theta_e|^2$ while the Z pole run is sensitive to all $|\theta_\alpha|$ independently. Therefore, the Z pole run allows to infer the relative strength of the different active-sterile mixing angles by probing the channel in fig. 18c for each flavour of the charged lepton ℓ_α. In principle, also the signal channel via the t-channel W boson exchange fig. 18a would allow to measure the $|\theta_\alpha|$. But, if there is a strong hierarchy in the flavour composition, for instance, $|\theta_e| \ll |\theta_\mu|, |\theta_\tau|$, then the heavy neutrino production via this channel is suppressed and not a sizeable amount of data could be gathered.

[108] The narrow width approximation is widely used to simplify the calculations of cross sections with intermediate unstable particles, confer e.g. [304–306]. The propagator of an unstable particle is given by the Breit-Wigner propagator $[s - (M - i\Gamma/2)^2]^{-1}$, where Γ denotes the decay width of the unstable particle [304]. The transition probability amounts to $[(s - M^2)^2 + M^2\Gamma^2]^{-1}$, which is enhanced when $\sqrt{s} = M$. This enhancement in the corresponding cross section constitutes the resonance of the intermediate unstable particle. The contributions to the cross section from the on-shell ($\sqrt{s} = M$) intermediate state is enhanced compared to the off-shell intermediate sates. The narrow width approximation extracts the dominant on-shell contribution to the cross section by taking the limit $\Gamma \ll M$ for which the transition probability becomes $\pi/M\Gamma \times \delta(s - M^2)$ [304]. The δ-function forces the intermediate particle to be on-shell and factorises the total cross section into its production process and decay. This means that production and decay are independent processes. The calculation of the total cross section simplifies to the product of the on-shell production cross section times the branching ratio of the unstable particle into its decay products.

Name	Final State	Channel from fig. 18	$\lvert\theta_\alpha\rvert$ dependency
lepton-dijet	$\ell_\alpha \nu jj$	(a), (c)	$\frac{\lvert\theta_e\theta_\alpha\rvert^{2\,(**)}}{\theta^2}$, $\lvert\theta_\alpha\rvert^{2\,(**)}$
dilepton	$\ell_\alpha \ell_\beta \nu\nu$	{(a),(b)}, {(c),(d)}	$\left\{\frac{\lvert\theta_e\theta_\alpha\rvert^{2\,(*)}}{\theta^2}, \lvert\theta_e\rvert^{2\,(*)}\right\}^{(**)}$, $\left\{\lvert\theta_\alpha\rvert^{2\,(*)}, \lvert\theta\rvert^2\right\}^{(**)}$
dijet	$\nu\nu jj$	(b), (d)	$\lvert\theta_e\rvert^{2\,(**)}$, $\lvert\theta\rvert^{2\,(**)}$
invisible	$\nu\nu\nu\nu$	(b), (d)	$\lvert\theta_e\rvert^{2\,(**)}$, $\lvert\theta\rvert^{2\,(**)}$

Table 2: Shown are various final states involving heavy neutrinos to leading order at e^+e^- colliders. The composition into signal channels, and the corresponding dependency on the active-sterile mixing parameters are also explained.
$^{(*)}$: Indicates that the dependency on the active-sterile mixing can be inferred when the origin of the charged leptons can be reconstructed.
$^{(**)}$: Indicates that the dependency on the active-sterile mixing can be determined by the center-of-mass energy of the physics run.

The shown signal channels give rise to various final states. In tab. 2, the resulting final states together with its different contributions from the signal channels and mixing angle dependency are shown. In order to differentiate between the different signal channels and its mixing dependencies, one can use the different center-of-mass energies of the physics runs in order to approximately separate the production processes. Further differentiation is possible if the origin of the charged leptons can be reconstructed, especially the charged lepton that accompanies the decay of the heavy neutrino. This may be discernible by studying the kinematical distributions of the decay products. It is no easy task because there is interference between the signal channels and possibly interference with the SM background. These two differentiation possibilities are also indicated in tab. 2.

Although, we discussed the heavy neutrino production and signal channels of the heavy neutrinos with the physics program of the future colliders in mind. They are also valid for the past LEP experiment. Although LEP is certainly limited by its much smaller luminosity and lower highest center-of-mass reach when compared to the proposed future colliders. Nonetheless, we would like to comment on the direct searches performed at LEP in section 92. During the Z pole run, i.e. LEP-1, DELPHI and the other experiments have searched for the signal channels 18c and 18d in order to constrain the production of heavy neutrinos from Z boson decays. For LEP-2, ALEPH analysed the SM process $e^+e^- \to W^+W^- \to \ell_\alpha^\pm \ell_\beta^\mp \nu\nu$ which can contain heavy neutrino contributions from the dilepton final state given by the signal channel 18a.

6.3 FUTURE PROTON-PROTON COLLIDERS

Hadron colliders are designed to collide protons at highest center-of-mass energies. Currently, the LHC is operating at $\sqrt{s} \sim 13$ TeV with a maximal center-of-mass energy of 14 TeV. With its upgrade to the HL-LHC after 2026, a total target luminosity of 3 ab^{-1} is aimed at by the late 2030s [278]. The proposed future circular proton colliders are the FCC-hh ($\sqrt{s} \sim 100$ TeV) and the SppC ($\sqrt{s} \sim 75$ TeV and with its upgrades $\sqrt{s} \sim 125 - 150$ TeV [290]). In

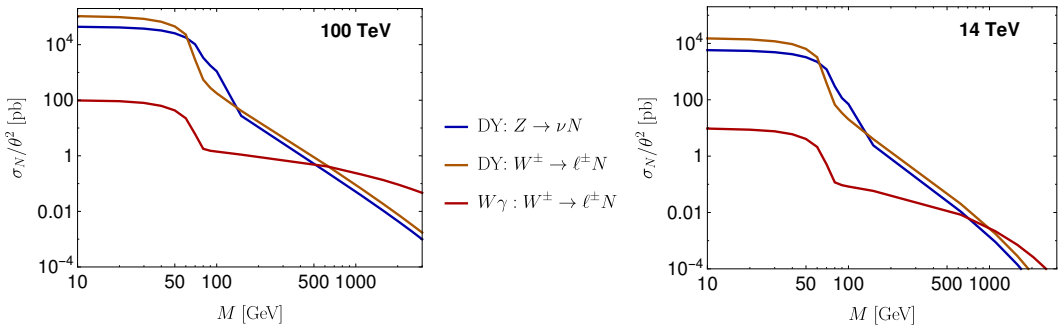

Figure 20: Shown are the cross sections, σ_N divided by θ^2, for the heavy neutrino production channels from Drell-Yan processes (DY) and from $W\gamma$ fusion as a function of the heavy neutrino mass for proton collisions at 100 TeV and 14 TeV, respectively. For Drell-Yan via a W boson, both contributions from W^+ and W^- are added together. The same goes for $W\gamma$ fusion, where only the contribution from the photon's PDF of the proton is taken into account. The cross sections have been calculated by WHIZARD with a requirement on the transverse momentum $P_T > 10$ GeV cut on the leptons and quarks in the final state.

ref. [307], an integrated luminosity of $10 - 20$ ab^{-1} per experiment is recommended for the FCC-hh [109], while for the SppC an integrated luminosity of 30 ab^{-1} for two experiments after 10 years of running is envisaged [290].

The physics goals of the proposed future pp colliders are amongst others [282–284, 290]: The measurement of the proton structure at highest energies, i.e. measurement of the parton distribution function (PDF) of the proton. The measurement of SM Higgs properties and top quark properties. Foremost, the Higgs self-coupling is regarded as one of the very important measurements.

Overall, hadron colliders are the prime tool designed for investigating the energy frontier, the FCC-hh and SppC could discover new particles with masses of order tens of TeV. Nonetheless, they are also suitable machines to study heavy neutrinos. They provide avenues by which heavy neutrinos cannot be studied at lepton colliders, for instance by the study of lepton-number violating signatures. This point is discussed in chapter 9.

[109] For the collider searches we usually consider 20 ab^{-1} for the FCC-hh.

6.3.1 *Production mechanism*

Here, we discuss the dominant production processes for heavy neutrinos at proton-proton colliders. One dominant production process for the heavy neutrino is given by a Drell-Yan process via the charged or neutral weak current interactions, i.e. it is a production mechanism from quark-antiquark pair annihilation into leptons. The s-channel diagram with the heavy neutrino and an accompanying light neutrino (charged lepton) for the Z boson (W boson) is shown in fig. 19a. The squared amplitude is dependent on the active-sterile mixing θ^2 for the Z boson channel when summed over all light neutrinos and on $|\theta_\alpha|^2$ for the W boson channel when the accompanying charged lepton has flavour α.

Another dominant production process stems from a higher order process, which is given by vector boson fusion of W boson and a photon, hence referred to as $W\gamma$ fusion [27, 308, 309]. One of the possible Feynman diagrams is shown in fig. 19b. $W\gamma$ fusion consists of two contributions [27], an inelastic part [110], which involves a t-channel exchange of a virtual photon from a quark line and an elastic part [111] with a real photon that can be calculated

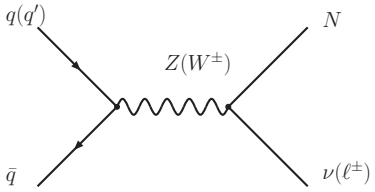

(a) Heavy neutrino from Drell-Yan s-channel Z (W) boson. The active-sterile mixing dependency of the cross section is θ^2 ($|\theta_\alpha|^2$) when the contributions are summed over all light neutrinos.

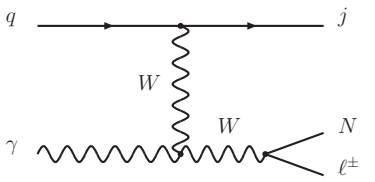

(b) Example diagram for heavy neutrino production from $W\gamma$ fusion, there are additional $W\gamma$ fusion diagrams.

Figure 19: Depicted are the Feynman diagrams that dominate the production of heavy neutrinos in proton-proton collisions.

[110] The kinetic energy of the incident particle is not conserved in the center-of-mass frame.

[111] The kinetic energy of the incident particle is conserved in the center-of-mass frame but its direction may have changed.

using the photon's PDF of the proton. For further details on the contributions and cross sections we refer the reader to ref. [27, 309].

Also for proton-proton colliders heavy neutrinos from Higgs boson decays constitute a sub-dominant production channel. Other production channels for hadron colliders are discussed, for instance, in ref. [310].

The heavy neutrino production cross sections, σ_N, for the Drell-Yan processes and the elastic contribution to $W\gamma$ fusion are shown in fig. 20 for 100 and 14 TeV center-of-mass energy. The Drell-Yan cross sections via Z is summed over all light neutrinos and is similar to one via W^+ and W^- which is summed over the 3 charged leptons. Assuming a mixing of $\theta^2 \sim 10^{-5}$, which is consistent with the present constraints, up to $\sim 10^6$ heavy neutrinos per ab^{-1} of integrated luminosity could be produced at the FCC-hh and SppC, respectively. Despite that $W\gamma$ fusion is a higher order process compared to the Drell-Yan processes, it becomes the dominating heavy neutrino production at proton colliders for larger heavy neutrino masses. This is due $W\gamma$ being a t-channel process which for larger heavy neutrino masses becomes less suppressed as the s-channel processes [112]. The dominating production mechanism is given by the discussed Drell-Yan processes while $W\gamma$ fusion becomes the dominating production for larger heavy neutrino masses [309]. The cross over point will be shifted a bit more to lower heavy neutrino masses with respect to the shown figure once the inelastic contribution is accounted for.

[112] Since for $M > m_z$ the on-shell heavy neutrino is produced from off-shell weak gauge bosons, the heavy neutrino production cross section becomes suppressed due to the high virtuality of the intermediate Z and W bosons.

6.3.2 *Signatures and searches*

In this section we focus on the signal channels and resulting finals states that arise from the previously discussed Drell-Yan production processes. The signal channels that appear after the subsequent decay of the heavy neutrino into SM particles (when kinematically allowed) are shown in fig. 21. Therein, the Feynman diagrams via the s-channel W and Z bosons from quark-antiquark annihilation are shown. For each of the diagrams, the active-sterile mixing angle dependency of the resulting cross section is given in the narrow width approximation of the heavy neutrino. Proton-proton colliders are sensitive to all $|\theta_\alpha|$ independently. Consequently, it is possible to infer the relative strength of the different active-sterile mixing angles by probing the channels in fig. 21b and/or 21c for each flavour of the charged lepton ℓ_α.

The resulting final states together with their different contributions from the signal channels and their mixing angle dependency are shown in tab. 3. One may be able to differentiate between the contributing signal channels for the trilepton and dilepton final states by reconstructing the origin of the charged leptons.

We comment that hadron colliders can give rise to the occurrence of lepton-number violating [113] and lepton-flavour violating effects at colliders [114].

[113] This refers to the violation of the total lepton number $\mathbb{L}$. This is discussed in chapter 9.

[114] This refers to the violation of the lepton number for each flavour $\mathbb{L}_{e,\mu,\tau}$. This is discussed in chapter 10.

6.4 FUTURE ELECTRON-PROTON COLLIDERS

Electron-proton colliders consist of a hadron ring accelerator with an intersecting electron beam. These machines are hybrids between electron-positron and hadron colliders which allow for a cleaner experimental environment

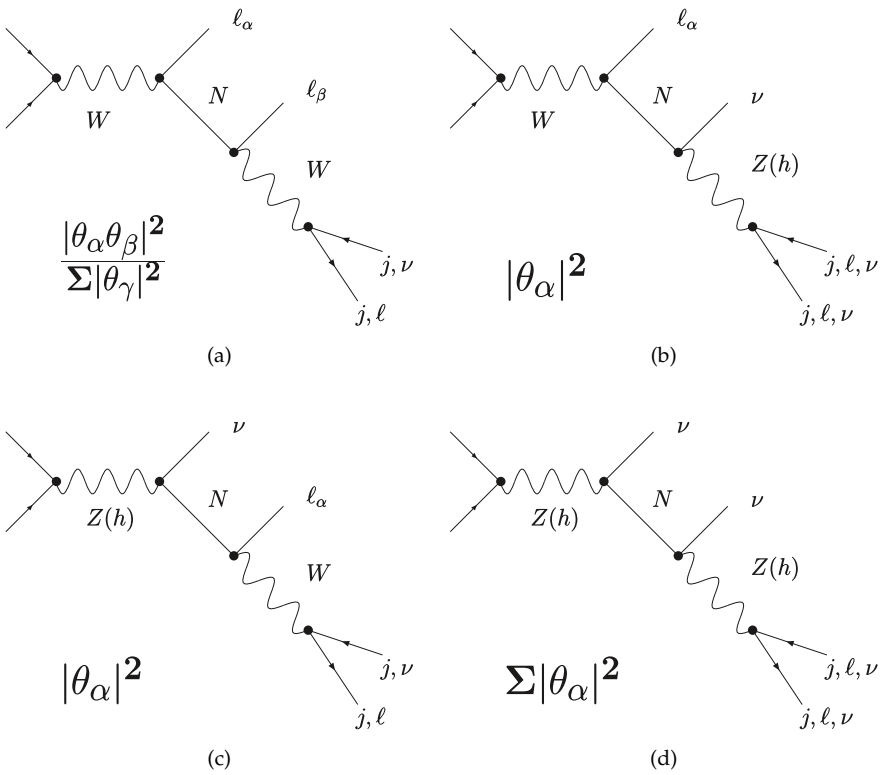

Figure 21: Shown are the Feynman diagrams for the heavy neutrino signal channels from the Drell-Yan production processes shown in fig. 19 for pp colliders. The leading order dependence on the active-sterile mixing angles are shown for the squared amplitude in the narrow width approximation of the heavy neutrino when summed over all light neutrinos. For each occurrence of a Z boson there is a corresponding diagram with a Higgs boson instead, which is dentoed by (h). The subseqeuent decay of the heavy neutrino into SM particles are also depicted and denoted. In this regard, we note that j denotes a quark jet.

compared to the hadron colliders and for higher center-of-mass energy reach compared to e^+e^- colliders.

There are currently two future e^-p collider that are being designed. The LHeC upgrade [296, 311] that offers a 60 GeV electron beam and with a possible spin polarisation of up to 80%. The electron beam colliding with the LHC's 7 TeV proton beam have a center-of-mass energy of ~ 1.3 TeV [115]. The LHeC intends to collect several 100 fb^{-1} with up to 1 ab^{-1} [312] while the HL-LHC is running [313].

[115] $\sqrt{s} \simeq 2\sqrt{E_p E_{e^-}}$

In the FCC design study, the FCC-eh [287] is discussed, it provides an electron beam similar to the LHeC which is brought to collision with the 50 TeV hadron beam from the FCC-hh instead. This setup would result in center-of-mass energies of ~ 3.5 TeV with luminosities that are comparable to the LHeC [287, 312].

The e^-p colliders offer an interesting physics case such as, e.g., deep inelastic physics programme, cf. ref. [296, 313], that can provide precision QCD

Name	Final State	Channel from fig. 21	$\lvert\theta_\alpha\rvert$ dependency
dilepton-dijet	$\ell_\alpha\ell_\beta jj$	(a)	$\frac{\lvert\theta_\alpha\theta_\beta\rvert^2}{\theta^2}$
trilepton	$\ell_\alpha\ell_\beta\ell_\gamma\nu$	{(a), (b)}	$\left\{\frac{\lvert\theta_\alpha\theta_\beta\rvert^{2\,(*)}}{\theta^2}, \lvert\theta_\alpha\rvert^{2(*)}\right\}$
lepton-dijet	$\ell_\alpha\nu jj$	(b), (c)	$\lvert\theta_\alpha\rvert^2$
dilepton	$\ell_\alpha\ell_\beta\nu\nu$	{(c), (d)}	$\left\{\lvert\theta_\alpha\rvert^{2(*)}, \lvert\theta\rvert^{2(*)}\right\}$
mono-lepton	$\ell_\alpha\nu\nu\nu$	(b)	$\lvert\theta_\alpha\rvert^2$
dijet	$\nu\nu jj$	(d)	$\lvert\theta\rvert^2$

Table 3: Shown are various final states involving heavy neutrinos to leading order at pp colliders. The composition into signal channels, and the corresponding dependency on the active-sterile mixing parameters are also explained. $^{(*)}$: Indicates that the dependency on the active-sterile mixing can be inferred when the origin of the charged leptons can be reconstructed.

measurements, measurements of the PDF of the proton and properties of the SM Higgs boson. Overall, electron-proton colliders are designed to investigate deep inelastic electron-proton scattering at the high-energy frontier which would allow to search for BSM physics. They also provide avenues by which heavy neutrinos cannot be studied at e^+e^- colliders, for instance by the study of lepton-flavour violating signatures.

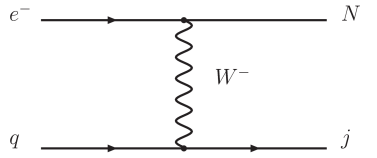

(a) Heavy neutrino from t-channel exchange of a W boson with the quark current.

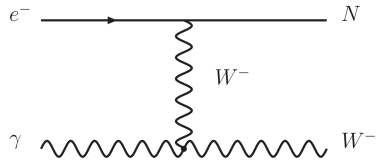

(b) Heavy neutrino production from $W\gamma$ fusion. As discussed for the pp colliders, there is an elastic and inelastic contribution. The negatively charged W boson would further decay into SM particles.

Figure 22: Depicted are the Feynman diagrams for the dominant production channels of the heavy neutrinos in electron-proton scattering at the leading order. Both amplitudes are dependent on the active-sterile mixing θ_e due to the incident electron beam.

6.4.1 *Production mechanism*

Here, we discuss the dominant heavy neutrino production processes at e^-p colliders. The heavy neutrino can be produced efficiently from the incident electron beam by interactions with the quark current of the proton via a t-channel W boson exchange. In this process the heavy neutrino is produced together with a quark jet, the corresponding Feynman diagram is shown in fig. 22a. Another relevant production channel is given by $W\gamma$ fusion and its Feynman diagram is shown in fig. 22b. Here, the electron beam interacts via a t-channel exchange of a W boson with a initial state photon from the proton instead the quark current. Therefore for e^-p colliders, $W\gamma$ fusion is a leading order diagram that is only suppressed by the photon's PDF. For both heavy neutrino production processes, the squared amplitude is proportional to active-sterile mixing angle $|\theta_e|^2$ due to the incident electron beam.

The heavy neutrino production cross section, σ_N, divided by $|\theta_e|^2$ for the t-channel process interacting with the quark current and the elastic contribution from $W\gamma$ fusion are shown for the LHeC and the FCC-eh in fig. 23. Assuming a squared active sterile mixing of $\theta^2 \sim 10^{-5}$ up to $\sim 10^4$ heavy neutrinos per ab^{-1} of integrated luminosity could be produced at electron-proton colliders. In contrast to pp colliders, $W\gamma$ fusion is competing with another t-channel diagram and as such there is no cross over point for the

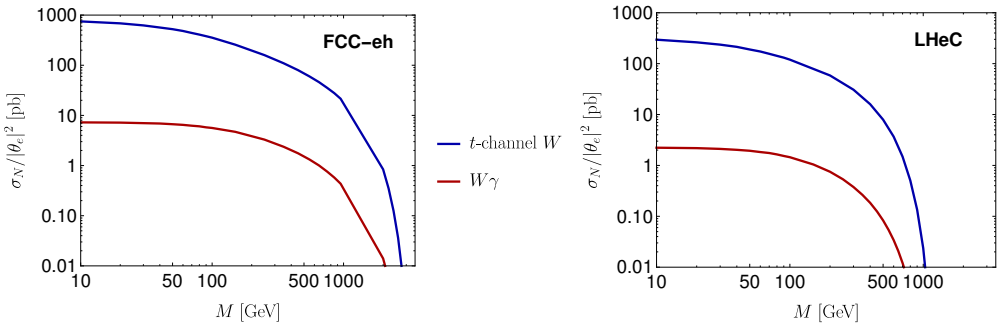

Figure 23: Shown are the heavy neutrino production cross sections σ_N divided by the square of the active-sterile mixing parameter $|\theta_e|^2$ as a function of the heavy neutrino mass for the production channels depicted in fig. 22 at the FCC-eh and LHeC, respectively. The cross section have been calculated by WHIZARD where an angular acceptance of $1^\circ \leqslant \vartheta \leqslant 179^\circ$ has been assumed in order to avoid soft and collinear divergences, confer e.g. ref. [314].

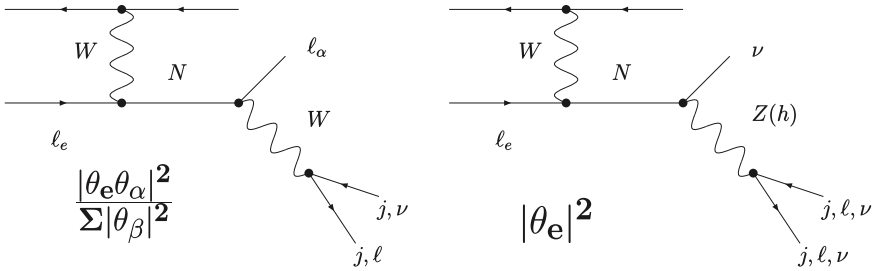

Figure 24: Shown are the Feynman diagrams for the heavy neutrino signal channels via the production processes shown in fig. 22a for e^-p colliders. The leading order dependence on the active-sterile mixing angles are shown for the squared amplitude in the narrow width approximation of the heavy neutrino when summed over all light neutrinos. For each occurrence of a Z boson there is a corresponding diagram with a Higgs boson instead, which is dentoed by (h). The subseqeuent decay of the heavy neutrino into SM particles are also depicted and denoted. In this regard, we note that j denotes a quark jet.

production cross sections as is the case for pp colliders. Therefore, heavy neutrino production proceeds predominantly via t-channel W boson exchange rather than gauge boson fusion.

6.4.2 *Signatures and searches*

Here we focus on the signal channels and resulting final states which arise from the dominating heavy neutrino production via the t-channel W boson exchange of the incident electron beam with the quark current from the proton. The arising signal channels from the decay of the heavy neutrino into SM particles (when kinematically allowed) are shown in fig. 24. For each of the signal channels the active-sterile mixing dependency of the corresponding cross section is given in the narrow width approximation of the heavy neutrino. It may be possible to infer the relative strength of the $|\theta_\alpha|$ by probing

the charged lepton labelled ℓ_α. However, since the production cross section at e^-p colliders is dependent on $|\theta_e|^2$, the signal channels are not sensitive to all flavours independently. Consequently, the argument regarding a strong hierarchy of the flavour composition applies also here, i.e. $|\theta_e| \ll |\theta_\mu|, |\theta_\tau|$, could considerably suppress the signal.But, the situation for the e^-p collider is worse in contrast to the t-channel W exchange diagram at the e^+e^- collider since there is no other signal channel at the leading order that would be independent in the θ_α.

The resulting final states with their contributions from the signal channels and respective active-sterile mixing angle combination are summarised in tab. 4. Only for the jet-dilepton final state both of the signal channels contribute, in which case the reconstruction of the origin of the charged leptons helps to differentiate the 2 contributions.

We comment that e^-p colliders can give rise to the occurrence of lepton-number violating [116] and lepton-flavour violating effects at colliders [117].

[116] This refers to the violation of the total lepton number $\mathbb{L}$. This is discussed in chapter 9.

[117] This refers to the violation of the lepton number for each flavour $\mathbb{L}_{e,\mu,\tau}$. This is discussed in chapter 10.

Name	Final State	Channel from fig. 24	$\lvert\theta_\alpha\rvert$ dependency
lepton-trijet	$jjj\ell_\alpha$	(a)	$\frac{\lvert\theta_e\theta_\alpha\rvert^2}{\theta^2}$
jet-dilepton	$j\ell_\alpha^\pm\ell_\beta^\mp\nu$	{(a), (b)}	$\left\{\frac{\lvert\theta_e\theta_\alpha\rvert^{2\,(*)}}{\theta^2}, \lvert\theta_e\rvert^{2\,(*)}\right\}$
trijet	$jjj\nu$	(b)	$\lvert\theta_e\rvert^2$
monojet	$j\nu\nu\nu$	(b)	$\lvert\theta_e\rvert^2$

Table 4: The various final states involving sterile neutrinos at leading order for e^-p colliders are shown in the table. Their compositions into signal channels, and the corresponding active-sterile mixing combination are summarised.
$^{(*)}$: Indicates that the dependency on the active-sterile mixing can be inferred when the origin of the charged leptons is known.

7 HIGGS PRODUCTION FROM STERILE NEUTRINOS

One of the main physics goals for the future colliders is to measure the SM Higgs properties. Hereby, the effects from sterile neutrinos can play a crucial role. In this thesis, we have already encountered ways how the Higgs properties are modified in the presence of sterile neutrinos. In section 92, we have seen that the Higgs boson branching ratios can be modified with respect to the SM prediction, because the Higgs boson features a new decay channel into a light and heavy neutrino (when $M < m_h$) which adds to the total Higgs boson decay width and consequently modifies the branching ratios. Another way, how sterile neutrinos can affect the Higgs boson properties, is to modify the expected SM single Higgs production cross section by contributing additional Higgs bosons from heavy neutrino decays when kinematically allowed. That is to say, the on-shell production of a heavy neutrino and its subsequent decay into a Higgs boson and a light neutrino constitutes a resonant contribution to the Higgs production mechanism when $M > m_h$. Also non-unitary effects, similarly to the ones discussed in section 4.3.3, may become relevant for $M \gg m_h$. Heavy neutrino decays as a source of Higgs bosons were first mentioned in ref. [217] and further studied in [1, 315].

First, we summarise the Higgs production processes in the SM and then discuss and compare possible direct contributions from heavy neutrino decays at e^+e^-, pp and e^-p colliders in section 7.1.Second, we discuss the Higgs production from sterile neutrinos at future e^+e^- colliders in section 7.2, which is based on work conducted and published in ref. [1]. Therein, the resonant contribution as well the contribution from non-unitarity effects is discussed and compared to the SM mono-Higgs production cross section for the physics runs of the FCC-ee and CEPC in section 7.2.1. In section 7.2.2, the contamination of the SM mono-Higgs sample is discussed. While an analysis on the sensitivity to the active-sterile mixing angles of the mono-Higgs channel is discussed on the parton and reconstructed level in section 7.2.3 and 7.2.4, respectively. We summarise in section 7.3.

7.1 SM HIGGS VS HIGGS PRODUCTION FROM HEAVY NEUTRINOS

There are various SM single Higgs production processes for the different collider types, we restrict ourselves to some of the more relevant processes shown in fig. 25, see, for instance, ref. [65] and references therein. These are: The well known gluon-fusion process, which is the most relevant Higgs contribution at the LHC. The resonant s-channel Higgs production, which is very small compared with the other production channels due to small Yukawa couplings and is hereby not discussed further. The Higgs-strahlung process, which is an associated production with a gauge boson. The vector-boson fusion (VBF) process of weak gauge bosons.

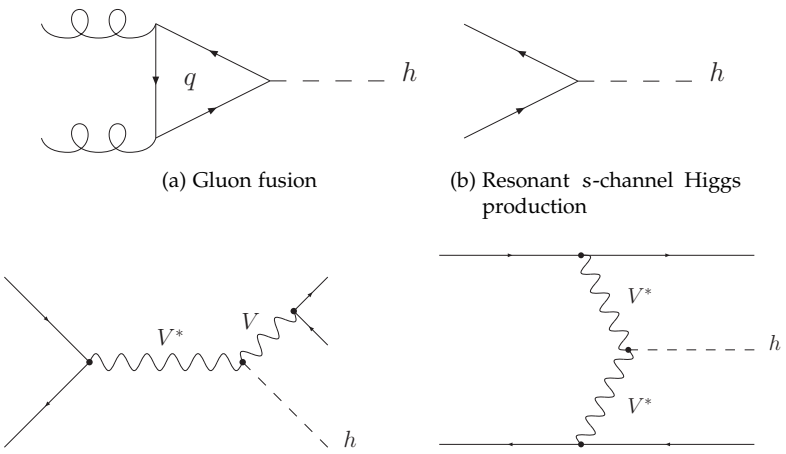

(a) Gluon fusion

(b) Resonant s-channel Higgs production

(c) Higgs-strahlung

(d) Vector-boson fusion

Figure 25: Relevant Higgs boson production mechanisms in the SM.

Electron-positron colliders

Especially, future e^+e^- colliders intend to measure the SM Higgs properties around $\sqrt{s} = 250$ GeV where the Higgs production cross section is dominated by the Higgs-strahlung process $e^+e^- \to Z^* \to hZ$, see for instance in section 7.2.1. While VBF from WW or ZZ become the dominating contribution for higher center-of-mass energies. For e^+e^- colliders, the Higgs boson from WW fusion is accompanied by two light neutrinos while ZZ fusion is accompanied by an electron-positron pair.

Higgs production from the decays of heavy neutrinos are possible by the two Feynman diagrams in fig. 18b and 18d, discussed in section 6.2.2, with the on-shell heavy neutrino decaying into the Higgs boson h and a light neutrino. Both, the t-channel W and the s-channel Z boson diagrams contribute directly to the $e^+e^- \to h\nu\nu$ cross section, referred to as mono-Higgs which yields a Higgs boson and missing energy due to the light neutrinos. Therefore they constitute a direct [118] contribution to the SM Higgs-strahlung process hZ, for which the Z decays into neutrinos, i.e. $e^+e^- \to hZ \to h\bar{\nu}\nu$, and for WW fusion. There is no direct contribution from heavy neutrino decays to the SM Higgs ZZ fusion cross section.

[118] Here, direct refers to the fact that they share the same final state.

We confront the resonant Higgs production process with SM mono-Higgs production processes by comparing the respective cross sections. The SM mono-Higgs production cross section ranges between ~ 50 fb to ~ 90 fb depending on the center-of-mass energy for $\sqrt{s} = 240$ GeV up to 500 GeV, see below in section 7.2.1. While mono-Higgs production from heavy neutrinos is of order 1 to 10 fb assuming an active-sterile mixing of $\theta^2 = |\theta_e|^2 \sim 10^{-3}$ in the narrow width approximation of the heavy neutrino, also see below for the dependence on $\sqrt{s}$. The resulting cross sections are roughly one order of magnitude lower than the SM mono-Higgs production cross section. For $\sqrt{s} = 240$ GeV, the produced Higgs bosons from the heavy neutrino decays

amount roughly to a few percent of the total number of produced Higgs bosons at the future e^+e^- colliders.

Proton-proton colliders

At pp colliders, the gluon fusion Higgs production cross section is by far the largest with 50 pb at the $\sqrt{s} = 14$ TeV HL-LHC and 740 pb at $\sqrt{s} = 100$ TeV, respectively. The VBF process via the weak gauge bosons follows with 4.4 pb at the 14 TeV HL-LHC and 82 pb at 100 TeV, respectively. Both, the weak charged and neutral currents give rise to a Higgs boson that is accompanied by two jets. The next important ones are the Higgs-strahlung processes via the W or Z boson with 2.6 pb at 14 TeV and 27 pb at 100 TeV. The NNLO [119] SM Higgs production cross sections for the LHC at 14 TeV and a 100 TeV collider such as the FCC-hh or SppC can be found in ref. [316].

[119] NNLO is an abbreviation for next-to-next-to-leading order.

Higgs production from the decay of the heavy neutrino is possible via the Feynman diagrams fig. 21b and fig. 21d, discussed in section 6.3.2, where the on-shell heavy neutrino decays into a Higgs boson and a light neutrino. The process with the heavy neutrino production proceeding via a off-shell W boson, namely fig. 21b, contributes directly to $pp \to h\ell\nu$ cross section. Therefore it contributes to the same final state as the Higgs-strahlung process $hW^\pm$ for which the W boson decays leptonically, i.e. $pp \to hW^\pm \to h\ell\nu$. On the other hand, the process in fig. 21d which proceeds via a off-shell Z boson contributes to the mono-Higgs cross section. Thus, it directly contributes to the Higgs-strahlung cross section hZ for which the accompanying Z boson decays to neutrinos. Moreover, it also contributes to the gluon fusion channel at the reconstructed level, i.e. due to a finite detector resolution the detector, it measures some missing energy even in the gluon fusion channel. There is no direct contribution to VBF process, due to no presence of quark lines in the leading order processes.

We want to confront the SM Higgs production processes and the Higgs production process from sterile neutrinos by comparing the respective cross sections. In the narrow width approximation of the heavy neutrino the total cross section factorises to $\sigma_N \times BR(N \to h\nu)$, where σ_N is the heavy neutrino production cross section, shown in fig. 20, and the branching ratio is shown in fig. 9b. Due to a high virtuality of the intermediate weak gauge boson, the heavy neutrino production cross section is suppressed. Considering a heavy neutrino mass of $M \sim 200$ GeV and assuming $\theta^2 \sim 10^{-3}$ a total cross section of order 0.1 fb and 1 fb can be expected at $\sqrt{s} = 14$ TeV and at $\sqrt{s} = 100$ TeV, respectively. Which is roughly 3 orders of magnitude below the Higgs-strahlung SM production processes [120] which it directly contributes to. However, of 10^5 Higgs boson produced from gluon fusion there is order 1 Higgs bosons from heavy neutrino decays.

[120] Where the branching ratios for the decays of the weak gauge bosons have to be taken into account.

The above mono-Higgs signature has been studied for the resonant mono-Higgs contribution from heavy neutrinos at the LHC and HL-LHC for $h \to \bar{b}b$ and $h \to \gamma\gamma$ in ref. [315]. However, it was found to be not promising to find a signal from heavy neutrinos by studying the mono-Higgs signature.

Electron-proton colliders

At electron-proton colliders, the higgs boson is produced by VBF. The Higgs is produced predominantly from *WW* boson fusion with a cross section of 200 fb and 1 pb assuming a spin polarisation of the electron of 80% at the LHeC and FCC-eh [317], respectively. The Higgs production cross section from ZZ fusion is 25 fb and 150 fb at the LHeC and FCC-eh [317], respectively. In *WW* fusion the Higgs boson is accompanied by a light neutrino and a jet while in ZZ fusion there is a electron instead of the neutrino.

Higgs production from the decay of the heavy neutrinos proceed via the process depicted in fig. 24b, discussed in section 6.4.2, with the on-shell neutrino decaying into a Higgs boson and a light neutrino. This process contributes directly to the *WW* Higgs production cross section. Assuming an active-sterile mixing of $|\theta_e|^2 \sim 10^{-3}$ and considering a heavy neutrino mass of $M \sim 200$ GeV a total cross of order 1 fb and 10 fb can be expected for the LHeC and FCC-eh, respectively. The resulting cross section is 2 orders of magnitude below the *WW* cross section but in contrast to the pp colliders, Higgs bosons produced from the decay of heavy neutrinos can amount up to a few percent of the total number of produced Higgs bosons at the future e^-p colliders.

Cross-sections-wise the future e^+e^- colliders seem more favourable with respect to the other colliders. We, therefore, have a closer look at the situation arising there.

7.2 MONO-HIGGS PRODUCTION FROM STERILE NEUTRINOS AT FUTURE e^+e^- COLLIDERS

Higgs production from the effects of sterile neutrinos contribute directly to the $e^+e^- \to h\nu\nu$ cross section at electron-positron colliders. This final state and the resulting signature, which corresponds to a Higgs boson and missing energy due to the light neutrinos, is referred to as mono-Higgs. The relevance of the mono-Higgs production from sterile neutrinos is investigated for the $\sqrt{s} = 240$ GeV physics run with 5 ab^{-1} at the FCC-ee and CEPC, 350 GeV run with 3.5 ab^{-1} at the FCC-ee, as discussed in fig. 15. Additionally, a possible 500 GeV run with an integrated luminosity of 1 ab^{-1} is also considered for the FCC-ee [318]. The investigation shown here is based on work conducted in ref. [1].

7.2.1 *Cross sections*

In this section, we study the contributions of sterile neutrinos to the mono-Higgs production cross section in the context of future e^+e^- colliders. The contributions to the total cross section for the mono-Higgs process,

$$e^+e^- \to h\bar{\nu}\nu\,, \tag{7.1}$$

can be split into the following three contributions

$$\sigma_{h\nu\nu} = \sigma^{\text{SM}}_{h\nu\nu} + \sigma^{\text{Direct}}_{h\nu\nu} + \sigma^{\text{Non-U}}_{h\nu\nu}\,. \tag{7.2}$$

The first contribution corresponds to the SM mono-Higgs production, given by the Higgs-strahlung process via a Z boson and its subsequent decay into light neutrinos and *WW* fusion. The second contribution corresponds to the resonant Higgs production from heavy neutrinos to the mono-Higgs production cross section. The third contribution contains non-unitarity effects which arise due to the modification of the low-energy input parameters as well as the mixing of the active neutrinos according to the PMNS matrix.

SM contribution

For the SM contributions to the mono-Higgs production, we note that for the *WW* fusion process, only electro-neutrinos are produced, $e^+e^- \to h\bar{\nu}_e\nu_e$, whereas for the Higgs-strahlung process all neutrino flavours are produced equally, $e^+e^- \to hZ \to h\bar{\nu}_\alpha\nu_\alpha$.

The contribution from the hZ cross section via Higgs-strahlung to the total cross section can be expressed in the narrow width approximation of the Z boson as

$$\sigma^{HZ}_{h\nu\nu} := \sigma^{SM}(e^+e^- \to hZ) \times \mathrm{Br}(Z \to \nu\bar{\nu})\,, \tag{7.3}$$

where a branching ratio of $\mathrm{BR}(Z \to \nu\bar{\nu})$ of 20.0% is assumed and the contributions are summed over all light neutrinos. The analytical expression for the hZ cross section is given by [319]

$$\sigma^{SM}(e^+e^- \to hZ) = \frac{G_f^2 m_Z^4}{24\pi}\left(v_e^2 + a_e^2\right)\lambda^{\frac{1}{2}}\frac{\lambda s + 12 m_Z^2}{\left(s - m_Z^2\right)^2}\,, \tag{7.4}$$

where s is the square of the center-of-mass energy $\sqrt{s}$, $a_e = -1/2$ and $v_e = -1/2 + 2s_W^2$ are the axial- and vector-coupling of the electron-current to the Z boson, and λ the phase-space factor, given by

$$\lambda = \left(1 - \frac{(m_h + m_Z)^2}{s}\right)\left(1 - \frac{(m_h - m_Z)^2}{s}\right)\,. \tag{7.5}$$

The contribution from the *WW* fusion cross section to the total cross section is given by [319]

$$\sigma^{WW}_{h\nu\nu} := \frac{G_f^3 m_W^4}{4\sqrt{2}\pi^3}\Pi_{h\nu\nu}\,, \tag{7.6}$$

where $\Pi_{h\nu\nu}$ is the phase space factor, given by

$$\Pi_{h\nu\nu} = \int_{x_h}^{1} dx \int_{x}^{1} \frac{dy\, F(x,y)}{(1 + (y-x)/x_W)^2}\,, \tag{7.7}$$

$$F(x,y) = \left(\frac{2x}{y^3} - \frac{1+3x}{y^2} + \frac{2+x}{y} - 1\right)\left(\frac{z}{1+z} - \ln[1+z]\right) + \frac{x}{y^3}\frac{z^2(1-y)}{1+z}\,, \tag{7.8}$$

with $x_h = m_h^2/s$, $x_W = m_W^2/s$ and $z = y(x - x_h)/(x\,x_W)$.

The SM mono-Higgs-production cross section, $\sigma^{SM}_{h\nu\nu}$, comprises the Higgs-strahlung, *WW* fusion contribution and an interference term. In fig. 26, the individual cross sections are shown as a function of the center-of-mass energy.

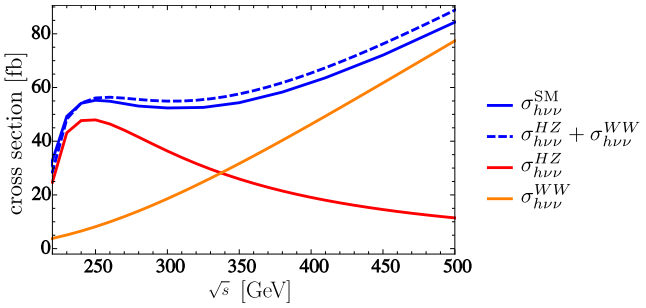

Figure 26: Shown is the SM mono-Higgs-production cross sections as a function of the center-of-mass energy. The individual contributions from Higgs-strahlung ($\sigma^{HZ}_{h\nu\nu}$) and from *WW* fusion ($\sigma^{WW}_{h\nu\nu}$) are displayed as well. The contribution from interference can also be assessed by the dashed blue line, which denotes the naive sum of $\sigma^{HZ}_{h\nu\nu}$ and $\sigma^{WW}_{h\nu\nu}$, and the blue solid line, which denotes the full expression including the interference. Reprinted from [1].

For the Higgs physics programme at $\sqrt{s} = 240$, the SM mono-Higgs production cross section, is dominated by the Higgs-strahlung contribution which peaks in that region. While for the energy runs at and above $\sqrt{s} = 350$ GeV the *WW* fusion contribution takes over. The interference term, whilst small around $\sqrt{s} = 240$ GeV, grows negatively with $\sqrt{s}$.

The second contribution corresponds to the resonant Higgs production from heavy neutrinos to the mono-Higgs production cross section.

Contribution from resonant Higgs production from heavy neutrinos

For the resonant Higgs contribution from heavy neutrinos to the mono-Higgs production, there is, on the one hand, the resonant production of the Higgs bosons via the discussed t-channel *W* and s-channel Z boson Feynman diagrams fig. 18b and 18d. And, on the other hand, the interference between the resonant mono-Higgs production processes and the previously discussed SM processes.

The interference term between these two sets of amplitudes can be neglected due to the following arguments. The interference term has an odd number of fermion lines, therefore it contains the trace over an odd number of γ matrices, which vanishes, and an even number of γ matrices that are however suppressed by the small ratios of $\frac{m_e^2}{s}$ and $\frac{m_\nu^2}{s}$.

Therefore, the direct contribution is given by the resonant Higgs production, which can be calculated in the narrow width approximation of the heavy neutrino and up to second order in the active-sterile mixing angles as

$$\sigma^{\mathrm{Direct}}_{h\nu\nu} = \sigma_{\nu N} \times \mathrm{BR}(N \to h\nu)\,, \tag{7.9}$$

where we implicitly summed over all the light neutrinos. Here, the heavy neutrino production cross section, $\sigma_{\nu N}$, is discussed in section 6.2.1, the branching ratios for the heavy neutrinos are derived in section 4.3.4, and

The resulting $\sigma^{\mathrm{Direct}}_{h\nu\nu}$ divided by the flavoured mixing angle square as a function of the heavy neutrino mass M for various center-of-mass energies and assuming different mixings is shown in fig. 27. For the calculation of

Figure 27: Shown are the mono-Higgs production cross section from heavy neutrinos divided by the mixing angle squared as a function of the heavy neutrino mass M for various physics runs of the future e^+e^- colliders. Only $|\theta_e| \neq 0$ and $|\theta_\tau| \neq 0$ was assumed for the left and right panel, respectively.

$\sigma_{\nu N}$, the analytical expression from ref. [190] was used, which agrees very well with the numerically derived values from WHIZARD. In the left panel of fig. 27, only $|\theta_e| \neq 0$ was assumed, while for the right panel only $|\theta_\tau| \neq 0$ [121]. Hence, in the left panel, the contributions from both of the involved Feynman diagrams are present. While, in the right panel, only the s-channel Z boson diagram can contribute for only $|\theta_\tau| \neq 0$ (or equivalently θ_μ) [122]. For the here considered center-of-mass energies, $\sigma^{\text{Direct}}_{h\nu\nu}$ is therefore dominated by the contribution from the t-channel W boson diagram since the s-channel Z boson diagram is suppressed by $\sim \frac{1}{s}$ for $s > m_Z$. Thus, the direct contribution from the decays of heavy neutrinos is mostly dependent on $|\theta_e|^2$ for the here considered masses and center-of-mass energies.

[121] This is equivalently to $|\theta_\mu| \neq 0$.

[122] Since the t-channel W boson diagram is proportional to θ_e.

Contributions from non-unitarity effects

For the contributions from non-unitary effects, there are two sources. One source is the contribution from the modification of the electroweak observables, as discussed in section 4.3.3. In particular, the dependence on the Fermi constant for $\sigma^{HZ}_{h\nu\nu}$ and $\sigma^{WW}_{h\nu\nu}$ in eq. (7.4) and (7.6) introduces a deviation according to eq. (4.48), respectively.

The other source stems from the modification of the vertices involving the light neutrinos only, where the non-unitary PMNS matrix $\mathcal{N}$ enters, as discussed in section 4.3.2. Therefore, mono-Higgs production cross section via Higgs-strahlung and via WW fusion become

$$\sigma^{HZ}_{h\nu\nu} \times \sum_{i,j=1,2,3} \left| \left(\mathcal{N}^\dagger \mathcal{N} \right)_{ij} \right|^2 , \tag{7.10}$$

$$\sigma^{WW}_{h\nu\nu} \left(\mathcal{N}\mathcal{N}^\dagger \right)^2_{ee} , \tag{7.11}$$

respectively. We note that for both processes it is possible to have different light neutrinos in the final state. And that, for $\sigma^{WW}_{h\nu\nu}$ the electron flavour is fixed due to the incident electron-positron beams.

One can parametrise the non-unitarity effects as the deviation from the SM mono-Higgs cross section in the active-sterile mixing parameters by plugging

in the above discussed non-unitarity effects and expand in the $|\theta_\alpha|$ up to second order as

$$\sigma^{\text{Non-U}}_{h\nu\nu} = \sigma^{\text{SM}}_{h\nu\nu} \sum_{\alpha=e,\mu,\tau} c_\alpha(\sqrt{s})\,|\theta_\alpha|^2\,, \tag{7.12}$$

where the coefficient c_α results from the expansion. The value of the coefficients vary with the center-of-mass energy because the non-uniarity effects to the Higgs-strahlung and *WW* fusion process have different active-sterile mixing dependencies and their relative contribution to the cross section varies with the center-of-mass energy. The coefficients are given in tab. 5 from ref. [1] for completeness. The contribution from non-unitarity effects add positively to the total mono-Higgs cross section, for instance, when $|\theta_\tau| \ll |\theta_{e,\mu}|$ but can add negatively when $|\theta_\tau| \gg |\theta_{e,\mu}|$. The latter case is due to c_τ being negative, which leads to a negative deviation that is here parametrised as a negative $\sigma^{\text{Non-U}}_{h\nu\nu}$ contribution.

$\frac{\sqrt{s}}{\text{GeV}}$	240	350	500
c_e	0.88	0.26	0.10
c_μ	1.08	1.28	1.70
c_τ	-0.53	-0.40	-0.05

Table 5: Shown are the values of the coefficients that parametrise the non-unitarity effects as a the deviation from the SM expectation via eq. (7.12), from ref. [1]. The numerical precision is roughly 5% across the center-of-mass energies.

7.2.2 *Possible deviation of the SM Higgs boson properties*

Future e^+e^- colliders aim at measuring the Higgs boson properties, for instance the SM mono-Higgs production cross section for the various physics runs. In the presence of sterile neutrinos, however, the theory prediction of the SM mono-Higgs production cross section can deviate from the experimentally measured value. By comparing the magnitudes of the various contributions $\sigma^{\text{SM}}_{h\nu\nu}$, $\sigma^{\text{Direct}}_{h\nu\nu}$, and $\sigma^{\text{Non-U}}_{h\nu\nu}$ the following can be expected: For not too small active-sterile mixing $|\theta_e|$, the direct contribution from heavy neutrinos can be sizeable compared to $\sigma^{\text{SM}}_{h\nu\nu}$ as long as the heavy neutrinos are kinematically allowed. For example, assuming an active-sterile mixing of $\theta^2 = |\theta_e|^2 \sim 10^{-3}$ cross sections for $\sigma^{\text{Direct}}_{h\nu\nu}$ [123] of the order of 1 fb and 10 fb are possible, as can be seen from fig. 27. The non-unitarity effects play in this regime a sub-leading role, they are roughly two orders of magnitude smaller than the direct contributions. But once, the heavy neutrinos are not kinematically accessible ($M > \sqrt{s}$) the non-unitarity effects are the only contributions from the effects of sterile neutrinos. This is the expectation which is based on the cross sections alone.

[123] Since $\sigma^{\text{Direct}}_{h\nu\nu}$ is mostly dependent on $|\theta_e|^2$.

Even when applying kinematic cuts to the mono-Higgs event sample, in order to extract as many SM mono-Higgs events compared to the SM background, still a few percent of additional Higgs bosons from heavy neutrinos can contaminate the Higgs event sample at future e^+e^- colliders. This would lead to a deviation of the measured mono-Higgs cross section with the SM prediction.

In the real experiment, only the decay products of the Higgs boson would be visible as reconstructed objects. Therefore, further SM processes which have a similar signature can be identified or misidentified as Higgs bosons, which would constitute the background. In order to best analyse the SM mono-Higgs properties, it is necessary to extract as many SM mono-Higgs events and reject as many background events as possible. This is achieved by applying a set of cuts on the kinematic observables of the signature. For this purpose so-called standard cuts, see tab. 6, have been defined in order to optimise the number of SM mono-Higgs events with respect to the SM

$\sqrt{s}$	240 GeV	350 GeV
Missing Mass [GeV]	$80 \leqslant M_{miss} \leqslant 140$	$50 \leqslant M_{miss} \leqslant 240$
Transverse P [GeV]	$20 \leqslant P_T \leqslant 70$	$10 \leqslant P_T \leqslant 140$
Longitudinal P [GeV]	$\lvert P_L \rvert < 60$	$\lvert P_L \rvert < 130$
Maximum P [GeV]	$\lvert P \rvert < 30$	$\lvert P \rvert < 60$
Di-jet Mass [GeV]	$100 \leqslant M_{jj} \leqslant 130$	$100 \leqslant M_{jj} \leqslant 130$
Angle (jets) [Rad]	$\alpha > 1.38$	$\alpha > 1.38$

Table 6: Standard cuts for future e^+e^- colliders in order to optimise the number of SM mono-Higgs signal events over to SM background events, taken from ref. [320].

background for future e^+e^- colliders in ref. [320]. Even when applying the optimised cuts for the SM to the mono-Higgs event sample, the resulting sample might contain resonantly produced mono-Higgs events from heavy neutrinos. From the point of view of the SM expectation, the SM mono-Higgs event sample is therefore contaminated with these events. This contamination can lead to a deviation from the theory prediction of the SM mono-Higgs production cross section and its derived SM Higgs properties.

In fig. 28 from ref. [1], it is shown by how much the SM prediction for the mono-Higgs cross section deviates when the standard cuts, tab. 6, are applied to the cross section [124]. For the active-sterile mixing $\theta^2 = |\theta_e|^2$ saturating the 1σ upper bound eq. (5.1) was assumed.

Also the relative statistical precision of the SM predicted mono-Higgs events N_{SM} is displayed as $1/\sqrt{N_{SM}}$, since the number of events is a Poisson variable, in fig. 28. The deviation after the cuts can be as much as 5% and significantly larger than the statistical precision. Altogether, mono-Higgs events from the effects of sterile neutrinos can amount to a few percent of the SM mono-Higgs events that would be wrongly used for the SM analyses. This would lead to a discrepancy with Higgs properties derived from the ZZ fusion Higgs production process, for which there is no Higgs contribution from the effects of sterile neutrinos.

[124] The cuts were applied to a Monte Carlo simulated mono-Higgs event sample from which cut efficiencies were inferred. These efficiencies were then multiplied with the corresponding cross sections.

7.2.3 *Sensitivity estimate to the sterile neutrino parameters at the parton level*

The mono-Higgs contribution from the effects of sterile neutrinos can be used as signal for a dedicated analysis of the sterile neutrino parameters. In this section, the sensitivity of the mono-Higgs signal to the sterile neutrino parameters is analysed at the parton level for future e^+e^- colliders. The parton level analysis allows to establish an order-of-magnitude estimate for the sensitivity to the sterile neutrino parameters.

We investigate the mono-Higgs signature which arises from the $h\nu\nu$ final state at the parton level. The signal constitutes the $h\nu\nu$ events [125] from the direct production of the decays of the heavy neutrinos as well as from the non-unitarity effects. Hence, the expected number of signal events, N_S, can be calculated by $N_S = \left|\sigma_{h\nu\nu} - \sigma^{SM}_{h\nu\nu}\right| \times \mathcal{L}$, where $\mathcal{L}$ corresponds to the

[125] For parton level analyses, all the particles in the final state are accessible, even the light neutrinos that would escape detection or the Higgs boson that would further decay into its decay products.

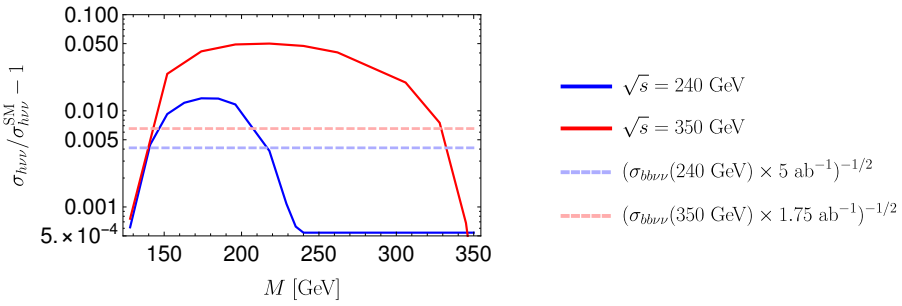

Figure 28: Shown is the deviation of the mono-Higgs cross section in the presence of sterile neutrinos from the SM mono-Higgs cross section. Standard cuts from tab. 6 are applied to the mono-Higgs event sample where the Higgs boson decays to $\bar{b}b$. For the active-sterile mixing angles, only non-zero $|\theta_e|$ is assumed which saturates the 1σ upper bound in eq. (5.1). An integrated luminosity of 5 ab^{-1} and 1.75 ab^{-1} for the physics runs at 240 GeV and 350 GeV is assumed. The horizontal dashed lines denote the relative statistical precision of the SM predicted mono-Higgs events, N^{SM}, which is given by $1/\sqrt{N^{SM}}$.

integrated luminosity for the considered physics runs. The background on the other hand, consists of the SM mono-Higgs contribution from Higgs-strahlung and *WW* fusion. The expected number of background events, N_B, is simply calculated from $N_B = \sigma^{SM}_{h\nu\nu} \times \mathcal{L}$.

The sensitivity to the active-sterile mixing angle $|\theta_e|$ is derived for a significance of $\mathcal{S} = 1$, confer eq. (A.4) for the definition of the significance and its used estimator in eq. (A.5) as well as the general procedure in the appendix A.1.1. The sensitivity corresponds to a signal at the 1σ level for various benchmark values of the heavy neutrino mass M. For the calculation, only $|\theta_e| \neq 0$ is assumed since the mono-Higgs production from the decays of the heavy neutrinos proceeds predominantly over the t-channel *W* boson Feynman diagram, which is dependent on θ_e. The resulting sensitivity on $|\theta_e|^2$ as a function of the heavy neutrino mass for the physics runs at $\sqrt{s} = 240$ GeV, 350 GeV, and 500 GeV is shown in fig. 29. The equivalent plot for the dependency on the neutrino Yukawa coupling $|y_{\nu_e}|$ can be found in ref. [1].

The highest sensitivity to $|\theta_e|^2$ is of course reached when the direct contributions from the decays of heavy neutrinos are kinematically allowed. For heavy neutrino masses above the center-of-mass energy only the non-unitarity effects remain. For heavy neutrino masses $M \lesssim 220$ GeV, the sensitivities of the three physics runs are comparable in magnitude. This is due to a combination of increasing signal cross section and decreasing of the integrated luminosity with increasing center-of-mass energies. The physics runs with a higher center-of-mass energy are sensitive to the active-sterile mixing parameter for a wider range of the heavy neutrino mass. We remark that even though the cross section $\sigma^{Direct}_{h\nu\nu}$ starts decreasing around $M \sim 180$ GeV, 210 GeV, 260 GeV for $\sqrt{s} = 240$ GeV, 350 GeV, and 500 GeV, the sensitivity can even improve. This effect is more pronounced for the 500 GeV run, where the cross section is falling for $M > 260$ GeV, but the sensitivity is improving well

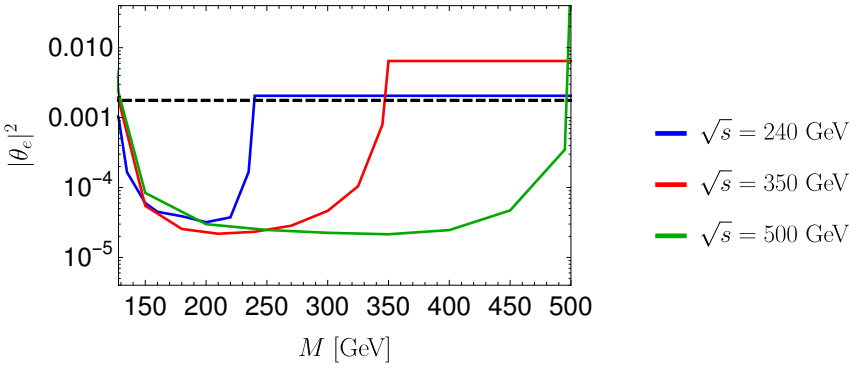

Figure 29: The 1σ sensitivity of the mono-Higgs signature from sterile neutrinos to $|\theta_e|^2$ is shown at the parton level. For the physics runs of 240 GeV, 350 GeV, and 500 GeV an integrated luminosity of 5 ab^{-1}, 1.75 ab^{-1}, and 1 ab^{-1} was assumed. The black dashed line represents the 1σ upper bound on $|\theta_e|$ from eq. (5.1). Cuts on the Higgs boson momentum have been applied to improve the sensitivity, cf. ref. [1].

into the $M > 300$ GeV range. This behaviour is due to a cut on the Higgs boson momentum in order to optimise the sensitivity.

7.2.4 *Sensitivity estimate to the sterile neutrino parameters at the reconstructed level*

To be more realistic in the assessment of the sensitivity, an analysis of the mono-Higgs signal at the reconstructed level is warranted. Because, like in the real experiment, the parton level events decay into stable particles which interact with the detector. Therefore the events have to be reconstructed from the simulation of the detector response. This means that for the partonic $h\nu\nu$ events, the light neutrinos manifest as missing energy, and the Higgs bosons decay into $b\bar{b}$ (58.2%), WW^* (21.4%), gg (8.2%), $\tau^+\tau^-$ (6.27%), $c\bar{c}$ (2.89%), and ZZ^* (2.62%), etc. for $m_h = 125$ GeV, cf. ref. [321]. At the reconstructed level, Higgs boson candidates are identified from the reconstructed decay products which have an invariant mass around m_h. In the following we define the signal for the analysis, discuss relevant SM backgrounds, and how to extract the mono-Higgs candidates from the effects of sterile neutrinos at the reconstructed level.

Signal

The mono-Higgs production from the effects of heavy neutrinos constitutes the signal. In order to obtain a high number of signal events, the Higgs boson decays into two hadronic jets, also referred to as dijet, is chosen which have a combined branching ratio of roughly 70%. Therefore, the dijet plus additional missing energy from the light neutrinos constitutes the signal signature for the mono-Higgs search channel. Besides the processes that give rise to the mono-Higgs production from heavy neutrinos also the Feynman diagrams with a Z boson instead of a Higgs boson contribute to the dijet plus missing

Final state	σ^{SM}@240 GeV [fb]	σ^{SM}@350 GeV [fb]	σ^{SM}@500 GeV [fb]
$b\bar{b}\nu\nu$	146.492	134.614	183.594
$c\bar{c}\nu\nu$	88.0172	73.7956	82.7041
$j_l j_l \nu\nu$	528.8	463.1	500.3
$\tau^+\tau^-\nu\nu$	235.89	163.851	119.989
$b\bar{b}b\bar{b}$	81.2629	47.6152	25.5571
$b\bar{b}c\bar{c}$	146.566	87.6518	51.6446
$b\bar{b}j_l j_l$	6820.6	4259.5	2537.8
$b\bar{b}e^+e^-$	2080.87	2500.82	2920.9
$b\bar{b}\tau^+\tau^-$	34.1905	19.7975	11.0619
$c\bar{c}\tau^+\tau^-$	25.2553	15.0695	9.15227
$j_l j_l \tau^+\tau^-$	116.0	72.4	37.6
single top	0.012	63.3	1092
$t\bar{t}$	—	322.	574.

Table 7: The evaluated cross sections for the included SM backgrounds from 4 fermion final states for the mono-Higgs search channel are shown for $\sqrt{s} = 240$ GeV, 350 GeV, and 500 GeV. j_l denotes a light jet from u, d, c quarks and gluons. This table has been published in [1].

energy signature once the Z boson decays hadronically. The invariant mass spectrum of the dijet system, M_{jj}, from the Z decays peaks at m_Z and is this referred to as mono-Z production from heavy neutrinos. We checked that the mono-Z contribution at the reconstructed level can be essentially removed by selecting events with an invariant mass of the dijet system between 100 and 140 GeV.

Background

For the SM background, we consider four fermion final states that can be identified or misidentified as mono-Higgs candidate events to be the most relevant source. The most relevant background for the mono-Higgs search channel is the $jj\nu\nu$ final state which stems from either the SM mono-Higgs production with the subsequent decay of the Higgs boson to $b\bar{b}, c\bar{c}, gg$ or from gauge boson decays and radiative processes where j can be any of the kinematically available quarks, gluons and hadronic decays of τ leptons. Other considered backgrounds for the mono-Higgs search channel stem from final states with four hadronic jets, such as $b\bar{b}b\bar{b}$, $c\bar{c}c\bar{c}$, $b\bar{b}j_l j_l$ [126], dielectrons and ditau plus dijets [127] such as $b\bar{b}e^+e^-$, $b\bar{b}\tau^+\tau^-$, $c\bar{c}\tau^+\tau^-$, $j_l j_l \tau^+\tau^-$, and $t\bar{t}$ and single top production. The cross sections for the inclusive processes are shown in tab. 7.

[126] Where j_l stands for a light jet from u, d, c quarks and gluons.

[127] For instance, dielectrons only in the final state are very unlikely to be misidentified as two jets and thus are omitted.

Simulation

For the $b\bar{b}\nu\nu$ final state 3×10^6 events and for the rest of the above listed final states 10^5 events were simulated by the Monte Carlo event generator WHIZARD 2.2.7 including initial state radiation. The subsequent parton showering and hadronisation has been carried out by PYTHIA 6. The events were reconstructed with the International Large Detector (ILD) [128] card in Delphes 3.2. The event samples have been analysed with madanalysis5. This is the employed analysis chain, confer for instance fig. 8.

[128] ILD is one of the detector concepts for the ILC.

The pre-selection criteria for the events are the selection of exactly two hadronic jets with an invariant mass of $100 \leqslant M_{jj} \leqslant 140$ GeV.

The resulting invariant mass distribution of the dijet system for an example benchmark point of the heavy neutrino mass is shown in fig. 30, from ref. [1], for $\sqrt{s} = 240$ GeV. Therein, the SM mono-Higgs contribution was simulated separately from the other backgrounds for illustrative purposes. It can be seen that the mono-Higgs production from sterile neutrinos contributes substantially to the SM predicted number of mono-Higgs events. Also the other backgrounds seem to be subdominant. Despite their large cross section, they do not contribute as much in the region of $M_{jj} \sim m_h$. We note that the peak corresponding to the mass of the Higgs boson is located at $M_{jj} \sim 120$ GeV instead of $m_h = 125$ GeV. The shift of the peak to lower values of the invariant mass of the dijet system is due to an energy loss of the hadronic jets via the light neutrinos during the hadronisation. For the analysis at hand, we do not intend to reconstruct the peak for the Higgs boson mass and thus the shift has no implications. But, for a correct reconstruction of the peak, the jet energy loss could be accounted for with the jet p_T corrected mass [322, 323].

After the application of the pre-selection cuts, the kinematic distributions of the event samples have been analysed by the cut-and-count method in order to enhance the significance. The dijet momentum, the missing transverse momentum, and the invariant mass of the dijet system were found the be the most efficient observables. The applied cuts are shown in the appendix A.2 tab. 14, 15 and 16 for completeness, which are taken from ref. [1]. We note that the therein displayed number of events correspond to an integrated luminosity of 10 ab^{-1}, 3.5 ab^{-1}, and 1 ab^{-1} for $\sqrt{s} = 240$ GeV, 350 GeV, and 500 GeV, respectively.

Sensitivity of the mono-Higgs search to the sterile neutrino parameters

The sensitivity to $|\theta_e|^2$ for various benchmark values of the heavy neutrino mass is inferred for a significance of $\mathcal{S} = 1$, confer eq. (A.4) for the definition of the significance and its used estimator in eq. (A.5) in the appendix A.1.1. The resulting number of signal and background events from the cut-and-count analysis are used from tab. 14, 15 and 15 as well as the general procedure in the appendix A.2. For the calculation of the sensitivity only $|\theta_e| \neq 0$ is assumed, i.e. $\theta^2 = |\theta_e|^2$. The resulting 1σ sensitivity at the reconstructed level is shown in fig. 31 for the physics runs at $\sqrt{s} = 240$ GeV, 350 GeV, and 500 GeV. The equivalent figure for the dependency on the neutrino Yukawa coupling $|y_{\nu_e}|$ and twice the integrated luminosities can be found in ref. [1]. For almost all the considered heavy neutrino benchmark points, $N_S \ll N_B$

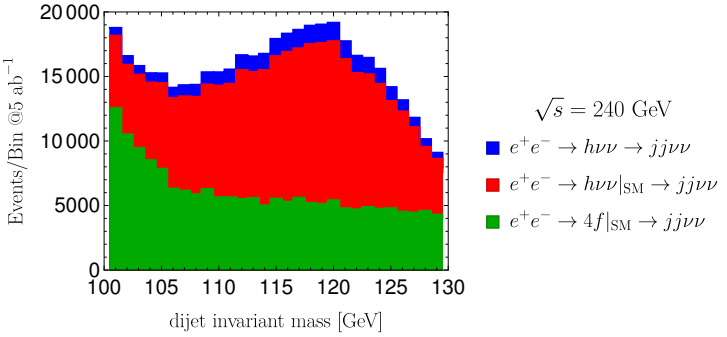

Figure 30: Shown is the dijet invariant mass distribution of the reconstructed events after pre-selection in the mono-Higgs search channel (jj plus missing energy) for a center-of-mass energy of 240 GeV. An integrated luminosity of 5 ab^{-1} is assumed. The blue area represents the mono-Higgs signal from sterile neutrinos with $M = 152$ GeV and $|\theta_e| = 0.042$. The red area represents the SM mono-Higgs background. The green area represents the remaining backgrounds taken together.

is valid, therefore the sensitivity to 2σ can be recast by multiplying the displayed sensitivity by a factor 2.

The estimated sensitivities at the reconstructed level are a bit weaker than the order of magnitude estimate from the parton level sensitivities. This is somewhat expected due to the additional backgrounds at the reconstructed level. Nonetheless, the sensitivity at the reconstructed level is comparable in magnitude with the parton level estimate. As for the partonic estimate of the sensitivity, also the sensitivities at the reconstructed level are comparable for the considered physics runs for heavy neutrino masses $M \lesssim 220$ GeV. For $M > \sqrt{s}$ the non-unitarity effects in mono-Higgs production are weaker than the 1σ bound shown in eq. (5.1).

The shown sensitivities correspond to the $\sqrt{s} = 240$ GeV and 350 GeV physics run for the FCC-ee with 2 interaction points as illustrated in fig. 15, and an additional hypothetical 500 GeV run with 1 ab^{-1}. The sensitivity for $\sqrt{s} = 240$ GeV is also valid for the CEPC since it has the same target integrated luminosity as the FCC-ee. The sensitivities for the $\sqrt{s} = 240$ GeV and 350 GeV physics run can be recast to the case of 4 interaction points, which is also discussed by the FCC-ee study group [301]. In that case, the integrated luminosity would be doubled and the sensitivities would improve by a factor $\sim 1/\sqrt{2}$. The sensitivity for the $\sqrt{s} = 500$ GeV run shown here can be seen as an indication for the capabilities of the ILC, but for the simulation no beam polarisation was employed.

7.3 SUMMARY

The on-shell production of heavy neutrinos and their subsequent decays into a Higgs boson and light neutrino constitutes a rather novel production mechanism that has not been discussed prior to [1, 217, 315]. The additionally produced Higgs bosons directly contribute to the same final states as some

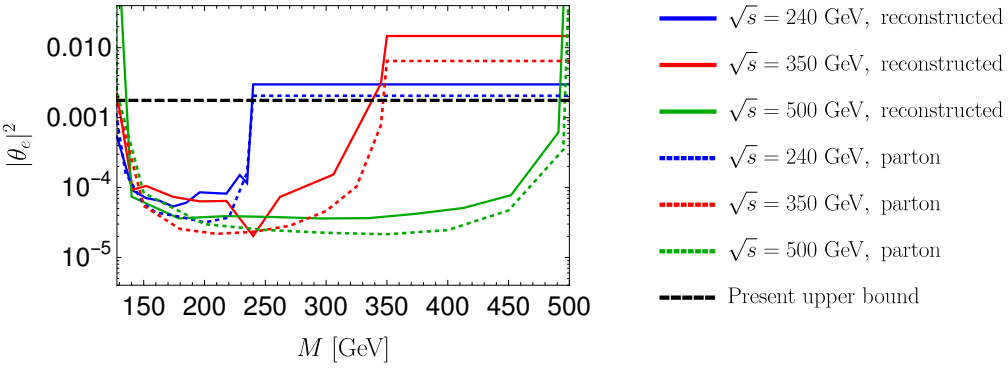

Figure 31: The 1σ sensitivity of the dijet plus missing energy signature of the mono-Higgs search channel to $|\theta_e|^2$ is shown from the analysis of ref. [1] at the reconstructed level for the physics runs of future e^+e^- colliders. The parton level estimate for the sensitivity represented by the dashed lines. The black dashed line represents the 1σ upper bound on $|\theta_e|$ from eq. (5.1). See text for details.

of the SM Higgs production processes. Therefore, they might affect the SM Higgs observables, such as the SM Higgs production cross sections and from those cross sections inferred observables. For future e^+e^- and e^-p colliders, this effect seems the be more pronounced, since up to a few percent of the possibly produced Higgs bosons could stem from heavy neutrino decays.

For e^+e^- colliders, Higgs bosons from the effects of sterile neutrinos can only contribute to the $h\nu\nu$ final state, whose signature is referred to as mono-Higgs. There are two effects that contribute the mono-Higgs cross section: The resonant production of Higgs bosons from heavy neutrino decays and the non-unitarity effects. Even when applying kinematic cuts to the mono-Higgs event sample, in order to extract as many SM mono-Higgs events compared to the SM background, still a few percent of additional Higgs bosons from heavy neutrinos can contaminate the Higgs event sample at future e^+e^- colliders. This would lead to a deviation of the measured mono-Higgs cross section with the SM prediction. While no deviation is expected for Higgs production from VBF via ZZ fusion from sterile neutrinos. This discrepancy would provide a consistency check for the sterile neutrino case.

Therefore, the deviation of the mono-Higgs cross section can be used as a potential probe for sterile neutrinos. The mono-Higgs search channel can practically only be used to probe the active-sterile mixing angle $|\theta_e|$. Since the heavy neutrino production cross section for the s-channel Z boson diagram, which could probe $|\theta_\mu|$ and $|\theta_\tau|$, is too small compared to the t-channel W boson contribution, which probes $|\theta_e|$, for the here considered physics run. The resulting sensitivity of the mono-Higgs channel to $|\theta_e|^2$ from an analysis on the parton level and for the dijet plus missing energy signature on the reconstructed level is shown here for the future e^+e^- colliders. The considered physics runs are $\sqrt{s} = 240$ GeV for the FCC-ee and CEPC, 350 GeV for the FCC-ee, and a possible 500 GeV run possibly for the FCC-ee. For higher $\sqrt{s}$, the sensitivity for the resonant mono-Higgs contribution has an increased mass reach and has a comparable sensitivity with the other physics runs. The contribution from non-unitarity effects are sub-dominant compared to the resonant mono-Higgs contribution, but it can probe $|\theta_e|^2$, just outside the 1σ upper limit eq. (5.1), for heavy neutrino masses above $\sqrt{s}$. The

$\sqrt{s} = 500$ GeV run might be indicative for the ILC, therefore an analysis for the ILC at $\sqrt{s} = 500$ GeV with beam polarisation or even for the high-energy runs for the CLIC would be desirable.

The analysis on the reconstructed level could also be improved in several ways. The inclusion of jj final states as backgrounds would worsen the sensitivities but might be brought under control by the missing energy and dijet momentum observables. Also an analysis of the $h \to \gamma\gamma$ channel would be interesting as a comparison. Employing multivariate analysis tools would also improve the sensitivity compared to the cut-and-count method.

Altogether, all three physics runs are suitable to probe the squared active-sterile mixing angle $|\theta_e|^2$ down to $\sim 10^{-5}$ at the 1σ level in the mono-Higgs channel at future e^+e^- colliders.

[129] More generally mono-X signatures, where X stands for a SM particle, are usually related to hidden sector searches where the missing energy is attributed to DM.

At hadron colliders, the mono-Higgs signature [129] is usually related to searches in the context of Dark Matter at the LHC. But, it provides a probe for sterile neutrinos at pp colliders. The mono-Higgs signature in the context of sterile neutrinos has been analysed for the LHC and HL-LHC in ref. [315] and found to not be promising. The situation might not be much favourable for the FCC-hh or SppC, since the cross section for mono-Higgs production from heavy neutrinos remains comparatively small compared to the SM Higgs production processes [130].

[130] Due to the suppression of the heavy neutrino production cross section in the high virtuality of the intermediate weak gauge bosons

For e^-p colliders, on the other hand, the Higgs contribution from the decays of heavy neutrinos might be very interesting to study due to not to small cross sections compared to the SM Higgs production cross section.

8

DISPLACED VERTEX SEARCHES FOR HEAVY NEUTRINOS AT FUTURE COLLIDERS

Heavy neutrinos that are produced in particle collisions, decay into SM particles (when kinematically allowed). When the heavy neutrinos have masses below the weak gauge bosons and small mixings, their decay rates to the SM particles are suppressed such that they become rather long-lived. Therefore, they can travel some time before they decay into the SM particles. This can lead to a potentially visible displacement of the decay products from the point of production. That is to say, the signature yields a secondary vertex from the decay products that is displaced from the primary vertex from which the heavy neutrino originates.

Such displaced vertex searches are promising when the decay lengths become macroscopic, since there is little to no SM background. Therefore, not many of such displaced vertex events are needed in order to establish an evidence or discovery.

For the different proposed future colliders, the produced heavy neutrino is accompanied by a fermion for the dominating production channels. In the case of e^+e^- colliders, the heavy neutrino is accompanied by a light neutrino for the leading order production processes shown in fig. 17. Hence, the signature features exactly one displaced vertex from which all visible particles originate. The arising displaced vertex signature from long-lived heavy neutrinos is illustrated fig. 32 for e^+e^- colliders.

In the case of pp colliders, the displaced vertex signature is schematically identical as shown in fig. 32 for the heavy neutrino production process via the weak neutral current Drell-Yan process, confer fig. 19a. For the charged weak current Drell-Yan production process, the heavy neutrino is produced in association with a charged lepton. This charged lepton may be referred to as a prompt charged lepton, meaning the charged lepton is produced promptly from the particle collision [131]. The prompt charged lepton carries the information regarding the mixing angle dependency which can be used to infer the relative strength of the active-sterile mixing angles. The prompt lepton can also be used to trigger on the event, as is discussed in ref. [324].

In the case of e^-p colliders, the production of the heavy neutrino proceed predominantly via the t-channel W boson exchange shown in fig. 22a. Therefore, the displaced vertex signature comprises a prompt quark jet.

After its production, the decays of the heavy neutrino proceed via the 3-body decay into semileptonic, hadronic, leptonic and invisible decay modes due to $M \lesssim m_W$. The approximate branching ratios for the corresponding decay modes are given in eq. (4.71). While all except the invisible decay mode deposit energy in some way inside the detector, the semileptonic decay mode provides the most information since there is no direct decay into a light neutrino [132]. From the semileptonic decay mode, the information on the active-sterile mixing angles can be accessed via the non-prompt charged lepton. This decay mode also provides almost no missing energy. Therefore, the mass of

[131] Whereas non-promptly would refer to a charged lepton being produced from the decays of particles instead, for instance from heavy neutrino decays.

[132] Directly refers here to a light neutrino from the heavy neutrino decay. Of course, the hadronic jets from the semileptonic decays can feature light neutrinos from hadronisation.

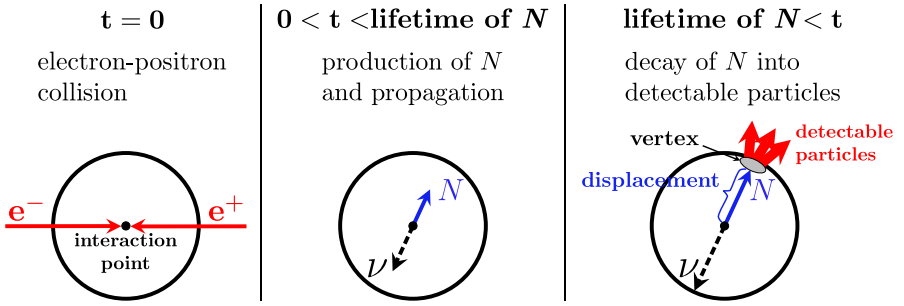

Figure 32: Shown is the displaced vertex signature from the decay of long-lived heavy neutrinos at electron-positron colliders. The displaced vertex refers to the visible displacement of the secondary vertex from the primary vertex. This figure has been published in ref. [6].

the heavy neutrino can be reconstructed by the peak in the invariant mass distribution of the decay products.

The displaced vertex signature from long-lived particles is searched for at the LHC, for instance by ATLAS and CMS [325–328], where they also search for the displaced vertex signature from long-lived neutral particles [329, 330]. The displaced vertex signature from heavy neutrinos is investigated for different setups, for the LHC [324, 331–339], for the HL-LHC [340–343] and also for proposed dedicated displaced vertex detectors at the HL-LHC [344–346]. For the proposed future colliders, estimates for the sensitivity of displaced vertices from heavy neutrinos are derived for the FCC-ee in ref. [2, 252], for the CEPC and ILC in ref. [2], for the FCC-hh and SppC in ref. [3], and for the LHeC and FCC-eh in ref. [3].

In the following sections, we discuss, among others, the work conducted in ref. [2–4]. In section 8.1, we discuss the vertex displacement that arises from the long-lived heavy neutrino and derive the expected number of displaced vertex events. We furthermore discuss possible backgrounds that could arise at future lepton colliders and assess the possible detector response for the detector components based on the ILC's Silicon Detector in section 8.2. In the subsequent section 8.3, the sensitivity of the displaced vertex search to the heavy neutrino parameters for the FCC-ee, CEPC, and ILC, featuring different physics programs as well as for the FCC-hh/SppC and the LHeC and FCC-eh are estimated. Special attention is given to the LHCb in section 8.4, where we derived possible exclusion limits from run 1 data as well as possible sensitivities for run 2 data and for the High-luminosity phase of the LHC.

8.1 VERTEX DISPLACEMENT FROM HEAVY NEUTRINOS

For heavy neutrino masses below m_W, the heavy neutrino decays via the 3-body decay into SM particles, as discussed in section 4.3.4. The total decay width becomes suppressed when the heavy neutrino decays via off-shell weak gauge and the Higgs boson, which is the case for $M < m_W$. The mean lifetime τ of the heavy neutrino, which is the inverse of the total decay width,

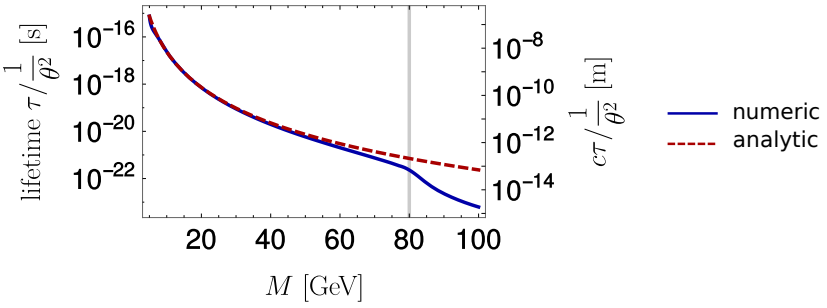

Figure 33: Shown are the proper lifetime τ and corresponding distances without relativistic effects $c\,\tau$, where velocities close to the speed of light c are assumed, of the heavy neutrino normalised by θ^2 as a function of its mass M. The lifetime was calculated numerically with WHIZARD 2.4 and analytically in the low-energy limit ($M \ll m_W$) from eq. (4.70).

becomes longer compared to SM particles for small θ^2. The proper lifetime of the heavy neutrino as a function of the heavy neutrino mass is shown in fig. 33. Therein, the lifetime is derived numerically from the total decay width obtained with WHIZARD 2.4 and compared to the derived, approximate, analytical formula from eq. (4.70). The analytical result is a good approximation in the low-energy limit, $M \ll m_W$. The opposite fact can also be seen in the figure. Once the decay channels via on-shell weak gauge bosons are opened, the lifetime drops considerably. Assuming velocities close to the speed of light, c, and mixings $\theta^2 \sim 10^{-5}$, distances without relativistic effects of $c\,\tau \sim 10^{-3}$ m can be reached.

When switching to the laboratory frame from the proper frame, the relativistic effects have to be included. The lifetime of the heavy neutrino in the laboratory frame becomes

$$\tau^{\text{lab}} = \gamma\,\tau\,, \tag{8.1}$$

where γ is the Lorentz factor [133]

$$\gamma = \sqrt{1 + \frac{|\vec{p}_N|^2}{M^2 c^2}} \tag{8.2}$$

in terms of the 3-momentum $\vec{p}_N$ and mass of the heavy neutrino. Since we intend to measure time and lengths in SI units instead of natural units, we give the relevant formulae here with the factors of c restored.

We mention here that the Lorentz boost of the heavy neutrino is fixed at e^+e^- colliders due to the known initial states when the heavy neutrino is produced. The 3-momentum in a $2 \to 2$ process for one massive particle in the final state, can be determined from the kinematics as [134]

$$|\vec{p_N}| = \frac{1}{2}\left(\sqrt{s} - \frac{M^2}{\sqrt{s}}\right). \tag{8.3}$$

The resulting Lorentz factor as a function of the heavy neutrino mass is displayed in fig. 34 for the physics run $\sqrt{s} = 90,\ 240,\ 350$ and 500 GeV at future electron-positron colliders.

[133] From the relativistic 3-momentum $|\vec{p}_N| = \gamma M|\vec{v}|$, one substitutes γ with the usual definition $\gamma = 1/\sqrt{1 - \frac{v^2}{c^2}}$. Squaring the 3-momentum equation, solving for v^2 and substituting v^2 back in the usual definition of γ, one obtains the Lorentz factor in terms of 3-momentum.

[134] From 3-momentum conservation in the center-of-mass frame it follows $\vec{p}_N + \vec{p}_\nu = 0$ with $|\vec{p}_N| = \sqrt{E_N^2 - M^2}$. Since the light neutrino can be well approximated as massless, the energy of the light neutrino is given as $E_\nu = |\vec{p}_\nu| = |\vec{p}_N|$. From the energy conservation equation $E_N + E_\nu = \sqrt{s}$ the energy E_N and then $|\vec{p}_N|$ can be calculated.

While for pp and e^-p colliders the momenta of the interacting quarks in the initial states are unknown, which results in many possible momenta for the heavy neutrino. This leads to a distribution of the Lorentz factor γ of the heavy neutrino according to the momentum distribution $|\vec{p}_N|$. An example histogram of the Lorentz factor as well as the sample mean and sample median as a function of the heavy neutrino mass is shown from Monte Carlo generated events in fig. 34 for the FCC-ee and SppC, respectively, and in fig. 36 for the FCC-eh. We note that the produced results for the LHeC are very similar to fig. 36 for the FCC-eh. Thus, fig. 36 can also be used to represent the Lorentz factor for the LHeC.

The mean distance that the heavy neutrino travels in the laboratory frame, which corresponds to the mean displacement from the primary vertex, is given by

$$\Delta x_{lab} = \tau_{lab}|\vec{v}| = \sqrt{\gamma^2 - 1}\,\tau c = \frac{|\vec{p}_N|}{Mc}\tau c\,, \tag{8.4}$$

with the velocity

$$|\vec{v}_N| = \frac{|\vec{p}_N|c^2}{E_N} = \sqrt{1 - \frac{1}{\gamma^2}}\,c\,. \tag{8.5}$$

However, due to the stochastic nature of the decay of the heavy neutrino it follows an exponential probability distribution. For a mean displacement from the primary vertex Δx_{lab} given a fixed Lorentz boost, the probability for the heavy neutrino to decay within the boundaries $x_{min} \leqslant \Delta x_{lab} \leqslant x_{max}$ is given in the laboratory frame as

$$\begin{aligned} P_{dv}(x_{min}, x_{max}) &= \int_{t_1=\frac{x_{min}}{|\vec{v}_N|}}^{t_2=\frac{x_{max}}{|\vec{v}_N|}} \frac{1}{\tau^{lab}}\,\exp\left(-\frac{t}{\tau^{lab}}\right) dt \\ &= \exp\left(\frac{-x_{min}}{\Delta x_{lab}}\right) - \exp\left(\frac{-x_{max}}{\Delta x_{lab}}\right)\,. \end{aligned} \tag{8.6}$$

We note here that if the Lorentz boost is not fixed, then one would need to include the many possible Lorentz factors by integrating over the distribution of the Lorentz factors. More generally, the above expression would become

$$\int D_N(\gamma)\, P_{dv}\left(x_{min}, x_{max}, \Delta x_{lab}(\tau,\gamma)\right)\, d\gamma\,, \tag{8.7}$$

where $D_N(\gamma)$ stands for the probability distribution function of γ factors of the heavy neutrinos. An application of such a general expression is discussed in section 8.4.

The expected number of heavy neutrinos to decay with displacements within the boundaries x_{min} and x_{max} is given by

$$N_{dv} = \sum_{prod.} P_{dv}(x_{min}, x_{max})\,\sigma_N(M, |\theta_\alpha|^2, \sqrt{s})\,\mathrm{BR}(N \to \text{visible})\,\mathcal{L}\,, \tag{8.8}$$

where σ_N denotes the heavy neutrino production cross section, which depends on the heavy neutrino mass M, the active-sterile mixing angles $|\theta_\alpha|^2$ (for $\alpha = e, \mu, \tau$) and the center-of-mass energy $\sqrt{s}$, $\mathcal{L}$ denotes the integrated luminosity, and $\sum_{prod.}$ denotes the sum over the different neutrino production processes.

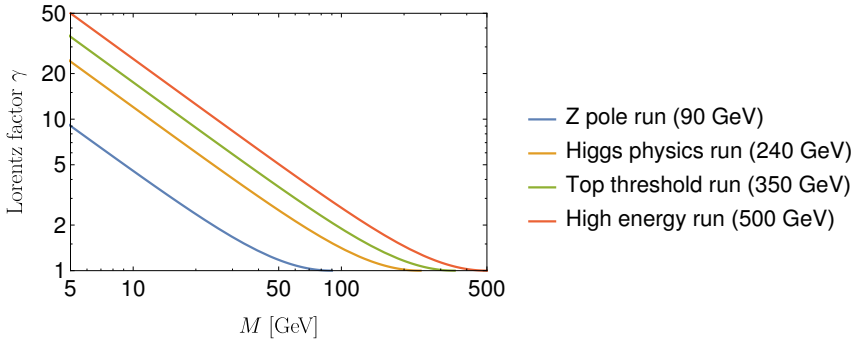

Figure 34: Shown is the Lorentz factor γ as a function of the heavy neutrino mass M for the various physics runs at the proposed future e^+e^- colliders.

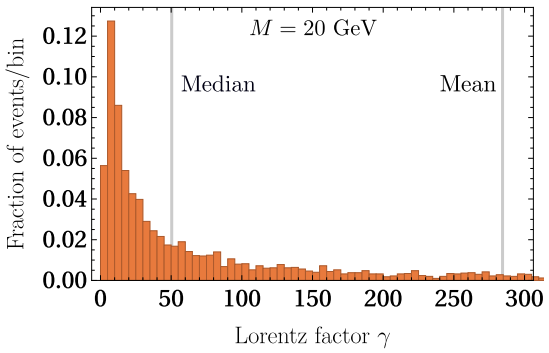

(a) An example histogram of the Lorentz factor γ is shown for the benchmark point $M = 20$ GeV at the FCC-hh and SppC, respectively. The sample mean and sample median are indicated by the grey lines.

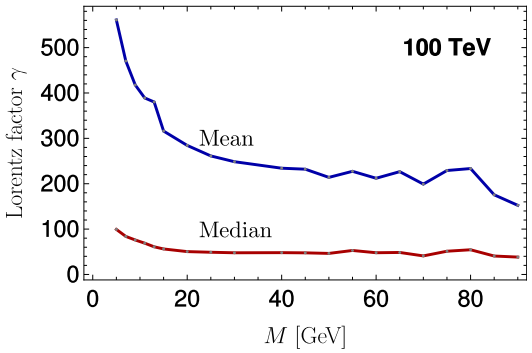

(b) Calculated sample means and medians for various benchmarks points of the heavy neutrino mass at the FCC-hh and SppC, respectively.

Figure 35: Shown is the simulated Lorentz factor γ from 5×10^3 Monte Carlo generated heavy neutrino events for various benchmark points of the heavy neutrino mass at future hadron colliders, such as the FCC-hh and SppC.

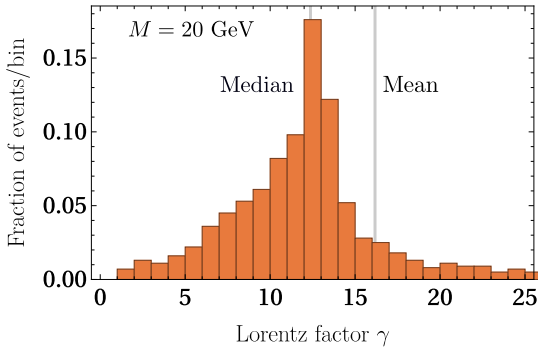

(a) An example histogram of the Lorentz factor γ is shown for the benchmark point $M = 20$ GeV at the FCC-eh. The sample mean and sample median are indicated by the grey lines.

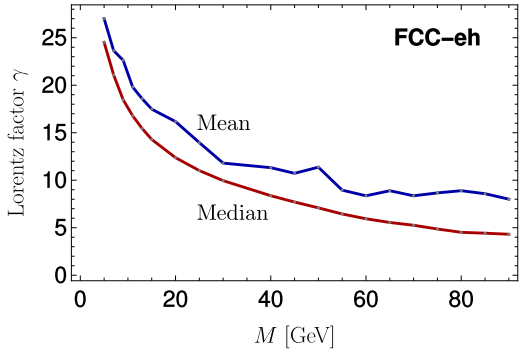

(b) Calculated sample means and medians for various benchmarks points of the heavy neutrino mass at the FCC-eh.

Figure 36: Shown is the simulated Lorentz factor γ from 5×10^3 Monte Carlo generated heavy neutrino events for various benchmark points of the heavy neutrino mass at future e^-p colliders, such as the FCC-eh. These figures are also representative for the LHeC, since it produces the almost same result.

8.2 SIGNAL AND BACKGROUND CONSIDERATIONS ON THE BASIS OF THE ILC'S SILICON DETECTOR

We attempt to asses the background situation for the displaced vertex signature from long-lived heavy neutrinos that could arise at future e^+e^- colliders as partly published in ref. [2].

8.2.1 *General background considerations*

As is illustrated in fig. 32, the signature of the heavy neutrino at e^+e^- colliders features a single displaced vertex, i.e., all the visible particles seen by the detector originate from the displaced vertex. It also results in a significant amount of momentum imbalance due to the light neutrino escaping detection. This is very different from SM signatures of long-lived particles from final states such as $f\bar{f}$, $f\bar{f}\gamma$, $f\bar{f}\gamma\gamma$, $f\bar{f}\nu\nu$, $\nu\ell q\bar{q}'$, where f denotes charged leptons or quarks that hadronise. These SM processes could constitute the following conceivable backgrounds to displaced vertices from heavy neutrinos at the reconstructed level:

- Particles lost in the beam pipe:
  Final state particles can be lost in the beam pipe for low transverse momenta, such as $f\bar{f}$ final states. In the case of $f\bar{f}$, both particles could be lost for low transverse momentum since they scatter back-to-back. One of the visible particles, represented by f, can be scattered into the detection volume, for instance by recoil against a photon. When this particle is long-lived, it may give rise to a single secondary vertex. This signature could feature small angles of the displaced vertex with respect to the beam axis, high transverse momentum photons [135] or non-zero charge of the measured decay products. These features could be used as a possible veto.

[135] Also referred to as hard γ.

- Event mis-reconstruction:
  Particles that are visible by the detector can be mis-reconstructed and mis-identified. This could lead to single displaced vertex from a SM particle when the accompanying particle is not reconstructed successfully. However, the mis-reconstructed particle might still leave its imprint as energy deposits in the detector, which is expected in the opposite region of the displaced vertex. The reconstructed charge of the displaced vertex could be non-zero that can be used as a veto.

- Merger of two secondary vertices:
  Long-lived particles that are produced in pairs and decay in a small spatial volume, might be resolved as one secondary vertex. In order for the two particles to decay close by they have to be emitted in a narrow solid angle and decay almost at the same time. For the particles to be emitted in a narrow solid angle, the overall momentum has to be balanced out by invisible particles. This also constitutes a possible SM background for displaced vertices from heavy neutrinos.

We assume that the first and second type of backgrounds can be removed, or at least brought under control at the expense of signal efficiency with

Figure 37: Shown is a schematic illustration of the signal signature and a possible SM background. The signal arises from the decay of a long-lived heavy neutrino with mean lifetime τ. While for the SM background, the merger of two secondary vertices is considered which arises from long-lived mesons m and m^* that decay sufficiently close to each other such that only one secondary vertex can be resolved. The detector resolution δx depends on the detector component. This figure has been published in ref. [2].

the above discussed vetoes. However, a dedicated analysis for these types of backgrounds are necessary in order to substantiate this assumption. We therefore, consider only the third type of backgrounds, given by the merger of two secondary vertices. An illustration of the heavy neutrino signature from displaced vertices as well as the possible background from the merging of secondary vertices is given in fig. 37.

In order to estimate the probability for the merging of two displaced vertices to happen within a spatial volume that is unresolvable, the decays have to happen at almost the same time, else the other particle has travelled too far away, and the long-lived particles have to be emitted in a narrow solid angle as well. For the particles to decay within the radial distance δ, eq. (8.6) can be used for the long-lived particles with a distance x from the IP to decay within $x_{\text{min}} = x - \delta/2$ and $x_{\text{max}} = x + \delta/2$. For the estimation of the narrow solid angle, an isotropic emission of the two long-lived particles is assumed. Thereof, the narrow solid angle $\Omega/4\pi$ can be estimated as $\Omega = 2\pi \int_0^\alpha \sin\theta \, d\theta$ for $\alpha = \arcsin(\delta x/2x)$, where δx is the diameter of a flat circle on the surface. The overall probability for the merging of two vertices is estimated as $\Omega/4\pi \times P_{dv}^2$.

8.2.2 *Assessment of the possible detector response for the different detector components of the SiD*

The detectability of the displaced vertex signal is confronted with background considerations. The detectability assessment is based on the performance parameters of the Silicon Detector (SiD) [347, 348], which is one of the detector designs for the ILC, as an example benchmark detector for future e^+e^- colldiers. Since certain performances are required in order to measure the SM properties, detectors of the other future colliders should be comparable in performance.

The SiD consists of a silicon pixel vertex detector, silicon tracker, silicon-tungsten electromagnetic calorimetry (ECAL), hadronic calorimetry (HCAL), a high-magnetic field solenoid and an iron flux return as muon identification system [348]. The detector dimension of the SiD are given in tab. 8.

(Barrel)	Inner radius	Outer radius	z extent
Vertex detector	1.4	6.0	+/- 6.25
Tracker Silicon	21.7	122.1	+/- 152.2
ECAL	126.5	140.9	+/- 176.5
HCAL	141.7	249.3	+/- 301.8
Solenoid	259.1	339.2	+/- 298.3
Flux return	340.2	604.2	+/- 303.3

Table 8: Shown are the dimensions (in units of cm) of the components of ILC's Silicon Detector. The numbers are taken from ref. [348].

The vertex detector is designed to identify particles of the heavy flavour such as hadrons from b and c quarks, and τ leptons by efficiently detecting their displacement due to a finite lifetime. The tracker together with the ECAL, allows to measure tracks of charge particles. In order to accurately measure the vertex displacement x, which is the distance between the primary and secondary vertices, the secondary vertex has to be determined. A common method to determine a secondary vertex is to measure the impact parameter of the tracks. The impact parameter is defined as the shortest distance of the reconstructed flight path of a particle from the primary vertex. The impact parameter resolution in the transverse plane can be as good as 2 μm for the SiD [348]. It is experimentally difficult to measure the primary vertex which emerges from the interaction point (IP) [136]. Therefore, the center of the interaction point with its spatial extension as uncertainty is considered as the primary vertex instead.

[136] The interaction point is the spatial volume of the intersecting beams.

The colorimetry of the SiD has imaging capabilities which allows one to follow the track and thus the energy clusters are associated correctly to the particle tracks. The SiD features a pixel size of 4 μm and 1 cm for the ECAL and HCAL, respectively. For the muon identification system, the muons are detected by the photomultipliers between the layers of the solenoid flux return while most of the hadrons are rejected.

The decays of the long-lived heavy neutrino could take place in any of the detector components of the SiD. In the following, we discuss how the heavy neutrino signature could behave and how it could be measured when it decays with displacements x inside the different regions of the detector. This is confronted with estimations for conceivable backgrounds, where an isotropic emission of final states is assumed. For the following estimates, we restrict ourselves to a spherical symmetry of the SiD, we therefore use the barrel radii and performance parameters in the transverse plane of the various detector components.

The following discussion comprises a first step towards assessing backgrounds to the displaced vertex signature from long-lived heavy neutrinos, before extensive simulations of the signatures and their detector response, best in a full detector simulation, are performed.

Inner region [137], $x < 1.4$ *cm:*

[137] We refer to the volume enclosed by the vertex detector as inner region.

When the heavy neutrino decays before it reaches the vertex detector, all kinematic information on the decay products are available from the vertex detector, tracker and calorimetry. The vertex displacement can be inferred from the measurement of the impact parameter from the tracks. The precision of measuring x is limited by the impact parameter resolution as well as the resolution for the primary vertex, which has been taken to be as the spatial extension of the IP. A vertical extension of $\sim$ 10 nm, $\sim$ 80 nm [290] and $\sim$ 250 nm [349] can be found for the physics runs of the ILC, CEPC and FCC-ee, respectively. The minimum vertex displacement that is separable at 3σ from the IP is defined as the resolution for displaced vertices, x_{res}. The ILC and CEPC can resolve displacements as small as $x_{res} \sim 6$ μm and the FCC-ee as small as $x_{res} \sim 7$ μm. We remind the reader that these are rough estimates for resolutions, which are based on the transverse parameters only.

For displacements of the heavy neutrino decay smaller than x_{res}, the displacement of the heavy neutrino is not resolvable. Thus, the search of the heavy neutrino reverts to a conventional search by the analysis of the kinematic distributions of the decay products.

For displacements of the heavy neutrino decay larger than x_{res}, there are long-lived SM particles that can provide a background by the merging of the two secondary vertices in the inner region. These are the π^0 meson ($c\tau \sim$ 20 nm), the τ lepton ($c\tau \sim 0.1$ mm), and the D and B mesons (with $c\tau \sim 0.1 - 0.5$ mm). In the inner region, these two secondary vertices cannot be resolved separately when they are closer than 6 μm or 7 μm.

The pion production cross section with light neutrinos is estimated from $\sigma(e^+e^- \to q\bar{q}\nu\nu)$ to be smaller than $\simeq$ 100 fb at $\sqrt{s} = m_Z$. Therefore, at most 10^7 isotropic pion events can be expected. Pions, however, decay predominantly into two photons, which are not misidentified as the heavy neutrino signal. Decays of the pions into $\nu\nu e^+e^-\gamma$ is of $\mathcal{O}(10^{-7})$, which can be signal like and drastically reduces the resulting number of events. Furthermore, the vertices of the two pions need to be closer than 6 μm in order to be misidentified as the signal, which further suppresses the number of events by $\Omega/4\pi \times P_{dv}^2 \sim \mathcal{O}(10^{-3})$.

The τ lepton production cross section is considered to be larger than the D and B meson production cross sections. The $\sigma(e^+e^- \to \tau^+\tau^-\nu\nu)$ cross section is $\simeq$ 1 fb at $\sqrt{s} = m_Z$. With 10^5 isotropically distributed events, a large enough suppression factor from the merging of the two vertices down to less than one event can be found for displacements $x \geqslant 10\,\mu$m at the FCC-ee. Also for the higher center-of-mass energies these backgrounds are suppressed enough.

A conceivable background at the Z pole could stem from $e^+e^- \to \tau^+\tau^-\gamma$ with a cross section of $\sim$ 1.6 nb. The photon, however, needs to be lost in beam pipe else one would veto against such events by the photon. Thus, the probability for a photon to be lost in the beam pipe should to be factored in. The suppression factor from the merging of the two vertices gives a suppression factor of $\Omega/4\pi \times P_{dv}^2 \sim \mathcal{O}(10^{-6})$ for displacements $x \geqslant 10\,\mu$m. However, the suppression from the merging of two vertices could also be much smaller when the assumption of the isotropic distribution is abandoned. It could be

checked by simulating the angle between the leptons, which would be required to be small such that they would merge. Moreover, the invariant mass distribution of the decay products may be used to further suppress the background. This possible background should be studied further.

Vertex detector and tracker, $1.4\ cm \leqslant x \lesssim 1.20\ m$*:*

Once the heavy neutrino decays inside the vertex detector or tracker a secondary vertex appears. The vertex displacements should be as such visible or it can be inferred by the measurement of the impact parameter of the tracks from the decay products. However, for decays taking place towards the outer part of the tracker, not as many silicon layers are available to reconstruct the tracks [348]. This leads to a decrease in the resolution of the impact parameter at the SiD. Detectors with continuous tracking, such as the ILD, have a larger number number of layers which should weaken this effect.

The hadrons K_S ($c\tau \sim 2.68$ cm) and Λ ($c\tau \sim 7.89$ cm) have decay lengths that lead to decays taking place predominantly in the vertex detector or tracker. However, if the background consists of the merging of two such secondary vertices then they would be suppressed due to the narrow solid angle.

ECAL and HCAL, $1.25\ m \lesssim x \lesssim 2.5\ m$*:*

Heavy neutrino decays inside the ECAL or HCAL lead to a connected cluster of energy deposit that is consistent with one secondary vertex. The striking features are that there are no tracks visible by the tracking system and a significant amount of momentum imbalance. The energy deposits of the decay products of the heavy neutrino may be identified as one or several electrically neutral particles due to the absence of tracks.

For the decays inside the ECAL, it would, under the above assumption, identify the leptonic decay products of the heavy neutrino as photon(s). While the hadronic decay products would then be identified in the HCAL as neutral hadrons.

For the decays inside the HCAL, the energy deposit from the decay products would be identified as neutral hadron(s). However, a study of the response of the ECAL and HCAL to the displaced decays of the heavy neutrino in a full detector simulation is necessary.

Possible backgrounds for the HCAL could arise from the long-lived K_L mesons ($c\tau \sim 15.34$ m), either directly produced from the particle collision or from the decays of τ leptons. However, when the τ lepton decays to a K_L there is an accompanied meson or charged lepton, which can be used as a possible veto.

Muon identification system, $3.4\ m \lesssim x \lesssim 6.0\ m$*:*

The decay products from the displaced decay of the heavy neutrinos inside the flux return yoke interact with the scintillating strips. The photomultipliers detect the subsequently produced photons from the several decay products. However, since the displaced heavy neutrino decay does not feature tracks nor energy deposits in the ECAL and HCAL, the signal from the photomultipliers should not be identified as a muon. For displaced decays of the heavy

neutrino in the outer parts the response of the muon identification system is unclear. Also here, a study of the response of the muon calorimetry to the displaced decays of the heavy neutrino in a full detector simulation is desirable.

Possible backgrounds for the energy deposit from heavy neutrinos in the muon calorimetry system come, for instance, from cosmic ray muons. However, they could be rejected by comparing the hits with the collision time of the electron-positron beams.

Altogether, each detector component can in principle record a signal from the displaced decay of the heavy neutrino. Although, backgrounds seem at first sight quite scarce, they have to be studied more carefully.

8.3 SENSITIVITY OF FUTURE COLLIDERS TO THE STERILE NEUTRINO PARAMETERS

In this section, the estimated sensitivity for the search of long-live heavy neutrinos via displaced vertices to the active-sterile mixing angles is presented for future e^+e^-, pp, and e^-p colliders.

A sensitivity of the signal at 95% C.L. over the zero background can be established for $N_{dv} > 3.09$ expected events, confer the appendix A.1.2. From this limit, the upper bound on the active-sterile mixing angles can be derived for the proposed future colliders.

Electron-positron colliders

The SiD as a benchmark detector could resolve displacements of the heavy neutrino decays as small as $x_{res} \sim 6-7$ µm [138] and as large as to the outer region of the muon identification system inside the flux return yoke. However, we assume that the region from 10 µm to the outer radius of the HCAL at 249 cm from the IP to be free of background and sensitive to the signal with an efficiency of 100% [139]. We consider the FCC-ee, CEPC, and ILC for the proposed future colliders together with the following physics programs: The Z pole run, the Higgs physics run, and the top-threshold scan of the FCC-ee; the Z pole run, and the Higgs physics run of the CEPC; the Z pole run and the high-energy run at $\sqrt{s} = 500$ GeV of the ILC.

As we discussed in section 6.2.1, the heavy neutrino production cross section at the Z pole is mostly dependent on θ^2 while for the higher energy runs the cross section is mostly dependent on $|\theta_e|^2$. For the Z pole run, the expected number of displaced vertex events from the decay of the heavy neutrino, N_{dv} in eq. (8.8), is thus dependent on θ^2 via the production cross section and via the decay width of the heavy neutrino. Therefore, N_{dv} is equally dependent on all the active-sterile mixing angles $|\theta_\alpha|$ for $\sqrt{s} = m_Z$. On the other hand, for the physics runs above the Z pole, the production cross section is dependent on $|\theta_e|^2$ while the decay width of the heavy neutrino is proportional to θ^2. In this case, N_{dv} has a much stronger dependency on $|\theta_e|$ than the other two mixing angles. The future sensitivities are derived under the assumption of only $|\theta_e| \neq 0$, i.e. $\theta^2 = |\theta_e|^2$. The estimated future sensitivities of the displaced vertex search of the heavy neutrino to θ^2 at the 95% C.L. are shown in fig. 38 for the FCC-ee, CEPC, and ILC.

[138] Where the performance parameters in the transverse plane were considered and a spherical symmetry of the SiD assumed, as discussed in the previous section.

[139] As stated above, a deeper study of the detector response to possible backgrounds and the signal are necessary.

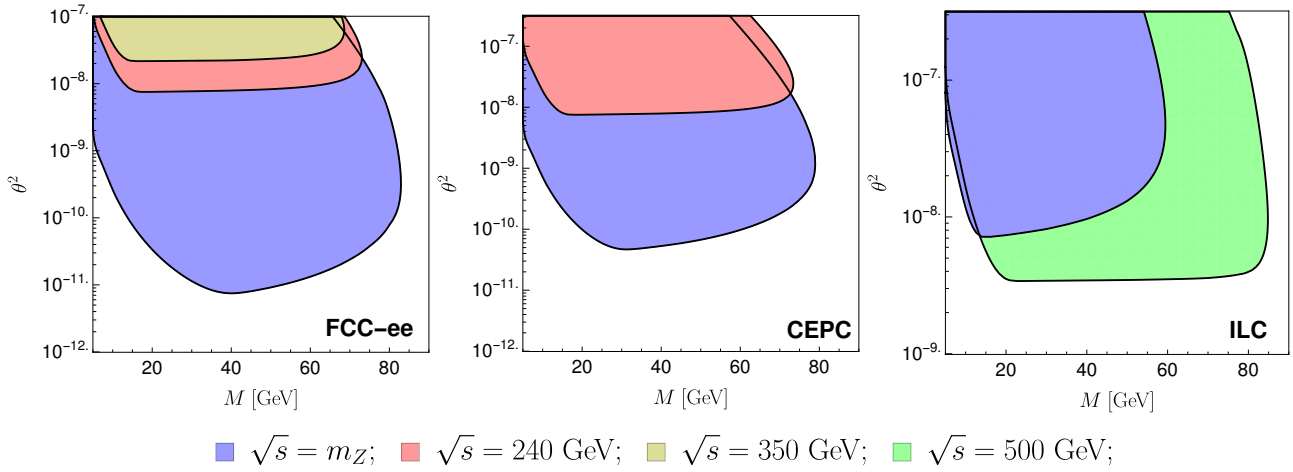

Figure 38: Projected sensitivity to θ^2 at the 95% C.L. for heavy neutrino searches via displaced vertices for various physics runs at the FCC-ee, the CEPC, and the ILC. The physics runs with the integrated luminosities from fig. 15 are considered. For the derivation of the estimated sensitivity, vertex displacements of the heavy neutrino between 10 µm and 249 cm are assumed to be background-free and detectable with a signal efficiency of 100%. For the active-sterile mixing angles $\theta^2 = |\theta_e|^2$ with θ_μ, $\theta_\tau = 0$ is assumed.

The FCC-ee with an integrated luminosity of 110 ab^{-1} shows the best sensitivity to θ^2. The sensitivities for the physics runs at higher center-of-mass energies are comparable across all colliders. It is noteworthy that the $\sqrt{s} = 500$ GeV physics run at the ILC outperforms the $\sqrt{s} = 240$ GeV physics run at the FCC-ee and CEPC, although they all have the same integrated target luminosity. The slight outperformance is due to the slightly larger heavy neutrino production cross section from beam polarisation. As can be seen, for all the physics runs the displaced vertex search is limited to masses $\lesssim m_W$ because the lifetime of the heavy neutrino decrease significantly when the decays via on-shell W and Z decays become efficient.

In order to have a better understanding of the shape of the curve, it is informative to plot the sensitivity when each of the previously discussed detector regions are considered independently as a probe for long-lived heavy neutrinos. Therefore, the sensitivity for each detector region of the SiD is derived by using their inner and outer radii as x_{min} and x_{max} for $N_{dv} \geqslant 1$ event [140]. This effectively maps each detector region to the sterile neutrino parameter space. The resulting sensitivity of each detector region of the SiD for the Z pole run of the FCC-ee is shown as an example in fig. 39.

[140] For the inner region, the minimal resolvable distance for displaced vertices x_{res} has been chosen as x_{min}.

The order of the sensitivity for the detector regions corresponds to the order of the layered detector components of the SiD. However, due to the stochastic nature of the decay of the long-lived heavy neutrino the sensitivity of the various detector regions do overlap. The following insight can also be gained from the figure: On the one hand, the parameter space to the right of the inner region features displaced decays of the heavy neutrino that are too short to fall into the resolvable range of the inner region, i.e., the lifetime of the heavy neutrino is too short. Although the displaced vertex cannot be resolved for these events of the heavy neutrino decays, they can still be studied by means of conventional searches. On the other hand, the parameter space to the left of the muon identification system features decays outside of the

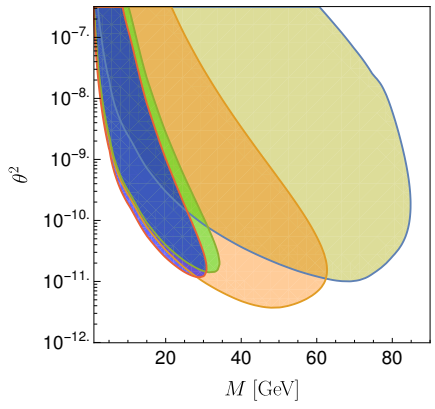

(a) Sensitivity to 1 displaced vertex event from long-lived heavy neutrinos for each detector region of the SiD.

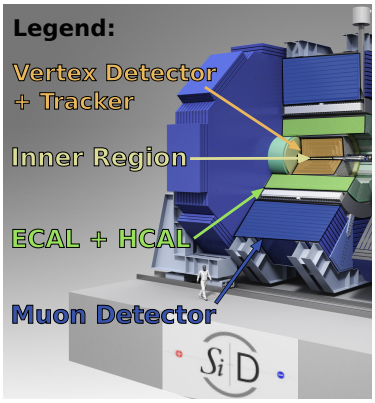

(b) Layout of the SiD with the considered detector regions. The 3-dimensional display of the SiD has been taken from ref. [350]

Figure 39: Example sensitivity of the detector regions of the SiD to the displaced vertex decays from heavy neutrinos at $\sqrt{s} = m_Z$ of the FCC-ee.

detector, these trigger no response inside the detector and these events are lost.

We notice that the inner region is so dominant compared to the other regions because it can detect displacements over several orders of magnitude, i.e., from the micron to cm range. Therefore, it is important to make sure that as small as possible displacement of the heavy neutrino can be resolved by improving the impact parameter resolution or optimising the background rejection such as exploiting features from the heavy neutrino decays. In order to detect larger displacements, the inclusion of the muon identification system does not improve the sensitivity by much, instead much larger detection volumes are needed. Therefore, one could go for the expensive option and enlarge the detector as a whole or, alternatively, projects like MATHUSLA [141] would be a less expensive option.

[141] MATHUSLA [351, 352] is a dedicated displaced vertex detector proposed to be built above ATLAS or CMS. It would be situated roughly 100 m from the IP.

Hadron and electron-proton colliders

Displaced vertex searches for heavy neutrinos can also be undertaken at the future 100 TeV hadron machines such as the FCC-ee and the SppC, and the electron-proton machines such as the LHeC and FCC-eh.

Hadron colliders offer a larger number of produced heavy neutrinos and provide much larger boost factors of the heavy neutrino compared to the e^+e^- machines [142]. However, the question of possible backgrounds is much more involved. We assume that displacements of 1 mm to 1 m from the IP to be free of background and detectable with 100% efficiency. The background assumption is in line with earlier studies performed for the LHC and HL-LHC, where a transverse impact parameter of 1 mm to 1 m is required in order for the displaced heavy neutrino to decay inside the tracker, cf. ref. [324, 335]. The signal efficiency assumption might be rather bold because compared to lepton colliders the hadron colliders are not known for their clean

[142] Compare fig. 35 and 34.

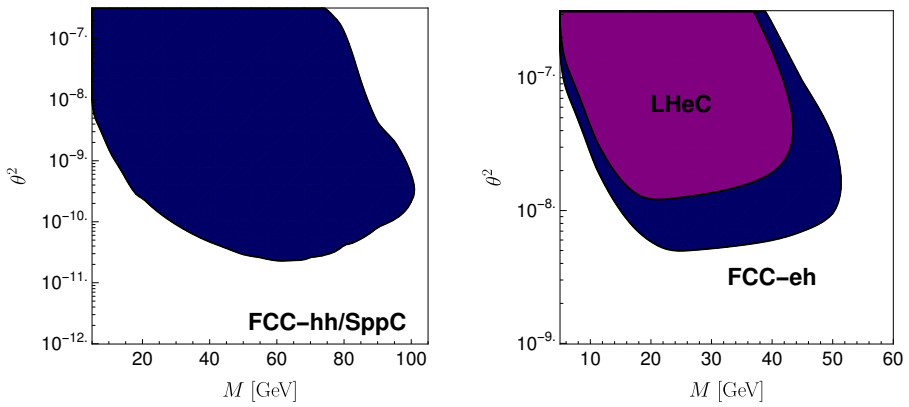

(a) Shown is the sensitivity to $\theta^2 = |\theta_e|^2$ at 2σ for the FCC-hh and SppC at $\sqrt{s} = 100$ TeV with an integrated luminosity of 20 ab^{-1}.

(b) Shown is the sensitivity to $\theta^2 = |\theta_e|^2$ at 2σ for the FCC-eh and LheC, respectively. An integrated luminosity of 1 ab^{-1} was assumed for both future colliders.

Figure 40: First look at a potential 2σ sensitivity to heavy neutrinos via the displaced vertex search at future hadron and proton-electron colliders. For both collider types, vertex displacements of the heavy neutrino of 1 mm to 1 m are assumed to be background-free and detectable with 100% efficiency.

environment, thus we would expect the signal efficiency to drop when a set of kinematic cuts is applied in order to reject possible backgrounds. Nevertheless, we make this assumption in order to have a first look at a potential sensitivity to heavy neutrinos via the displaced vertex search for future hadron colliders. A thorough study would be necessary in order to estimate a realistic sensitivity.

Electron-proton colliders, feature the lowest number of heavy neutrino due to a small production cross section and lower integrated luminosities. We make the same assumption regarding the background and signal efficiency as for the FCC-hh and SppC as comparison. A dedicated study for this signature would be desirable. Although, recently ref. [353] concluded that displaced vertices down to 40 μm could be resolved in an optimistic case. Therein, τ leptons as backgrounds related to long-lived Higgsinos are discussed. We note that the displaced vertex signature is also studied for the LHeC and FCC-eh in the context of gauged $B - L$ extended SM inref. [346].

For the calculation of the sensitivity, the distribution of the Lorentz boost has to be taken into account. We take the derived sample mean in fig. 35b and 36b for the calculation of the sensitivity instead of integrating over the distribution as is explained in eq. (8.7). The resulting potential sensitivity to θ^2 at the 95% C.L., assuming only $\theta^2 = |\theta_e|^2$, for the FCC-hh and SppC is shown in fig. 40a while for the LHeC and FCC-eh in fig. fig. 40b.

The FCC-hh and SppC could achieve sensitivities comparable to electron-positron colliders. However, hadron colliders can be sensitive to θ^2 with heavy neutrino masses well above m_W, despite, them being sensitive to displacements only as small as 1 mm compared to the electron-positron colliders, which could reach down to 10 μm. This can be somewhat expected, since the

parameter space above m_W would correspond to smaller lifetimes, but due to the large Lorentz boosts, the displacements become large enough for the heavy neutrinos to fall inside the detectable region above 1 mm.

The sensitivity to the search for displaced decays of the heavy neutrino at the LHeC and FCC-eh is comparable to the ILC. Altogether, the proposed future colliders demonstrate remarkable improvements in the sensitivity to the active-sterile mixing angles over the current exclusion limits in the mass range of a few GeV up to 100 GeV. The current exclusion limits from DELPHI's direct search for heavy neutrinos constrains active-sterile mixing θ^2 down to 10^{-5} at the 95% C.L. [272] in this mass range, which we discussed in in section 92.

The sensitivity of the LHC and possible future sensitivity for the HL-LHC based on the LHCb, is discussed in section 8.4, since for the current LHCb there is data available from which a sensitivity of the displaced decays of the heavy neutrino can be inferred.

8.4 DISPLACED VERTICES FROM HEAVY NEUTRINOS AT LHCB - PRESENT AND HL-LHC

In this section, estimates for the constraints on heavy neutrinos are derived from a published displaced vertex search of long-lived particles from run 1 data at the LHCb. Based on that analysis, also projected sensitivities to the displaced vertex search for heavy neutrinos are derived for run 2 and the high-luminosity phase of LHCb. This corresponds to work conducted in ref. [4].

The LHCb collaboration analysed data from run 1 for the center-of-mass energies of 7 and 8 TeV for the search of long-lived particles decaying into μjj final states, confer ref. [354]. In their analysis of displaced vertices within the VErtex LOcator (VELO) [143] of the LHCb, they found displaced vertices up to 2 cm in the transverse plane, above 2 cm no events were found. When applying the filter for lepton isolation, displaced vertex events up to 5 mm were found. The analysis concluded that the findings are in agreement with the SM prediction. From the non-observation of displaced vertex events with a transverse displacement larger than 2cm, puts constraints on the heavy neutrino parameters which can be derived.

Displaced μjj decays can stem from semileptonic decays of the heavy neutrinos when they decay via a W boson and an accompanying muon for $|\theta_\mu| \neq 0$. For the expected number of long-lived heavy neutrinos, N_{dv}, that decay within the VELO, the inclusion of the detector geometry is required as well as the inclusion of process kinematics.

For the detector geometry, this means that the spherical symmetry assumption is abandoned and that the cylindrical shape and dimensions of the LHCb's VELO are considered. An example schematic of a displaced vertex from a heavy neutrino within the VELO is shown in fig. 41. The boundaries for the displacements to be detected within x_{min} and x_{max} are then dependent on the polar angle, ϑ [144] . And they can be expressed as

$$x_{max}(\vartheta) = \begin{cases} \frac{z_{max}}{\cos(\vartheta)} & \text{if } 0 \leqslant \vartheta \leqslant \arctan(r_{max}/z_{max}) \\ \frac{r_{max}}{\sin(\vartheta)} & \text{if } \arctan(r_{max}/z_{max}) \leqslant \vartheta < \frac{\pi}{2} \end{cases}$$

[143] The LHCb detector is a forward spectrometer, aimed at measuring particles in the forward region. The first subdetector closest to the beam line is the cylindrical VELO [355]. Its main purpose is to identify B mesons.

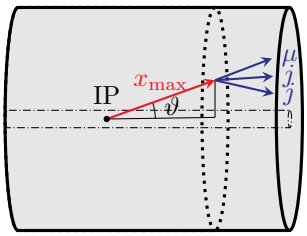

Figure 41: Shown is an example schematic of the displaced vertex decay from a heavy neutrinos to μjj final sate inside LHCB's VELO. Marked is also the direction dependent displacement by the angle ϑ. This figure has been published in ref. [4].

[144] The angle between the propagating heavy neutrino and the beam axis (more specific the positive z axis).

$$x_{min}(\vartheta) = \begin{cases} \frac{r_{min}}{\sin(\vartheta)} & \text{if } \arctan(r_{min}/z_{max}) \leqslant \vartheta < \frac{\pi}{2} \\ \text{n.a.} & \text{otherwise} \end{cases} \tag{8.9}$$

where r_{max} is the maximal radial distance for which vertex displacements can be measured, which can be up to the radius of the cylindrical VELO, z_{max} is taken as the maximal extension from the IP in the z-direction for which displaced vertices can be measured, r_{min} is taken as the minimal displacement required in the transverse plane in order to be background free.

For the process kinematics, the isotropic emission of particles is also abandoned which necessitates the inclusion of the direction dependency of the heavy neutrino momentum $\vec{p}_N$. This implies that the probability distribution function for the Lorentz factor $D_N(\vartheta, \gamma)$ has a polar angle dependency. $D_N(\vartheta, \gamma)$ is the probability distribution function of producing a heavy neutrino with a momentum vector under the angle ϑ and Lorentz factor γ, rather than $D_N(\gamma)$.

The former expression for the expected number of displaced vertex events of the heavy neutrinos between the boundaries x_{min} and x_{max}, eq. (8.8), becomes

$$N_{dv} = \sum_{x=\nu,\ell^\pm} \sigma_{xN}(M, |\theta_\alpha|^2, \sqrt{s})\ \mathrm{BR}(N \to \mu jj)\, \mathcal{L} \times \int D_{xN}(\vartheta, \gamma)\, P_{dv}(x_{min}(\vartheta), x_{max}(\vartheta), \Delta x_{lab}(\tau, \gamma))\, d\vartheta d\gamma\,. \tag{8.10}$$

Here, the branching ratio into semileptonic μjj final states can be approximated as $0.5 \times |\theta_\mu|^2/\theta^2$ for M below the W boson mass [145], $\sigma_{\nu N}$ ($D_{\nu N}$) and $\sigma_{\ell^\pm N}$ ($D_{\ell^\pm N}$) are the production cross section (probability distribution function for the Lorentz factor γ) from the Drell-Yan process $pp \to Z \to \nu N$ and $pp \to W \to \ell^\pm N$, respectively. The prompt charge leptons that arise in the $pp \to W \to \ell^\pm N$ process and have no consequence, they could be used to trigger on the event, but LHCb's analysis has not put any veto on prompt charged leptons.

[145] The branching ratios into ejj and τjj final states would be dependent on $|\theta_e|$ and $|\theta_\tau|$, respectively, which could thus be tested in an analysis.

$\sqrt{s}$	7 TeV	8 TeV
$\frac{\sigma_{\nu N}}{\theta^2}\,\mathrm{BR}(N \to \mu jj)$	114	142
$\frac{\sigma_{\ell^- N}}{\theta^2}\,\mathrm{BR}(N \to \mu jj)$	175	233
$\frac{\sigma_{\ell^+ N}}{\theta^2}\,\mathrm{BR}(N \to \mu jj)$	311	400

Table 9: The base signal cross sections divided by θ^2 in units of pb for the benchmark mass $M = 5$ GeV are given for the fiducial volume covered by LHCb detector. The cross sections correspond to the Drell-Yan production processes of the heavy neutrino that are obtained from Monte Carlo generated event samples from WHIZARD 2.4 with the criteria specified in the text, e.g., CTEQ6L as the PDF of the proton, applying cuts on the signal, using a $\mathrm{BR}(N \to \mu jj) = 0.5$, and assuming $\theta^2 = |\theta_\mu|^2$.

8.4.1 *LHCb (run 1) exclusion limits on the sterile neutrino parameters*

LHCb's search in ref. [354] for long-lived particles decaying into μjj final states via displaced vertices was performed on run 1 data for $\sqrt{s} = 7$ TeV and 8 TeV with integrated luminosities of 1 and 2 fb^{-1}, respectively.

Our aim is to derive estimated constraints on the sterile neutrino parameters that could be achieved in a dedicated analysis for displaced vertices from heavy neutrinos by the LHCb collaboration. For the calculation of the expected number of displaced heavy neutrino decays, samples of 10^4 Monte Carlo generated events were simulated for the processes $pp \to nN \to n\mu jj$, $pp \to \ell^\pm N \to \ell^\pm \mu^\mp jj$ by WHIZARD 2.4 with the PDF of the proton CTEQ6L for various benchmark points of the heavy neutrino mass. For the simulation we assumed only $\theta_\mu \neq 0$, i.e., $\theta^2 = |\theta_\mu|^2$, we restricted the events to a value $\vartheta[\mu jj] < 0.34$ due to the geometric acceptance of the LHCb detector, and applied a number of cuts, which are taken into account by LHCb's analysis [354], on the generated event samples:

- $N(\mu) = 1$ and $N(j) > 0$
- $2 < \eta(f) < 5$, $f = \mu, j$
- $P_t(\mu) > 12$ GeV
- $M[\mu jj] > 4.5$ GeV

We note that for the last cut, $M[\mu jj] > 4.5$ GeV would select masses of the heavy neutrino above 4.5 GeV since the invariant mass of the displaced decays corresponds to the mass of the heavy neutrino. For the estimates, we choose heavy neutrino benchmark masses above $M = 4.5$ GeV for the simulation of the event samples without simulating the ensuing reconstruction of the invariant mass. We also assume that after LHCb's track reconstruction the events after cuts have at least 4 tracks in the forward direction.

The resulting cross sections for the benchmark mass $M = 5$ GeV that are covered by the fiducial volume by the LHCb detector with the above fulfilled criteria are given as an example in tab. 9 for the center-of-mass energies 7 and 8 TeV. We note that the cross section does not vary much in the range of $M \sim 10$ GeV as can be seen in fig. 20.

From the generated event samples, example probability distribution functions $D_{xN}(\vartheta, \gamma)$ for the three considered Drell-Yan processes are constructed for the integral part of eq. (8.10). Example distributions $D_{\nu N}$ and $D_{\ell^+ N}$ are shown for $\sqrt{s} = 8$ TeV in fig. 42. We note that for higher masses of the heavy neutrino the right end of the distribution shrinks, which corresponding to the highest Lorentz boosts.

We consider two detection regions of the displaced decays of the heavy neutrino. A conservative and a more enlarged region which could be tested at the expense of signal reconstruction efficiency in a dedicated analysis:

- Region 1: Displaced heavy neutrino decays are restricted to be within the VELO. The maximal radial and longitudinal distance of $r_{max} = 50$ cm, $z_{max} = 40$ cm are considered. For the minimal transverse displacement $r_{min} = 2$ cm is chosen which corresponds to the maximal transverse distance displacements were found in LHCb's analysis without lepton isolation. A signal reconstruction efficiency of 100% is assumed in this region.
- Region 2: Displaced heavy neutrino decays are restricted to be within the outer boundaries $r_{max} = 60$ cm and $z_{max} = 2$ m, which is the radial extension and distance to the TT tracking station of LHCb's silicon tracker. For the minimal transverse displacement $r_{min} = 5$ mm are considered but at a cost of signal reconstruction efficiency. For the region corresponding to region 1, still an efficiency of 100% is assumed. But, for longitudinal displacements further than 40 cm and for transverse displacements below 2 cm an efficiency of 50% is assumed.

The constraints on the sterile neutrino parameters via the displaced vertex search at LHCb are derived from the condition

$$N_{dv}(\sqrt{s} = 7 \text{ TeV}, M, \theta^2) + N_{dv}(\sqrt{s} = 8 \text{ TeV}, M, \theta^2) > 3.09\,, \tag{8.11}$$

for the two regions. Above the expected number of events of 3.09, at least one event is yielded, which is incompatible with LHCb's observation, confer the

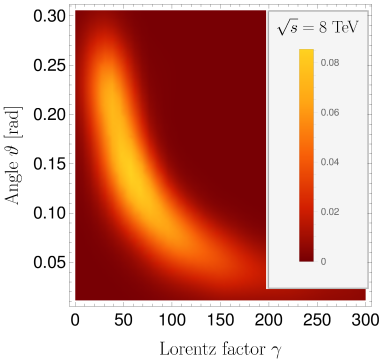

(a) Example probability distribution function $D_{\nu N}$ for the benchmark mass $M = 5$ GeV.

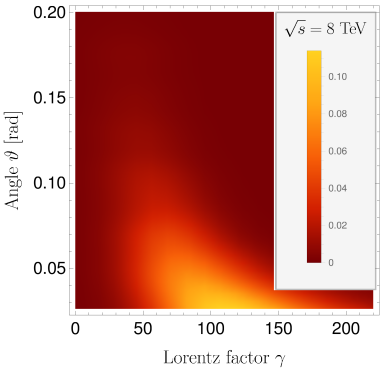

(b) Example probability distribution function $D_{\ell^+ N}$ for the benchmark mass $M = 5$ GeV. The probability distribution function for $D_{\ell^- N}$ looks very similarly.

Figure 42: Example probability distribution functions for a heavy neutrino produced via Drell-Yan and propagating with the angle ϑ and Lorentz boost γ for $\sqrt{s} = 8$ TeV.

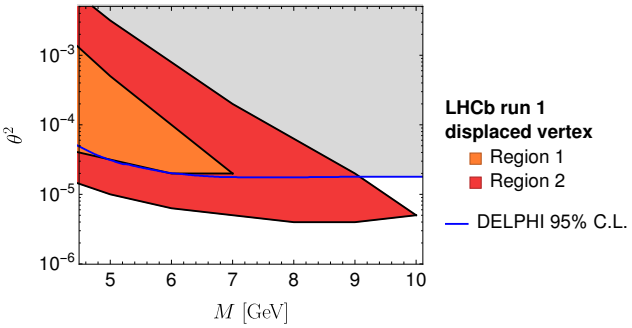

Figure 44: Shown are the estimated exclusion limits from displaced vertices to $\theta^2 = |\theta_\mu|^2$ at 95% C.L. for the two considered regions based on LHCb's analysis of run 1 data. The exclusion limits at the 95% C.L. from DELPHI [272] are shown for comparison. For further details see text.

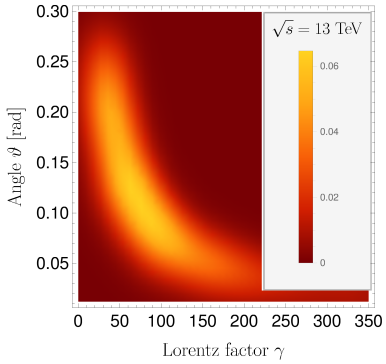

(a) Example probability distribution function $D_{\nu N}$ for the benchmark mass $M = 5$ GeV.

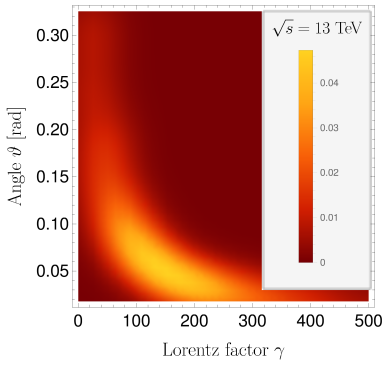

(b) Example probability distribution function $D_{\ell^+ N}$ for the benchmark mass $M = 5$ GeV. The probability distribution function for $D_{\ell^- N}$ looks very similarly.

Figure 43: Example probability distribution functions for a heavy neutrino produced via Drell-Yan and propagating with the angle ϑ and Lorentz boost γ for $\sqrt{s} = 13$ TeV.

appendix A.1.2. The upper limit on the active-sterile mixing $\theta^2 = |\theta_\mu|^2$ is derived, which excludes the observation of one or more events at the 95% C.L. The resulting estimated exclusion limits on θ^2 at the 95% C.L. for a dedicated displaced vertex search for sterile neutrinos in the μjj final state with run 1 data of LHCb are shown in fig. 44. We note that for different active-sterile mixing angle combinations with non-zero $|\theta_e|$ and $|\theta_\tau|$ the expected number of events N_{dv} is rescaled by the branching ratio $BR(N \to \mu jj) \approx 0.5 \times |\theta_\mu|^2/\theta^2$ for fixed θ^2. Therein, the estimated constraints on the sterile neutrino parameters for the two considered regions show that LHCb could constrain heavy neutrino masses up to 10 GeV with run 1 data. Furthermore, for region 2 it would already provide the strongest exclusion limits on $\theta^2 \sim 3 \times 10^{-6}$ at the 95% C.L. in the $5 \lesssim M \lesssim 10$ GeV range with run 1 data alone.

8.4.2 *LHCb (run 2 and HL-LHC) future sensitivities on the sterile neutrino parameters*

We discuss projected sensitivities of LHCb that could be obtained from a displaced vertex search with run 2 data at $\sqrt{s} = 13$ TeV with $\mathcal{L} = 5$ fb^{-1} as well as future sensitivities during the HL-LHC with an assumed $\mathcal{L} = 380$ fb^{-1}. The same assumptions for the derivation of the exclusion limits for run 1 are adopted here, with the exception of the invariant mass cut, $M[\mu jj] > 4.5$ GeV, which is relaxed in the following for comparison purposes. The assumptions comprise, in particular, that the discussed detection regions remain free of background with the same signal reconstruction efficiencies for the applied cuts. Although, a new background analysis is necessary at $\sqrt{s} = 13$ TeV.

The cross sections for the benchmark mass $M = 5$ GeV, with the previously stated assumptions are given in tab. 10 for $\sqrt{s} = 13$ TeV. From the generated event samples at 13 TeV, also example probability distribution functions $D_{xN}(\vartheta, \gamma)$ are constructed for the calculation of the sensitivities. The resulting example distributions $D_{\nu N}$ and $D_{\ell^+ N}$ are shown in fig. 43. The sensitivity to $\theta^2 = |\theta_\mu|^2$ at 95% C.L. is derived from the condition $N_{dv}(\sqrt{s} = 13 \text{ TeV}, M, \theta^2) > 3.09$ for run 2 and the high-luminosity phase of

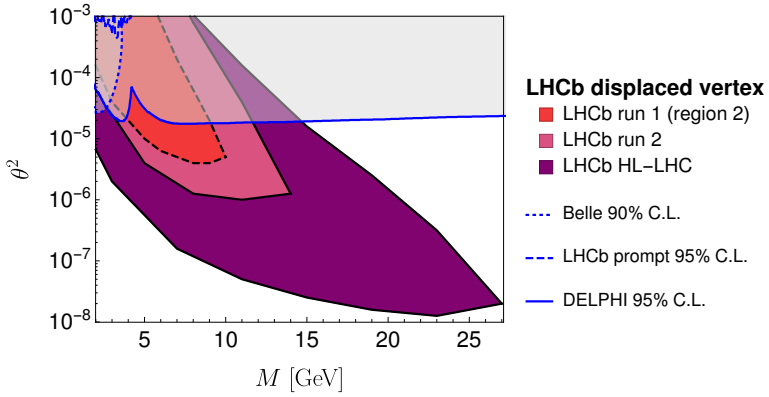

Figure 45: Shown are the estimated sensitivities of $\theta^2 = |\theta_\mu|^2$ at the 95% C.L. for the displaced vertex search of region 2 for the run 2 and high-luminosity phase of the LHC at LHCb. For the calculation of the sensitivities the integrated luminosities of 5 fb^{-1} and 380 fb^{-1} are assumed. Existing limits are shown by the blue lines as comparison, see text for details. Although, the run 1 search would reject the signal for $M < 4.5$ GeV, we show the region below that cut as comparison when the invariant mass cut could be relaxed.

LHCb. The derived sensitivities at 95% C.L. for region 2 are shown in fig. 45. Existing limits are also shown as a comparison [146], such as DELPHI's exclusion limits at the 95% C.L. [272], which corresponds to the direct search in section 92, Belle's exclusion limit at the 90% C.L. [356], which stems from B-meson decays, and LHCb's exclusion limit from B-meson decays at the 95% C.L. [357](with the revised limits derived in ref. [358]). Fig 45 shows that the estimated displaced vertex search at LHCb has the potential to probe sterile neutrino parameters well outside the current exclusion limits. During the HL phase, LHCb could probe active-sterile mixings θ^2 as small as 10^{-8}. These values are comparable to the sensitivity of the ILC for its Z pole run but only up to masses of ~ 25 GeV, see fig. 38. Also on the low end range of the heavy neutrino mass between 2 and 4.5 GeV LCHb could probe active-sterile mixing angles smaller than explored by Belle and DELPHI if the invariant mass cut can be be relaxed.

$\sqrt{s}$	13 TeV
$\frac{\sigma_{\nu N}}{\theta^2}$ BR($N \to \mu jj$)	316
$\frac{\sigma_{\ell^- N}}{\theta^2}$ BR($N \to \mu jj$)	653
$\frac{\sigma_{\ell^+ N}}{\theta^2}$ BR($N \to \mu jj$)	460

Table 10: The base signal cross sections divided by θ^2 in units of pb for the benchmark mass $M = 5$ GeV are given for the fiducial volume covered by LHCb detector. For details see, for instance, the caption of tab. 9

[146] In ref. [4] it was pointed out that "the other analyses consider a simplified model with only one sterile neutrino, which strictly speaking yields a too large mass of the light neutrino. We can nevertheless compare our constraint derived in the SPSS model with these bounds, since for the considered processes the heavy neutrino production cross section and the kinematics are identical."

9 LEPTON NUMBER VIOLATION AT COLLIDERS

In the SM, lepton number conservation (LNC) is an accidental global symmetry of the Lagrangian, i.e. one cannot write a gauge invariant and renormalisable term that breaks the total lepton number in the Lagrangian. In fact, lepton number is not only conserved at tree-level but to any order in perturbation theory [359]. However, non-perturbative effects give rise to lepton-number violating processes in the SM [360] such as sphaleron and instanton processes. These processes might have played a significant role in the early universe towards explaining the baryon asymmetry of the universe [361–363]. We regard such non-perturbative effects as negligible at colliders and view the SM as lepton-number conserving for our purposes.

The symmetry protected seesaw scenario in the limit of exact symmetry features no lepton number violation (LNV). Once, the small perturbations are introduced to generate the light neutrino masses, lepton number violating effects are possible. As is mentioned in section 4.2.3 and discussed in e.g. ref. [187], lepton-number violating effects are proportional to the perturbations which are required to be small due to the light neutrino masses. This also means that LNV goes to zero in the limit that the perturbations vanish. In this chapter, we therefore investigate the occurrence and relevance of LNV at colliders, that has been partly published in ref. [3, 5].

In section 9.1, we discuss the occurring lepton-number violating signatures from the heavy neutrinos at electron-positron, hadron and electron-proton colliders. We study the effects of LNV from the pseudo-Dirac nature of the heavy neutrinos and derive the ratios between lepton-number violating and conserving decays of the heavy neutrino in section 9.2. In order to quantify the amount of LNV, the heavy neutrino mass splitting is required, which is calculated for the case of the linear seesaw and inverse seesaw in section 9.3. In section 9.4, the amount of LNV is assessed and the relevance of LNV for the sterile neutrino parameters is discussed.

9.1 LEPTON-NUMBER VIOLATING SIGNATURES AT COLLIDERS

To start with, we discuss the lepton-number violating signatures which arise by the lepton number violation caused by the heavy neutrinos [147] at colliders as partly published in ref. [3].

In general, processes with no light neutrinos in the final states, i.e. when charged leptons and possibly some hadronic jets are present, feature an unambiguous signal for LNV when the charged leptons violate lepton number. On the contrary, when light neutrinos are present in the final states, they escape detection and their lepton number is not revealed, which makes the study of such signatures more difficult. In order for the two charged leptons to violate lepton number, they have to interact with the heavy neutrinos. Therefore, only processes that interact via the charged weak current can give rise to measurable lepton number violation at colliders.

[147] In ref. [3] it is remarked that "[...] the small Majorana masses of the light neutrinos [...] violate lepton number. However for collider phenomenology this is subdominant compared to the lepton number violation from the perturbed heavy neutrino sector, and can safely be neglected. In this sense one can attribute a lepton number to the light neutrinos produced in a given process."

At e^+e^- colliders, diagram 18a can feature a lepton-number violating process when the incoming electron becomes a charged antilepton after the interaction with the heavy neutrino and vice versa for the incoming positron. But since the heavy neutrino is always accompanied by a light neutrino, it cannot be immediately determined if the charged lepton came from the electron or positron current, thus LNV is well hidden. However, there is the possibility to have lepton-number violating final states without light neutrinos in the final states namely via higher order processes. For instance the process, $e^+e^- \to N\ell^\pm W^\mp \to (\ell^\pm W^\mp)\ell^\pm W^\mp \to \ell^\pm(jj)\ell^\pm(jj)$ features an unambiguous signal for LNV at e^+e^- colliders [226].

At hadron colliders, diagram 21a features lepton-number violating processes. The resulting dilepton-dijet final state $\ell^\pm\ell^\pm jj$ features an unambiguous signal for LNV in the form of same-sign dileptons. It violates lepton number by two units. This is a highly looked for process at ATLAS and CMS [329, 330, 364] since it is often referred to as the smoking gun signature for heavy Majorana neutrinos. It is also widely studied by the particle physics community for the LHC, see, for instance, ref. [228, 264, 365–372] and somewhat for the FCC-hh ref. [309]. On the other hand, the resulting trilepton final state $\ell^\pm\ell^\pm\ell^\mp\nu$ may proceed via both lepton-number violating as well as lepton-number conserving processes. Hence, the trilepton final state does not feature an unambiguous signal for LNV. This final state has been studied for the LHC in the context of sterile neutrinos in ref. [264, 368, 369, 371, 373, 374]. CMS has rather recently also conducted a search for heavy neutrinos in the trilepton final state [375]. In ref. [229, 376], it was studied how the lepton-number violating and conserving channels may separated in order to study LNV.

At e^-p colliders, visible LNV is produced by diagram 24a. LNV manifests itself, similarly to e^+e^- collisions, when the incoming charged electron becomes a charged antilepton after the interaction with the heavy neutrino. But contrary to e^+e^- colliders, here it is clear that the charged antilepton came from the incoming electron current. Therefore, the resulting lepton-trijet final state ℓ^+jjj features an unambiguous signal for LNV. It also violates lepton number by two units. This final state has been studied for the LHeC, see, e.g. ref. [377–382]. The jet-dilepton final state, $j\ell^\pm\ell^\mp\nu$, can be produced by either LNV or LNC processes. Thus, the jet-dilepton final state does not provide an unambiguous signal for LNV but if the origin of the charged lepton can be inferred, then it is possible to measure LNV.

9.2 LEPTON NUMBER VIOLATION FROM HEAVY NEUTRINOS

Although, there are possible processes for unambiguous signals of LNV at hadron and electron-proton colliders, the amount of LNV has to be quantified.

For a qualitative argument, let us consider the schematic in fig. 46 for a pair of heavy Majorana neutrinos with a mass splitting ΔM [148]. When the mass splitting is zero, the heavy neutrinos form a Dirac pair (as described in section 4.2.2) and due to their couplings to the SM particles the amplitudes for LNV processes do interfere destructively, resulting in only non-vanishing am-

[148] As discussed in section 4.2.3, the introduced small perturbations to generate the light neutrino masses can also generate contributions to the heavy neutrino mass matrix. This results in non-degenerate masses for the heavy neutrinos, and hence a mass splitting as the mass difference.

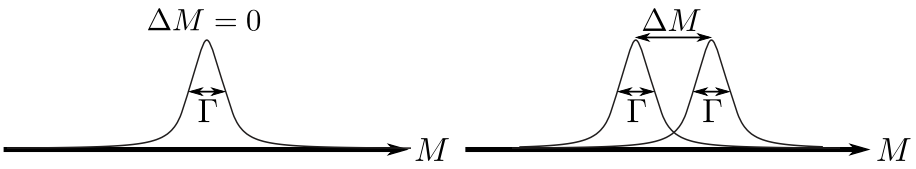

Figure 46: Schematic of two propagating and interfering mass eigenstates of the heavy neutrinos with mass splitting ΔM and total width Γ. For $\Delta M = 0$, the amplitudes for LNV processes do interfere destructively, resulting in only non-vanishing amplitudes for LNC processes. When the mass splitting becomes considerable compared to their total decay width Γ, the LNV effects do not cancel exactly.

plitudes for LNC processes. For non-zero ΔM, the heavy neutrinos are said to form a pseudo-Dirac particle which refers to a pair of heavy Majorana neutrinos that are separated by a mass splitting ΔM. Qualitatively speaking, when the mass splitting induced by the perturbations becomes of the same order as their total decay width Γ, the mass eigenstates do not interfere destructively. In other words, the contributions from the heavy neutrinos to LNV processes do not exactly cancel any more, therefore, leading to non-vanishing LNV. When the mass splitting is much larger than the total decay width, the cancellation is negligible and the effects from LNV can be of the same size as the ones from LNC. Altogether, the amount of LNV is directly controlled by the ratio of the mass splitting ΔM and the total decay width Γ.

This qualitative picture has to be substantiated by studying the effects of LNV due to the pseudo-Dirac nature of the heavy neutrinos that stems from the phenomenon referred to as heavy neutrino-antineutrino oscillations. This phenomenon is in analogy to the well studied heavy neutral particle-antiparticle oscillations responsible for, e.g., $K^0 - \overline{K}^0$ and $B^0 - \overline{B}^0$ oscillations, cf. ref. [383] and references therein. LNV violation from the pseudo-Dirac nature of the heavy neutrinos is studied, for instance, in the context of the SPSS in ref. [5] and left-right symmetric extensions of the SM in ref. [384–386], respectively.

As we established above, the heavy neutrinos have to interact by the charged weak interactions in order for the lepton-number violating effects to be visible at colliders. From the weak charged current interaction [149], we refer to the combination of heavy neutrino mass eigenstates that interacts with a $\overline{\ell}$ or ℓ as the heavy neutrino state N_ℓ or heavy antineutrino state $N_{\overline{\ell}}$, respectively. These states are defined as [385]

$$N_\ell = \frac{1}{\sqrt{2}}(N_2 - iN_1)\,, \qquad N_{\overline{\ell}} = \frac{1}{\sqrt{2}}(N_2 + iN_1)\,. \tag{9.1}$$

The time evolved mass eigenstates, which are the solution to the Schrödinger equation [150] can be written as [383]

$$N_i(t) = N_i \exp(-iM_i t - \Gamma_i/2\, t) \tag{9.2}$$

with $M_{1,2}$ being the eigenvalues of the mass matrix, and $\Gamma_{1,2}$ being the total decay widths to the corresponding mass eigenstates. The time evolution of an initially pure N_ℓ can be calculated [151] as

[149] Confer eq. (4.40): $\frac{g}{\sqrt{2}}\,\theta_\alpha\,\overline{\ell}_\alpha\,\gamma_\mu P_L\,\frac{1}{\sqrt{2}}\,(-iN_1 + N_2) + \text{H.c.}$

[150] With the Hamiltonian $H = M - \frac{i}{2}\Gamma$.

[151] And by using the re-expressed mass eigenstates $N_1 = \frac{i}{\sqrt{2}}(N_\ell - N_{\overline{\ell}})$ and $N_2 = \frac{1}{\sqrt{2}}(N_\ell + N_{\overline{\ell}})$.

$$
\begin{aligned}
N_\ell(t) &= \frac{1}{\sqrt{2}}(N_2(t) - iN_1(t)) \\
&= \frac{1}{2}\left[N_\ell\left(\exp(-iM_2 t - \Gamma_2/2\,t) + \exp(-iM_1 t - \Gamma_1/2\,t)\right)\right. \\
&\left. + N_{\overline{\ell}}\left(\exp(-iM_2 t - \Gamma_2/2\,t) - \exp(-iM_1 t - \Gamma_1/2\,t)\right)\right] . \qquad (9.3)
\end{aligned}
$$

By re-expressing the mass eigenvalues in terms of the average mass and the mass splitting of the two states as

$$
\overline{M} = \frac{1}{2}(M_1 + M_2)\,, \qquad \Delta M = M_2 - M_1\,, \qquad (9.4)
$$

or, equivalently, as

$$
M_1 = \overline{M} - \tfrac{1}{2}\Delta M\,, \qquad M_2 = \overline{M} + \tfrac{1}{2}\Delta M\,, \qquad (9.5)
$$

[152] The difference for the total decay width $\Delta\Gamma = \Gamma_1 - \Gamma_2$ is expected to be much smaller than ΔM. Therefore, $\Delta\Gamma$ can be neglected and the total decay widths can be approximated as $\Gamma_1 \simeq \Gamma \simeq \Gamma_2$.

the time evolution of the state N_ℓ is then given by [152]

$$
\begin{aligned}
N_\ell(t) &= \frac{1}{2}\left[N_\ell\, e^{-i\overline{M}t - \Gamma/2\,t}\left(e^{-i\frac{\Delta M}{2}t} + e^{+i\frac{\Delta M}{2}t}\right)\right. \\
&\left. + N_{\overline{\ell}}\, e^{-i\overline{M}t - \Gamma/2\,t}\left(e^{-i\frac{\Delta M}{2}t} - e^{+i\frac{\Delta M}{2}t}\right)\right] \\
&= N_\ell\, e^{-i\overline{M}t - \Gamma/2\,t}\cos\left(\tfrac{\Delta M}{2}t\right) - iN_{\overline{\ell}}\, e^{-i\overline{M}t - \Gamma/2\,t}\sin\left(\tfrac{\Delta M}{2}t\right) . \qquad (9.6)
\end{aligned}
$$

Therefore, both states evolve as [383, 385]

$$
\begin{aligned}
N_\ell(t) &= g_+(t)N_\ell + g_-(t)N_{\overline{\ell}}\,, \\
N_{\overline{\ell}}(t) &= g_-(t)N_\ell + g_+(t)N_{\overline{\ell}}\,, \qquad (9.7)
\end{aligned}
$$

with the oscillating amplitudes

$$
\begin{aligned}
g_+(t) &= e^{-i\overline{M}t - \Gamma/2\,t}\cos\left(\tfrac{\Delta M}{2}t\right)\,, \\
g_-(t) &= -ie^{-i\overline{M}t - \Gamma/2\,t}\sin\left(\tfrac{\Delta M}{2}t\right)\,. \qquad (9.8)
\end{aligned}
$$

The modulus squared amplitude, $|g_-(t)|^2$, gives the time-dependent transition probability for a heavy neutrino state N_ℓ to oscillate into an antineutrino state $N_{\overline{\ell}}$ and vice versa. This corresponds to the probability for a lepton-number violating transition of the heavy neutrino. While $|g_+(t)|^2$ gives the survival probability of the neutrino state N_ℓ and antineutrino sate $N_{\overline{\ell}}$, which corresponds to the probability for lepton-number conserving transitions of the heavy neutrino. We note that the oscillation frequency of the probabilities are only dependent on the heavy neutrino mass splitting. The evolution for the amplitude and probability of $g_+(t)$ and $g_-(t)$ are shown for an example point in fig. 47. The example point shows that for $\Delta M = \Gamma$ a significant probability for lepton-number violating decays is possible.

The ratio between LNV and LNC decays of the heavy neutrino, referred to as $R_{\ell\ell}$, which manifests itself in the ratio of same-sign dileptons versus opposite-sign dileptons, is calculated from the integrated probabilities [385]

$$
R_{\ell\ell} = \frac{\#(\ell^+\ell^+) + \#(\ell^-\ell^-)}{\#(\ell^+\ell^-)} = \frac{\int_0^\infty |g_-(t)|^2\,dt}{\int_0^\infty |g_+(t)|^2\,dt} = \frac{(\Delta M)^2}{2\Gamma^2 + (\Delta M)^2}\,. \qquad (9.9)
$$

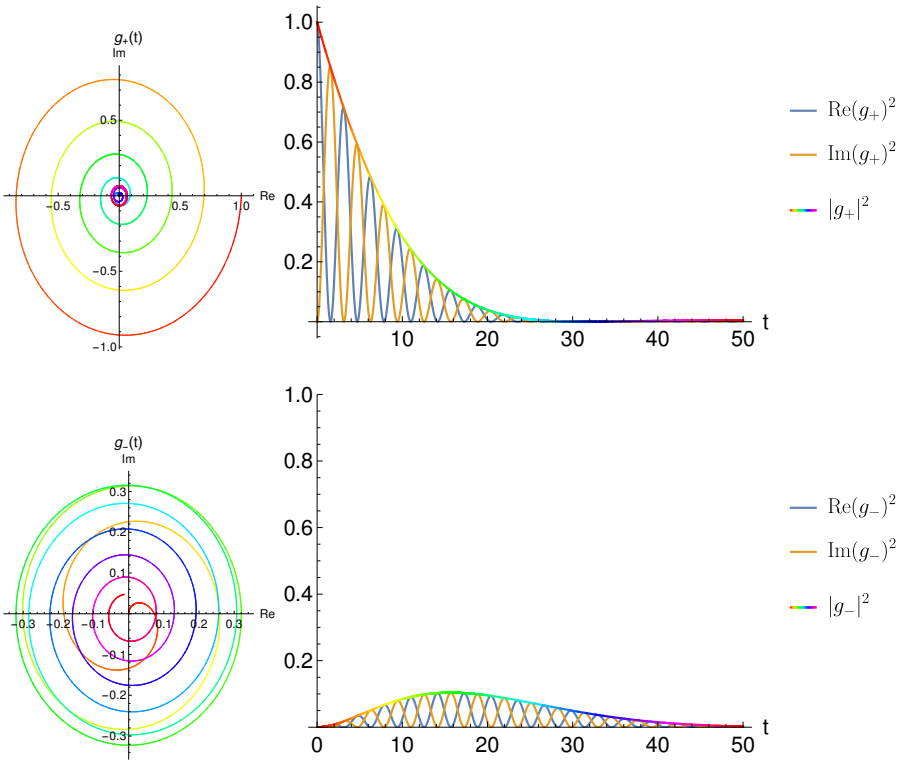

Figure 47: The figure shows the time evolution of the amplitude in the complex plane as well as the corresponding time-dependent probability of g_+ (top) and g_- (bottom) for the example point $\overline{M} = 1, \Delta M = 0.1, \Gamma = 0.1$. The hue of the color for g_+ and g_- changes as the time increases.

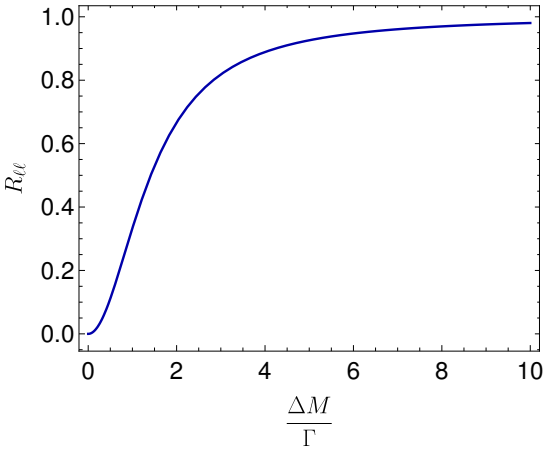

Figure 48: $R_{\ell\ell} = \frac{\#(\ell^+\ell^+)+\#(\ell^-\ell^-)}{\#(\ell^+\ell^-)}$ which is the ratio between LNV and LNC decays of the heavy neutrino is plotted versus the ratio of the heavy neutrino mass splitting ΔM and the total decay width Γ.

The ratio $R_{\ell\ell}$ is plotted versus the ratio $\frac{\Delta M}{\Gamma}$ in fig. 48. Therein, we clearly see, that the qualitative arguments are validated: For a vanishing mass splitting ΔM, LNV vanishes and the decays of the heavy neutrino proceed lepton-number conserving due to the Dirac nature. For ΔM and Γ of the same order, a sizeable fraction of the decays of the heavy neutrino are LNV, which can be as large as the fraction of lepton-number conserving decays.

We comment on the fact that the considered pair of heavy Majorana neutrinos feature a relative CP-sign, corresponding to a CP phase of $\pi/2$, which naturally appears in the considered SPSS with linear and inverse seesaw cases. For this configuration, there can be destructive interference between the mass eigenstates which cancels the lepton-number violating contributions. For other CP phases, lepton-number violating effects would not interfere completely destructively which would result in a non-zero lower bound for $R_{\ell\ell}$, cf. ref. [386]. Furthermore, we note that in heavy neutrino oscillations the effects of CP phases could be observed at future experiments [387].

9.3 PREDICTIONS ON THE HEAVY NEUTRINO MASS SPLITTING

In order to assess the expected amount of LNV in relation to the heavy neutrino parameters, we investigate the heavy neutrino sector further to have estimates on the mass splitting ΔM of the heavy neutrinos in the inverse and linear seesaw cases.

In order to have an expectation for the result, let us, for an instance, pretend that the full neutrino mass matrix, $\mathcal{M}'$, is not complex symmetric but real symmetric, i.e., all the phases are set to zero. In this case, $\mathcal{M}'$ is diagonalised by orthogonal rather than unitary transformations, which results in the $\mathrm{Tr}(\mathcal{M}')$ being invariant [153]. The diagonalisation of the real symmetric matrix would result in $\mathcal{M} = \mathrm{diag}(0, -m_2, m_3, -M_1, M_2)$ for the linear seesaw case. This means that the trace relates the difference in the heavy neutrino masses to differences in the light neutrino masses. However, $\mathcal{M}'$ is complex symmetric,

[153] $\mathrm{Tr}(\mathcal{M}') = \mathrm{Tr}(O^\top \mathcal{M}' O)$ for orthogonal transformations O.

therefore there are phases involved and the above relation is tainted. Nonetheless, something similar is expected for the heavy neutrino mass splitting, and it can be investigated for the linear and inverse seesaw case.

Linear seesaw

For the mass splitting of the heavy neutrinos in the linear seesaw case, we return to the diagonalisation of the full mass matrix in section 2.2. For the 2×2 sub-block of the heavy neutrino mass matrix in eq. (2.41), the higher order corrections to M_R have been omitted up to this point. But they are delivered subsequently: After block-diagonalisation with the matrix U_{BD} from eq. (2.40), one obtains for the 2×2 sub-block of the heavy neutrino

$$\begin{aligned} M_{N,BD} =& M_R + \tfrac{1}{2}\Theta^T m_D^T + \tfrac{1}{2} m_D \Theta \\ =& M_R + \tfrac{1}{2} M_R^{*-1} m_D^* m_D^T + \tfrac{1}{2} m_D m_D^\dagger M_R^{\dagger -1} \,. \end{aligned} \tag{9.10}$$

As was discussed for the linear seesaw in section 4.2.3, one has in addition to the ordinary Yukawa vector $\vec{y}$ also the vector $\vec{y}'$ as small perturbations of the Dirac mass matrix m_D

$$m_D = \frac{v_{EW}}{\sqrt{2}} \begin{pmatrix} \vec{y}^T \\ \vec{y}'^T \end{pmatrix} . \tag{9.11}$$

For the calculation of the sub-block of the heavy neutrino after block-diagonalisation, we choose a basis where the matrix

$$M_R = \begin{pmatrix} 0 & M \\ M & 0 \end{pmatrix} . \tag{9.12}$$

is real and where both Yukawa vectors $\vec{y}$ and $\vec{y}'$ are complex. After a short calculation [154] the sub-block of the heavy neutrino results in

$$M_{N,BD} = \begin{pmatrix} \vec{y}'^\dagger \vec{y} \frac{v_{EW}^2}{2M} & M + \frac{1}{2}\left(|\vec{y}|^2 + |\vec{y}'|^2\right) \frac{v_{EW}^2}{2M} \\ M + \frac{1}{2}\left(|\vec{y}|^2 + |\vec{y}'|^2\right) \frac{v_{EW}^2}{2M} & \vec{y}^\dagger \vec{y}' \frac{v_{EW}^2}{2M} \end{pmatrix} . \tag{9.13}$$

[154] Where we used $\vec{y}^T \vec{y}'^* = (\vec{y}^T \vec{y}'^*)^T = \vec{y}'^\dagger \vec{y}$ for the diagonal elements, and $\vec{y}^T \vec{y}^* = \vec{y}^\dagger \vec{y} = |\vec{y}|^2$ for the off-diagonal elements.

By writing the complex neutrino Yukawa vectors as

$$\vec{y} = y \vec{u} \,, \qquad \vec{y}' = y' \vec{v} \,, \tag{9.14}$$

with the complex vector of unit length $\vec{u}$ and $\vec{v}$, the product of both Yukawa vectors can be written as [204] $\vec{y}'^\dagger \vec{y} = y y' \vec{u}^\dagger \vec{v} = y y' \rho e^{i\theta}$, where ρ corresponds to the previously considered parameter in eq. (4.20) and where θ represents a phase. As explained in ref. [204], this product can be chosen to be real, since the phase θ is unphysical because it can be absorbed by a phase redefinition of the fields N_R^1 and N_R^2 [155] by $e^{i\theta/2}$ and $e^{-i\theta/2}$, respectively. This rephasing of the fields leaves M also real, since the mass term $\overline{N_R^1} M N_R^{2\,c}$ is invariant under the rephasing [156]. The products of the Yukawa vectors result in

$$|\vec{y}|^2 = y^2 , \qquad |\vec{y}'|^2 = y'^2 , \qquad \vec{y}'^\dagger \vec{y} = y y' \rho \,, \tag{9.15}$$

[155] Since the fields N_R^1 and N_R^2 are connected to the Yukawa couplings by the Yukawa terms $-y_{\nu_\alpha} \overline{N_R^1} \tilde{\phi}^\dagger L^\alpha - y'_{\nu_\alpha} \overline{N_R^2} \tilde{\phi}^\dagger L^\alpha$.

[156] Under the rephasing of the fields, the mass term of the sterile neutrinos transforms as $\overline{N_R^1} M N_R^{2\,c} \to \overline{N_R^1} M N_R^{2\,c} e^{-i\theta/2 + i\theta/2}$

which can also be checked by plugging in the Yukawa vectors derived in eq. (4.21) and (4.22).

Since the product $\vec{y}'^{\dagger}\vec{y}$ is real, the block-matrix $M_{N,BD}$ ineq. (9.13) is real and can be diagonalised by a $\pi/4$ rotation, $R^{T}_{\pi/4} M_{N,BD} R_{\pi/4}$, from which the real positive mass eigenstates are obtained[157]

$$\underbrace{M + \frac{1}{2}\left(|\vec{y}|^2 + |\vec{y}'|^2\right)\frac{v_{EW}^2}{2M}}_{\overline{M}} \pm \underbrace{\vec{y}'^{\dagger}\vec{y}\frac{v_{EW}^2}{2M}}_{\frac{1}{2}\Delta M} . \tag{9.16}$$

Expressed as the average mass $\overline{M}$ and the mass splitting ΔM of the heavy neutrino, one obtains the expressions

$$\overline{M} = M + \frac{1}{2}\left(y^2 + y'^2\right)\frac{v_{EW}^2}{2M} , \tag{9.17}$$

$$\Delta M^{\text{lin}} = 2yy'\rho\frac{v_{EW}^2}{2M} , \tag{9.18}$$

in the linear seesaw case.

In this case, the heavy neutrino mass splitting depends on the light neutrino parameters and it can be inferred from the neutrino oscillation data. Specifically it can be inferred from eq. (4.21) and (4.22) for the normal ordering (NO) and inverse ordering (IO) of light neutrino masses. The mass squared differences can be written as

$$\text{NO:} \qquad \Delta m^2_{21} = \left(\frac{yy'v_{EW}^2}{2M}\right)^2 (1-\rho_{NO})^2 , \tag{9.19}$$

$$\text{IO:} \qquad \Delta m^2_{23} = \left(\frac{yy'v_{EW}^2}{2M}\right)^2 (1+\rho_{IO})^2 , \tag{9.20}$$

which yields [158] the mass splitting of the heavy neutrino

$$\Delta M^{\text{lin}}_{NO} = \frac{2\rho_{NO}\sqrt{\Delta m^2_{21}}}{1-\rho_{NO}} = |m_3| - |m_1| = 4.16\times 10^{-2}\ \text{eV} , \tag{9.21}$$

$$\Delta M^{\text{lin}}_{IO} = \frac{2\rho_{IO}\sqrt{\Delta m^2_{23}}}{1+\rho_{IO}} = |m_2| - |m_1| = 7.53\times 10^{-4}\ \text{eV} , \tag{9.22}$$

in the case of NO and IO of the light neutrino masses. The mass splitting ΔM is fixed by the measured mass squared differences of the light neutrinos from neutrino oscillation experiments. Therefore, ΔM is predicted for the two orderings of the light neutrinos in the linear seesaw case.

Inverse Seesaw

In the inverse seesaw, the perturbation ε_{22} is introduced in the 2-2 element of the sterile neutrino mass matrix M_R, cf. section 4.2.4. As we discussed in section 4.2.4, this generates a mass term for only one of the light neutrinos, which may correspond to the mass of the lightest or even the heaviest of the light neutrinos.

For the inverse seesaw case, the Yukawa couplings, the mass parameter M and ε_{22} can be chosen real and positive without loss of generality since

[157] Note that one mass is negative, that sign can be flipped by the matrix $\begin{pmatrix} \pm i & 0 \\ 0 & 1 \end{pmatrix}$.

[158] The best-fit values for the oscillation data in tab. 1 are used, which also yields $\rho_{NO} = 0.7059$ and $\rho_{IO} = 7.572\times 10^{-3}$.

the corresponding unphysical phases can be absorbed by a redefinition of the neutrino fields. Since the parameters can be chosen as real, the full mass matrix $\mathcal{M}'$ is real symmetric and it can be diagonalised in terms of orthogonal matrices O. This yields for the trace of the mass matrix the following relation,

$$\varepsilon_{22} = \mathrm{Tr}(\mathcal{M}') = \mathrm{Tr}(O^T \mathcal{M}' O) = \mathrm{Tr}(\mathcal{M}) = m_{\nu_i} + \Delta M^{\mathrm{inv}}\,, \tag{9.23}$$

where m_{ν_i} is the mass of the light neutrino. Since the mass of the light neutrino, cf. eq. (4.14), can be related to the usual active-sterile mixing squared $\theta^2 = \frac{v_{EW}^2}{2M^2}\vec{y}^\dagger\vec{y} = \Sigma_\alpha \frac{v_{EW}^2}{2M^2}|y_{\nu_\alpha}|^2$ by

$$m_{\nu_i} = \mathrm{Tr}\left(\varepsilon_{22}\frac{v_{EW}^2}{2M^2}\vec{y}\vec{y}^T\right) = \varepsilon_{22}\frac{v_{EW}^2}{2M^2}\vec{y}^\dagger\vec{y} = \varepsilon_{22}\theta^2\,. \tag{9.24}$$

The mass splitting ΔM^{inv} can be approximated to

$$\Delta M^{\mathrm{inv}} = \varepsilon_{22} - m_{\nu_i} = \varepsilon_{22}(1-\theta^2) \approx \frac{m_{\nu_i}}{\theta^2} \tag{9.25}$$

in the inverse seesaw case. The mass splitting is dependent on the light neutrino mass m_{ν_i}, for which we consider example values of m_{ν_i} in the 10^{-4} to 10^{-1} eV range. In general, the mass of the lightest neutrino can be arbitrarily small, while one of the neutrinos should at least have a mass determined by the atmospheric mass squared difference $\Delta m^2_{32} \sim 0.05$ eV when the lightest neutrino is massless. We also note that when additionally allowing the ε_{11} perturbation in the 1-1 element of the sterile neutrino mass matrix M_R, it affects the heavy mass splitting via eq. (9.23), but it does not contribute to the light neutrino mass matrix as we discussed below eq. (4.14), and therefore leaves eq. (9.24) unchanged. This would allow for larger or smaller values of ΔM^{inv}.

9.4 RELEVANCE OF LEPTON NUMBER VIOLATION AT COLLIDERS

The amount of LNV from the heavy neutrino-antineutrino oscillation can now be calculated with the estimates on the heavy neutrino mass splitting in the linear and inverse seesaw cases, cf. eq. (9.21), (9.22) and (9.25). In this way, the relevance of LNV at colliders can be assessed by mapping the $R_{\ell\ell}$ ratio, eq. (9.9), to the active-sterile mixing angles and heavy neutrino mass M. For the mapping onto the sterile neutrino parameter space, we remark that the total decay width of the heavy neutrino introduce the dependency on the active-sterile mixing angles and the heavy neutrino M. The 10% and 90% contours of the $R_{\ell\ell}$ ratio are drawn for the inverse seesaw and linear seesaw case in fig. 49. The figure demonstrated for which parameter space sizeable amount of LNV could be found at colliders. Due to the different connection to the light neutrino masses, the linear and inverse seesaw cases feature different values for ΔM and thus different parameter regions for the relevance of LNV at colliders. We emphasise that in the case of the linear seesaw the mass splitting ΔM, see eq. (9.21) and (9.21), is sharply predicted and therefore also the amount of LNV is predicted. For the inverse seesaw case, however, one has the freedom in choosing ΔM.

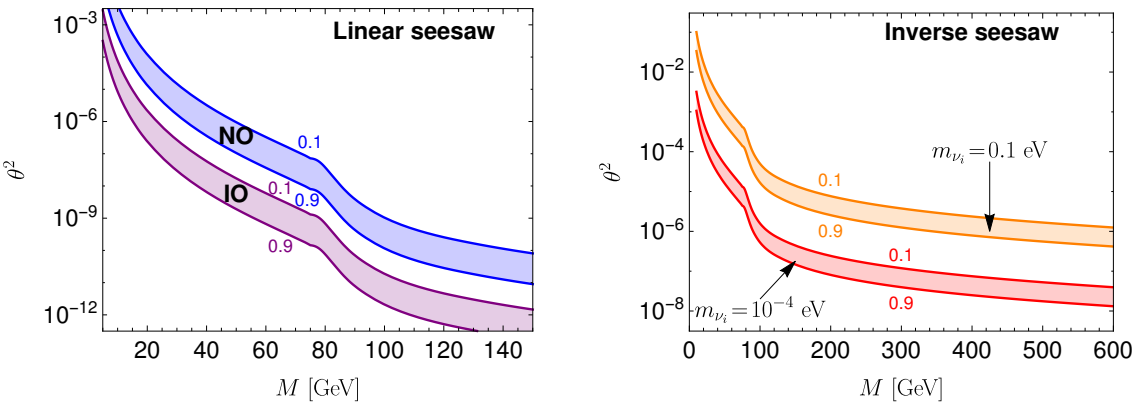

Figure 49: Shown are the $R_{\ell\ell} = 0.1$ and 0.9 contours in the heavy neutrino mass versus active-sterile mixing θ^2 plane for the linear seesaw and inverse seesaw. Sizeable amount of LNV from the pseudo-Dirac nature of the heavy neutrinos is expected for the parameter space below the contours. In the left plot, the linear seesaw case with NO and IO of the light neutrino masses is shown. In the right plot, the inverse seesaw case with the light neutrino mass being either $m_{\nu_i} = 10^{-1}$ eV and 10^{-4} eV is shown. This figure is published in ref. [5].

Overall, the inverse seesaw can feature a much larger mass splitting of the heavy neutrinos relative to the inverse seesaw case , therefore LNV becomes relevant at comparatively much larger active-sterile mixings θ^2.

For searches of the heavy neutrino with masses below $\sim$ 100 GeV, a large amount of LNV (at least $R_{\ell\ell} = 0.9$) can be expected for active-sterile mixings θ^2 just below the upper exclusion limits of $\sim 10^{-5}$ in the case of the inverse seesaw with $m_{\nu_i} = 0.1$ eV. But it can also be expected for much smaller θ^2 depending on the mass of the heavy neutrino, e.g., in the linear seesaw case with IO of the light neutrino masses. Therefore, displaced vertex searches provide an interesting avenue to study LNV at colliders. Because the displaced vertex search could measure the displaced LNV and LNC decays of the heavy neutrinos which would lead to an oscillating pattern of the decays spectra as a consequence of the heavy neutrino-antineutrino oscillations. This possibility is discussed in detail in section 11.1 as an application of the displaced vertex search.

For searches of the heavy neutrino with masses above $\sim$ 100 GeV, a large amount of LNV (at least $R_{\ell\ell} = 0.9$) could be expected for θ^2 of the order of 10^{-6} in the case of the inverse seesaw with $m_{\nu_i} = 0.1$ eV. As previously noted, with even larger ΔM by allowing ε_{11} to the inverse seesaw case, LNV could be present at larger active-sterile mixing angles. But LNV can, as well, be expected just for θ^2 below the order of $\sim 10^{-12}$ in the predicted linear seesaw case with IO. In which case it is safe to assume that collider searches could only probe lepton-number conserving processes.

In this regard, we comment on LHC searches for LNV from heavy neutrinos in the mass range above $\sim$ 100 GeV. In this mass range, the LHC constrains the mixing θ^2 for $M \gtrsim 100$ GeV down to 10^{-3} while for $M \sim 500$ GeV down to 10^{-1}, see, e.g., ref. [329, 375]. However, in obtaining these limits, which are derived in simplified models with one sterile neutrino, quantities such as $\sigma \times$ BR (or equivalently the number of expected events) are calculated for the heavy neutrino signal as if it were lepton-number conserving in magnitude, i.e. assuming $R_{\ell\ell} = 1$ [159]. In the lepton-number violating case with two sterile neutrinos, which is consistent with neutrino oscillation

[159] In the case of one sterile neutrinos, on would also get an equal numbers of LNV and LNC.

data as opposed to the one sterile neutrino case (cf. side note 85), however, $\sigma \times \mathrm{BR}$ would be multiplied by the $R_{\ell\ell}$ ratio, which for the parameter point $M = 100\,\mathrm{GeV}$, $\theta^2 = 10^{-3}$ would reduce the number of events by $R_{\ell\ell} \sim 10^{-6}$ in the case of the inverse seesaw with $m_{\nu_i} = 0.1\,\mathrm{eV}$. This would therefore greatly weaken the limits on the active-sterile mixing angles for lepton-number violating searches above $\sim 100\,\mathrm{GeV}$. Altogether, LNV from heavy neutrinos in the inverse seesaw scenario might potentially be observable at future colliders while it may be very well expected for future collider searches to not find any lepton-number violating signatures in this regime as predicted by the linear seesaw. Therefore, other avenues to search for LNC signatures at future colliders might be much more promising in the search of heavy neutrinos. This leads us directly to the signature of the heavy neutrinos that violate lepton flavour, i.e. they violate the respective lepton flavour numbers, but conserve the total lepton number and are as such lepton-number conserving.

10 LEPTON FLAVOUR VIOLATION AT COLLIDERS

In the SM, the lepton flavour numbers $\mathbb{L}_e, \mathbb{L}_\mu, \mathbb{L}_\tau$ are conserved, i.e, lepton flavour is a symmetry of the SM Lagrangian density. The lepton flavour numbers are an accidental global symmetry of the SM, since neutrinos are massless. As a consequence, neutrinos are always produced in their flavour eigenstate which can be determined from the accompanying charged lepton's flavour eigenstate (which is also equivalent to its mass eigenstate). Extending the SM by sterile neutrinos, the lepton flavour numbers are no longer conserved (in particle physics processes), therefore lepton flavour violation (LFV) for particle physics processes can be expected. This can happen in a way that the respective lepton flavour numbers are not conserved but the total lepton number is still conserved. Therefore, LFV commonly appears in the symmetry protected seesaw scenario in the limit of exact symmetry, i.e., a given process can be lepton-flavour violating although the overall process is lepton-number conserving.

As concluded in the end of section 9.4, searches for heavy neutrinos with masses above $\sim$ 100 GeV may fare better by searches for lepton-number conserving signatures rather than lepton-number violating. Therefore, the lepton-flavour violating but lepton-number conserving signatures provide a promising avenue to search for heavy neutrinos at colliders. In this chapter, we investigate the prospects for testing LFV in direct searches of the heavy neutrinos with masses above 100 GeV at future colliders, based on work that is partly published in ref. [3, 7].

In section 10.1, the occurrence of lepton-flavour violating signatures from the heavy neutrinos at electron-positron, hadron and electron-proton colliders is discussed. In a parton level analysis, the possible sensitivity of LFV at the hadron colliders and electron-proton colliders are estimated in section 10.2. The sensitivity of the lepton-flavour violating $e^\pm\mu^\mp jj$ final sate to the sterile neutrino parameters is investigated at the reconstructed level for the HL-LHC and the FCC-hh in section 10.3.

10.1 LEPTON-FLAVOUR VIOLATING SIGNATURES AT COLLIDERS

We discuss the occurrence of lepton-flavour violating signatures that arise due to the heavy neutrinos at colliders as partly published in ref. [3, 7].

LFV requires, as for LNV, the charged leptons to interact with the heavy neutrinos by the charged weak current interaction in order to provide visible LFV in form of the flavour-violating charged leptons. Similarly to lepton-number violating final states, when light neutrinos are present in the final state, they escape detection which makes it difficult to measure LFV. But there can still be unambiguous signatures for LFV at the parton level when the final states feature less light neutrinos than charged leptons for the tree-level processes. We remark that only at the parton level, the lepton-flavour violating signature has no background. While at the reconstructed level, SM

processes from final states with additional neutrinos provide a background, due to a finite missing momentum resolution of the detector.

By comparing searches for LNV and LFV from heavy neutrinos, they both have advantages and disadvantages. On the one hand, lepton-number violating signatures feature no SM background but their signal strength can be weak compared to the lepton-number conserving signatures depending on the scenario that generates the light neutrino masses [160]. But on the other hand, lepton-flavour violating signatures can arise from lepton-number conserving as well as lepton-number violating processes but they only provide unambiguous signals for LFV at the parton level and not the full ´´no SM background" feature.

[160] In our case, we discussed the amount of LNV that arises in the linear and inverse seesaw case in the previous chapter

At pp colliders, diagram 21a features a lepton-number violating process when the charged leptons ℓ_α and ℓ_β have different flavours, i.e. $\alpha \neq \beta$. In the case that the W boson decays hadronically, the arising dilepton-dijet final state $\ell_\alpha^\pm \ell_\beta^\mp jj$ features no light neutrino in the final state [161]. But nonetheless, processes with additional neutrinos, such as $\ell_\alpha^+ \ell_\beta^- \nu_\alpha \overline{\nu}_\beta jj$, constitute the SM background at the reconstructed level. The $\ell_\alpha^\pm \ell_\beta^\mp jj$ final state has been investigated at the parton level in the context of low scale seesaw scenarios for the LHC in ref. [388] and for the future hadron colliders in ref. [3]. In the same way, also when the W boson decays leptonically, the arising trilepton final state $\ell_e \ell_\mu \ell_\tau \nu$ features an unambiguous signal for LFV at the parton level.

[161] We remark that with dilepton we refer in generally to two leptons of any flavour combination, rather than two of the same flavour.

At e^-p colliders, diagram 24a leads to LFV which is apparent when the negatively charged lepton ℓ_α is not an electron, i.e., $\alpha \neq e$. The resulting lepton-trijet $\ell_\alpha^- jjj$ and jet-dilepton $j\ell_\alpha^- \ell_\beta^+$ final state provide an unambiguous signal for LFV at the parton level for $\alpha \neq e$ and $\beta \neq \alpha$.

At e^+e^- colliders, none of the tree-level diagrams provide unambiguous signatures for LFV. However, lepton-flavour violating decays of the Z and Higgs boson into two charged leptons of different flavours can be induced by the heavy neutrinos at the loop level. Two example diagrams are shown in fig. 50 as illustration. We remark that these lepton-flavour violating loop level signatures are also present in pp and e^-p collisions. These signatures have been investigated in ref. [389–396] in the context of sterile neutrino models at colliders.

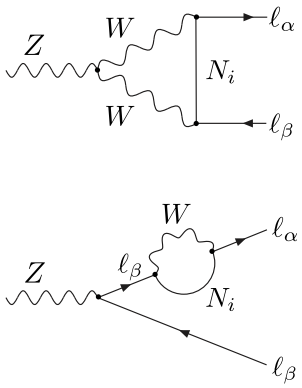

Figure 50: Shown are two example Feynman diagrams for the lepton-flavour violating Z boson decays that arise from heavy neutrinos at the one-loop level.

10.2 SENSITIVITY ESTIMATE TO THE STERILE NEUTRINO PARAMETERS AT THE PARTON LEVEL

In this section, the sensitivity of LFV from heavy neutrinos to the sterile neutrino parameters is investigated at the parton level as partly published in ref. [3]. With the parton level analysis we aim for an order of magnitude estimate for the possible sensitivity of the future colliders. We focus on the lepton-flavour violating dilepton-dijet signature for the future hadron colliders and the lepton-trijet signature at electron-proton colliders. Since both signatures feature no missing energy nor momentum at the parton level, they feature missing energy and momentum only due to the finite resolution of the detector at the reconstructed level. These processes are expected to be more promising than the processes from the trilepton and jet-dilepton final states at the reconstructed level since there is a light neutrino present and therefore additional missing energy and momentum.

We consider two scenarios, a best case scenario and a more realistic scenario for the estimation of the sensitivity. In the best case scenario, we assume that the lepton-flavour violating signatures present an unambiguous signal and therefore have no SM background. For the more realistic scenario, we include an estimate for the SM background that could arise at the reconstructed level. To this end, we chose a conceivable SM background that should be the most important and estimate the number of events that would be below the missing momentum resolution and thus be indiscernible from the supposed "missing-momentum-free" signal events.

For the lepton-flavour violating dilepton-dijet signature at the reconstructed level, the SM background from ditop production is considered as dominant. The SM background process from $t\bar{t}$ decays via $pp \to t\bar{t} \to (bW^+)(\bar{b}W^-) \to (b\ell^+_\alpha\nu_\alpha)(\bar{b}\ell^-_\beta\bar{\nu}_\beta)$ for $\alpha \neq \beta$ to a signal-like final state with additional neutrinos. The ditop production cross section is shown in tab. 11.

For the lepton-flavour violating lepton-trijet signature, the SM background processes $e^-p \to W^-\nu_e V\,j \to (\ell^-_\alpha\bar{\nu}_\alpha)\nu_e(jj)\,j$, where $\alpha \neq e$ and $V = W^\pm, Z$ which decay hadronically, are considered. We remark that these processes feature the hadronic decay from the weak gauge bosons for two of the jets, which is signal-like. The production cross section is shown in tab. 11.

For the estimate, a Monte Carlo event sample of several 10^5 events of the above SM backgrounds was generated by WHIZARD. The estimate is based on the assumption that events with a missing transverse momentum lower than 20 GeV constitute the background.

The LFV signature at the HL-LHC and the FCC-hh/SppC features a peak in the invariant mass of the dijet system at m_W. Therefore, further background events can be rejected by selecting events with the invariant mass of the b-jet system between 70 and 100 GeV. Furthermore, a b-tag veto with an efficiency of 0.3 per jet is considered. The resulting missing transverse momentum distribution is shown in fig. 51 for the HL-LHC and the FCC-hh/SppC. The number of events with a missing transverse momentum lower than 20 GeV yield ~ 800 and $\sim 6 \times 10^4$ background events for the HL-LHC and the FCC-hh/SppC, respectively.

The missing transverse momentum distribution from the three processes $W^-\nu_e V\,j$ with $V = W^\pm, Z$ decaying to the $(\ell^-_\alpha\bar{\nu}_\alpha)\nu_e(jj)\,j$ final state is shown in fig. 52 for the LHeC and FCC-eh, respectively. For the LHeC and the FCC-eh this results in ~ 100 and ~ 800 background events with a missing transverse momentum below 20 GeV.

The signal is given by the $\ell^+_\alpha\ell^-_\beta jj$ final state at hadron colliders which is sensitive to the active-sterile mixing angle combination $|\theta_\alpha\theta_\beta|^2/\theta^2$, while the $\ell^-_\alpha jjj$ final state is sensitive to the mixing angle combination $|\theta_e\theta_\alpha|^2/\theta^2$. The dilepton-dijet final state can test all mixing angle combinations while the leptron-trijet signature can only test the e-μ and e-τ combinations. For the signal we assume that all events pass the imposed missing transverse momentum cut. For the calculation of the sensitivity $|\theta_\alpha|^2 = |\theta_\beta|^2$ ($|\theta_\alpha|^2 = |\theta_e|^2$) is assumed and the mixing angle of the third flavour is set to zero, which results in the dependency $|\theta_\alpha\theta_\beta|^2/\theta^2 = \frac{1}{2}|\theta_\alpha|^2 = \frac{1}{2}|\theta_\alpha\theta_\beta| = \frac{1}{2}|\theta_\beta|^2$ ($\frac{1}{2}|\theta_e\theta_\alpha|$), in the dilepton-dijet (lepton-trijet) case. The sensitivity to the active-sterile mixing angles is derived for a significance $\mathcal{S} = 1$ in the realistic case as well the optimistic case, confer eq. (A.4) for the definition of the significance and

BKG	HL-LHC	FCC-hh SppC
$t\bar{t}$	35 pb	410 pb

BKG	LHeC	FCC-eh
$W^-\nu_e W^+\,j$	3.6 fb	46.3 fb
$W^-\nu_e W^-\,j$	1.4 fb	24.9 fb
$W^-\nu_e Z\,j$	2.1 fb	31.7 fb

Table 11: Shown are the production cross sections of the SM background processes, which are calculated by WHIZARD, for the future hadron and electron-proton colliders at the parton-level. For the incident protons only the first two quark generations were assumed. Ditops decay with a branching ratio of 10% into the dilepton channel [65]. The $W^-\nu_e V\,j$ background decays with the follwing branching ratios to the final state: $\mathrm{BR}(W^- \to \ell^-_\alpha\bar{\nu}_\alpha) \simeq 0.1$, $\mathrm{BR}(W^- \to jj) \simeq 2/3$ and $\mathrm{BR}(Z \to jj) \simeq 0.7$.

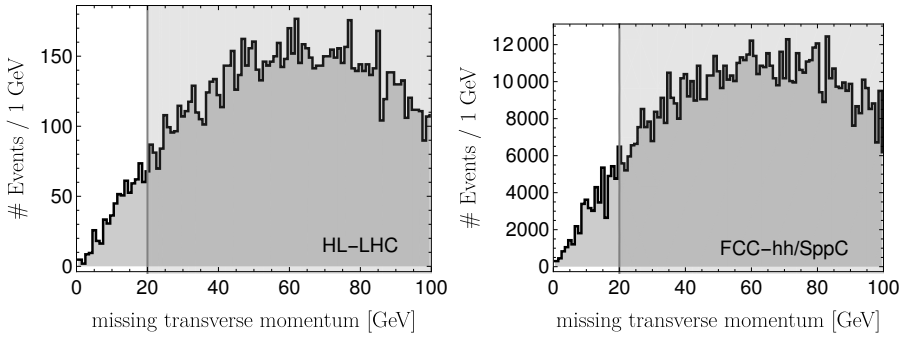

Figure 51: Shown is the missing transverse momentum distribution for the background process $pp \to t\bar{t} \to (bW^+)(\bar{b}W^-) \to (b\ell_\alpha^+\nu_\alpha)(\bar{b}\ell_\beta^-\bar{\nu}_\beta)$ for the HL-LHC and FCC-hh/SppC with an integrated luminosity of 3 ab^{-1} and 20 ab^{-1}, respectively.

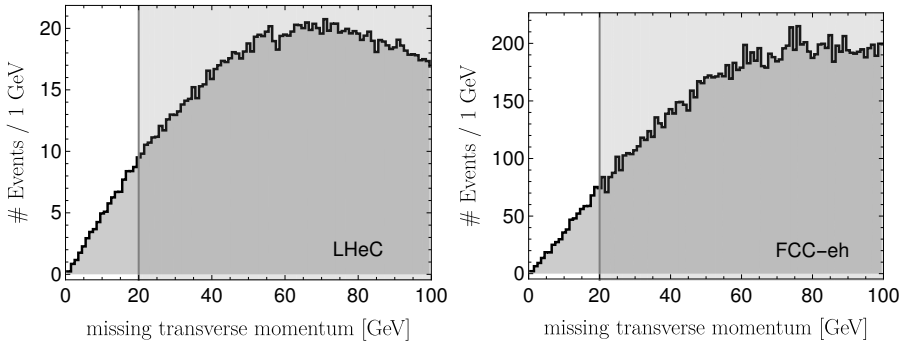

Figure 52: Shown is the missing transverse momentum distribution for the background processes $e^-p \to W^-\nu_e V j \to (\ell_\alpha^-\bar{\nu}_\alpha)\nu_e(jj)j$, where $\alpha \neq e$ and $V = W^\pm, Z$ for the LHeC and FCC-eh with an integrated luminosity of 1 ab^{-1} for both.

its used estimator in eq. (A.5) as well as the general procedure in the appendix A.1.1. The resulting sensitivities at the 1σ level are displayed in fig. 53 for the hadron and electron-hadron colliders. Compared to the bounds at 1σ Bayesian C.L. for the e-μ , e-τ and μ-τ flavour ratios, as discussed in eq. (5.2), LFV at hadron colliders would test active-sterile mixing angles just above the bound on the e-μ flavour while it would be able to test parameters below the e-τ and μ-τ flavours already at the HL-LHC. Furthermore, the possible potential is shown for the FCC-hh for the estimate in the best case scenario that all the backgrounds can be rejected without the loss of signal events. Depending on how well one can separate the signal from the background by kinematic cuts at the reconstructed level, the sensitivity might improve up to a factor of 10^3 (10^2) compared to the estimated for the more realistic sensitivity at the FCC-hh (HL-LHC). This would also represent a major improvement for the sensitivity on the e-μ flavour combination and is thus interesting to investigate further since the HL-LHC will be running around the year 2030. The proton-electron colliders are very promising since the LHeC could test active-sterile mixings beyond the bound on the e-μ combination. They also demonstrate more promising sensitivities to test LFV due to lower backgrounds. However, this has to be investigated more thoroughly at the reconstructed level. The sensitivity might improve by a factor 10^2 (10^1) in the best case scenario.

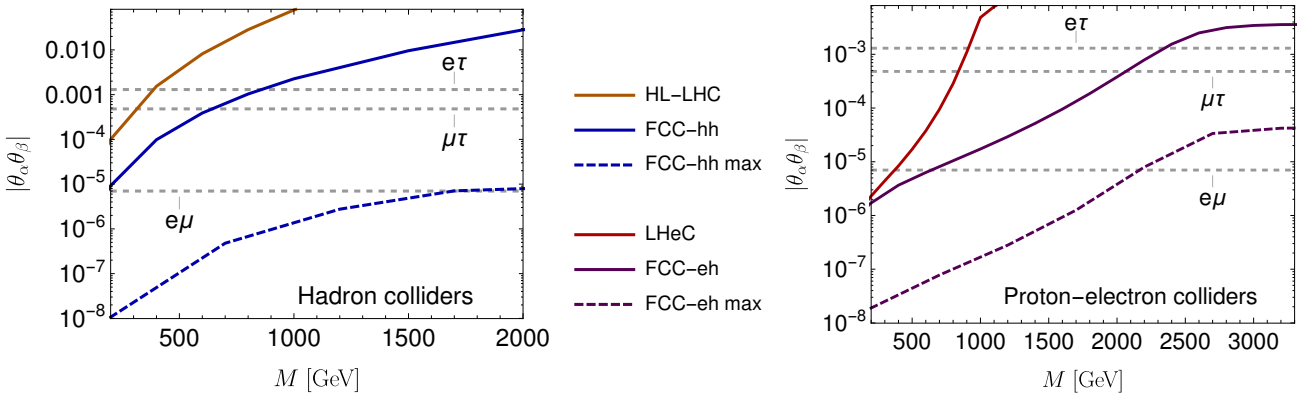

Figure 53: Shown are the estimated possible sensitivities of the lepton-flavour violating search to the active-sterile mixing angle combination $|\theta_\alpha\theta_\beta|$ (assuming $|\theta_\alpha| = |\theta_\beta|$) at the 1σ level. The $\ell_\alpha^+\ell_\beta^-jj$ final state is considered for the HL-LHC and FCC-hh with an assumed integrated luminosity of 3 ab^{-1} and 20 ab^{-1}, respectively. The ℓ_α^-jjj final state is is considered for the LHeC and the FCC-eh with an assumed integrated luminosity of 1 ab^{-1} for both. The horizontal lines represent the bounds which are derived for the active-sterile mixing combinations $|\theta_\alpha\theta_\beta|$ at the 1σ Bayesian C.L. ,cf. eq. (5.2) for the bounds.

10.3 LEPTON FLAVOUR VIOALTION FROM $e^{\pm}\mu^{\mp}jj$ SIGNATURE AT THE RECONSTRUCTED LEVEL

The previously estimated sensitivity of the lepton-flavour violating but lepton-number conserving dilepton-dijet signature on the parton level demonstrates great possible improvements in sensitivity when kinematic cuts could be applied to separate the signal from the background. Although the bound on the e-μ flavour combination is more restrictive than for the other combinations, the possible improvements on the sensitivity of the future hadron collider such as the FCC-hh and SppC but especially for the HL-LHC in the not to far future is interesting to be investigated. For the analysis on the reconstructed level, we therefore focus on the e-μ flavour combination. The discussion of the simulation of signal and SM background is based on work conducted in ref. [7].

Signal

We focus on the $e^{\pm}\mu^{\mp}jj$ final state where the dominant production mechanism of the heavy neutrino is given by the Drell-Yan process via the weak charged current. The $W\gamma$ process would become the dominant heavy neutrino production mechanism around $M \sim 1$ TeV, however, the contribution from $W\gamma$ would add 20%-30% to the leading order cross section. Thus its contributions are omitted due to the limited improvements to the sensitivity.

Furthermore, we focus signal on processes that feature two hadronic jets with an invariant mass around m_W with possible further hadronic activity. However, when the decay products are strongly boosted the hadronic decays of the W boson may be collimated enough for the two jet to appear as a single fat-jet, confer, for instance, [397, 398]. This may become relevant for large heavy neutrino masses but is not considered in the following.

The e-μ flavour combination is chosen as $\alpha = e(\mu)$ and $\beta = \mu(e)$, which tests the active-sterile mixing angle combination $|\theta_e\theta_\mu|^2/\theta^2$. For the calcula-

tion of the sensitivity the special case for the active-sterile mixing angles is assumed:

$$|\theta_e|^2 = |\theta_\mu|^2 \neq 0 \qquad \text{and} \qquad |\theta_\tau|^2 = 0\,, \tag{10.1}$$

which results in the dependency $|\theta_e\theta_\mu|^2/\theta^2 = \frac{1}{2}|\theta_e|^2 = \frac{1}{2}|\theta_e\theta_\mu| = \frac{1}{2}|\theta_\mu|^2$.

Background

As discussed in the parton level section, SM processes constitute a background to the $e^\pm\mu^\mp jj$ signature dominantly from dilepton-dijet final states with additional neutrinos in the final state that manifest as missing energy and momentum, i.e., $e\mu jj\nu\nu$. In principle, these backgrounds could be rejected if it were not for the finite resolution of the missing energy and momentum of the detector. Although a great portion of these backgrounds should still be able to be rejected with a small missing energy or momentum cut, similarly to what was done in the previous section, there are still surviving background events. Therefore, the distributions of other kinematic observables have to be considered in order to improve the sensitivity.

Due to the signal topology, mainly SM processes where the invariant mass of two jets can be reconstructed to the W boson mass are considered. Otherwise, these could more easily be rejected. This mainly promotes the ditop production process with the subsequent semileptonic decay of the top quarks and the ditau-dijet final state with the subsequent leptonic decay of the tau leptons. Since it was not feasible to simulate a large number of events in a reasonable time frame for the inclusive processes $e\mu jj\nu\nu$, we chose to simulate exclusive processes instead.

The simulated background processes include [7]:

- ditop processes with leptonic decays
  - $pp \to t\bar{t} \to (bW^+)(\bar{b}W^-) \to (b\,l^+\nu)(\bar{b}\,l^-\bar{\nu})$, where the charged leptons can be either e or μ ;
- diboson processes with the ditau-dijet final state and with the subsequent leptonic decays of the tau leptons:
  - $pp \to WZ \to (jj)(\tau^+\tau^-)$;
  - $pp \to ZZ \to (jj)(\tau^+\tau^-)$;
- triboson processes with at least 2 jets and at least 2 leptons (including tau leptons) in the final state:
  - $pp \to WWZ \to (l\nu)(l\nu)(jj)$;
  - $pp \to WWZ \to (jj)(jj)(\tau^+\tau^-)$;
  - $pp \to WWZ \to (jj)(l\nu)(\tau^+\tau^-)$;
  - $pp \to WWZ \to (jj)(l\nu)(l^+l^-)$.

  For the triboson processes with 3 charged leptons one of them has to be outside the detection volume or misidentified in order to contribute.

Moreover, further possible background processes were checked:

For instance, $Zjj \to (\tau^+\tau^-)jj$ and $WWjj \to (\ell\nu)(\ell\nu)jj$ processes where the jets stem from QCD radiation. For these processes, the jets reconstruct to the

W boson mass only for a small fraction of events. Furthermore, a transverse momentum cut on the jets for the pre-selection renders these processes sub-dominant, see below.

The above listed processes with an additional gluon jet or photon in the final state, as well as $VVgg$, $\gamma\mu\mu W$, $\gamma\mu\mu Z$ and $\gamma\mu\nu W$ could be misidentified as the signal. A misidentification rate of $\sim 10^{-3}$ for the gluon and photon as an electron is assumed for the FCC-hh [7], which is comparable to the LHC. Also here the processes are rendered sub-dominant with a transverse momentum cut from the pre-selection.

Simulation

The signal and above listed background processes, were simulated by the Monte Carlo event generator MadGraph5 version 2.4.3 [238–243]. The parton showering and hadronization is performed by Pythia6 [231] which also uses Tauola for the tau decays. A set of loose cuts were applied at the parton level within MadGraph in order to enhance the quality of the simulated backgrounds which makes the simulation also computationally more time efficient. These cuts are based on a preliminary study of the kinematic distributions of the signal and backgrounds for which events were chosen with a minimal transverse momentum $p_T(j) > 20$ GeV for the jets, $p_T(l) > 20$ GeV for the charged leptons, values of the pseudorapidity $|\eta(j)| < 10$ for jets (including b-jets), $|\eta(l)| < 7$ for charged leptons [162], and a missing energy $\not{E}_T < 30$ GeV. The missing energy cut is obviously due to the low amount of missing energy that arises by the signal during the reconstruction. For the FCC-hh, 5.4×10^8 background events for the $t\bar{t}$ process, 3.9×10^8 for the WZ process, 3.9×10^8 for the ZZ process and 3.2×10^7 for each of the WWZ processes were simulated. While for the HL-LHC, $\sim 10^8$ for each of the background events were simulated. A number of 5×10^5 signal events were simulated for the benchmark masses $M = 200, 400, 500, 600, 800, 1000$ GeV of the heavy neutrino. We remark that multijet matching and merging could not be simulated for these large number of events in a reasonable time frame [163]. The subsequent detector simulation is performed by Delphes [232] with the ATLAS configuration card (version 3.4.1 [164]) for the HL-LHC and with the FCC-hh configuration card (October 2016 version) for the FCC-hh. We remark that, for instance, the ATLAS detector has the acceptances $|\eta(j)| < 5$ and $|\eta(l)| < 2.5$ which are applied at the detector level by Delphes. These cuts on the detector level are not affected by the loose cuts on $|\eta|$ at the parton level. The resulting cross sections for the signal and above listed background processes are shown in tab. 12.

From the simulated event sample, events with the following pre-selection criteria are chosen:

- exactly one muon and exactly one electron flavoured charged leptons with opposite charges (i.e. $e^{\pm}\mu^{\mp}$).
- at least two jets.
- no b-jet.
- no tau leptons.

BKG	HL-LHC	FCC-hh SppC
$t\bar{t}$	3.4 pb	137 pb
WZ	1.8 pb	5.6 pb
ZZ	0.5 pb	4.4 pb
WWZ	7 fb	96 fb
Signal		
$M = 200$	5.3 fb	89 fb
$M = 400$	0.44 fb	10.7 fb
$M = 500$	0.19 fb	5.4 fb
$M = 600$	92 ab	3.0 fb
$M = 800$	28 ab	1.2 fb
$M = 1000$	10 ab	0.56 fb

Table 12: Resulting cross sections that would correspond to the number of events after the detector simulation when multiplied by the integrated luminosity for the signal and background processes discussed above. For the signal a active-sterile mixing of $|\theta_e|^2 = |\theta_\mu|^2 = 10^{-2}$ and $|\theta_\tau| = 0$ was chosen. The cross section for the WWZ processes is combined.

[162] The pseudorapidity η is defined as $-\ln(\tan(\vartheta/2))$ with the ϑ denoting the polar angle.

[163] Ref. [399] states: "The aim of any parton-jets matching procedure is mainly to avoid overlapping between phase-space descriptions given by matrix-element generators and showering/hadronization softwares in multi-jets process simulation."

[164] With version 3.4.0 we experienced a bug for the $\not{E}_T$ distribution.

- both jets and leptons requiring a transverse momentum of $p_T > 30$ GeV.
- missing energy $\not{E}_T < 20$ GeV.

The resulting event sample is then ready to be analysed.

At first, it is for our purpose necessary to discriminate the final state charged leptons for the signal. The charged lepton arising from the Drell-Yan's off-shell $W^{*\pm}$ is labelled as $\ell^{\pm}_{W^*}$, while the charged lepton arising from the heavy neutrino decay as $\ell^{\mp}_N$. The charged lepton ℓ_N is identified when the invariant mass of one lepton and the jets from the decay of the W boson is around the mass of the heavy neutrino. The decay of the W boson is considered to give rise to the first two leading jets j_1 and j_2. For each of the two charged leptons, the invariant mass of the lepton and the two leading jets is calculated. The charged lepton that gives together with the two leading jets an invariant mass closest to the heavy neutrino mass is identified as ℓ_N, while the other charged lepton is identified as ℓ_{W^*}.

In order to separate the signal from the background and therefore enhance the sensitivity, a multivariate analysis of 40 kinematic observables has been performed. The analysis includes global observables such as the missing energy $\not{E}_T$, observables for the jet and leptons such as the transverse momentum for ℓ_N and the first two leading jets $j_1 + j_2$, observables for the reconstructed heavy neutrino system such as the invariant mass $M(j_1 + j_2 + \ell_N)$ and observables for the reconstructed off-shell W^* system such as the invariant mass $M(j_1 + j_2 + \ell_N + \ell_{W^*})$. The example kinematic distributions for some of the mentioned observables, based on the benchmark point of the heavy neutrino mass $M = 500$ GeV, are shown in fig. 54a and fig. 54b for the HL-LHC and FCC-hh, respectively. We remark that the fraction of signal events should decrease with increasing $\not{E}_T$ as is clearly visible for the FCC-hh, therefore the $\not{E}_T$ observable has more discriminating power at the FCC-hh than at the HL-LHC. The transverse momentum distributions $p_T(\ell_N)$ and $p_T(j_1 + j_2)$ allow for higher momenta for the signal than for the backgrounds. The invariant mass distribution $M(j_1 + j_2 + \ell_N)$ shows that the reconstruction of the heavy neutrino mass works reasonably well.

For details on the observables and the multivariate analysis, the interested reader is referred to ref. [7]. In short for each benchmark point of the heavy neutrino mass a multivariate analysis is performed to separate the signal from the background. The resulting number of events after the pre-selection and the multivariate analysis are shown in the appendix A.3 for the HL-LHC in tab. 17 and for the FCC-hh in tab. 18.

Sensitivity estimate to the sterile neutrino parameters

Based on the results of the multivariate analysis, the sensitivity of the lepton-flavour violating but lepton-number conserving $e^{\pm}\mu^{\mp}jj$ signature to the active-sterile mixing angles $|\theta_e|^2 = |\theta_e\theta_\mu| = |\theta_\mu|^2$, based on the assumption discussed in eq. (10.1), is derived including a systematic uncertainty on the background. The sensitivity is derived with a more sophisticated estimator for the significance compared to the one in eq. (A.5). For details on the derivation of the sensitivity, the reader is referred to ref. [7].

A comparison of the median expected sensitivities at the 1, 2, 3 and 5σ C.L. are illustrated in fig. 55 with a systematic uncertainty of 0% and 10%

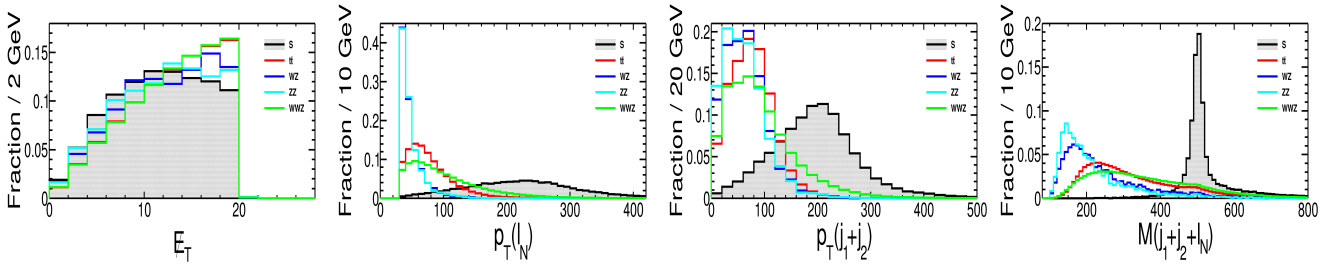

(a) Example kinematic distributions for the signal and background at the HL-LHC which are taken from ref. [7].

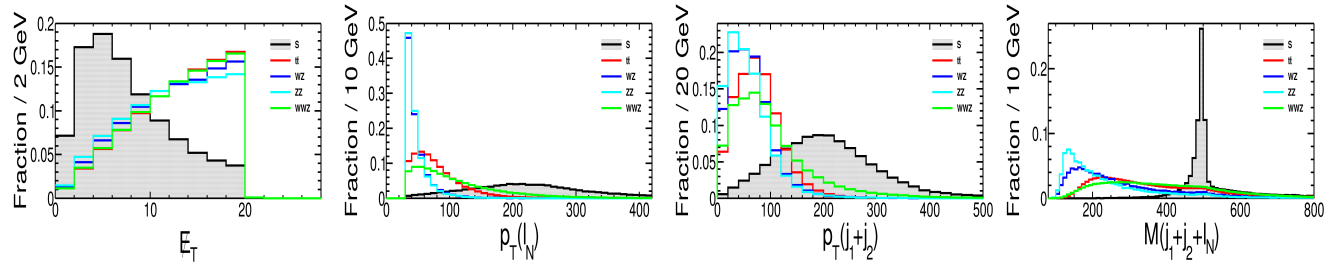

(b) Example kinematic distributions for the signal and background which are taken from ref. [7].

Figure 54: Shown are some example kinematic distributions of the observables: missing momentum, transverse momentum of the charged lepton ℓ_N, transverse momentum of the two leading jets j_1 and j_2, and the invariant mass distribution of the $j_1 + j_2 + \ell_N$ system. The distributions are shown for the lepton-flavour violating signal with $M = 500$ GeV, labelled as S (grey filled area), and for the considered SM background processes $t\bar{t}$ (red), WZ (blue), ZZ (cyan), and WWZ (green) after applying the pre-selection discussed in the main text. The figures are reprinted from ref. [7].

on the backgrounds for both the HL-LHC and the FCC-hh. Let us first discuss the sensitivities without the inclusion of the systematic uncertainty on the backgrounds. The comparison of the 1σ sensitivities with the previously estimated sensitivities at the parton level, see fig. 53, show that the estimate was not too far off, despite the simplistic approach. Although, the sensitivity at the reconstructed level is weaker for the lower heavy neutrino masses compared to the parton level estimate, it has comparably a better sensitivity for the larger heavy neutrino masses. Despite the employment of the multivariate analysis in order to optimise the sensitivity, the performance of the lepton-flavour violating search at hadron colliders remains far from the best possible sensitivity in the best case scenario, see fig. 53. This is predominantly due to the surviving $t\bar{t}$ background, confer tab. 17 and tab. 18 in the appendix A.3.

The effects of the systematic uncertainty on the backgrounds can be seen to be relevant for the lower heavy neutrino masses, because the number of background events is larger with decreasing heavy neutrino mass. Especially, at the FCC-hh the effect of the systematic uncertainty on the sensitivity can weaken the sensitivity considerably.

The expected median sensitivity at the 95% C.L. including the 1σ and 2σ confidence interval is shown in fig. 56 for the HL-LHC with an integrated luminosity of 3 ab^{-1} and for the FCC-hh with 20 ab^{-1}. We note that the sensitivity for the FCC-hh is somewhat also representative for the SppC, however it is subdue to changes depending mostly on the design and performance of the detector. Furthermore, we remark that for the considered e-μ

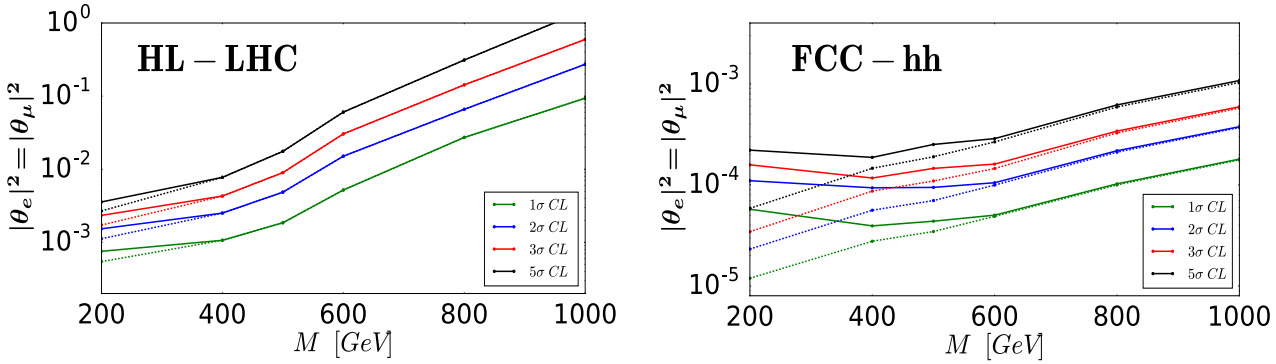

Figure 55: Shown are the median expected sensitivities of the $e^{\pm}\mu^{\mp}jj$ search to the active-sterile mixing angles $|\theta_e|^2 = |\theta_\mu|^2$ including a systematic uncertainty of 0% (dashed line) and 10% (solid line) on the background at the 1, 2, 3 and 5σ C.L., which are taken from ref. [7]. The limits are derived under the assumption in eq. (10.1), where an integrated luminosity of 3 ab^{-1} and 20 ab^{-1} is considered for the HL-LHC and the FCC-hh. The figures are reprinted from ref. [7].

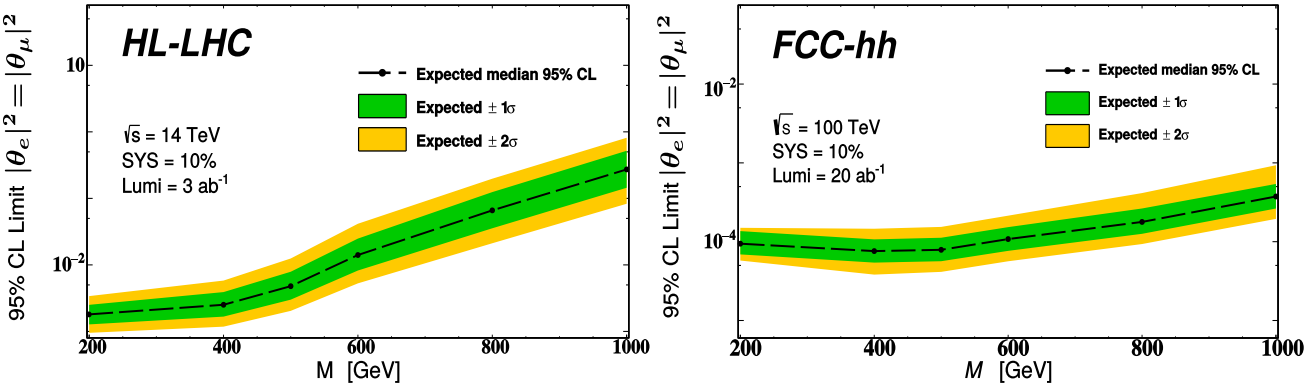

Figure 56: Shown are the median expected sensitivities of the $e^{\pm}\mu^{\mp}jj$ search to the active-sterile mixing angles $|\theta_e|^2 = |\theta_\mu|^2$ including a systematic uncertainty of 10% on the background at the 95% C.L. for the HL-LHC and the FCC-hh. The figures are reprinted from ref. [7].

flavour ratio of $|\theta_e|^2 = |\theta_\mu|^2 \neq 0$ and $|\theta_\tau|^2 = 0$ the sensitivity is maximal, while in the case that one flavour becomes dominant the overall sensitivity becomes suppressed (for constant θ^2) [165]. The lepton-flavour violating search at hadron colliders seems not to be competitive with the limits on the e-μ flavour combinations [166]. However, would this mean that lepton-flavour violation from the e-μ flavour combination is excluded at hadron colliders? Not necessarily. In the case that only two sterile neutrinos are present in the SPSS, then the low energy constraint from $\mu \to e\gamma$ would be stringent. In the case that there are additional sterile neutrinos present in the SPSS, which are decoupled from the collider phenomenology, the contributions from the additional sterile neutrinos may well contribute to the low energy process and suppress the branching ratio BR($\mu \to e\gamma$). Therefore, the finding of a signal in the lepton-flavour violating final state $e^{\pm}\mu^{\mp}jj$ is possible at hadron colliders, which would indicate that more than two sterile neutrinos are present when interpreted in the framework of the SPPS.

The analysis for the $e^{\pm}\tau^{\mp}jj$ and $\mu^{\pm}\tau^{\mp}jj$ final states at the reconstructed level is commented here. Differently to the parton level analysis, the tau leptons have to be reconstructed either from their leptonic or their hadronic decays. In the case of leptonic decays, the tau lepton has to be reconstructed

[165] This can be seen when the active-sterile mixing angles are written as $|\theta_e|^2 = x\theta^2$ and $|\theta_\mu|^2 = (1-x)\theta^2$ which results for the active-sterile mixing angle combination $|\theta_e\theta_\mu|^2/\theta^2$ to $x(1-x)\theta^2$.

[166] The limit on $|\theta_e\theta_\mu|$ is mostly determined by the constraint on BR($\mu \to e\gamma$) from the MEG experiment, cf. section 5.1.2. The constraint on the branching ratio limits the active-sterile mixing angle combination $|\theta_e\theta_\mu|$ to 1.5×10^{-5} at the 90% C.L. [222].

from a muon or electron flavoured lepton with a non-vanishing impact parameter, which is due to the long-lived tau lepton giving rise to a small displacement of the secondary vertex. However, the accompanying neutrino in the leptonic decay of the tau lepton also introduces additional missing energy. In the case of hadronic decays of the tau lepton, the reconstruction should work better since one can use observables such as the invariant mass, but at the same time it is required to consider additional backgrounds. The reconstruction of the tau decays for the $e^{\pm}\tau^{\mp}jj$ and $\mu^{\pm}\tau^{\mp}jj$ is more involved and requires definitely a dedicated analysis. Consequently, one would expect the sensitivities for the e-τ and μ-τ flavour combinations to be weaker than the sensitivity for e-μ. But together with the much weaker constraints for the e-τ and μ-τ flavour combinations, the $e^{\pm}\tau^{\mp}jj$ and $\mu^{\pm}\tau^{\mp}jj$ searches could provide a great discovery potential.

11 POSSIBLE APPLICATIONS OF THE DISPLACED VERTEX SEARCH FOR HEAVY NEUTRINOS

The displaced vertex search for heavy neutrinos with possible future sensitivities as calculated in section 8, is a powerful search that goes beyond testing the sterile neutrino parameters M and active-sterile mixing angles. Not only has it the potential to probe LNV as the manifestation of the neutrino-antineutrino oscillation, confer fig. 49, but also the potential to probe the viable parameter region for leptogenesis as a mechanism for the observed baryon asymmetry of the universe. The displaced vertex search therefore constitutes an interesting avenue to study LNV as well as leptogenesis at future colliders.

In section 11.1, we discuss the effects of heavy neutrino-antineutrino oscillations when the heavy neutrinos are long-lived and investigate whether these effects can be probed by the displaced vertex search as partly published in ref. [5]. Section 11.2 is concerned with testing the parameter region for leptogensis in the context of low-scale seesaw scenarios via displaced vertices as partly published in ref. [6].

11.1 RESOLVABLE HEAVY NEUTRINO-ANTINEUTRINO OSCILLATIONS VIA DISPLACED VERTICES

For masses of the heavy neutrinos below $\sim$ 100 GeV, the heavy neutrino decays can occur with a visible displacement from the primary vertex due to the relatively long lifetimes. The signature from heavy neutrino-antineutrino oscillations manifests itself as displaced lepton-number violating and conserving decays of the heavy neutrinos which leads to an oscillation pattern of the decay spectra. To give an example of the resulting signature, let us consider the dilepton-dijet final state at hadron colliders: the lepton-number violating decays manifest as $pp \to \ell^{\pm}(\ell^{\pm}jj)_{\text{displaced}}$ and the lepton-number conserving decays as $pp \to \ell^{\pm}(\ell^{\mp}jj)_{\text{displaced}}$. Since the fraction of LNV to LNC is dictated by the oscillating amplitudes g_- and g_+ in eq. (9.8), the decay spectra reflect this oscillating pattern.

In this section, we investigate these effect of the oscillating pattern and whether they can be resolved at colliders via the displaced vertex search, based on the results published in ref. [5].

To start with, the question of the coherence of the heavy neutrinos becomes increasingly important for the oscillations. Because only when the mass eigenstates are in a coherent superposition the oscillations can occur. This imposes the following coherence conditions, which are discussed in ref. [5, 76, 386, 400]:

- Coherence in the production and detection point:
  It is required that the quantum mechanical uncertainty in the squared mass of the heavy neutrino σ_{M^2} [167] is larger than the mass squared difference of the heavy neutrinos $\Delta(M^2)$. The uncertainty in the squared

[167] When the squared mass is determined by the energy-momentum relation, the uncertainty is given by $\sigma_{M^2} = \sqrt{(2E\sigma_E)^2 + (2p\sigma_p)^2}$ for uncorrelated uncertainties σ_E and σ_p [400].

mass can be approximated as $\sigma_{M^2} \simeq 2\sqrt{2} E_N \Gamma_W \geqslant$, where E_N is the average energy of the heavy neutrino and Γ_W the width of the parent particle of the heavy neutrino [168]. Since the mass squared difference of the heavy neutrinos, given by $\Delta(M^2) = (M_2^2 - M_1^2) = 2M\,\Delta M$, is much smaller than σ_M^2 [169], it is impossible to determine which mass eigenstate was produced or detected. Therefore, the heavy neutrinos would be in a coherent superposition when emitted and detected.

- Coherence during propagation:
  Coherence can be lost during propagation when the propagating wave packets of the heavy neutrinos separate due to different group velocities. Coherence during propagation is preserved for the maximum coherence length $x_{coh} \simeq [\Gamma_W \Delta(v_g)]^{-1}$ with $\Delta(v_g)$ being the minimum group velocity difference. The coherence condition during propagation are satisfied for the considered heavy neutrino masses, mass splittings, and boosts where displaced vertices from heavy neutrino decays could be detected at colliders.

[168] Since the energy uncertainty of the heavy neutrino is given by the parent's particle decay width of the heavy neutrino, i.e. the decay width of the W boson.

[169] For the calculated heavy neutrino mass splitting in the linear and inverse seesaw anyway.

Therefore, the heavy neutrino-antineutrino oscillations proceed via the discussed oscillating amplitudes $g_-(t)$ and $g_+(t)$ in eq. (9.8). The oscillation period for the time-dependent probabilities $|g_-(t)|^2$ and $|g_+(t)|^2$ depends only on the mass splitting ΔM of the heavy neutrino mass eigenstates, and is given by

$$t_{osc} = \frac{4\pi}{\Delta M}\,. \tag{11.1}$$

For the linear seesaw case, the mass splitting ΔM is predicted, cf. eq. (9.21) and(9.22), therefore also the oscillation period is predicted. We show the oscillating amplitudes and squared amplitudes $g_-(t)$ and $g_+(t)$ for the benchmark point $\overline{M} \approx M = 50$ GeV and $\theta^2 = 10^{-8}$ in the linear seesaw case for NO and IO of the light neutrino masses in fig. 57 and 58. Compared to the example shown in fig. 47, the overall oscillation frequency in the complex plane, which is due the mass $\overline{M}$, is much larger compared to ΔM. In the case of NO, the heavy neutrino mass splitting is much larger than the total decay width for the given benchmark point. Therefore, the fraction of LNV to LNC, given by the $R_{\ell\ell}$ ratio defined in eq. (9.9), approaches one. While for the case of IO, ΔM is of order of the total decay width and thus for the considered benchmark point a value of $R_{\ell\ell}$ inside the 10% and 90% ratio is obtained, as can be seen from fig. 49. When comparing the figures for NO to IO, t_{osc} in the NO case is much shorter due to a much larger predicted mass splitting of the heavy neutrinos. The time evolution of the probabilities is shown for times in the proper frame up to the range of $\sim 3 \times 10^{-12}$ s, which would correspond to lengths in the mm range when multiplied by the speed of light. However, for the decay lengths in the laboratory frame the relativistic corrections need to be included. In a similar way, the oscillation period in the proper frame can be converted to an oscillation length in the laboratory frame, which for

the different heavy neutrino mass splittings eq. (9.21), (9.22) and (9.25) are given by

$$\lambda_{\text{osc}}^{\text{lin,NO}} = 5.96 \cdot 10^{-5} \sqrt{\gamma^2 - 1}\,\text{m}\,, \tag{11.2}$$

$$\lambda_{\text{osc}}^{\text{lin,IO}} = 3.29 \cdot 10^{-3} \sqrt{\gamma^2 - 1}\,\text{m}\,, \tag{11.3}$$

$$\lambda_{\text{osc}}^{\text{inv}} \approx 2.48 \cdot 10^{-7} \left(\frac{|\theta|^2}{10^{-5}}\right) \left(\frac{10^{-4}\,\text{eV}}{m_{\nu_i}}\right) \sqrt{\gamma^2 - 1}\,\text{m}\,, \tag{11.4}$$

where γ is the Lorentz factor. The linear seesaw case with IO of the light neutrino masses, yields the longest oscillation length since it features the smallest mass splitting of the heavy neutrinos [170]. The oscillation length for NO of the linear seesaw case is roughly 50 times shorter than for IO. The inverse seesaw case can feature the smallest oscillation lengths. As discussed at the beginning of this section, the oscillating pattern of the LNV and LNC decays of the heavy neutrino reflect the same oscillation frequency. Which could be seen in position space, since the oscillation length in the laboratory frame can be macroscopically large and, for instance, be well into the cm range with large enough Lorentz boosts for the IO of the linear seesaw case.

[170] When values of m_{ν_i} in the 10^{-4} to 10^{-1} eV range are considered for the inverse seesaw case.

We want to discuss, the observability of the heavy neutrino oscillations via the displaced vertex search at the HL-LHCb, which we discussed in section 8.4, based on the benchmark point $M = 7$ GeV, $\theta^2 = 10^{-5}$ as an example. This benchmark point lies just outside the exclusion limits from the conservative region (region 1), which is shown in fig. 44, for the run 1 data of LHCb.

We investigate the linear sessaw case with IO of the light neutrino masses in detail since it is the most promising scenario to observe the signature from heavy neutrino-antineutrino oscillations. A Lorentz factor of 50 can be typical for heavy neutrinos from Z decays at $\sqrt{s} = 13$ TeV for the considered benchmark point, cf. fig. 43 for instance. The resulting oscillation length is in this case $\sim$ 15 cm. As an illustration, we show the fraction of LNV and LNC events as a function of the vertex displacement in the laboratory frame in an idealised plot assuming a fixed Lorentz factor of $\gamma = 50$ in fig. 59a. This would easily be visible, however, this idealised illustration is far from reality, since the distribution of Lorentz factors leads to a smearing out of the oscillation pattern in position space. This fact is illustrated in fig. 59b for displaced vertices from heavy neutrino decays in the range of 2 cm and 50 cm, corresponding to decays taking place inside LHCb's VELO. In position space no oscillation pattern can be recognised at hadron colliders nor electron-proton colliders due to the smearing out of the Lorentz distribution. Nevertheless, the oscillating pattern can be reconstructed as a function of time in the proper frame. This requires to measure the Lorentz factor γ for each event and to account for the Lorentz factor when calculating the lifetime of the heavy neutrino for each event.

The reconstruction of the oscillating pattern we proceed as follows: We start with 10^4 Monte Carlo generated displaced vertices from heavy neutrinos decaying to the μjj final state between 2 cm and 50 cm for the high-luminosity phase of LHCb, which are shown in fig. 59b. For this region, we assume a resolution of the displacement measurement of 3 mm and a signal reconstruction efficiency of 100%. For each of the Monte Carlo generated

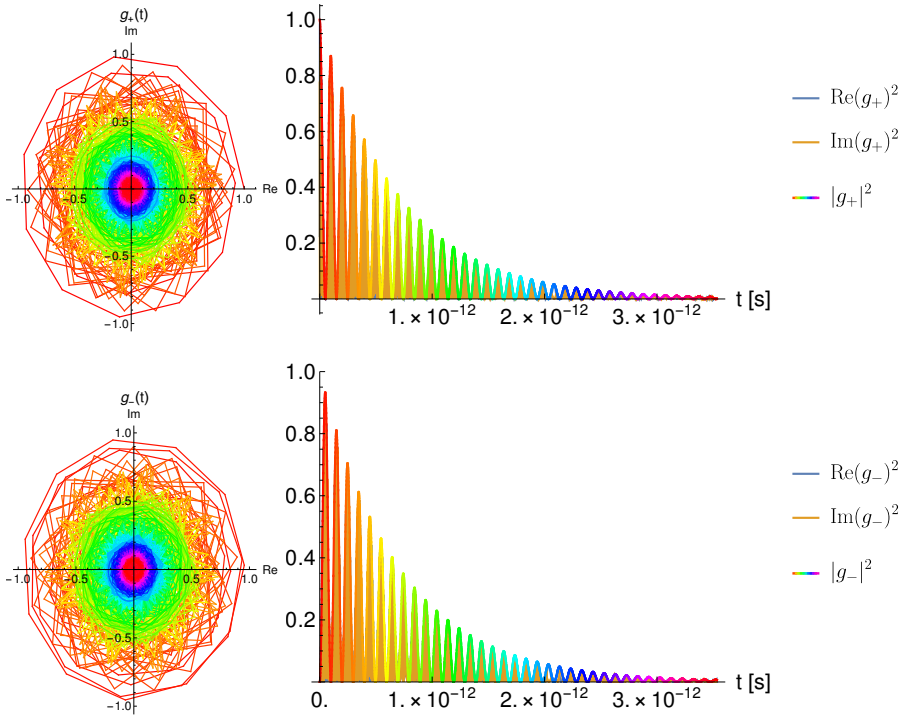

Figure 57: The figure shows the time evolution of the amplitude in the complex plane as well as the corresponding time-dependent probability of g_+ (top) and g_- (bottom) for the example point $\overline{M} \approx M = 50$ GeV and $\theta^2 = 10^{-8}$ in the case of the linear seesaw with NO of the light neutrino masses. The predicted mass splitting of the heavy neutrino is $\Delta M^{\text{lin}}_{\text{NO}} = 4.16 \times 10^{-2}$ eV which results in $R_{\ell\ell} = 0.999$.

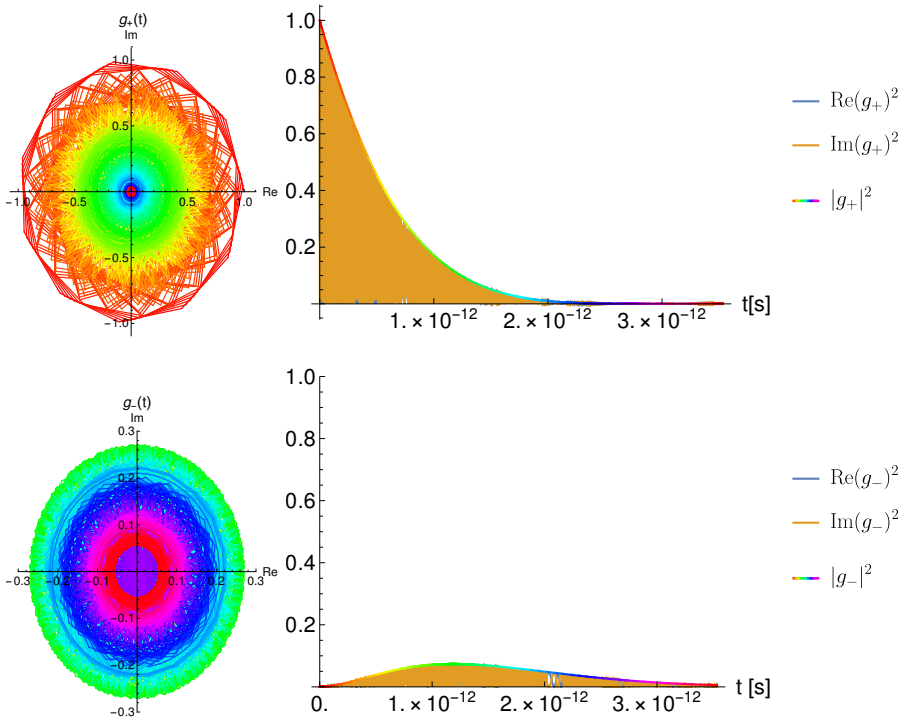

Figure 58: The figure shows the time evolution of the amplitude in the complex plane as well as the corresponding time-dependent probability of g_+ (top) and g_- (bottom) for the example point $\overline{M} \approx M = 50$ GeV and $\theta^2 = 10^{-8}$ in the case of the linear seesaw with IO of the light neutrino masses. The predicted mass splitting of the heavy neutrino is $\Delta M^{\text{lin}}_{\text{NO}} = 7.53 \times 10^{-4}$ eV which results in $R_{\ell\ell} = 0.247$.

events, the Lorentz factor was reconstructed with an assumed 10% uncertainty. The hereby calculated lifetime of the heavy neutrino for each event in the proper frame results in the reconstructed oscillating pattern which is shown in fig. 59c. The first few oscillations are clearly visible, but the oscillating pattern becomes smeared out due to the position resolution and the error on the Lorentz factor γ. This works very well as demonstrated for 10^4 events, but for the high-luminosity phase of LHCb with 380 fb^{-1} around 620 displaced vertices from heavy neutrinos decaying to the μjj final state can be expected between 2 cm and 50 cm for the considered benchmark point. The oscillating pattern can also be reconstructed for 620 events, shown in fig. 59d, which demonstrates the feasibility to observe the signature of heavy neutrino oscillations at LHCb. To confirm the feasibility further studies that analyse the detector response and efficiencies for the detector regions are required. In particular, the prompt charged lepton has to be measured together with the decay products of the displaced vertex decay in order to determine the LNV or LNC nature of the process.

The oscillation pattern for the NO of the light neutrinos in the linear seesaw case is, in principle, still resolvable by the tracking resolution of LHCb. However, together with the experimental uncertainties, this scenario is more difficult to observe than the IO case. Therefore, we conclude for the NO case that the feasibility at LHCb has to be proven, but for the proposed future colliders this case should become accessible.

The inverse seesaw case generally features the smallest oscillation lengths, cf. eq. (11.4). For the assumed benchmark point with $\theta^2 = 10^{-5}$ and with the mass of the lightest neutrino being 10^{-4} eV, the oscillations are not resolvable at LHCb.

Finally, we checked that the reconstruction also works for other benchmark points of the heavy neutrino mass and mixings. For the reconstruction of the oscillating pattern, it seems advantageous to have an event sample of roughly over 100 displaced vertex events from the decay of the heavy neutrinos. But also for lower number of events it is possible to determine the oscillation period. Also in the case that the oscillations cannot be resolved, the $R_{\ell\ell}$ ratio can be measured and be an useful observable. Since the threshold on the number of events is not so clear, it is difficult to make predictions for which parameter space the reconstruction and determination of the oscillation period works.

We investigated the observability of the signature from heavy neutrino-antineutrino oscillations for the LHCb during the HL-LHC, the proposed FCC-hh and SppC should be more promising for probing these signatures. Since they provide larger cross sections, larger Lorentz boosts and higher luminosities. This signature is also not exclusively testable at hadron colliders, the proposed LHeC and FCC-eh do also provide unambiguous signals for LNV where the signature from heavy neutrino-anitneutrino oscillation can arise. Therefore, future colliders provide promising conditions to observe the oscillating pattern from heavy neutrino-antineutrino oscillations which would allow to determine the oscillation period and thus infer the heavy neutrino mass splitting ΔM. Especially for the linear seesaw with NO or IO orderings, where the oscillation period and the heavy neutrino mass splitting are predicted.

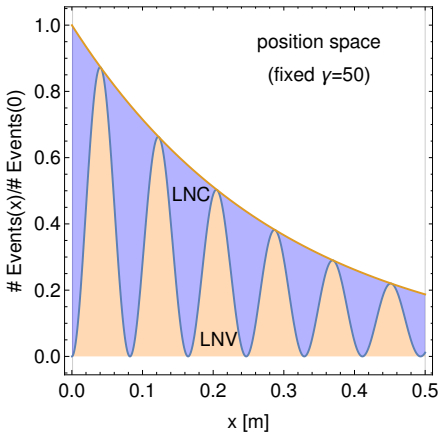

(a) The oscillating pattern in position space as a function of the distance x from the primary vertex in the laboratory frame is shown in the idealised situation for which a fixed Lorentz factor of $\gamma = 50$ is assumed. This figure is published in ref. [5].

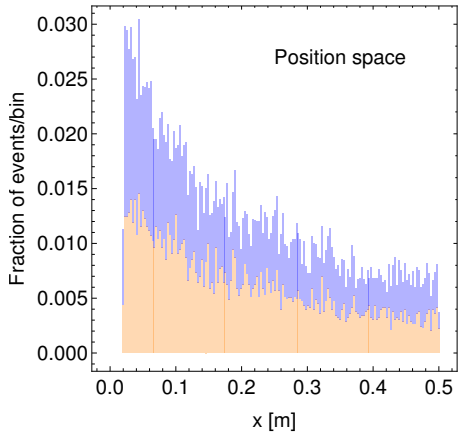

(b) The smeared out oscillating pattern in position space is shown as a function of the distance x from the primary vertex when the distribution of Lorentz factors is taken into account. See text for details.

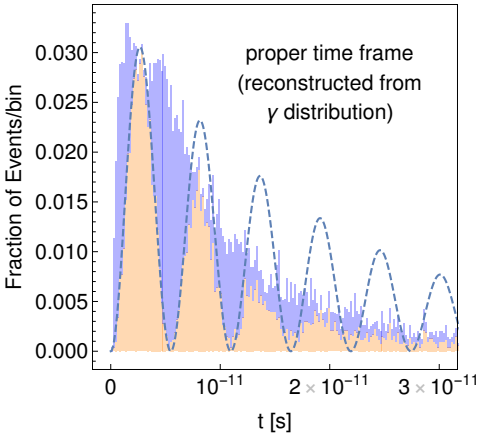

(c) The reconstructed oscillating pattern in the proper frame is shown as a function of the proper time for a Monte Carlo generated event sample of 10^4 events. See text for details.

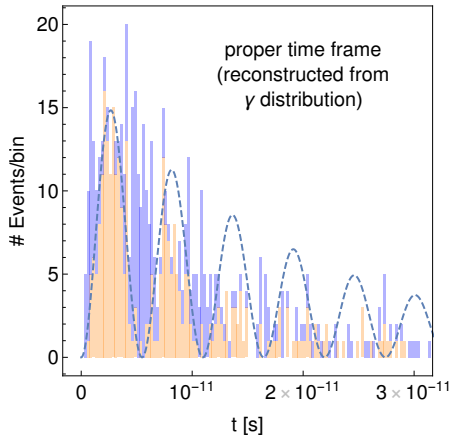

(d) Reconstructed oscillating pattern in the proper frame for a Monte Carlo generated event sample of 620 events, which corresponds to the expected number of μjj events to take place inside the VELO for the high-luminosity phase of LHCb with 380 fb^{-1}. This figure is published in ref. [5].

Figure 59: Shown is the signature from heavy neutrino-antineutrino oscillations for the benchmark point $\overline{M} \approx M = 7$ GeV, $\theta^2 = 10^{-5}$ in the linear seesaw case for the IO of the light neutrino masses at the HL-LHCb. The orange and blue areas denote the fractions of LNV events to LNC events which are given by the processes $pp \to \ell^{\pm}(\ell^{\pm}jj)_{\text{displaced}}$ and $pp \to \ell^{\pm}(\ell^{\mp}jj)_{\text{displaced}}$ that take place inside LHCb's VELO, respectively.

In conclusion, this signature demonstrates great possibilities, since it would provide a proof for the existence of LNV and allow a deep insight into the neutrino mass mechanism. Therefore, the search for this signature should be an integral part of the future collider experiments.

11.2 PROBING LEPTOGENESIS AT FUTURE COLLIDERS VIA DISPLACED VERTICES

Low scale seesaw scenarios with $n_s = 2$ sterile neutrinos can not only give an explanation for the neutrino mass differences observed in neutrino oscillation experiments but also give simultaneously an explanation for the baryon asymmetry of the universe (BAU). For heavy neutrino masses below the electroweak scale, the BAU can be generated by the mechanism referred to as leptogenesis from right-handed neutrino oscillations [177, 186]. This mechanism can give rise to successful leptogenesis for heavy neutrinos in the mass range below 50 GeV and with active-sterile mixings angles which could be probed by the displaced vertex search at future colliders [6, 269]. We discuss how to test the viable region for leptogenesis via the displaced vertex search of the heavy neutrino with masses above 5 GeV at future e^+e^- colliders as-partly published in ref. [6]. For masses of the heavy neutrinos below 5 GeV, heavy neutrinos could be better probed in the decay of mesons, and fixed target experiments such as the NA62 experiment [401–403] and the proposed SHiP experiment [403–405].

In the general instalment of the low scale seesaw scenario with $n_s = 2$ sterile neutrinos, i.e. with all the allowed perturbations in the neutrino mass matrix, the active-sterile mixing is more generally expressed by the matrix elements $|\mathcal{U}_{\alpha i}|^2$ in eq. (4.36). The relevant parameters for the active-sterile mixing are the squared active-sterile mixing angles $|\mathcal{U}_\alpha|^2 = \sum_{i=4,5} |\mathcal{U}_{\alpha i}|^2$ and the active-sterile mixing squared $\mathcal{U}^2 = \sum_\alpha \mathcal{U}_\alpha^2$. While the relevant leptogenesis parameters of the heavy neutrino masses are the average mass $\overline{M}$ and the mass splitting ΔM of the heavy neutrinos, cf. eq. (9.4). The masses of the heavy neutrinos are required to be almost degenerate, i.e. $\Delta M \ll \overline{M}$, therefore the average mass can be well approximated by the heavy neutrino mass parameter $M \approx \overline{M}$. In the limit of approximately intact lepton-number-like symmetry, i.e. vanishing perturbations, they are translated to the usual quantities

$$|\mathcal{U}_\alpha|^2 \to |\theta_\alpha|^2\,, \qquad \mathcal{U}^2 \to \theta^2\,, \qquad \overline{M} \to M\,, \quad \text{and} \qquad \Delta M \to 0 \tag{11.5}$$

as was previously discussed for the symmetry protected seesaw scenario in chapter 4.3

The viable active-sterile mixing for successful leptogenesis depends not only on $\mathcal{U}^2$ but also on the different flavour mixing ratios $|\mathcal{U}_\alpha|^2/\mathcal{U}^2$ for $\alpha = e, \mu$ and τ, i.e., the composition of the flavour mixing ratios. An example for the viable parameter region, including the constraints from neutrino oscillation data in the case of NO and IO of the light neutrino masses, is shown for a benchmark point of the heavy neutrino mass in fig. 60. The reader is referred to [6] for details on the leptogenesis parameter region and its performed scan. The parameter region for leptogenesis in the low scale seesaw

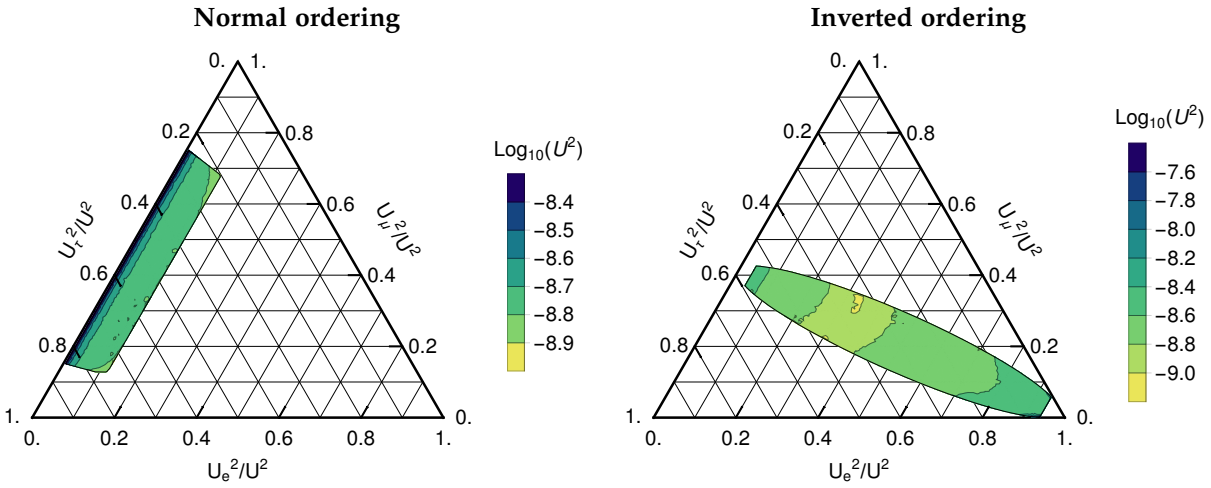

Figure 60: Shown is the viable parameter region for leptogenesis that is consistent with neutrino oscillation data for the different flavour mixing ratios in the NO (right) and IO (left) case with an average mass $\overline{M} = 30$ GeV. The parameters can be translated to the usual quantities see eq. (11.5). The color indicates the largest possible mixing angle $\mathcal{U}^2$. The figure is reprinted from ref. [6].

scenario consistent with neutrino oscillation data has been investigated for instance in ref. [6, 258, 269, 270, 403, 406–414].

Although, the leptogenesis parameter region has often been compared to the sensitivity of future experiments, e.g., [252, 269, 270, 391, 404, 414, 415], the comparison has been done by projecting these two onto the $\overline{M} - |\mathcal{U}_\alpha|^2$ plane for each flavour. This, however, bears the risk that the comparison of a parameter point in the projected plane $\overline{M} - |\mathcal{U}_\alpha|^2$ is not consistent. Because it does not immediately follow that this parameter point can be probed by the displaced vertex search. Especially when the sensitivity of the future experiments are calculated for fixed flavour mixing ratios. A given parameter point of successful leptogenesis in the $\overline{M} - |\mathcal{U}_\alpha|^2$ plane has many possible flavour mixing ratio compositions,cf. fig. 60, which results in different experimental sensitivities since they also depend on the flavour mixing ratios. Therefore, it is important to consider the relative size of the active-sterile mixing angles. To make it consistent, each point of the parameter region for successful leptogenesis is checked whether it also fulfils the requirement to produce a large enough expected number of displaced vertex events with its corresponding flavour mixing ratios at future colliders. Here we focus on future electron-positron colliders as an example. Although, the proposed hadron and electron-proton colliders should also be capable albeit with different performance.

The expected number of displaced vertex events from visible decays of the heavy neutrinos, N_{dv}, is discussed in eq. (8.8) for future e^+e^- colliders. From the visible decays, the semileptonic decays of the heavy neutrino are the most interesting since they allow to probe the active-sterile mixing angle $|\mathcal{U}_\alpha|$ from the charged lepton $\ell_\alpha^\pm$. The expected number of semileptonic displaced vertex events, N_{sl}, is obtained by substituting the branching ratio of the visible decays in the formula for N_{dv} with the branching ratio into semileptonic decays $\mathrm{BR}(N \to \Sigma_\alpha \ell_a jj) \simeq 0.5 \times \Sigma_\alpha |\mathcal{U}_\alpha|^2/\mathcal{U}^2$. As discussed in section 8.3, between

the boundaries of $x_{min} = 10$ μm inside the inner region and the outer radius of the tracker $x_{max} = 1.22$ m the displaced vertex search is free of SM background assuming a SiD-like detector for the proposed future e^+e^- colliders. A viable parameter point of leptogenesis is required to have at least 4 expected semileptonic events N_{sl} which corresponds to a signal above the 2σ level.

As we discussed in section 6.2.1, N_{sl} is subdue to different dependencies on the active-sterile mixing angles depending on the dominating production process of the heavy neutrino for the physics runs at future e^+e^- colliders. For the Z-pole run at e^+e^- colliders, N_{sl} depends mostly on U^2 because the heavy neutrino production proceeds via the s-channel Z boson diagram, which depends on all $|U_\alpha|$ equally. Therefore, the parameter region in the $\overline{M} - U^2$ plane where leptogenesis gives rise to an expected number of 4 events and above is uniquely defined. For the physics runs above the Z-pole, N_{sl} depends not only on U^2 but also on $|U_e|^2$. The latter is due to the production cross section of the heavy neutrino to proceed via the t-channel W bosons exchange with the incident electron-positron beams. Therefore, the dependency on $|U_e|^2$ is differently than for $|U_\mu|^2$ and $|U_\tau|^2$. Contrarily to the Z-pole run, the parameter region is not uniquely defined in the $\overline{M} - U^2$ plane and it depends on the flavour mixing ratios $|U_\alpha|^2/U^2$, mostly for the electron flavour. In this case, two regions are considered instead: A region that is testable irrespective of the flavour mixing ratio composition, which is referred to as the "guaranteed discovery" region, and a region that yields only for the most optimistic flavour ratio composition at least $N_{sl} \geqslant 4$, which is referred to as the "potential discovery" region.

Fig. 61 shows the resulting parameter region for successful leptogenesis which could be probed via the displaced vertex search of the semileptonic decays of the heavy neutrinos at future e^+e^- colliders. This corresponds to the region that is enclosed by the blue "Leptogenesis (upper bound)" line and the coloured lines for considered physics runs. The left (right) column shows the NO (IO) case of the light neutrino masses. In the top row, the Z-pole run of the FCC-ee with an integrated luminosity of 110 ab^{-1} is considered. With its large integrated luminosity the FCC-ee can probe a large part of the viable parameter space for leptogenesis. In the middle row, the ILC is considered with its Z-pole run with 0.1 ab^{-1} and high-energy run at $\sqrt{s} = 500$ GeV with 5 ab^{-1}. In the bottom row, the CEPC is considered with a Z-pole run with 0.1 ab^{-1} [171] and a Higgs physics run at $\sqrt{s} = 240$ GeV with 5 ab^{-1} [172]. For the physics runs above the Z-pole, only in the IO case of the light neutrino masses does the viable region for leptogenesis yield a large enough number of events for the displaced vertex search. Because the flavour mixing ratio of the electron flavour is suppressed in the NO case, cf. fig. 60.

[171] In an early iteration, the CEPC considered a short physics run at the Z-pole ref. [416].

[172] The result of the Higgs physics run applies also to the FCC-ee since they both consider the same center-of-mass energy and integrated luminosity.

Being able to measure the active-sterile mixing angle $|U_\alpha|^2$ and the corresponding flavour mixing ratios $|U_\alpha|^2/U^2$ of the heavy neutrinos at a future experiment is crucial in order to test whether the heavy neutrinos can also be responsible for successful leptogenesis.

The flavour mixing ratio composition can be determined by measuring the numbers of the semileptonic decays of the heavy neutrino with a charged lepton ℓ_α, labelled as $\hat{N}_\alpha$ for $\alpha = e, \mu, \tau$. The corresponding expected number of events N_α is obtained by substituting the branching ratio in the formula

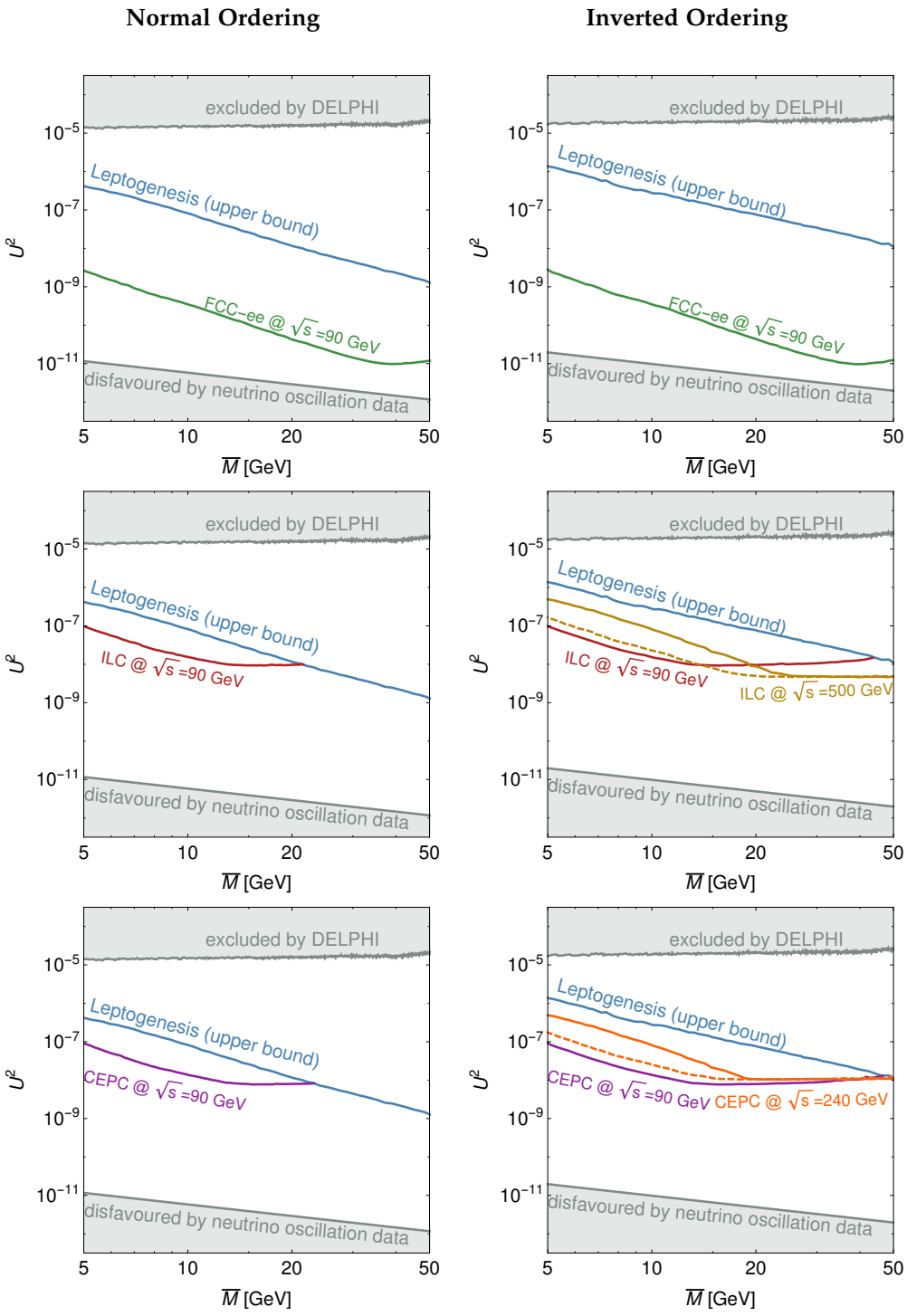

Figure 61: Below the "Leptogenesis (upper bound)" line the parameter region for successful leptogenesis is shown. The other colored lines correspond to sets of parameters (consistent with leptogenesis) that give rise to an expected number of displaced vertex events of 4 via the semileptonic decays of the heavy neutrinos for the considered future colliders, for details see text. The solid and dashed lines correspond to the "guaranteed discovery" region and "potential discovery" region. The grey area is excluded by DELPHI (top) and disfavoured by neutrino oscillation data (bottom). The parameters can be translated to the usual quantities see eq. (11.5). The figure is reprinted from ref. [6].

for N_{dv} with the branching ratio $BR(N \to \ell_\alpha jj) \simeq 0.5 \times |\mathcal{U}_\alpha|^2/\mathcal{U}^2$ which results in $N_\alpha = N_{sl} \times |\mathcal{U}_\alpha|^2/\mathcal{U}^2$. In this context also the precision by which the future experiments could determine the individual flavour mixing ratios $|\mathcal{U}_\alpha|^2/\mathcal{U}^2$ should be discussed. For estimating the precision in measuring the flavour mixing ratios, only the statistical uncertainties are considered. The number of semileptonic displaced vertex events, $\hat{N}_{sl}$, is Poisson distributed with mean N_{sl}, while the numbers $\hat{N}_e$, $\hat{N}_\mu$ and $\hat{N}_\tau$ follow a multinomial distribution with probability $p_\alpha = |\mathcal{U}_\alpha|^2/\mathcal{U}^2$ for $\alpha = e, \mu, \tau$. The probability density function for a number of $\hat{N}_\alpha$ events out of $\hat{N}_{sl}$ events is given by

$$P(\hat{N}_{sl}, \hat{N}_\alpha) = \frac{e^{-N_{sl}} \times N_{sl}^{\hat{N}_{sl}}}{\hat{N}_{sl}!} \binom{\hat{N}_{sl}}{\hat{N}_\alpha} p_\alpha^{\hat{N}_\alpha} (1-p_\alpha)^{\hat{N}_{sl}-\hat{N}_\alpha}\,, \tag{11.6}$$

which results in the expected number of events $\langle \hat{N}_{sl} \rangle = N_{sl}$ and $\langle \hat{N}_\alpha \rangle = N_{sl} \times p_\alpha = N_\alpha$. The precision in measuring the flavour mixing ratios is defined as the ratio of the standard deviation δ to the expected value which is determined by the statistical uncertainty on the ratio $\hat{N}_\alpha/\hat{N}_{sl}$:

$$\frac{\delta(|\mathcal{U}_\alpha|^2/\mathcal{U}^2)}{|\mathcal{U}_\alpha|^2/\mathcal{U}^2} = \frac{\sqrt{\text{Variance}(\hat{N}_\alpha/\hat{N}_{sl})}}{\langle \hat{N}_\alpha/\hat{N}_{sl} \rangle}\,. \tag{11.7}$$

The expected value and the variance can be calculated from the probability density function

$$\langle \hat{N}_\alpha/\hat{N}_{sl} \rangle = \langle \hat{N}_\alpha \rangle / \langle \hat{N}_{sl} \rangle = N_\alpha/N_{sl}\,, \tag{11.8}$$

$$\begin{aligned}\text{Variance}(\hat{N}_\alpha/\hat{N}_{sl}) =& e^{-N_{sl}}(1-p_\alpha) \\ & \times (1 - p_\alpha(1 - \gamma_E + \Gamma(0, -N_{sl}) + \ln(-N_{sl}))\,,\end{aligned} \tag{11.9}$$

where γ_E is the Euler-Mascheroni constant and Γ is the incomplete gamma function. The precision for determining the flavour mixing ratios can be approximated to

$$\frac{\delta(|\mathcal{U}_\alpha|^2/\mathcal{U}^2)}{|\mathcal{U}_\alpha|^2/\mathcal{U}^2} \approx \sqrt{\frac{1}{N_\alpha} - \frac{1}{N_{sl}}}\,. \tag{11.10}$$

Note that unlike for the usual propagation of error where the uncertainties add, here they do not since $\hat{N}_\alpha$ is not independent of $\hat{N}_{sl}$.

The parameter region for successful leptogenesis is confronted with the precision on the flavour mixing ratio $|\mathcal{U}_e|^2/\mathcal{U}^2$ as an example in fig. 62. For the example mass of $\overline{M} = 30$ GeV, the Z-pole run of the FCC-ee could probe $|\mathcal{U}_e|^2/\mathcal{U}^2$ with a precision close to the 5% and at sub-percent level in the case of NO and IO, respectively. While the physics runs above the Z pole allows to test $|\mathcal{U}_e|^2/\mathcal{U}^2$ up to the 5%-10% level. Higher precision could be achieved when going to lower masses since the possible number of displaced vertex events increases. The parameter region for the other flavour mixing ratios confronted with the precision can be found in ref. [6].

Also the measurement of the heavy neutrino mass parameters $\overline{M}$ and ΔM are relevant in order to probe leptogenesis. For the measurement of the heavy neutrino mass M, the invariant mass measurement of the decay products of

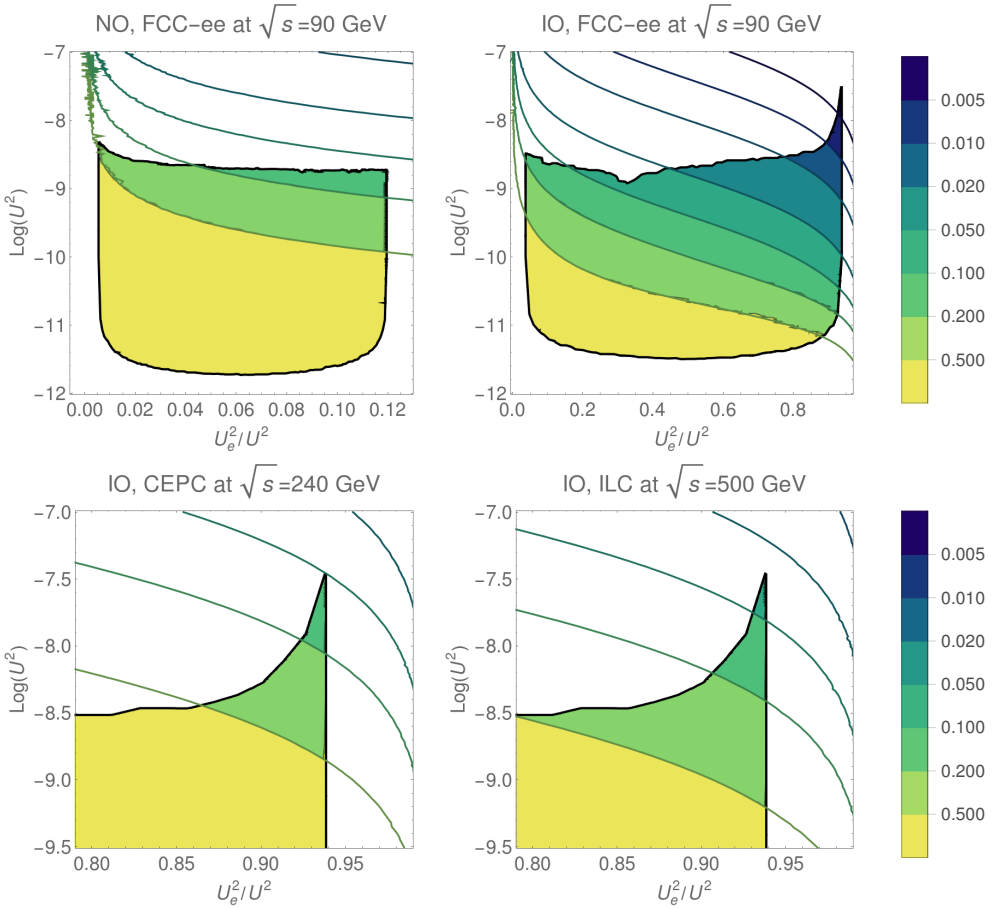

Figure 62: Shown is the parameter region for successful leptogenesis in the $|\mathcal{U}_e|^2 - \mathcal{U}^2$ plane for the example mass $\overline{M} = 30$. The color indicates the achievable precision in measuring the flavour mixing ratio for the FCC-ee with $\sqrt{s} = 90\,\text{GeV}$ in the top row for NO (left) and IO (right), and in the bottom row for the CEPC with $\sqrt{s} = 240\,\text{GeV}$ IO (left) and ILC $\sqrt{s} = 500\,\text{GeV}$ IO (left). Since the precision also depends on the flavour ratio composition via the expected number of events, the composition with the most conservative precision is chosen. The parameters can be translated to the usual quantities see eq. (11.5). The figure is reprinted from ref. [6].

the displaced heavy neutrino decay would yield the heavy neutrino mass M. The semileptonic decays of the heavy neutrino allow to directly compute the invariant mass $M(\ell jj)$. The precision on the jet-mass reconstruction with the CLIC's and ILC's Pandora particle flow algorithm is $\sim$ 4% for jet energies of 45 GeV [417]. The precision of the invariant mass measurement $M(\ell jj)$ has been assumed in ref. [6] to be of the same order as the jet-mass reconstruction capabilities of the CLIC and ILC. In ref. [6], was also argued that the leptonic decays of the heavy neutrino into the $\nu\mu^+\mu^-$ final state could provide more precision in measuring the heavy neutrino mass. Although the muon and antimuon could be measured precisely, the light neutrino would not be detected. But the momentum of the heavy neutrino could still be reconstructed from the requirement that the momentum originates from the primary vertex, which could be used to reconstruct the invariant mass $M(\nu\mu^+\mu^-)$.

With the measurement of the heavy neutrino mass $M \approx \overline{M}$ and the active-sterile mixing angles $|\mathcal{U}_e|^2$, $|\mathcal{U}_\mu|^2$ and $|\mathcal{U}_\tau|^2$, one can check whether the re-

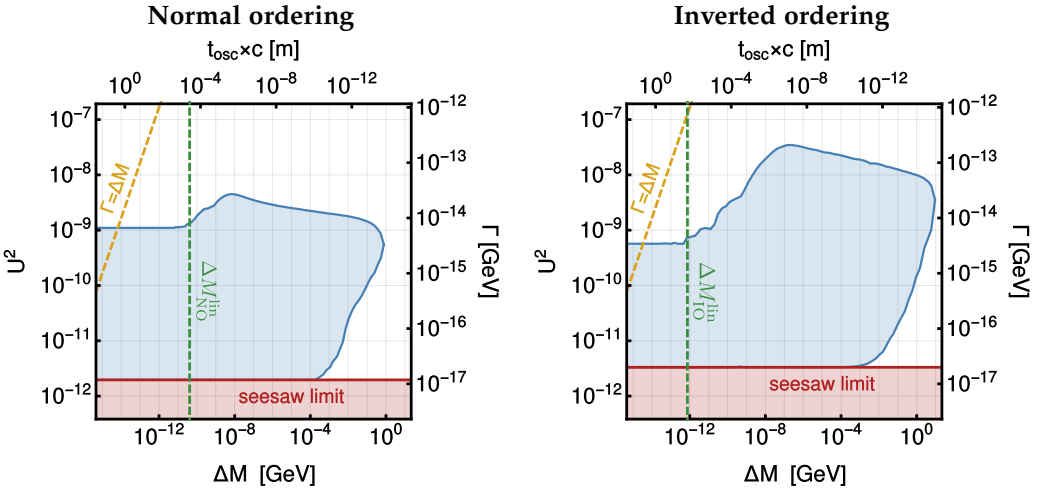

Figure 63: Shown is the viable parameter space for leptogenesis by the blue region in the $\Delta M - U^2$ plane for the average mass $\overline{M} = 30$ GeV in the case of NO (left) and IO (right). The yellow dashed line satisfies $\Delta M = \Gamma$ for the total decay width of the heavy neutrino Γ. The green dashed line correspond to the predicted value of heavy neutrino mass splitting in the linear seesaw case, confer eq. (9.22). The corresponding oscillation period for the heavy neutrino-antineutrino oscillation t_{osc} is given by eq. (11.1). The parameters can be translated to the usual quantities see eq. (11.5). The figure is reprinted from ref. [6].

alised parameter point, which is smeared out due to the uncertainties on the mass as well as the mixing angles, lies within the parameter region for successful leptogenesis. This would only constitute a first step towards probing leptogenesis as the mechansism for baryogenesis, since in order to generate the baryon asymmetry also a viable mass splitting ΔM of the heavy neutrinos is required. Therefore, the measurement of ΔM and comparing it to the allowed parameter space by leptogenesis is the crucial next step. The parameter region for successful leptogenisis in the $\Delta M - U^2$ plane is shown in fig. 63.

For the largest viable mass splittings, which are around the GeV scale, ΔM could be inferred directly from the kinematic measurements of the heavy neutrino masses at future colliders.

As we discussed in chapter 9, non-zero ΔM can lead to a considerable amount of LNV when the width of the heavy neutrino Γ is of the same order and below the heavy neutrino mass splitting. Therefore, there are also possibilities to infer information on ΔM by studying lepton-number violating signatures. In order the measure lepton-number violating effects of the heavy neutrinos at colliders, one might be better off to search these at future hadron or electron-proton colliders. This is because LNV is well hidden at lepton colliders while the others feature unambiguous signals for LNV.

Therefore, hadron and electron-proton colliders provide the possibility to infer ΔM from non-trivial ratios between the lepton-number violating and lepton-number conserving final states involving the heavy neutrinos. That is to say, ΔM is inferred from a non-trivial $R_{\ell\ell}$ ratio, cf. eq. (9.9), for a given decay width Γ of the heavy neutrino. Non-trivial ratios emerge when the heavy neutrino mass splitting is of the same order as the decay width of the heavy neutrino as we have seen in fig. 48. The yellow dashed line, for which $\Gamma = \Delta M$ is satisfied, indicates a possible parameter region of the heavy neutrino mass splitting that could be probed in fig. 63. In this way, viable

heavy neutrino mass splittings below $\sim 10^{-14}$ GeV could be probed. The parameter region further to right from the $\Gamma = \Delta M$ line features $R_{\ell\ell}$ ratios close to 1.

The other possibility has been demonstrated previously in section 11.1, by observing the oscillation pattern from heavy neutrino-antineutrino oscillations from which the oscillation period and hence the heavy neutrino mass splitting could be inferred. Therein we concluded that future hadron colliders provide good prospects to reconstruct the oscillations for the case of the linear seesaw with NO and IO of the light neutrino masses provided enough displaced vertex events. The FCC-hh and SppC would provide a large enough number of displaced vertex events in order to probe the heavy neutrino mass splitting with a mixing of U^2 even below $\sim 10^{-9}$. The heavy neutrino mass splitting in linear seesaw with NO and IO of the light neutrino masses are indicated by the green dashed line in fig. 63. However, a detailed investigation is necessary in order to estimate the sensitivity of the future collider experiments in the leptogenesis parameter region $\Delta M - U^2$.

Future collider experiments feature prospects to measure the active-sterile mixing angles with few percent level precision for parts of the sterile neutrino parameter space, heavy neutrino mass and heavy neutrino mass splitting. This would allow to confront these measurements with the parameter region for successful leptogenesis which would probe low scale seesaw scenarios as an explanation for the BAU.

12 SUMMARY AND CONCLUSIONS

Focusing on low scale seesaw scenarios with $n_s = 2$ sterile neutrinos which have masses around the electroweak scale, we studied several aspects of the sterile neutrino phenomenology and assessed the prospects of various searches for sterile neutrinos at future colliders. Low scale seesaw scenarios give a natural explanation for the smallness of neutrino masses in terms of symmetries. They allow for large and unsuppressed neutrino Yukawa couplings (equivalently active-sterile mixing angles) which makes this scenario testable at present and future colliders. The used benchmark scenario captures the essential features of these low scale seesaw scenarios while being more general as specific models by allowing additional sterile neutrinos which are decoupled from the collider phenomenology. Hence it is a valuable scenario to investigate the sterile neutrino phenomenology at future colliders experiments in terms of the sterile neutrino parameters given by the mass parameter M and the active-sterile mixing angles θ_α for $\alpha = e$, μ, τ. In particular, we investigated a Higgs boson production mechanism from the decays of the heavy neutrinos, LNV as the manifestation of the heavy neutrino-antineutrino oscillations, LFV from the heavy neutrinos, displaced vertex searches from long-lived heavy neutrinos and the possibilities to resolve heavy neutrino-antineutrino oscillations as well as to test the viable leptogenesis parameter space for future colliders. We considered future e^+e^- colliders (CEPC, FCC-ee, ILC), future pp colliders (HL-LHC, FCC-hh, SppC) and future e^-p collider (LHeC, FCC-eh). A summary of the findings is presented in fig. 64 as an illustration.

We studied a novel production mechanism of the Higgs boson - the on-shell production of a heavy neutrino and its subsequent decay into a Higgs boson. We found that up to a few percent of the possibly produced Higgs bosons could stem from this contribution at e^+e^- and e^-p colliders, which could lead to a deviation of the measured Higgs boson properties with the SM prediction. Furthermore, we investigated the mono-Higgs channel in e^+e^- collisions and derived sensitivities to the sterile neutrino parameters by simulating the signal and the SM background at the reconstructed level for various physics runs. The considered physics runs demonstrated comparable sensitivities to the active-sterile mixing angle $|\theta_e|$ whereas for M the physics runs with higher center-of-mass energies are able to probe larger masses of the heavy neutrinos. The summarised sensitivity for the mono-Higgs search channel at future e^+e^- colliders is shown by the line labelled "Higgs" in fig. 64.

We investigated the widely discussed signature from sterile neutrinos at colliders - lepton number violation. The dominating production processes of the heavy neutrinos only feature unambiguous signals for lepton number violation at pp and e^-p colliders. We studied LNV from heavy neutrino-antineutrino oscillations as the effect of heavy neutrinos with nearly degenerate masses that are separated by a mass splitting ΔM. In order to asses

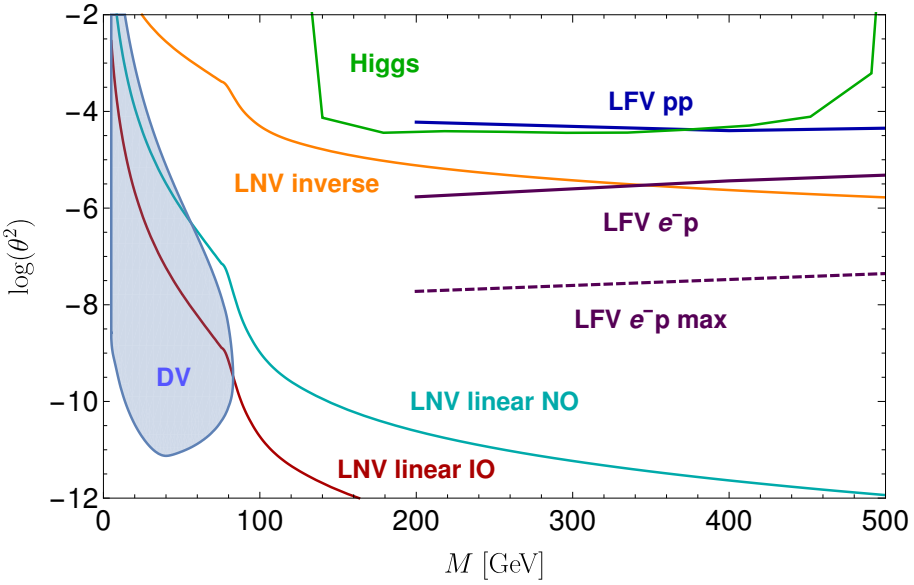

Figure 64: Shown is a summary of the findings for illustrative purposes:
•"Higgs" denotes the 1σ sensitivity to $|\theta_e|^2$ of the mono-Higgs search channel with $\sqrt{s} = 500$ GeV at e^+e^- colliders, confer fig. 31.
•"DV" denotes the sensitivity to θ^2 of the displaced vertex search for $\sqrt{s} = 90$ GeV at the FCC-ee, confer fig. 38.
•"LNV inverse" denotes the $R_{\ell\ell} = 0.1$ contour for the inverse seesaw case with $m_{\nu_i} = 0.1$ eV, confer fig. 49.
•"LNV linear NO/IO" denotes the $R_{\ell\ell} = 0.1$ contour for the linear seesaw case with NO and IO of the light neutrino masses, confer fig. 49.
•"LFV pp" denotes the sensitivity to $|\theta_e\theta_\mu|$ at the 95% C.L. of the lepton-flavour violating $e^\pm\mu^\mp jj$ process for the FCC-hh, confer fig. 56.
•"LFV e^-p (max)" denotes the estimated (maximal achievable) 1σ sensitivity to $|\theta_e\theta_\alpha|$ for $\alpha \neq e$ of the lepton-flavour violating $\ell_\alpha^- jjj$ final state for the FCC-eh, confer fig. 53.

its relevance at colliders, we considered the lepton-number violating transition probabilities versus the lepton-number conserving survival probabilities of the heavy neutrino and antineutrino states. We therefore calculated the heavy neutrino mass splitting ΔM for the linear and inverse seesaw cases. We found that ΔM is predicted in the linear seesaw case for NO and IO of the light neutrino masses and its magnitude is determined by the light neutrino masses. From these mass splittings, we derived the parameter regions where the ratio for LNV versus LNC becomes larger than 10% at colliders. Depending on the realisation of the light neutrino masses, searches for heavy neutrinos could therefore probe LNV around and below the "LNV inverse" line in fig. 64 in the favourable case of the inverse seesaw. We remark that this line is not fixed but varies with ΔM. However in the linear seesaw case, LNV is predicted and expected with ratios larger than 10% below the "LNV linear NO" and "LNV linear IO" lines in fig. 64 for the two possible orderings of the heavy neutrino masses. We concluded that searches for lepton-number violating signatures of the heavy neutrinos with masses above the 100 GeV range might not be promising probes since the rates for LNV can be quite suppressed at the LHC and future colliders.

For masses of the heavy neutrino above the 100 GeV range, lepton flavour violating signatures might, therefore, be more promising. Their signal strength is not suppressed such as for LNV since LFV can be realised in a lepton-number conserving way. However, this comes at the expense of possible SM backgrounds but only at the reconstructed level. On the parton level, LFV

from heavy neutrinos would even provide an unambiguous signal at pp and e^-p colliders. We estimated the sensitivities on the parton level for the lepton-flavour violating $\ell_\alpha^\pm \ell_\beta^\mp jj$ $\alpha \neq \beta$ and $\ell_\alpha^- jjj$ $\alpha \neq e$ final state at hadron and electron-proton colliders, respectively. Therein, we considered a case where we estimated the SM background, which is represented by the line labelled "LFV e^-p" for the e^-p collider in fig. 64 and the maximal achievable case where the background can be completely separated from the signal, which is represented by the line labelled "LFV e^-p max" for the e^-p collider in fig. 64. These estimated sensitivities for LFV to the active-sterile mixing angles demonstrate that the sensitivity could improve considerably if the SM backgrounds could be well separated in an analysis at the reconstructed level. We further investigated the $e^\pm\mu^\mp jj$ final state at the reconstructed level, where we simulated the signal and backgrounds for the HL-LHC and the FCC-hh. The resulting sensitivities is shown by the line labelled "LFV pp" in fig. 64. A finding of a signal would be in tension with the constraints on $\mu \to e\gamma$ only when the results are interpreted strictly in the case of two sterile neutrinos only. The investigation of the $e^\pm\tau^\mp jj$ and $\mu^\pm\tau^\mp jj$ final states, although more challenging, could provide great discovery potential due to weaker constraints.

For masses of the heavy neutrino below the 100 GeV range, we investigated the search for long-lived heavy neutrinos at colliders which give rise to the displaced vertex signature. Although, there are little to no SM backgrounds, we discussed possible SM backgrounds that could fake the signature at lepton colliders for different detection regions of the ILC's Silicon Detector. In principle, each detector component could record and probe the displaced vertex signal from the decay of heavy neutrinos. We derived estimated limits for the displaced vertex search at LHCb from an analysis of LHCb's vertex locator with run 1 data. We found that with run 1 data alone, LHCb would provide the most stringent limits on the active-sterile mixing in the mass range of 5-10 GeV. Furthermore, we estimated the future sensitivities to the sterile neutrino parameters for the future e^+e^-, pp, e^-p colliders, which is represented by the region labelled "DV" in fig. 64.

Moreover, the displaced vertex search is a very powerful tool, since it allows to probe LNV at pp and e^-p colliders and to test leptogenesis.

For the investigation of LNV from the heavy neutrino-antineutrino oscillations via the displaced vertex search, we studied the ensuing oscillation pattern of the lepton-number violating and conserving decay spectra of the heavy neutrinos. Although the oscillation pattern is smeared out in position space due to the distribution of Lorentz factors at pp colliders, it can be reconstructed in the proper time frame. A very important result is that we demonstrated this reconstruction to be possible for the predicted mass splitting of the linear seesaw with IO of the light neutrino masses and that the oscillation time is resolvable at the LHCb experiment during the HL-LHC. More generally this would allow one to infer the heavy neutrino mass splitting from the resolved oscillation time. Further investigations such as the testable parameter region by this search would be desirable. The FCC-hh and SppC would provide even better prospects since they allow for larger number of events. Therefore, the search for heavy neutrino-antineutrino oscillations should be an integral part of the future collider experiments.

The possibility to test the viable parameter region for leptogenesis via the displaced vertex search at future e^+e^- colliders is discussed. We moreover derived the precision for measuring the active-sterile mixing angles which is crucial in determining the flavour composition. We found that a significant part of the parameter region can be probed via the displaced vertex search at future e^+e^- colliders.

The various collider types are complementary in many ways such as providing various testable signatures, having different active-sterile mixing angle dependencies and probing sterile neutrinos at different center-of-mass energies. The pp and e^-p colliders provide pronounced signatures for LNV and LFV with the leading order production processes of the heavy neutrinos. The hadron colliders are versatile in the sense that they are equally sensitive to all active-sterile mixing angles. They can be well suited for displaced vertex searches, probing LNV and testing leptogenesis. Although, e^+e^- colliders do not provide lepton-number violating and lepton-flavour violating signatures that are as pronounced as at pp and e^-p colliders, they have solid discovery potential via the displaced vertex, the mono-Higgs search and also via tests of the electroweak precision observables due to the modification of the predictions. They can also be well suited to test the viable parameter region for leptogenesis. The e^-p colliders are present in every search discussed in this thesis. They provide probes for LNV, LFV, displaced vertices and also for Higgs bosons from heavy neutrinos. But the sensitivities to the sterile neutrino parameters might be a bit weaker compared to the corresponding searches at e^+e^- and pp colliders except for LFV which they can be well suited for.

Finally, the different mass scales of the sterile neutrinos may have an impact on cosmological, astrophysical and particle physics related observables, which needs an involvement of different disciplines in order to thoroughly investigate all aspects of this class of new physics. The collider searches for heavy neutrinos are one of the many aspects of the sterile neutrino phenomenology. The collider searches should be used to their fullest if these expensive future colliders are built. The future collider experiments are powerful tools not only to probe active-sterile mixings and masses of the heavy neutrinos but also to test leptogenesis and to probe the heavy neutrino mass splitting in a unique way.

Part IV

APPENDIX

APPENDIX

A.1 SIGNAL SIGNIFICANCE

A.1.1 *Large number of events*

For the discussion of the signal significance, we follow the discussions in ref. [17, 418–421].

The goal is to establish an estimation of the discovery potential of the proposed future experiments in the search for a signal from heavy neutrinos. For this estimation, we calculate or simulate from Monte Carlo event generators the expected number of signal events $N_S = \sigma_S \times \mathcal{L}$ from the signal cross section σ_S and the proposed target integrated luminosity $\mathcal{L}$ of the collider experiments. Let us consider that SM processes can lead to the same signature as the heavy neutrino signal process, these processes constitute the background to the signal and the expected number of background events is calculated or simulated accordingly to $N_B = \sigma_B \times \mathcal{L}$. Hence, the total expected number of events is given by $\langle n \rangle = N_S + N_B$, which can lead to an excess or deficit [173] of the expected number of events when compared with N_B. In high-energy physics, the observed number of events n is assumed to be a Poisson variable. The probability density function is given by

[173] A deficit in the total number of expected events could stem from a smaller total cross section due to destructive interference of amplitudes [418].

$$\mathcal{P}(n;\mu) = \frac{\mu^n}{n!} e^{-\mu}\,, \tag{A.1}$$

where n would corresponds to the number of observed events and μ is the expected number of events. The standard deviation σ is given by $\sqrt{\mu}$ for a Poisson distribution. Since we only know the expected number of events for the signal and background, the Poisson distributions $P(n;\mu = N_S + N_B)$ and $P(n;\mu = N_B)$ have to be compared in order to determine if there is new physics present. This is a typical application of hypothesis testing in particle physics experiments. One can consider the null hypothesis H_0 as no new physics ($\mu = N_B$) versus the alternative hypothesis H_1 as new physics ($\mu = N_S + N_B$).

To quantify the degree of confidence between the experimental observation and a hypothesis, let us consider a test statistic t, which is a random variable, and is observed to be t_o [174]. We further consider that the hypothesis H_0 is true, then the test statistic has a probability density function $P(t|H_0)$ [420, 421]. Assuming that observations of t can be categorised into those more consistent with H_0 for smaller values of t while larger values of t are less consistent with H_0, then the p-value can be defined as [420, 421]

[174] In our case the test statistics is the number of events.

$$p(t_o) = P(t > t_o|H_0) = \int_{t_0}^{\infty} P(t|H_0)dt\,. \tag{A.2}$$

The p-values is a probability to observe a t which is greater or equal t_o. This gives a measure of the consistency of the observed test statistic t_o, since a small p-value would correspond to a small probability that H_0 is true.

Suppose that for the test statistic n the experiment observed n_o number of events. The p-value for the hypothesis H_0 corresponds to the probability to measure n_o or more events from the background alone and is given by

$$p(n_o) = P(n > n_o|H_0) = \sum_{n=n_o}^{\infty} \mathcal{P}(n;\mu = N_B) = 1 - \sum_{n=0}^{n_o-1} \mathcal{P}(n;\mu = N_B)$$
$$= 1 - \sum_{n=0}^{n_o-1} \frac{N_B^n}{n!} e^{-N_B} . \tag{A.3}$$

In other words, the p-value gives here the probability that random fluctuations of the background would give the observed number of events. In the case of large number of events, the Poisson distribution can be very well approximated by a normal distribution. In this limiting case, the statistical significance $\mathcal{S}$ is related to the p-value as [421]

$$\int_{-\mathcal{S}}^{\mathcal{S}} \frac{1}{\sqrt{2\pi}} e^{-\frac{x^2}{2}} dx = 1 - p(n_o) , \tag{A.4}$$

$\mathcal{S}\sigma$	p-value
1σ	0.3173
2σ	4.55×10^{-2}
3σ	2.7×10^{-3}
5σ	5.7×10^{-7}

Table 13: Significance $\mathcal{S}$ and corresponding p-values, values from [17].

where the left-hand side of the equation gives the probability of the normal distribution within $\mathcal{S}$ standard deviations (or equivalently $\mathcal{S}\sigma$). The p-values for a significance of 1σ, 2σ, 3σ and 5σ are shown in tab. 13. The convention for evidence and discovery of new physics [17] is met when the significance is above 3σ and 5σ, respectively. The significance can then be derived from eq. (A.4). One of the simplest estimators for the significance, is given in terms of signal and background events by [418]

$$\mathcal{S} = \frac{N_S}{\sqrt{N_S + N_B}} \tag{A.5}$$

for large numbers of events. For our purposes, N_B is fixed after it has been calculated while the expected number of signal events are dependent on the active-sterile mixing angles θ_α for $\alpha = e, \mu, \tau$, which to good approximation can be expressed as (assuming a dependency of θ^2 on the cross section)

$$N_S = \sigma_S(\theta^2) \times \mathcal{L} = \sigma'_S \times \theta^2 \times \mathcal{L} = N'_S \times \theta^2 \times \mathcal{L} \tag{A.6}$$

where σ'_S and N'_S is the cross section and number of signal events normalised by the θ^2, respectively. From this relation, we define the sensitivity to the active-sterile mixing angles at $\mathcal{S}\sigma$ as the required value for the active-sterile mixing angles that gives rise to exact number of N_S that fulfils eq. (A.5) for that given value of $\mathcal{S}$.

A.1.2 *Small number of events*

For the analysis of signals with small number of events over the zero expected background, we consider classical confidence intervals as discussed

in ref. [422]. In general, confidence intervals $[\mu_{\text{lower}}, \mu_{\text{upper}}]$ are defined as the set that fulfils the condition $P(\mu \in [\mu_{\text{lower}}, \mu_{\text{lower}}]) = \alpha$ for each of the fixed μ. For the case of a Poisson distribution, for each element of μ inside this set its acceptance interval $[n_1, n_2]$ for the number of events is chosen such that $\mathcal{P}(n \in [n_1, n_2]; \mu) \geqslant \alpha$. We proceed by the method of "confidence belts" proposed in ref. [422] for the construction of confidence intervals, i.e. the choosing. We show the obtained confidence belts with $\alpha = 0.95$ and 0.9 in fig. 65 for the signal $N_S = \mu$ in the case of zero expected background $N_B = 0$ for low number of events n. The tables in fig. 65, gives the confidence intervals $[\mu_{\text{lower}}, \mu_{\text{upper}}]$ for the expected number of signal events over the zero background $N_B = 0$ for the 90% and 95% confidence levels (C.L.). For $N_S > \mu_{\text{upper}} = 3.09$ (2.43) at the 95% (90%) C.L., the $n = 0$ observation is outside the acceptance interval $[n_1, n_2]$ and therefore excluded at the given C.L. The sensitivity to the active-sterile mixing angles can be derived via eq. (A.6), which for $N_S > \mu_{\text{upper}} = 3.09$ (2.43) would establish a sensitivity of the signal over the zero background to the active-sterile mixing angles at the 95% (90%) C.L.

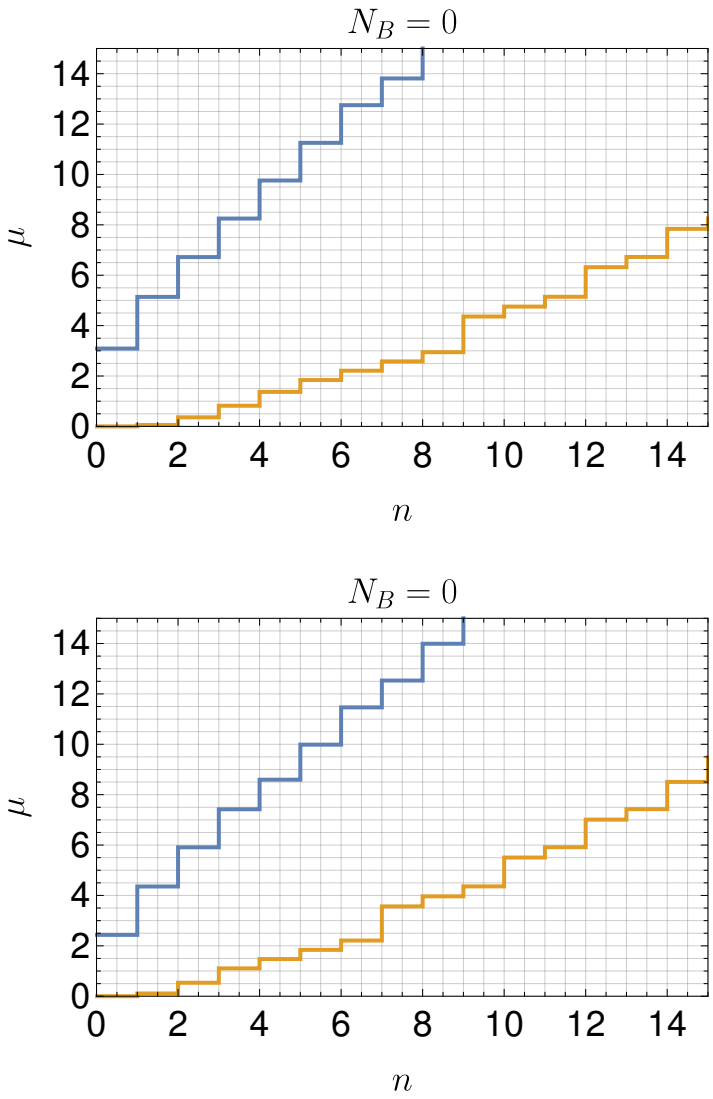

$N_B = 0$	95%C.L.
n	$[\mu_{lower}, \mu_{upper}]$
0	[0., 3.09]
1	[0.05, 5.14]
2	[0.36, 6.72]
3	[0.82, 8.25]
4	[1.37, 9.76]
5	[1.84, 11.26]
6	[2.21, 12.75]
7	[2.58, 13.81]
8	[2.94, 15.29]
9	[4.36, 16.77]
10	[4.75, 17.82]

$N_B = 0$	90%C.L.
n	$[\mu_{lower}, \mu_{upper}]$
0	[0., 2.43]
1	[0.11, 4.35]
2	[0.54, 5.91]
3	[1.1, 7.42]
4	[1.47, 8.59]
5	[1.84, 9.99]
6	[2.21, 11.47]
7	[3.56, 12.53]
8	[3.96, 13.99]
9	[4.36, 15.3]
10	[5.5, 16.5]

Figure 65: Shown are the calculated confidence belts after the method described in ref. [422] for the 95% and 90% C.L. for an expected signal mean μ in the presence of zero expected background of a Poisson process. The corresponding values of the upper and lower limit of the confidence intervals are also explicitly given.

A.2 MONO-HIGGS SIGNATURE: KINEMATIC CUTS

M [GeV]	P_{jj} [GeV]	N_S	N_B	N_S^{SM}
128	> 80	308	4287	25.1
141	> 70	3780	18627	1327
152	> 70	4846	18627	2951
163	> 70	5286	18627	3924
174	> 60	8759	34946	4387
185	> 70	5652	18627	4358
196	> 80	1935	4287	3762
218	> 70	4192	18637	1113
229	> 75	1505	8147	182
235	> 75	1966	8147	29

Table 14: Resulting number of events for the signal and background at $\sqrt{s} = 240$ GeV from the cut-and-count method performed in ref. [1]. Furthermore, events with 110 GeV $\leqslant M_{jj} \leqslant$ 125 GeV and $\not{E}_T > 15$ GeV have been selected. The numbers correspond to an integrated luminosity of 10 ab^{-1}. The table is reprinted from ref. [1].

M [GeV]	M_{jj} [GeV]	P_{jj} [GeV]	$\not{E}_T$ [GeV]	N_S	N_B	N_S^{SM}
128	100 - 130	100 - 170	—	384	109908	210
141	110 - 125	70 - 160	—	3581	17695	8652
152	110 - 125	80 - 160	20 - 100	6991	86650	14874
174	110 - 125	50 - 150	20 - 100	11800	120975	17562
196	100 - 130	50 - 150	20 - 100	16331	171483	17937
218	100 - 130	50 - 150	20 - 100	16113	171483	16948
240	100 - 130	50 - 150	50 - 100	15009	14656	14504
262	100 - 130	70 - 150	60 - 100	12151	126722	7016
306	100 - 130	110 - 150	50 - 150	6529	160592	2636
345	100 - 130	120 - 160	20 - 150	331	163809	183

Table 15: Resulting number of events for the signal and background at $\sqrt{s} = 350$ GeV from the cut-and-count method performed in ref. [1]. The numbers correspond to an integrated luminosity of 3.5 ab^{-1}. The table is reprinted from ref. [1].

M [GeV]	P_{jj} [GeV]	$\not{E}_T$ [GeV]	N_S	N_B
140	> 170	< 100	6248	7550
179	> 100	< 100	25176	29453
218	—	—	43304	101672
257	—	—	44691	101672
296	—	50 - 200	37571	65326
335	—	70 - 180	30710	44572
374	—	90 - 180	21766	29854
413	160 - 220	—	14926	20541
452	170 - 230	—	8551	15643
495	> 220	—	845	9533

Table 16: Resulting number of events for the signal and background at $\sqrt{s} = 500$ GeV from the cut-and-count method performed in ref. [1]. The numbers correspond to an integrated luminosity of 1 ab^{-1}. The table is reprinted from ref. [1].

A.3 LEPTON-FLAVOUR VIOLATING DILEPTON-DIJET SIGNATURE: KINEMATIC CUTS

In ref. [7] the multivariate analysis has been performed by the Boosted Decision Tree (BDT) method from the TMVA package [423]. We show the result from the multivariate analysis for completeness in tab. 17 and tab. 18.

Cuts		M_N [GeV]						Background			
		200	400	500	600	800	1000	$t\bar{t}$	WZ	ZZ	WWZ
initial		1.56×10^4	1307	563	275	83.2	30.7	1.03×10^7	5.36×10^6	1.40×10^6	2.05×10^4
pre-sel.	cut 1	2545	260	109	50.6	14.1	5.0	3.26×10^5	2.63×10^4	6008	343
	cut 2	1830	229	97.7	45.2	12.4	4.4	1.83×10^5	1462	337	164
	cut 3	1376	130	46.9	18.5	3.7	0.99	5.44×10^4	265	64	58
BDT	> 0.2013	111	-	-	-	-	-	19.1	0.10	0.027	0.56
	> 0.2162	-	37.8	-	-	-	-	2.3	-	0.027	0.41
	> 0.2148	-	-	13.9	-	-	-	0.63	-	0.014	0.16
	> 0.2263	-	-	-	3.6	-	-	0.13	-	0.014	0.046
	> 0.2264	-	-	-	-	0.63	-	0.0068	-	-	0.013
	> 0.2348	-	-	-	-	-	0.15	0.00012	-	-	0.0041

Table 17: Shown are the number of surviving signal and background events after each cut stage for the HL-LHC with integrated luminosity of 3 ab^{-1}. For the signal a mixing of $|\theta_e|^2 = |\theta_\mu|^2 = 10^{-2}$ was assumed for each benchmark mass. The table is reprinted from ref. [7].

Cuts		M_N [GeV]						Background			
		200	400	500	600	800	1000	$t\bar{t}$	WZ	ZZ	WWZ
initial		1.78×10^6	2.14×10^5	1.07×10^5	6.03×10^4	2.38×10^4	1.13×10^4	2.75×10^9	1.13×10^8	8.97×10^7	1.91×10^6
pre-sel.	cut 1	3.84×10^5	5.98×10^4	3.03×10^4	1.70×10^4	6347	2856	6.08×10^7	1.96×10^6	1.46×10^6	5.45×10^4
	cut 2	3.39×10^5	5.76×10^4	2.95×10^4	1.66×10^4	6257	2824	3.61×10^7	6.20×10^4	4.24×10^4	1.96×10^4
	cut 3	2.90×10^5	4.36×10^4	2.10×10^4	1.12×10^4	3722	1484	9.08×10^6	7090	5497	6657
BDT	> 0.2935	6611	-	-	-	-	-	238.4	0.6	0.5	15.9
	> 0.2827	-	5762	-	-	-	-	81.5	0.9	0.7	20.3
	> 0.2654	-	-	4666	-	-	-	53.8	0.3	0.5	16.4
	> 0.2611	-	-	-	2701	-	-	33.9	-	-	8.9
	> 0.2428	-	-	-	-	1261	-	27.1	0.3	-	6.7
	> 0.2262	-	-	-	-	-	693	27.6	0.3	-	6.7

Table 18: Shown are the number of surviving signal and background events after each cut stage for the FCC-hh with integrated luminosity of 20 ab^{-1}. For the signal a mixing of $|\theta_e|^2 = |\theta_\mu|^2 = 10^{-2}$ was assumed for each benchmark mass. The table is reprinted from ref. [7].

BIBLIOGRAPHY

[1] Stefan Antusch, Eros Cazzato, and Oliver Fischer. "Higgs production from sterile neutrinos at future lepton colliders." In: *JHEP* 04 (2016), p. 189. DOI: 10.1007/JHEP04(2016)189. arXiv: 1512.06035 [hep-ph].

[2] Stefan Antusch, Eros Cazzato, and Oliver Fischer. "Displaced vertex searches for sterile neutrinos at future lepton colliders." In: *JHEP* 12 (2016), p. 007. DOI: 10.1007/JHEP12(2016)007. arXiv: 1604.02420 [hep-ph].

[3] Stefan Antusch, Eros Cazzato, and Oliver Fischer. "Sterile neutrino searches at future e^-e^+, pp, and e^-p colliders." In: *Int. J. Mod. Phys.* A32.14 (2017), p. 1750078. DOI: 10.1142/S0217751X17500786. arXiv: 1612.02728 [hep-ph].

[4] Stefan Antusch, Eros Cazzato, and Oliver Fischer. "Sterile neutrino searches via displaced vertices at LHCb." In: *Phys. Lett.* B774 (2017), pp. 114–118. DOI: 10.1016/j.physletb.2017.09.057. arXiv: 1706.05990 [hep-ph].

[5] Stefan Antusch, Eros Cazzato, and Oliver Fischer. "Resolvable heavy neutrino-antineutrino oscillations at colliders." In: *Mod. Phys. Lett.* A34. 07n08 (2019), p. 1950061. DOI: 10.1142/S0217732319500615. arXiv: 1709.03797 [hep-ph].

[6] Stefan Antusch, Eros Cazzato, Marco Drewes, Oliver Fischer, Bjorn Garbrecht, Dario Gueter, and Juraj Klaric. "Probing Leptogenesis at Future Colliders." In: *JHEP* 09 (2018), p. 124. DOI: 10.1007/JHEP09(2018)124. arXiv: 1710.03744 [hep-ph].

[7] Stefan Antusch, Eros Cazzato, Oliver Fischer, A. Hammad, and Kechen Wang. "Lepton Flavor Violating Dilepton Dijet Signatures from Sterile Neutrinos at Proton Colliders." In: (2018). arXiv: 1805.11400 [hep-ph].

[8] H. A. Bethe. "Energy production in stars." In: *Phys. Rev.* 55 (1939), pp. 434–456. DOI: 10.1103/PhysRev.55.434.

[9] Raymond Davis Jr., Don S. Harmer, and Kenneth C. Hoffman. "Search for neutrinos from the sun." In: *Phys. Rev. Lett.* 20 (1968), pp. 1205–1209. DOI: 10.1103/PhysRevLett.20.1205.

[10] John N. Bahcall and Roger K. Ulrich. "Solar Models, Neutrino Experiments and Helioseismology." In: *Rev. Mod. Phys.* 60 (1988), pp. 297–372. DOI: 10.1103/RevModPhys.60.297.

[11] B. Pontecorvo. "Neutrino Experiments and the Problem of Conservation of Leptonic Charge." In: *Sov. Phys. JETP* 26 (1968). [Zh. Eksp. Teor. Fiz.53,1717(1967)], pp. 984–988.

[12] Y. Fukuda et al. "Evidence for oscillation of atmospheric neutrinos." In: *Phys. Rev. Lett.* 81 (1998), pp. 1562–1567. DOI: 10.1103/PhysRevLett.81.1562. arXiv: hep-ex/9807003 [hep-ex].

[13] L. Wolfenstein. "Neutrino Oscillations in Matter." In: *Phys. Rev.* D17 (1978). [,294(1977)], pp. 2369–2374. DOI: 10.1103/PhysRevD.17.2369.

[14] S. P. Mikheyev and A. Yu. Smirnov. "Resonance Amplification of Oscillations in Matter and Spectroscopy of Solar Neutrinos." In: *Sov. J. Nucl. Phys.* 42 (1985). [,305(1986)], pp. 913–917.

[15] S. P. Mikheev and A. Yu. Smirnov. "Resonant amplification of neutrino oscillations in matter and solar neutrino spectroscopy." In: *Nuovo Cim.* C9 (1986), pp. 17–26. DOI: 10.1007/BF02508049.

[16] Q. R. Ahmad et al. "Direct evidence for neutrino flavor transformation from neutral current interactions in the Sudbury Neutrino Observatory." In: *Phys. Rev. Lett.* 89 (2002), p. 011301. DOI: 10.1103/PhysRevLett.89.011301. arXiv: nucl-ex/0204008 [nucl-ex].

[17] M. Tanabashi et al. "Review of Particle Physics." In: *Phys. Rev.* D98.3 (2018), p. 030001. DOI: 10.1103/PhysRevD.98.030001.

[18] Peter Minkowski. "$\mu \to e\gamma$ at a Rate of One Out of 10^9 Muon Decays?" In: *Phys. Lett.* 67B (1977), pp. 421–428. DOI: 10.1016/0370-2693(77)90435-X.

[19] Murray Gell-Mann, Pierre Ramond, and Richard Slansky. "Complex Spinors and Unified Theories." In: *Conf. Proc.* C790927 (1979), pp. 315–321. arXiv: 1306.4669 [hep-th].

[20] Tsutomu Yanagida. "HORIZONTAL SYMMETRY AND MASSES OF NEUTRINOS." In: *Conf. Proc.* C7902131 (1979), pp. 95–99.

[21] Rabindra N. Mohapatra and Goran Senjanovic. "Neutrino Mass and Spontaneous Parity Violation." In: *Phys. Rev. Lett.* 44 (1980). [,231(1979)], p. 912. DOI: 10.1103/PhysRevLett.44.912.

[22] J. Schechter and J. W. F. Valle. "Neutrino Masses in SU(2) x U(1) Theories." In: *Phys. Rev.* D22 (1980), p. 2227. DOI: 10.1103/PhysRevD.22.2227.

[23] Alexey Boyarsky, Oleg Ruchayskiy, and Mikhail Shaposhnikov. "The Role of sterile neutrinos in cosmology and astrophysics." In: *Ann. Rev. Nucl. Part. Sci.* 59 (2009), pp. 191–214. DOI: 10.1146/annurev.nucl.010909.083654. arXiv: 0901.0011 [hep-ph].

[24] A. Boyarsky, M. Drewes, T. Lasserre, S. Mertens, and O. Ruchayskiy. "Sterile Neutrino Dark Matter." In: (2018). arXiv: 1807.07938 [hep-ph].

[25] K. N. Abazajian et al. "Light Sterile Neutrinos: A White Paper." In: (2012). arXiv: 1204.5379 [hep-ph].

[26] Alessandro Strumia and Francesco Vissani. "Neutrino masses and mixings and..." In: (2006). arXiv: hep-ph/0606054 [hep-ph].

[27] Frank F. Deppisch, P. S. Bhupal Dev, and Apostolos Pilaftsis. "Neutrinos and Collider Physics." In: *New J. Phys.* 17.7 (2015), p. 075019. DOI: 10.1088/1367-2630/17/7/075019. arXiv: 1502.06541 [hep-ph].

[28] Carlo Giunti and Chung W. Kim. *Fundamentals of Neutrino Physics and Astrophysics*. 2007. ISBN: 9780198508717.

[29] Dr Julien Lesgourgues, Dr Gianpiero Mangano, Professor Gennaro Miele, and Dr Sergio Pastor. *Neutrino Cosmology*. Cambridge University Press, 2013. ISBN: 110701395X.

[30] André de Gouvêa. "Neutrino Mass Models." In: *Ann. Rev. Nucl. Part. Sci.* 66 (2016), pp. 197–217. DOI: 10.1146/annurev-nucl-102115-044600.

[31] Nicola Cabibbo. "Unitary Symmetry and Leptonic Decays." In: *Phys. Rev. Lett.* 10 (1963). [,648(1963)], pp. 531–533. DOI: 10.1103/PhysRevLett.10.531.

[32] Makoto Kobayashi and Toshihide Maskawa. "CP Violation in the Renormalizable Theory of Weak Interaction." In: *Prog. Theor. Phys.* 49 (1973), pp. 652–657. DOI: 10.1143/PTP.49.652.

[33] B. Pontecorvo. "Mesonium and anti-mesonium." In: *Sov. Phys. JETP* 6 (1957). [Zh. Eksp. Teor. Fiz.33,549(1957)], p. 429.

[34] B. Pontecorvo. "Inverse beta processes and nonconservation of lepton charge." In: *Sov. Phys. JETP* 7 (1958). [Zh. Eksp. Teor. Fiz.34,247(1957)], pp. 172–173.

[35] Ziro Maki, Masami Nakagawa, and Shoichi Sakata. "Remarks on the unified model of elementary particles." In: *Prog. Theor. Phys.* 28 (1962). [,34(1962)], pp. 870–880. DOI: 10.1143/PTP.28.870.

[36] A. Bandyopadhyay. "Physics at a future Neutrino Factory and superbeam facility." In: *Rept. Prog. Phys.* 72 (2009). Ed. by S. Choubey, R. Gandhi, S. Goswami, B. L. Roberts, J. Bouchez, I. Antoniadis, J. Ellis, G. F. Giudice, T. Schwetz, S. Umasankar, et al., p. 106201. DOI: 10.1088/0034-4885/72/10/106201. arXiv: 0710.4947 [hep-ph].

[37] Stephen F. King and Christoph Luhn. "Neutrino Mass and Mixing with Discrete Symmetry." In: *Rept. Prog. Phys.* 76 (2013), p. 056201. DOI: 10.1088/0034-4885/76/5/056201. arXiv: 1301.1340 [hep-ph].

[38] Stephen F. King, Alexander Merle, Stefano Morisi, Yusuke Shimizu, and Morimitsu Tanimoto. "Neutrino Mass and Mixing: from Theory to Experiment." In: *New J. Phys.* 16 (2014), p. 045018. DOI: 10.1088/1367-2630/16/4/045018. arXiv: 1402.4271 [hep-ph].

[39] S. T. Petcov. "Discrete Flavour Symmetries, Neutrino Mixing and Leptonic CP Violation." In: *Eur. Phys. J.* C78.9 (2018), p. 709. DOI: 10.1140/epjc/s10052-018-6158-5. arXiv: 1711.10806 [hep-ph].

[40] M. Magg and C. Wetterich. "Neutrino Mass Problem and Gauge Hierarchy." In: *Phys. Lett.* 94B (1980), pp. 61–64. DOI: 10.1016/0370-2693(80)90825-4.

[41] George Lazarides, Q. Shafi, and C. Wetterich. "Proton Lifetime and Fermion Masses in an SO(10) Model." In: *Nucl. Phys.* B181 (1981), pp. 287–300. DOI: 10.1016/0550-3213(81)90354-0.

[42] Rabindra N. Mohapatra and Goran Senjanovic. "Neutrino Masses and Mixings in Gauge Models with Spontaneous Parity Violation." In: *Phys. Rev.* D23 (1981), p. 165. DOI: 10.1103/PhysRevD.23.165.

[43] C. Wetterich. "Neutrino Masses and the Scale of B-L Violation." In: *Nucl. Phys.* B187 (1981), pp. 343–375. DOI: 10.1016/0550-3213(81)90279-0.

[44] Alejandra Melfo, Miha Nemevsek, Fabrizio Nesti, Goran Senjanovic, and Yue Zhang. "Type II Seesaw at LHC: The Roadmap." In: *Phys. Rev.* D85 (2012), p. 055018. DOI: 10.1103/PhysRevD.85.055018. arXiv: 1108.4416 [hep-ph].

[45] Robert Foot, H. Lew, X. G. He, and Girish C. Joshi. "Seesaw Neutrino Masses Induced by a Triplet of Leptons." In: *Z. Phys.* C44 (1989), p. 441. DOI: 10.1007/BF01415558.

[46] Jogesh C. Pati and Abdus Salam. "Lepton Number as the Fourth Color." In: *Phys. Rev.* D10 (1974). [Erratum: Phys. Rev.D11,703(1975)], pp. 275–289. DOI: 10.1103/PhysRevD.10.275,10.1103/PhysRevD.11.703.2.

[47] Paul Langacker. "Neutrino Masses from the Top Down." In: *Ann. Rev. Nucl. Part. Sci.* 62 (2012), pp. 215–235. DOI: 10.1146/annurev-nucl-102711-094925. arXiv: 1112.5992 [hep-ph].

[48] A. Zee. "Quantum Numbers of Majorana Neutrino Masses." In: *Nucl. Phys.* B264 (1986), pp. 99–110. DOI: 10.1016/0550-3213(86)90475-X.

[49] K. S. Babu. "Model of 'Calculable' Majorana Neutrino Masses." In: *Phys. Lett.* B203 (1988), pp. 132–136. DOI: 10.1016/0370-2693(88)91584-5.

[50] Ernest Ma. "Verifiable radiative seesaw mechanism of neutrino mass and dark matter." In: *Phys. Rev.* D73 (2006), p. 077301. DOI: 10.1103/PhysRevD.73.077301. arXiv: hep-ph/0601225 [hep-ph].

[51] Herbert K. Dreiner. "An Introduction to explicit R-parity violation." In: (1997). [Adv. Ser. Direct. High Energy Phys.21,565(2010)], pp. 462–479. DOI: 10.1142/9789814307505_0017. arXiv: hep-ph/9707435 [hep-ph].

[52] Joel Giedt, G. L. Kane, Paul Langacker, and Brent D. Nelson. "Massive neutrinos and (heterotic) string theory." In: *Phys. Rev.* D71 (2005), p. 115013. DOI: 10.1103/PhysRevD.71.115013. arXiv: hep-th/0502032 [hep-th].

[53] Mirjam Cvetic and Paul Langacker. "D-Instanton Generated Dirac Neutrino Masses." In: *Phys. Rev.* D78 (2008), p. 066012. DOI: 10.1103/PhysRevD.78.066012. arXiv: 0803.2876 [hep-th].

[54] Keith R. Dienes, Emilian Dudas, and Tony Gherghetta. "Neutrino oscillations without neutrino masses or heavy mass scales: A Higher dimensional seesaw mechanism." In: *Nucl. Phys.* B557 (1999), p. 25. DOI: 10.1016/S0550-3213(99)00377-6. arXiv: hep-ph/9811428 [hep-ph].

[55] Ettore Majorana. "Teoria simmetrica dell'elettrone e del positrone." In: *Nuovo Cim.* 14 (1937), pp. 171–184. DOI: 10.1007/BF02961314.

[56] Andreas Aste. "A direct road to Majorana fields." In: *Symmetry* 2 (2010), pp. 1776–1809. DOI: 10.3390/sym2041776. arXiv: 0806.1690 [hep-th].

[57] Palash B. Pal. "Dirac, Majorana and Weyl fermions." In: *Am. J. Phys.* 79 (2011), pp. 485–498. DOI: 10.1119/1.3549729. arXiv: 1006.1718 [hep-ph].

[58] Herbi K. Dreiner, Howard E. Haber, and Stephen P. Martin. "Two-component spinor techniques and Feynman rules for quantum field theory and supersymmetry." In: *Phys. Rept.* 494 (2010), pp. 1–196. DOI: 10.1016/j.physrep.2010.05.002. arXiv: 0812.1594 [hep-ph].

[59] S. T. Petcov. "On Pseudodirac Neutrinos, Neutrino Oscillations and Neutrinoless Double beta Decay." In: *Phys. Lett.* 110B (1982), pp. 245–249. DOI: 10.1016/0370-2693(82)91246-1.

[60] Makoto Kobayashi and C. S. Lim. "Pseudo Dirac scenario for neutrino oscillations." In: *Phys. Rev.* D64 (2001), p. 013003. DOI: 10.1103/PhysRevD.64.013003. arXiv: hep-ph/0012266 [hep-ph].

[61] Stefan Antusch, Steve Blanchet, Mattias Blennow, and Enrique Fernandez-Martinez. "Non-unitary Leptonic Mixing and Leptogenesis." In: *JHEP* 01 (2010), p. 017. DOI: 10.1007/JHEP01(2010)017. arXiv: 0910.5957 [hep-ph].

[62] Takehiko Asaka, Shintaro Eijima, and Hiroyuki Ishida. "Mixing of Active and Sterile Neutrinos." In: *JHEP* 04 (2011), p. 011. DOI: 10.1007/JHEP04(2011)011. arXiv: 1101.1382 [hep-ph].

[63] Mattias Blennow and Enrique Fernandez-Martinez. "Parametrization of Seesaw Models and Light Sterile Neutrinos." In: *Phys. Lett.* B704 (2011), pp. 223–229. DOI: 10.1016/j.physletb.2011.09.028. arXiv: 1107.3992 [hep-ph].

[64] Paul Langacker and David London. "Mixing Between Ordinary and Exotic Fermions." In: *Phys. Rev.* D38 (1988), p. 886. DOI: 10.1103/PhysRevD.38.886.

[65] C. Patrignani et al. "Review of Particle Physics." In: *Chin. Phys.* C40.10 (2016), p. 100001. DOI: 10.1088/1674-1137/40/10/100001.

[66] Evgeny K. Akhmedov. "Neutrino physics." In: *Proceedings, Summer School in Particle Physics: Trieste, Italy, June 21-July 9, 1999*. 1999, pp. 103–164. arXiv: hep-ph/0001264 [hep-ph].

[67] P. Hernandez. "Neutrino Physics." In: *Proceedings, 8th CERN–Latin-American School of High-Energy Physics (CLASHEP2015): Ibarra, Ecuador, March 05-17, 2015*. 2016, pp. 85–142. DOI: 10.5170/CERN-2016-005.85. arXiv: 1708.01046 [hep-ph].

[68] I. Gil-Botella. "Neutrino Physics." In: *Proceedings, 6th CERN - Latin-American School of High-Energy Physics (CLASHEP 2011): Natal, Brazil , March 23 - April 5, 2011*. 2013, pp. 157–205. DOI: 10.5170/CERN-2013-003.157. arXiv: 1504.03551 [hep-ph].

[69] Samoil M. Bilenky and B. Pontecorvo. "The Quark-Lepton Analogy and the Muonic Charge." In: *Yad. Fiz.* 24 (1976). [Sov. J. Nucl. Phys.24,316(1976)], pp. 603–608.

[70] Samoil M. Bilenky and B. Pontecorvo. "Again on Neutrino Oscillations." In: *Lett. Nuovo Cim.* 17 (1976), p. 569. DOI: 10.1007/BF02746567.

[71] Samoil M. Bilenky and B. Pontecorvo. "Lepton Mixing and Neutrino Oscillations." In: *Phys. Rept.* 41 (1978), pp. 225–261. DOI: 10.1016/0370-1573(78)90095-9.

[72] Shalom Eliezer and Arthur R. Swift. "Experimental Consequences of electron Neutrino-Muon-neutrino Mixing in Neutrino Beams." In: *Nucl. Phys.* B105 (1976), pp. 45–51. DOI: 10.1016/0550-3213(76)90059-6.

[73] Harald Fritzsch and Peter Minkowski. "Vector-Like Weak Currents, Massive Neutrinos, and Neutrino Beam Oscillations." In: *Phys. Lett.* 62B (1976), pp. 72–76. DOI: 10.1016/0370-2693(76)90051-4.

[74] Carlo Giunti. "Theory of neutrino oscillations." In: *Proceedings, 16th Conference on High Energy Physics (IFAE 2004): Turin, Italy, April 14-16, 2004*. 2004, pp. 427–438. DOI: 10.1142/9789812702074_0005. arXiv: hep-ph/0409230 [hep-ph].

[75] Ken Kiers, Shmuel Nussinov, and Nathan Weiss. "Coherence effects in neutrino oscillations." In: *Phys. Rev.* D53 (1996), pp. 537–547. DOI: 10.1103/PhysRevD.53.537. arXiv: hep-ph/9506271 [hep-ph].

[76] Boris Kayser. "On the Quantum Mechanics of Neutrino Oscillation." In: *Phys. Rev.* D24 (1981), p. 110. DOI: 10.1103/PhysRevD.24.110.

[77] S. Nussinov. "Solar Neutrinos and Neutrino Mixing." In: *Phys. Lett.* 63B (1976), pp. 201–203. DOI: 10.1016/0370-2693(76)90648-1.

[78] C. Giunti, C. W. Kim, and U. W. Lee. "When do neutrinos really oscillate?: Quantum mechanics of neutrino oscillations." In: *Phys. Rev.* D44 (1991), pp. 3635–3640. DOI: 10.1103/PhysRevD.44.3635.

[79] C. Giunti and C. W. Kim. "Coherence of neutrino oscillations in the wave packet approach." In: *Phys. Rev.* D58 (1998), p. 017301. DOI: 10.1103/PhysRevD.58.017301. arXiv: hep-ph/9711363 [hep-ph].

[80] C. Giunti, C. W. Kim, J. A. Lee, and U. W. Lee. "On the treatment of neutrino oscillations without resort to weak eigenstates." In: *Phys. Rev.* D48 (1993), pp. 4310–4317. DOI: 10.1103/PhysRevD.48.4310. arXiv: hep-ph/9305276 [hep-ph].

[81] Marek Zralek. "From kaons to neutrinos: Quantum mechanics of particle oscillations." In: *Acta Phys. Polon.* B29 (1998), pp. 3925–3956. arXiv: hep-ph/9810543 [hep-ph].

[82] Christian Y. Cardall. "Coherence of neutrino flavor mixing in quantum field theory." In: *Phys. Rev.* D61 (2000), p. 073006. DOI: 10.1103/PhysRevD.61.073006. arXiv: hep-ph/9909332 [hep-ph].

[83] C. Giunti. "Neutrino wave packets in quantum field theory." In: *JHEP* 11 (2002), p. 017. DOI: 10.1088/1126-6708/2002/11/017. arXiv: hep-ph/0205014 [hep-ph].

[84] M. Beuthe. "Towards a unique formula for neutrino oscillations in vacuum." In: *Phys. Rev.* D66 (2002), p. 013003. DOI: 10.1103/PhysRevD.66.013003. arXiv: hep-ph/0202068 [hep-ph].

[85] Mikael Beuthe. "Oscillations of neutrinos and mesons in quantum field theory." In: *Phys. Rept.* 375 (2003), pp. 105–218. DOI: 10.1016/S0370-1573(02)00538-0. arXiv: hep-ph/0109119 [hep-ph].

[86] Evgeny Kh. Akhmedov and Joachim Kopp. "Neutrino oscillations: Quantum mechanics vs. quantum field theory." In: *JHEP* 04 (2010). [Erratum: JHEP10,052(2013)], p. 008. DOI: 10.1007/JHEP04(2010)008, 10.1007/JHEP10(2013)052. arXiv: 1001.4815 [hep-ph].

[87] H. Kwon, F. Boehm, A. A. Hahn, H. E. Henrikson, J. L. Vuilleumier, J. F. Cavaignac, D. H. Koang, B. Vignon, F. Von Feilitzsch, and R. L. Mossbauer. "Search for Neutrino Oscillations at a Fission Reactor." In: *Phys. Rev.* D24 (1981), pp. 1097–1111. DOI: 10.1103/PhysRevD.24.1097.

[88] G. Zacek et al. "Neutrino Oscillation Experiments at the Gosgen Nuclear Power Reactor." In: *Phys. Rev.* D34 (1986), pp. 2621–2636. DOI: 10.1103/PhysRevD.34.2621.

[89] A. I. Afonin et al. "$\bar{\nu}_e$ Spectra at Two Distances From the Reactor of the Rovno Nuclear Power Plant: Search for Oscillations." In: *JETP Lett.* 45 (1987). [Pisma Zh. Eksp. Teor. Fiz.45,201(1987)], pp. 247–251.

[90] G. S. Vidyakin et al. "Limitations on the characteristics of neutrino oscillations." In: *JETP Lett.* 59 (1994). [Pisma Zh. Eksp. Teor. Fiz.59,364(1994)], pp. 390–393.

[91] Y. Declais et al. "Search for neutrino oscillations at 15-meters, 40-meters, and 95-meters from a nuclear power reactor at Bugey." In: *Nucl. Phys.* B434 (1995), pp. 503–534. DOI: 10.1016/0550-3213(94)00513-E.

[92] Z. D. Greenwood et al. "Results of a two position reactor neutrino oscillation experiment." In: *Phys. Rev.* D53 (1996), pp. 6054–6064. DOI: 10.1103/PhysRevD.53.6054.

[93] Y. J. Ko et al. "Sterile Neutrino Search at the NEOS Experiment." In: *Phys. Rev. Lett.* 118.12 (2017), p. 121802. DOI: 10.1103/PhysRevLett.118.121802. arXiv: 1610.05134 [hep-ex].

[94] M. Apollonio et al. "Search for neutrino oscillations on a long baseline at the CHOOZ nuclear power station." In: *Eur. Phys. J.* C27 (2003), pp. 331–374. DOI: 10.1140/epjc/s2002-01127-9. arXiv: hep-ex/0301017 [hep-ex].

[95] F. Boehm et al. "Final results from the Palo Verde neutrino oscillation experiment." In: *Phys. Rev.* D64 (2001), p. 112001. DOI: 10.1103/PhysRevD.64.112001. arXiv: hep-ex/0107009 [hep-ex].

[96] F. Ardellier et al. "Double Chooz: A Search for the neutrino mixing angle theta(13)." In: (2006). arXiv: hep-ex/0606025 [hep-ex].

[97] F. P. An et al. "Observation of electron-antineutrino disappearance at Daya Bay." In: *Phys. Rev. Lett.* 108 (2012), p. 171803. DOI: 10.1103/PhysRevLett.108.171803. arXiv: 1203.1669 [hep-ex].

[98] J. K. Ahn et al. "Observation of Reactor Electron Antineutrino Disappearance in the RENO Experiment." In: *Phys. Rev. Lett.* 108 (2012), p. 191802. DOI: 10.1103/PhysRevLett.108.191802. arXiv: 1204.0626 [hep-ex].

[99] K. Eguchi et al. "First results from KamLAND: Evidence for reactor anti-neutrino disappearance." In: *Phys. Rev. Lett.* 90 (2003), p. 021802. DOI: 10.1103/PhysRevLett.90.021802. arXiv: hep-ex/0212021 [hep-ex].

[100] Fengpeng An et al. "Neutrino Physics with JUNO." In: *J. Phys.* G43.3 (2016), p. 030401. DOI: 10.1088/0954-3899/43/3/030401. arXiv: 1507.05613 [physics.ins-det].

[101] F. Bergsma et al. "A Search for Neutrino Oscillations." In: *Z. Phys.* C40 (1988), p. 171. DOI: 10.1007/BF01555880.

[102] L. Borodovsky et al. "Search for muon-neutrino oscillations muon-neutrino —> electron-neutrino (anti-muon-neutrino —> anti-electron-neutrino in a wide band neutrino beam." In: *Phys. Rev. Lett.* 68 (1992), pp. 274–277. DOI: 10.1103/PhysRevLett.68.274.

[103] E. Eskut et al. "New results from a search for nu/mu –> nu/tau and nu/e –> nu/tau oscillation." In: *Phys. Lett.* B497 (2001), pp. 8–22. DOI: 10.1016/S0370-2693(00)01317-4.

[104] P. Astier et al. "Search for nu(mu) —> nu(e) oscillations in the NOMAD experiment." In: *Phys. Lett.* B570 (2003), pp. 19–31. DOI: 10.1016/j.physletb.2003.07.029. arXiv: hep-ex/0306037 [hep-ex].

[105] C. Athanassopoulos et al. "Evidence for nu(mu) —> nu(e) neutrino oscillations from LSND." In: *Phys. Rev. Lett.* 81 (1998), pp. 1774–1777. DOI: 10.1103/PhysRevLett.81.1774. arXiv: nucl-ex/9709006 [nucl-ex].

[106] S. Avvakumov et al. "A Search for muon-neutrino —> electron-neutrino and muon-anti-neutrino —> electron-anti-neutrino oscillations at NuTeV." In: *Phys. Rev. Lett.* 89 (2002), p. 011804. DOI: 10.1103/PhysRevLett.89.011804. arXiv: hep-ex/0203018 [hep-ex].

[107] A. Aguilar-Arevalo et al. "Evidence for neutrino oscillations from the observation of anti-neutrino(electron) appearance in a anti-neutrino(muon) beam." In: *Phys. Rev.* D64 (2001), p. 112007. DOI: 10.1103/PhysRevD.64.112007. arXiv: hep-ex/0104049 [hep-ex].

[108] B. Armbruster et al. "Upper limits for neutrino oscillations muon-anti-neutrino —> electron-anti-neutrino from muon decay at rest." In: *Phys. Rev.* D65 (2002), p. 112001. DOI: 10.1103/PhysRevD.65.112001. arXiv: hep-ex/0203021 [hep-ex].

[109] P. Fritze et al. "Further Study of the Prompt Neutrino Flux From 400 GeV Proton - Nucleus Collisions Using BEBC." In: *Phys. Lett.* 96B (1980), pp. 427–434. DOI: 10.1016/0370-2693(80)90802-3.

[110] J. Dorenbosch et al. "Prompt Neutrino Production in 400 GeV Proton - Copper Interactions." In: *Z. Phys.* C40 (1988), p. 497. DOI: 10.1007/BF01560221.

[111] P. Berge et al. "Prompt neutrino results from a proton beam dump experiment." In: *Z. Phys.* C56 (1992), pp. 175–180. DOI: 10.1007/BF01555511.

[112] M. H. Ahn et al. "Measurement of Neutrino Oscillation by the K2K Experiment." In: *Phys. Rev.* D74 (2006), p. 072003. DOI: 10.1103/PhysRevD.74.072003. arXiv: hep-ex/0606032 [hep-ex].

[113] P. Adamson et al. "Measurement of Neutrino Oscillations with the MINOS Detectors in the NuMI Beam." In: *Phys. Rev. Lett.* 101 (2008), p. 131802. DOI: 10.1103/PhysRevLett.101.131802. arXiv: 0806.2237 [hep-ex].

[114] M. Guler et al. "OPERA: An appearance experiment to search for nu/mu <–> nu/tau oscillations in the CNGS beam. Experimental proposal." In: (2000).

[115] K. Abe et al. "Observation of Electron Neutrino Appearance in a Muon Neutrino Beam." In: *Phys. Rev. Lett.* 112 (2014), p. 061802. DOI: 10.1103/PhysRevLett.112.061802. arXiv: 1311.4750 [hep-ex].

[116] P. Adamson et al. "First measurement of electron neutrino appearance in NOvA." In: *Phys. Rev. Lett.* 116.15 (2016), p. 151806. DOI: 10.1103/PhysRevLett.116.151806. arXiv: 1601.05022 [hep-ex].

[117] R. Acciarri et al. "Long-Baseline Neutrino Facility (LBNF) and Deep Underground Neutrino Experiment (DUNE)." In: (2015). arXiv: 1512.06148 [physics.ins-det].

[118] B. T. Cleveland, Timothy Daily, Raymond Davis Jr., James R. Distel, Kenneth Lande, C. K. Lee, Paul S. Wildenhain, and Jack Ullman. "Measurement of the solar electron neutrino flux with the Homestake chlorine detector." In: *Astrophys. J.* 496 (1998), pp. 505–526. DOI: 10.1086/305343.

[119] John N. Bahcall, M. H. Pinsonneault, and Sarbani Basu. "Solar models: Current epoch and time dependences, neutrinos, and helioseismological properties." In: *Astrophys. J.* 555 (2001), pp. 990–1012. DOI: 10.1086/321493. arXiv: astro-ph/0010346 [astro-ph].

[120] Sylvaine Turck-Chieze and Sebastien Couvidat. "Solar neutrinos, helioseismology and the solar internal dynamics." In: *Rept. Prog. Phys.* 74 (2011), p. 086901. DOI: 10.1088/0034-4885/74/8/086901. arXiv: 1009.0852 [astro-ph.SR].

[121] Y. Fukuda et al. "Solar neutrino data covering solar cycle 22." In: *Phys. Rev. Lett.* 77 (1996), pp. 1683–1686. DOI: 10.1103/PhysRevLett.77.1683.

[122] S. Fukuda et al. "Solar B-8 and hep neutrino measurements from 1258 days of Super-Kamiokande data." In: *Phys. Rev. Lett.* 86 (2001), pp. 5651–5655. DOI: 10.1103/PhysRevLett.86.5651. arXiv: hep-ex/0103032 [hep-ex].

[123] W. Hampel et al. "GALLEX solar neutrino observations: Results for GALLEX IV." In: *Phys. Lett.* B447 (1999), pp. 127–133. DOI: 10.1016/S0370-2693(98)01579-2.

[124] J. N. Abdurashitov et al. "Solar neutrino flux measurements by the Soviet-American Gallium Experiment (SAGE) for half the 22 year solar cycle." In: *J. Exp. Theor. Phys.* 95 (2002). [Zh. Eksp. Teor. Fiz.122,211(2002)], pp. 181–193. DOI: 10.1134/1.1506424. arXiv: astro-ph/0204245 [astro-ph].

[125] M. Altmann et al. "GNO solar neutrino observations: Results for GNO I." In: *Phys. Lett.* B490 (2000), pp. 16–26. DOI: 10.1016/S0370-2693(00)00915-1. arXiv: hep-ex/0006034 [hep-ex].

[126] S. N. Ahmed et al. "Measurement of the total active B-8 solar neutrino flux at the Sudbury Neutrino Observatory with enhanced neutral current sensitivity." In: *Phys. Rev. Lett.* 92 (2004), p. 181301. DOI: 10.1103/PhysRevLett.92.181301. arXiv: nucl-ex/0309004 [nucl-ex].

[127] G. Alimonti et al. "Science and technology of BOREXINO: A Real time detector for low-energy solar neutrinos." In: *Astropart. Phys.* 16 (2002), pp. 205–234. DOI: 10.1016/S0927-6505(01)00110-4. arXiv: hep-ex/0012030 [hep-ex].

[128] Y. Fukuda et al. "Atmospheric muon-neutrino / electron-neutrino ratio in the multiGeV energy range." In: *Phys. Lett.* B335 (1994), pp. 237–245. DOI: 10.1016/0370-2693(94)91420-6.

[129] R. Becker-Szendy et al. "A Search for muon-neutrino oscillations with the IMB detector." In: *Phys. Rev. Lett.* 69 (1992), pp. 1010–1013. DOI: 10.1103/PhysRevLett.69.1010.

[130] M. Aglietta et al. "Experimental study of upward stopping muons in NUSEX." In: *Europhys. Lett.* 15 (1991), pp. 559–564. DOI: 10.1209/0295-5075/15/5/015.

[131] K. Daum et al. "Determination of the atmospheric neutrino spectra with the Frejus detector." In: *Z. Phys.* C66 (1995), pp. 417–428. DOI: 10.1007/BF01556368.

[132] M. Ambrosio et al. "Atmospheric neutrino oscillations from upward through going muon multiple scattering in MACRO." In: *Phys. Lett.* B566 (2003), pp. 35–44. DOI: 10.1016/S0370-2693(03)00806-2. arXiv: hep-ex/0304037 [hep-ex].

[133] Mayly C. Sanchez et al. "Measurement of the L/E distributions of atmospheric neutrinos in Soudan 2 and their interpretation as neutrino oscillations." In: *Phys. Rev.* D68 (2003), p. 113004. DOI: 10.1103/PhysRevD.68.113004. arXiv: hep-ex/0307069 [hep-ex].

[134] M. G. Aartsen et al. "Determining neutrino oscillation parameters from atmospheric muon neutrino disappearance with three years of IceCube DeepCore data." In: *Phys. Rev.* D91.7 (2015), p. 072004. DOI: 10.1103/PhysRevD.91.072004. arXiv: 1410.7227 [hep-ex].

[135] Ivan Esteban, M. C. Gonzalez-Garcia, Michele Maltoni, Ivan Martinez-Soler, and Thomas Schwetz. "Updated fit to three neutrino mixing: exploring the accelerator-reactor complementarity." In: *JHEP* 01 (2017), p. 087. DOI: 10.1007/JHEP01(2017)087. arXiv: 1611.01514 [hep-ph].

[136] Francesco Capozzi, Eleonora Di Valentino, Eligio Lisi, Antonio Marrone, Alessandro Melchiorri, and Antonio Palazzo. "Global constraints on absolute neutrino masses and their ordering." In: *Phys. Rev.* D95.9 (2017), p. 096014. DOI: 10.1103/PhysRevD.95.096014. arXiv: 1703.04471 [hep-ph].

[137] P. F. de Salas, D. V. Forero, C. A. Ternes, M. Tortola, and J. W. F. Valle. "Status of neutrino oscillations 2018: 3σ hint for normal mass ordering and improved CP sensitivity." In: *Phys. Lett.* B782 (2018), pp. 633–640. DOI: 10.1016/j.physletb.2018.06.019. arXiv: 1708.01186 [hep-ph].

[138] A. A. Aguilar-Arevalo et al. "A Search for electron neutrino appearance at the $\Delta m^2 \sim 1eV^2$ scale." In: *Phys. Rev. Lett.* 98 (2007), p. 231801. DOI: 10.1103/PhysRevLett.98.231801. arXiv: 0704.1500 [hep-ex].

[139] A. A. Aguilar-Arevalo et al. "Unexplained Excess of Electron-Like Events From a 1-GeV Neutrino Beam." In: *Phys. Rev. Lett.* 102 (2009), p. 101802. DOI: 10.1103/PhysRevLett.102.101802. arXiv: 0812.2243 [hep-ex].

[140] A. A. Aguilar-Arevalo et al. "Event Excess in the MiniBooNE Search for $\bar{\nu}_\mu \to \bar{\nu}_e$ Oscillations." In: *Phys. Rev. Lett.* 105 (2010), p. 181801. DOI: 10.1103/PhysRevLett.105.181801. arXiv: 1007.1150 [hep-ex].

[141] A. A. Aguilar-Arevalo et al. "Observation of a Significant Excess of Electron-Like Events in the MiniBooNE Short-Baseline Neutrino Experiment." In: (2018). arXiv: 1805.12028 [hep-ex].

[142] F. Kaether, W. Hampel, G. Heusser, J. Kiko, and T. Kirsten. "Reanalysis of the GALLEX solar neutrino flux and source experiments." In: *Phys. Lett.* B685 (2010), pp. 47–54. DOI: 10.1016/j.physletb.2010.01.030. arXiv: 1001.2731 [hep-ex].

[143] J. N. Abdurashitov et al. "Measurement of the response of the Russian-American gallium experiment to neutrinos from a Cr-51 source." In: *Phys. Rev.* C59 (1999), pp. 2246–2263. DOI: 10.1103/PhysRevC.59.2246. arXiv: hep-ph/9803418 [hep-ph].

[144] J. N. Abdurashitov et al. "Measurement of the response of a Ga solar neutrino experiment to neutrinos from an Ar-37 source." In: *Phys. Rev.* C73 (2006), p. 045805. DOI: 10.1103/PhysRevC.73.045805. arXiv: nucl-ex/0512041 [nucl-ex].

[145] G. Mention, M. Fechner, Th. Lasserre, Th. A. Mueller, D. Lhuillier, M. Cribier, and A. Letourneau. "The Reactor Antineutrino Anomaly." In: *Phys. Rev.* D83 (2011), p. 073006. DOI: 10.1103/PhysRevD.83.073006. arXiv: 1101.2755 [hep-ex].

[146] J. Schechter and J. W. F. Valle. "Neutrinoless Double beta Decay in SU(2) x U(1) Theories." In: *Phys. Rev.* D25 (1982). [,289(1981)], p. 2951. DOI: 10.1103/PhysRevD.25.2951.

[147] Stefano Dell'Oro, Simone Marcocci, Matteo Viel, and Francesco Vissani. "Neutrinoless double beta decay: 2015 review." In: *Adv. High Energy Phys.* 2016 (2016), p. 2162659. DOI: 10.1155/2016/2162659. arXiv: 1601.07512 [hep-ph].

[148] Ch. Kraus et al. "Final results from phase II of the Mainz neutrino mass search in tritium beta decay." In: *Eur. Phys. J.* C40 (2005), pp. 447–468. DOI: 10.1140/epjc/s2005-02139-7. arXiv: hep-ex/0412056 [hep-ex].

[149] V. M. Lobashev. "The search for the neutrino mass by direct method in the tritium beta-decay and perspectives of study it in the project KATRIN." In: *Nucl. Phys.* A719 (2003), pp. 153–160. DOI: 10.1016/S0375-9474(03)00985-0.

[150] Carlo Giunti and Marco Laveder. "Short-Baseline Electron Neutrino Disappearance, Tritium Beta Decay and Neutrinoless Double-Beta Decay." In: *Phys. Rev.* D82 (2010), p. 053005. DOI: 10.1103/PhysRevD.82.053005. arXiv: 1005.4599 [hep-ph].

[151] F. M. Fraenkle. "KATRIN: an experiment to determine the neutrino mass." In: *Particles and fields. Proceedings, Meeting of the Division of the American Physical Society, DPF 2011, Providence, USA, August 9-13, 2011*. 2011. arXiv: 1110.0087 [physics.ins-det].

[152] C. E. Aalseth et al. "Neutrinoless double-beta decay of Ge-76: First results from the International Germanium Experiment (IGEX) with six isotopically enriched detectors." In: *Phys. Rev.* C59 (1999), pp. 2108–2113. DOI: 10.1103/PhysRevC.59.2108.

[153] H. V. Klapdor-Kleingrothaus et al. "Latest results from the Heidelberg-Moscow double beta decay experiment." In: *Eur. Phys. J.* A12 (2001), pp. 147–154. DOI: 10.1007/s100500170022. arXiv: hep-ph/0103062 [hep-ph].

[154] Fedor A. Danevich et al. "Search for 2 beta decay of cadmium and tungsten isotopes: Final results of the Solotvina experiment." In: *Phys. Rev.* C68 (2003), p. 035501. DOI: 10.1103/PhysRevC.68.035501.

[155] E. Andreotti et al. "130Te Neutrinoless Double-Beta Decay with CUORICINO." In: *Astropart. Phys.* 34 (2011), pp. 822–831. DOI: 10.1016/j.astropartphys.2011.02.002. arXiv: 1012.3266 [nucl-ex].

[156] A. Gando et al. "Limit on Neutrinoless $\beta\beta$ Decay of ^{136}Xe from the First Phase of KamLAND-Zen and Comparison with the Positive Claim in ^{76}Ge." In: *Phys. Rev. Lett.* 110.6 (2013), p. 062502. DOI: 10.1103/PhysRevLett.110.062502. arXiv: 1211.3863 [hep-ex].

[157] R. Arnold et al. "Search for neutrinoless double-beta decay of ^{100}Mo with the NEMO-3 detector." In: *Phys. Rev.* D89.11 (2014), p. 111101. DOI: 10.1103/PhysRevD.89.111101. arXiv: 1311.5695 [hep-ex].

[158] M. Agostini et al. "Results on Neutrinoless Double-β Decay of ^{76}Ge from Phase I of the GERDA Experiment." In: *Phys. Rev. Lett.* 111.12 (2013), p. 122503. DOI: 10.1103/PhysRevLett.111.122503. arXiv: 1307.4720 [nucl-ex].

[159] J. B. Albert et al. "Search for Majorana neutrinos with the first two years of EXO-200 data." In: *Nature* 510 (2014), pp. 229–234. DOI: 10.1038/nature13432. arXiv: 1402.6956 [nucl-ex].

[160] K. Alfonso et al. "Search for Neutrinoless Double-Beta Decay of ^{130}Te with CUORE-0." In: *Phys. Rev. Lett.* 115.10 (2015), p. 102502. DOI: 10.1103/PhysRevLett.115.102502. arXiv: 1504.02454 [nucl-ex].

[161] N. Abgrall et al. "The Majorana Demonstrator Neutrinoless Double-Beta Decay Experiment." In: *Adv. High Energy Phys.* 2014 (2014), p. 365432. DOI: 10.1155/2014/365432. arXiv: 1308.1633 [physics.ins-det].

[162] Julien Lesgourgues and Sergio Pastor. "Massive neutrinos and cosmology." In: *Phys. Rept.* 429 (2006), pp. 307–379. DOI: 10.1016/j.physrep.2006.04.001. arXiv: astro-ph/0603494 [astro-ph].

[163] Andre de Gouvea, Wei-Chih Huang, and James Jenkins. "Pseudo-Dirac Neutrinos in the New Standard Model." In: *Phys. Rev.* D80 (2009), p. 073007. DOI: 10.1103/PhysRevD.80.073007. arXiv: 0906.1611 [hep-ph].

[164] A. Donini, P. Hernandez, J. Lopez-Pavon, and M. Maltoni. "Minimal models with light sterile neutrinos." In: *JHEP* 07 (2011), p. 105. DOI: 10.1007/JHEP07(2011)105. arXiv: 1106.0064 [hep-ph].

[165] Andre de Gouvea. "See-saw energy scale and the LSND anomaly." In: *Phys. Rev.* D72 (2005), p. 033005. DOI: 10.1103/PhysRevD.72.033005. arXiv: hep-ph/0501039 [hep-ph].

[166] Marco Drewes. "The Phenomenology of Right Handed Neutrinos." In: *Int. J. Mod. Phys.* E22 (2013), p. 1330019. DOI: 10.1142/S0218301313300191. arXiv: 1303.6912 [hep-ph].

[167] N. Aghanim et al. "Planck 2018 results. VI. Cosmological parameters." In: (2018). arXiv: 1807.06209 [astro-ph.CO].

[168] Edward W. Kolb and Michael S. Turner. "The Early Universe." In: *Front. Phys.* 69 (1990), pp. 1–547.

[169] R. N. Mohapatra et al. "Theory of neutrinos: A White paper." In: *Rept. Prog. Phys.* 70 (2007), pp. 1757–1867. DOI: 10.1088/0034-4885/70/11/R02. arXiv: hep-ph/0510213 [hep-ph].

[170] Stefan Antusch. "Models for Neutrino Masses and Mixings." In: (2013). [Nucl. Phys. Proc. Suppl.235-236,303(2013)]. DOI: 10.1016/j.nuclphysbps.2013.04.026. arXiv: 1301.5511 [hep-ph].

[171] Howard Georgi. "The State of the Art—Gauge Theories." In: *AIP Conf. Proc.* 23 (1975), pp. 575–582. DOI: 10.1063/1.2947450.

[172] Harald Fritzsch and Peter Minkowski. "Unified Interactions of Leptons and Hadrons." In: *Annals Phys.* 93 (1975), pp. 193–266. DOI: 10.1016/0003-4916(75)90211-0.

[173] A. D. Sakharov. "Violation of CP Invariance, C asymmetry, and baryon asymmetry of the universe." In: *Pisma Zh. Eksp. Teor. Fiz.* 5 (1967). [Usp. Fiz. Nauk161,no.5,61(1991)], pp. 32–35. DOI: 10.1070/PU1991v034n05ABEH002497.

[174] M. Fukugita and T. Yanagida. "Baryogenesis Without Grand Unification." In: *Phys. Lett.* B174 (1986), pp. 45–47. DOI: 10.1016/0370-2693(86)91126-3.

[175] Enrico Nardi, Yosef Nir, Esteban Roulet, and Juan Racker. "The Importance of flavor in leptogenesis." In: *JHEP* 01 (2006), p. 164. DOI: 10.1088/1126-6708/2006/01/164. arXiv: hep-ph/0601084 [hep-ph].

[176] Apostolos Pilaftsis and Thomas E. J. Underwood. "Resonant leptogenesis." In: *Nucl. Phys.* B692 (2004), pp. 303–345. DOI: 10.1016/j.nuclphysb.2004.05.029. arXiv: hep-ph/0309342 [hep-ph].

[177] Evgeny K. Akhmedov, V. A. Rubakov, and A. Yu. Smirnov. "Baryogenesis via neutrino oscillations." In: *Phys. Rev. Lett.* 81 (1998), pp. 1359–1362. DOI: 10.1103/PhysRevLett.81.1359. arXiv: hep-ph/9803255 [hep-ph].

[178] Kevork N. Abazajian, John F. Beacom, and Nicole F. Bell. "Stringent constraints on cosmological neutrino anti-neutrino asymmetries from synchronized flavor transformation." In: *Phys. Rev.* D66 (2002), p. 013008. DOI: 10.1103/PhysRevD.66.013008. arXiv: astro-ph/0203442 [astro-ph].

[179] Yuval Grossman, Tamar Kashti, Yosef Nir, and Esteban Roulet. "Leptogenesis from supersymmetry breaking." In: *Phys. Rev. Lett.* 91 (2003), p. 251801. DOI: 10.1103/PhysRevLett.91.251801. arXiv: hep-ph/0307081 [hep-ph].

[180] Giancarlo D'Ambrosio, Gian F. Giudice, and Martti Raidal. "Soft leptogenesis." In: *Phys. Lett.* B575 (2003), pp. 75–84. DOI: 10.1016/j.physletb.2003.09.037. arXiv: hep-ph/0308031 [hep-ph].

[181] Yvonne Y. Y. Wong. "Analytical treatment of neutrino asymmetry equilibration from flavor oscillations in the early universe." In: *Phys. Rev.* D66 (2002), p. 025015. DOI: 10.1103/PhysRevD.66.025015. arXiv: hep-ph/0203180 [hep-ph].

[182] Scott Dodelson and Lawrence M. Widrow. "Sterile-neutrinos as dark matter." In: *Phys. Rev. Lett.* 72 (1994), pp. 17–20. DOI: 10.1103/PhysRevLett.72.17. arXiv: hep-ph/9303287 [hep-ph].

[183] Alexander Kusenko. "Sterile neutrinos: The Dark side of the light fermions." In: *Phys. Rept.* 481 (2009), pp. 1–28. DOI: 10.1016/j.physrep.2009.07.004. arXiv: 0906.2968 [hep-ph].

[184] Alexander Merle. "keV Neutrino Model Building." In: *Int. J. Mod. Phys.* D22 (2013), p. 1330020. DOI: 10.1142/S0218271813300206. arXiv: 1302.2625 [hep-ph].

[185] Takehiko Asaka, Steve Blanchet, and Mikhail Shaposhnikov. "The nuMSM, dark matter and neutrino masses." In: *Phys. Lett.* B631 (2005), pp. 151–156. DOI: 10.1016/j.physletb.2005.09.070. arXiv: hep-ph/0503065 [hep-ph].

[186] Takehiko Asaka and Mikhail Shaposhnikov. "The nuMSM, dark matter and baryon asymmetry of the universe." In: *Phys. Lett.* B620 (2005), pp. 17–26. DOI: 10.1016/j.physletb.2005.06.020. arXiv: hep-ph/0505013 [hep-ph].

[187] Jörn Kersten and Alexei Yu. Smirnov. "Right-Handed Neutrinos at CERN LHC and the Mechanism of Neutrino Mass Generation." In: *Phys. Rev.* D76 (2007), p. 073005. DOI: 10.1103/PhysRevD.76.073005. arXiv: 0705.3221 [hep-ph].

[188] Amitava Datta and Apostolos Pilaftsis. "Revealing the Majorana nature of heavy neutrinos via a heavy Higgs boson." In: *Phys. Lett.* B278 (1992), pp. 162–166. DOI: 10.1016/0370-2693(92)90727-L.

[189] Apostolos Pilaftsis. "Radiatively induced neutrino masses and large Higgs neutrino couplings in the standard model with Majorana fields." In: *Z. Phys.* C55 (1992), pp. 275–282. DOI: 10.1007/BF01482590. arXiv: hep-ph/9901206 [hep-ph].

[190] W. Buchmuller and C. Greub. "Heavy Majorana neutrinos in electron - positron and electron - proton collisions." In: *Nucl. Phys.* B363 (1991), pp. 345–368. DOI: 10.1016/0550-3213(91)80024-G.

[191] G. Ingelman and J. Rathsman. "Heavy Majorana neutrinos at e p colliders." In: *Z. Phys.* C60 (1993), pp. 243–254. DOI: 10.1007/BF01474620.

[192] C. A. Heusch and P. Minkowski. "Lepton flavor violation induced by heavy Majorana neutrinos." In: *Nucl. Phys.* B416 (1994), pp. 3–45. DOI: 10.1016/0550-3213(94)90576-2.

[193] D. Wyler and L. Wolfenstein. "Massless Neutrinos in Left-Right Symmetric Models." In: *Nucl. Phys.* B218 (1983), pp. 205–214. DOI: 10.1016/0550-3213(83)90482-0.

[194] J. Bernabeu, A. Santamaria, J. Vidal, A. Mendez, and J. W. F. Valle. "Lepton Flavor Nonconservation at High-Energies in a Superstring Inspired Standard Model." In: *Phys. Lett.* B187 (1987), pp. 303–308. DOI: 10.1016/0370-2693(87)91100-2.

[195] G. C. Branco, W. Grimus, and L. Lavoura. "The Seesaw Mechanism in the Presence of a Conserved Lepton Number." In: *Nucl. Phys.* B312 (1989), pp. 492–508. DOI: 10.1016/0550-3213(89)90304-0.

[196] W. Buchmuller and D. Wyler. "Dilatons and majorana neutrinos." In: *Phys. Lett.* B249 (1990), pp. 458–462. DOI: 10.1016/0370-2693(90)91016-5.

[197] D. Tommasini, G. Barenboim, J. Bernabeu, and C. Jarlskog. "Nondecoupling of heavy neutrinos and lepton flavor violation." In: *Nucl. Phys.* B444 (1995), pp. 451–467. DOI: 10.1016/0550-3213(95)00201-3. arXiv: hep-ph/9503228 [hep-ph].

[198] Janusz Gluza. "On teraelectronvolt Majorana neutrinos." In: *Acta Phys. Polon.* B33 (2002), pp. 1735–1746. arXiv: hep-ph/0201002 [hep-ph].

[199] Apostolos Pilaftsis. "Resonant tau-leptogenesis with observable lepton number violation." In: *Phys. Rev. Lett.* 95 (2005), p. 081602. DOI: 10.1103/PhysRevLett.95.081602. arXiv: hep-ph/0408103 [hep-ph].

[200] Apostolos Pilaftsis and Thomas E. J. Underwood. "Electroweak-scale resonant leptogenesis." In: *Phys. Rev.* D72 (2005), p. 113001. DOI: 10.1103/PhysRevD.72.113001. arXiv: hep-ph/0506107 [hep-ph].

[201] Evgeny K. Akhmedov and M. Frigerio. "Interplay of type I and type II seesaw contributions to neutrino mass." In: *JHEP* 01 (2007), p. 043. DOI: 10.1088/1126-6708/2007/01/043. arXiv: hep-ph/0609046 [hep-ph].

[202] Mikhail Shaposhnikov. "A Possible symmetry of the nuMSM." In: *Nucl. Phys.* B763 (2007), pp. 49–59. DOI: 10.1016/j.nuclphysb.2006.11.003. arXiv: hep-ph/0605047 [hep-ph].

[203] A. Abada, C. Biggio, F. Bonnet, M. B. Gavela, and T. Hambye. "Low energy effects of neutrino masses." In: *JHEP* 12 (2007), p. 061. DOI: 10.1088/1126-6708/2007/12/061. arXiv: 0707.4058 [hep-ph].

[204] M. B. Gavela, T. Hambye, D. Hernandez, and P. Hernandez. "Minimal Flavour Seesaw Models." In: *JHEP* 09 (2009), p. 038. DOI: 10.1088/1126-6708/2009/09/038. arXiv: 0906.1461 [hep-ph].

[205] D. Aristizabal Sierra, A. Degee, and J. F. Kamenik. "Minimal Lepton Flavor Violating Realizations of Minimal Seesaw Models." In: *JHEP* 07 (2012), p. 135. DOI: 10.1007/JHEP07(2012)135. arXiv: 1205.5547 [hep-ph].

[206] Claudio O. Dib, Gaston R. Moreno, and Nicolas A. Neill. "Neutrinos with a linear seesaw mechanism in a scenario of gauged B-L symmetry." In: *Phys. Rev.* D90.11 (2014), p. 113003. DOI: 10.1103/PhysRevD.90.113003. arXiv: 1409.1868 [hep-ph].

[207] Lincoln Wolfenstein. "Different Varieties of Massive Dirac Neutrinos." In: *Nucl. Phys.* B186 (1981), pp. 147–152. DOI: 10.1016/0550-3213(81)90096-1.

[208] J. T. Penedo, S. T. Petcov, and T. Yanagida. "Low-Scale Seesaw and the CP Violation in Neutrino Oscillations." In: *Nucl. Phys.* B929 (2018), pp. 377–396. DOI: 10.1016/j.nuclphysb.2018.02.018. arXiv: 1712.09922 [hep-ph].

[209] Wai-Yee Keung and Goran Senjanovic. "Majorana Neutrinos and the Production of the Right-handed Charged Gauge Boson." In: *Phys. Rev. Lett.* 50 (1983), p. 1427. DOI: 10.1103/PhysRevLett.50.1427.

[210] R. N. Mohapatra and J. W. F. Valle. "Neutrino Mass and Baryon Number Nonconservation in Superstring Models." In: *Phys. Rev.* D34 (1986). [,235(1986)], p. 1642. DOI: 10.1103/PhysRevD.34.1642.

[211] R. N. Mohapatra. "Mechanism for Understanding Small Neutrino Mass in Superstring Theories." In: *Phys. Rev. Lett.* 56 (1986), pp. 561–563. DOI: 10.1103/PhysRevLett.56.561.

[212] M. C. Gonzalez-Garcia and J. W. F. Valle. "Fast Decaying Neutrinos and Observable Flavor Violation in a New Class of Majoron Models." In: *Phys. Lett.* B216 (1989), pp. 360–366. DOI: 10.1016/0370-2693(89)91131-3.

[213] Evgeny K. Akhmedov, Manfred Lindner, Erhard Schnapka, and J. W. F. Valle. "Dynamical left-right symmetry breaking." In: *Phys. Rev.* D53 (1996), pp. 2752–2780. DOI: 10.1103/PhysRevD.53.2752. arXiv: hep-ph/9509255 [hep-ph].

[214] Evgeny K. Akhmedov, Manfred Lindner, Erhard Schnapka, and J. W. F. Valle. "Left-right symmetry breaking in NJL approach." In: *Phys. Lett.* B368 (1996), pp. 270–280. DOI: 10.1016/0370-2693(95)01504-3. arXiv: hep-ph/9507275 [hep-ph].

[215] S. M. Barr. "A Different seesaw formula for neutrino masses." In: *Phys. Rev. Lett.* 92 (2004), p. 101601. DOI: 10.1103/PhysRevLett.92.101601. arXiv: hep-ph/0309152 [hep-ph].

[216] Michal Malinsky, J. C. Romao, and J. W. F. Valle. "Novel supersymmetric SO(10) seesaw mechanism." In: *Phys. Rev. Lett.* 95 (2005), p. 161801. DOI: 10.1103/PhysRevLett.95.161801. arXiv: hep-ph/0506296 [hep-ph].

[217] Stefan Antusch and Oliver Fischer. "Testing sterile neutrino extensions of the Standard Model at future lepton colliders." In: *JHEP* 05 (2015), p. 053. DOI: 10.1007/JHEP05(2015)053. arXiv: 1502.05915 [hep-ph].

[218] S. Antusch, C. Biggio, E. Fernandez-Martinez, M. B. Gavela, and J. Lopez-Pavon. "Unitarity of the Leptonic Mixing Matrix." In: *JHEP* 10 (2006), p. 084. DOI: 10.1088/1126-6708/2006/10/084. arXiv: hep-ph/0607020 [hep-ph].

[219] E. Fernandez-Martinez, M. B. Gavela, J. Lopez-Pavon, and O. Yasuda. "CP-violation from non-unitary leptonic mixing." In: *Phys. Lett.* B649 (2007), pp. 427–435. DOI: 10.1016/j.physletb.2007.03.069. arXiv: hep-ph/0703098 [hep-ph].

[220] Stefan Antusch, Mattias Blennow, Enrique Fernandez-Martinez, and Jacobo Lopez-Pavon. "Probing non-unitary mixing and CP-violation at a Neutrino Factory." In: *Phys. Rev.* D80 (2009), p. 033002. DOI: 10.1103/PhysRevD.80.033002. arXiv: 0903.3986 [hep-ph].

[221] Ansgar Denner, H. Eck, O. Hahn, and J. Kublbeck. "Feynman rules for fermion number violating interactions." In: *Nucl. Phys.* B387 (1992), pp. 467–481. DOI: 10.1016/0550-3213(92)90169-C.

[222] Stefan Antusch and Oliver Fischer. "Non-unitarity of the leptonic mixing matrix: Present bounds and future sensitivities." In: *JHEP* 10 (2014), p. 094. DOI: 10.1007/JHEP10(2014)094. arXiv: 1407.6607 [hep-ph].

[223] Enrique Fernandez-Martinez, Josu Hernandez-Garcia, and Jacobo Lopez-Pavon. "Global constraints on heavy neutrino mixing." In: *JHEP* 08 (2016), p. 033. DOI: 10.1007/JHEP08(2016)033. arXiv: 1605.08774 [hep-ph].

[224] J. Gluza and M. Zralek. "Heavy neutrinos production and decay in future e+ e- colliders." In: *Phys. Rev.* D55 (1997), pp. 7030–7037. DOI: 10.1103/PhysRevD.55.7030. arXiv: hep-ph/9612227 [hep-ph].

[225] F. del Aguila and J. A. Aguilar-Saavedra. "l W nu production at CLIC: A Window to TeV scale non-decoupled neutrinos." In: *JHEP* 05 (2005), p. 026. DOI: 10.1088/1126-6708/2005/05/026. arXiv: hep-ph/0503026 [hep-ph].

[226] Shankha Banerjee, P. S. Bhupal Dev, Alejandro Ibarra, Tanumoy Mandal, and Manimala Mitra. "Prospects of Heavy Neutrino Searches at Future Lepton Colliders." In: *Phys. Rev.* D92 (2015), p. 075002. DOI: 10.1103/PhysRevD.92.075002. arXiv: 1503.05491 [hep-ph].

[227] Arindam Das, P. S. Bhupal Dev, and C. S. Kim. "Constraining Sterile Neutrinos from Precision Higgs Data." In: *Phys. Rev.* D95.11 (2017), p. 115013. DOI: 10.1103/PhysRevD.95.115013. arXiv: 1704.00880 [hep-ph].

[228] Anupama Atre, Tao Han, Silvia Pascoli, and Bin Zhang. "The Search for Heavy Majorana Neutrinos." In: *JHEP* 05 (2009), p. 030. DOI: 10.1088/1126-6708/2009/05/030. arXiv: 0901.3589 [hep-ph].

[229] Claudio O. Dib and Choong Sun Kim. "Discovering sterile Neutrinos ligther than M_W at the LHC." In: *Phys. Rev.* D92.9 (2015), p. 093009. DOI: 10.1103/PhysRevD.92.093009. arXiv: 1509.05981 [hep-ph].

[230] Wei Liao and Xiao-Hong Wu. "Signature of heavy sterile neutrinos at CEPC." In: *Phys. Rev.* D97.5 (2018), p. 055005. DOI: 10.1103/PhysRevD.97.055005. arXiv: 1710.09266 [hep-ph].

[231] Torbjorn Sjostrand, Stephen Mrenna, and Peter Z. Skands. "PYTHIA 6.4 Physics and Manual." In: *JHEP* 05 (2006), p. 026. DOI: 10.1088/1126-6708/2006/05/026. arXiv: hep-ph/0603175 [hep-ph].

[232] J. de Favereau, C. Delaere, P. Demin, A. Giammanco, V. Lemaître, A. Mertens, and M. Selvaggi. "DELPHES 3, A modular framework for fast simulation of a generic collider experiment." In: *JHEP* 02 (2014), p. 057. DOI: 10.1007/JHEP02(2014)057. arXiv: 1307.6346 [hep-ex].

[233] Eric Conte, Benjamin Fuks, and Guillaume Serret. "MadAnalysis 5, A User-Friendly Framework for Collider Phenomenology." In: *Comput. Phys. Commun.* 184 (2013), pp. 222–256. DOI: 10.1016/j.cpc.2012.09.009. arXiv: 1206.1599 [hep-ph].

[234] Eric Conte, Béranger Dumont, Benjamin Fuks, and Chris Wymant. "Designing and recasting LHC analyses with MadAnalysis 5." In: *Eur. Phys. J.* C74.10 (2014), p. 3103. DOI: 10.1140/epjc/s10052-014-3103-0. arXiv: 1405.3982 [hep-ph].

[235] B. Dumont, B. Fuks, S. Kraml, S. Bein, G. Chalons, E. Conte, S. Kulkarni, D. Sengupta, and C. Wymant. "Toward a public analysis database for LHC new physics searches using MADANALYSIS 5." In: *Eur. Phys. J.* C75.2 (2015), p. 56. DOI: 10.1140/epjc/s10052-014-3242-3. arXiv: 1407.3278 [hep-ph].

[236] Neil D. Christensen and Claude Duhr. "FeynRules - Feynman rules made easy." In: *Comput. Phys. Commun.* 180 (2009), pp. 1614–1641. DOI: 10.1016/j.cpc.2009.02.018. arXiv: 0806.4194 [hep-ph].

[237] Celine Degrande, Claude Duhr, Benjamin Fuks, David Grellscheid, Olivier Mattelaer, and Thomas Reiter. "UFO - The Universal FeynRules Output." In: *Comput. Phys. Commun.* 183 (2012), pp. 1201–1214. DOI: 10.1016/j.cpc.2012.01.022. arXiv: 1108.2040 [hep-ph].

[238] T. Stelzer and W. F. Long. "Automatic generation of tree level helicity amplitudes." In: *Comput. Phys. Commun.* 81 (1994), pp. 357–371. DOI: 10.1016/0010-4655(94)90084-1. arXiv: hep-ph/9401258 [hep-ph].

[239] Fabio Maltoni and Tim Stelzer. "MadEvent: Automatic event generation with MadGraph." In: *JHEP* 02 (2003), p. 027. DOI: 10.1088/1126-6708/2003/02/027. arXiv: hep-ph/0208156 [hep-ph].

[240] Johan Alwall, Pavel Demin, Simon de Visscher, Rikkert Frederix, Michel Herquet, Fabio Maltoni, Tilman Plehn, David L. Rainwater, and Tim Stelzer. "MadGraph/MadEvent v4: The New Web Generation." In: *JHEP* 09 (2007), p. 028. DOI: 10.1088/1126-6708/2007/09/028. arXiv: 0706.2334 [hep-ph].

[241] Johan Alwall, Pierre Artoisenet, Simon de Visscher, Claude Duhr, Rikkert Frederix, Michel Herquet, and Olivier Mattelaer. "New Developments in MadGraph/MadEvent." In: *AIP Conf. Proc.* 1078 (2009), pp. 84–89. DOI: 10.1063/1.3052056. arXiv: 0809.2410 [hep-ph].

[242] Johan Alwall, Michel Herquet, Fabio Maltoni, Olivier Mattelaer, and Tim Stelzer. "MadGraph 5 : Going Beyond." In: *JHEP* 06 (2011), p. 128. DOI: 10.1007/JHEP06(2011)128. arXiv: 1106.0522 [hep-ph].

[243] J. Alwall, R. Frederix, S. Frixione, V. Hirschi, F. Maltoni, O. Mattelaer, H. S. Shao, T. Stelzer, P. Torrielli, and M. Zaro. "The automated computation of tree-level and next-to-leading order differential cross sections, and their matching to parton shower simulations." In: *JHEP* 07 (2014), p. 079. DOI: 10.1007/JHEP07(2014)079. arXiv: 1405.0301 [hep-ph].

[244] Neil D. Christensen, Claude Duhr, Benjamin Fuks, Jurgen Reuter, and Christian Speckner. "Introducing an interface between WHIZARD and FeynRules." In: *Eur. Phys. J.* C72 (2012), p. 1990. DOI: 10.1140/epjc/s10052-012-1990-5. arXiv: 1010.3251 [hep-ph].

[245] Wolfgang Kilian, Thorsten Ohl, and Jurgen Reuter. "WHIZARD: Simulating Multi-Particle Processes at LHC and ILC." In: *Eur. Phys. J.* C71 (2011), p. 1742. DOI: 10.1140/epjc/s10052-011-1742-y. arXiv: 0708.4233 [hep-ph].

[246] Mauro Moretti, Thorsten Ohl, and Jurgen Reuter. "O'Mega: An Optimizing matrix element generator." In: (2001), pp. 1981–2009. arXiv: hep-ph/0102195 [hep-ph].

[247] Sergey Alekhin et al. "A facility to Search for Hidden Particles at the CERN SPS: the SHiP physics case." In: *Rept. Prog. Phys.* 79.12 (2016), p. 124201. DOI: 10.1088/0034-4885/79/12/124201. arXiv: 1504.04855 [hep-ph].

[248] Marco Drewes and Björn Garbrecht. "Combining experimental and cosmological constraints on heavy neutrinos." In: *Nucl. Phys.* B921 (2017), pp. 250–315. DOI: 10.1016/j.nuclphysb.2017.05.001. arXiv: 1502.00477 [hep-ph].

[249] M. Anelli et al. "A facility to Search for Hidden Particles (SHiP) at the CERN SPS." In: (2015). arXiv: 1504.04956 [physics.ins-det].

[250] C. Adams et al. "The Long-Baseline Neutrino Experiment: Exploring Fundamental Symmetries of the Universe." In: (2013). arXiv: 1307.7335 [hep-ex].

[251] S. Schael et al. "Precision electroweak measurements on the Z resonance." In: *Phys. Rept.* 427 (2006), pp. 257–454. DOI: 10.1016/j.physrep.2005.12.006. arXiv: hep-ex/0509008 [hep-ex].

[252] Alain Blondel, E. Graverini, N. Serra, and M. Shaposhnikov. "Search for Heavy Right Handed Neutrinos at the FCC-ee." In: *Nucl. Part. Phys. Proc.* 273-275 (2016), pp. 1883–1890. DOI: 10.1016/j.nuclphysbps.2015.09.304. arXiv: 1411.5230 [hep-ex].

[253] A. Heister et al. "Measurement of W-pair production in e+ e- collisions at centre-of-mass energies from 183-GeV to 209-GeV." In: *Eur. Phys. J.* C38 (2004), pp. 147–160. DOI: 10.1140/epjc/s2004-02048-3.

[254] Marcela Carena, Andre de Gouvea, Ayres Freitas, and Michael Schmitt. "Invisible Z boson decays at e+ e- colliders." In: *Phys. Rev.* D68 (2003), p. 113007. DOI: 10.1103/PhysRevD.68.113007. arXiv: hep-ph/0308053 [hep-ph].

[255] J. Adam et al. "New constraint on the existence of the $\mu^+ \to e^+\gamma$ decay." In: *Phys. Rev. Lett.* 110 (2013), p. 201801. DOI: 10.1103/PhysRevLett.110.201801. arXiv: 1303.0754 [hep-ex].

[256] R. Alonso, M. Dhen, M. B. Gavela, and T. Hambye. "Muon conversion to electron in nuclei in type-I seesaw models." In: *JHEP* 01 (2013), p. 118. DOI: 10.1007/JHEP01(2013)118. arXiv: 1209.2679 [hep-ph].

[257] A. Abada, V. De Romeri, and A. M. Teixeira. "Impact of sterile neutrinos on nuclear-assisted cLFV processes." In: *JHEP* 02 (2016), p. 083. DOI: 10.1007/JHEP02(2016)083. arXiv: 1510.06657 [hep-ph].

[258] Marco Drewes, Bjorn Garbrecht, Dario Gueter, and Juraj Klaric. "Leptogenesis from Oscillations of Heavy Neutrinos with Large Mixing Angles." In: *JHEP* 12 (2016), p. 150. DOI: 10.1007/JHEP12(2016)150. arXiv: 1606.06690 [hep-ph].

[259] Lucien Heurtier and Daniele Teresi. "Dark matter and observable lepton flavor violation." In: *Phys. Rev.* D94.12 (2016), p. 125022. DOI: 10.1103/PhysRevD.94.125022. arXiv: 1607.01798 [hep-ph].

[260] A. Ferrari, Johann Collot, M-L. Andrieux, B. Belhorma, P. de Saintignon, J-Y. Hostachy, Ph. Martin, and M. Wielers. "Sensitivity study for new gauge bosons and right-handed Majorana neutrinos in pp collisions at s = 14-TeV." In: *Phys. Rev.* D62 (2000), p. 013001. DOI: 10.1103/PhysRevD.62.013001.

[261] Pascal Humbert, Manfred Lindner, and Juri Smirnov. "The Inverse Seesaw in Conformal Electro-Weak Symmetry Breaking and Phenomenological Consequences." In: *JHEP* 06 (2015), p. 035. DOI: 10.1007/JHEP06(2015)035. arXiv: 1503.03066 [hep-ph].

[262] Lucia Duarte, Javier Peressutti, and Oscar A. Sampayo. "Majorana neutrino decay in an Effective Approach." In: *Phys. Rev.* D92.9 (2015), p. 093002. DOI: 10.1103/PhysRevD.92.093002. arXiv: 1508.01588 [hep-ph].

[263] Zhaofeng Kang, P. Ko, and Jinmian Li. "New Avenues to Heavy Right-handed Neutrinos with Pair Production at Hadronic Colliders." In: *Phys. Rev.* D93.7 (2016), p. 075037. DOI: 10.1103/PhysRevD.93.075037. arXiv: 1512.08373 [hep-ph].

[264] Arindam Das and Nobuchika Okada. "Improved bounds on the heavy neutrino productions at the LHC." In: *Phys. Rev.* D93.3 (2016), p. 033003. DOI: 10.1103/PhysRevD.93.033003. arXiv: 1510.04790 [hep-ph].

[265] P. S. Bhupal Dev, Rabindra N. Mohapatra, and Yongchao Zhang. "Probing the Higgs Sector of the Minimal Left-Right Symmetric Model at Future Hadron Colliders." In: *JHEP* 05 (2016), p. 174. DOI: 10.1007/JHEP05(2016)174. arXiv: 1602.05947 [hep-ph].

[266] Julien Baglio and Cédric Weiland. "Heavy neutrino impact on the triple Higgs coupling." In: *Phys. Rev.* D94.1 (2016), p. 013002. DOI: 10.1103/PhysRevD.94.013002. arXiv: 1603.00879 [hep-ph].

[267] T. T. Thuc, L. T. Hue, H. N. Long, and T. Phong Nguyen. "Lepton flavor violating decay of SM-like Higgs boson in a radiative neutrino mass model." In: *Phys. Rev.* D93.11 (2016), p. 115026. DOI: 10.1103/PhysRevD.93.115026. arXiv: 1604.03285 [hep-ph].

[268] Debasish Borah and Arnab Dasgupta. "Charged lepton flavour violcxmation and neutrinoless double beta decay in left-right symmetric models with type I+II seesaw." In: *JHEP* 07 (2016), p. 022. DOI: 10.1007/JHEP07(2016)022. arXiv: 1606.00378 [hep-ph].

[269] Marco Drewes, Bjorn Garbrecht, Dario Gueter, and Juraj Klaric. "Testing the low scale seesaw and leptogenesis." In: *JHEP* 08 (2017), p. 018. DOI: 10.1007/JHEP08(2017)018. arXiv: 1609.09069 [hep-ph].

[270] Thomas Hambye and Daniele Teresi. "Higgs doublet decay as the origin of the baryon asymmetry." In: *Phys. Rev. Lett.* 117.9 (2016), p. 091801. DOI: 10.1103/PhysRevLett.117.091801. arXiv: 1606.00017 [hep-ph].

[271] Arindam Das and Nobuchika Okada. "Bounds on heavy Majorana neutrinos in type-I seesaw and implications for collider searches." In: *Phys. Lett.* B774 (2017), pp. 32–40. DOI: 10.1016/j.physletb.2017.09.042. arXiv: 1702.04668 [hep-ph].

[272] P. Abreu et al. "Search for neutral heavy leptons produced in Z decays." In: *Z. Phys.* C74 (1997). [Erratum: Z. Phys.C75,580(1997)], pp. 57–71. DOI: 10.1007/s002880050370.

[273] M. Z. Akrawy et al. "Limits on neutral heavy lepton production from Zo decay." In: *Phys. Lett.* B247 (1990), pp. 448–457. DOI: 10.1016/0370-2693(90)90924-U.

[274] D. Decamp et al. "Searches for new particles in Z decays using the ALEPH detector." In: *Phys. Rept.* 216 (1992), pp. 253–340. DOI: 10.1016/0370-1573(92)90177-2.

[275] O. Adriani et al. "Results from the L3 experiment at LEP." In: *Phys. Rept.* 236 (1993), pp. 1–146. DOI: 10.1016/0370-1573(93)90027-B.

[276] Georges Aad et al. "Observation of a new particle in the search for the Standard Model Higgs boson with the ATLAS detector at the LHC." In: *Phys. Lett.* B716 (2012), pp. 1–29. DOI: 10.1016/j.physletb.2012.08.020. arXiv: 1207.7214 [hep-ex].

[277] Serguei Chatrchyan et al. "Observation of a new boson at a mass of 125 GeV with the CMS experiment at the LHC." In: *Phys. Lett.* B716 (2012), pp. 30–61. DOI: 10.1016/j.physletb.2012.08.021. arXiv: 1207.7235 [hep-ex].

[278] G. Apollinari, I. Béjar Alonso, O. Brüning, P. Fessia, M. Lamont, L. Rossi, and L. Tavian. "High-Luminosity Large Hadron Collider (HL-LHC)." In: (2017). DOI: 10.23731/CYRM-2017-004.

[279] CEPC-SPPC Study Group. "CEPC-SPPC Preliminary Conceptual Design Report. 1. Physics and Detector." In: (2015).

[280] *Longer term LHC schedule*. http://lhc-commissioning.web.cern.ch/lhc-commissioning/schedule/LHC-long-term.htm. Accessed online on July 2018.

[281] "The European Strategy for Particle Physics Update 2013. La stratégie européenne pour la physique des particules Mise à jour 2013. 16th Session of European Strategy Council." In: (2013). URL: http://cds.cern.ch/record/1567258.

[282] T. Golling et al. "Physics at a 100 TeV pp collider: beyond the Standard Model phenomena." In: *CERN Yellow Report* 3 (2017), pp. 441–634. DOI: 10.23731/CYRM-2017-003.441. arXiv: 1606.00947 [hep-ph].

[283] M. L. Mangano et al. "Physics at a 100 TeV pp Collider: Standard Model Processes." In: *CERN Yellow Report* 3 (2017), pp. 1–254. DOI: 10.23731/CYRM-2017-003.1. arXiv: 1607.01831 [hep-ph].

[284] R. Contino et al. "Physics at a 100 TeV pp collider: Higgs and EW symmetry breaking studies." In: *CERN Yellow Report* 3 (2017), pp. 255–440. DOI: 10.23731/CYRM-2017-003.255. arXiv: 1606.09408 [hep-ph].

[285] M. Bicer et al. "First Look at the Physics Case of TLEP." In: *JHEP* 01 (2014), p. 164. DOI: 10.1007/JHEP01(2014)164. arXiv: 1308.6176 [hep-ex].

[286] Frank Zimmermann, Michael Benedikt, Daniel Schulte, and Jorg Wenninger. "Challenges for Highest Energy Circular Colliders." In: *Proceedings, 5th International Particle Accelerator Conference (IPAC 2014): Dresden, Germany, June 15-20, 2014*. 2014, MOXAA01. URL: http://jacow.org/IPAC2014/papers/moxaa01.pdf.

[287] Oliver Bruning, John Jowett, Max Klein, Dario Pellegrini, Daniel Schulte, and Frank Zimmermann. *Future Circular Collider Study FCC-he Baseline Parameters*. Tech. rep. CERN-ACC-2017-0019. Geneva: CERN, 2017. URL: http://cds.cern.ch/record/2260408.

[288] F. Zimmermann M. Benedikt. "Future Circular Collider Study - Status and Plans." https://indico.cern.ch/event/656491/contributions/2932205/attachments/1628761/2595133/180409. Conference talk at the FCC Week 2018, Amsterdam. 2018.

[289] The CEPC-SPPC Study Group. *CEPC-SPPC Progress Report (2015 - 2016) - Accelerator*. Tech. rep. IHEP-CEPC-DR-2017-01. IHEP, 2017. URL: http://cepc.ihep.ac.cn/ProgressReport.pdf.

[290] The CEPC Study Group. *CEPC Conceptual Design Report - Accelerator*. Tech. rep. IHEP-CEPC-DR-2018-01. Draft version 3, accessed only on July 2018. IHEP, 2018. URL: http://cepc.ihep.ac.cn/CDR_v6_201808.pdf.

[291] *ICFA Statement on Linear Colliders February 2004*. http://icfa.fnal.gov/statements/icfa_lcstatement0204/. Accessed online on July 2018. 2004.

[292] Ties Behnke, James E. Brau, Brian Foster, Juan Fuster, Mike Harrison, James McEwan Paterson, Michael Peskin, Marcel Stanitzki, Nicholas Walker, and Hitoshi Yamamoto. "The International Linear Collider Technical Design Report - Volume 1: Executive Summary." In: (2013). arXiv: 1306.6327 [physics.acc-ph].

[293] *ILC - Status of the project*. http://www.linearcollider.org/ILC/What-is-the-ILC/Status-of-the-project. Accessed online on July 2018.

[294] M Aicheler, P Burrows, M Draper, T Garvey, P Lebrun, K Peach, N Phinney, H Schmickler, D Schulte, and N Toge. "A Multi-TeV Linear Collider Based on CLIC Technology." In: (2012). DOI: 10.5170/CERN-2012-007.

[295] M J Boland et al. "Updated baseline for a staged Compact Linear Collider." In: (2016). Ed. by P Lebrun, L Linssen, D Schulte, E Sicking, S Stapnes, M A Thomson, and P N Burrows. DOI: 10.5170/CERN-2016-004. arXiv: 1608.07537 [physics.acc-ph].

[296] J. L. Abelleira Fernandez et al. "A Large Hadron Electron Collider at CERN: Report on the Physics and Design Concepts for Machine and Detector." In: *J. Phys.* G39 (2012), p. 075001. DOI: 10.1088/0954-3899/39/7/075001. arXiv: 1206.2913 [physics.acc-ph].

[297] *What is the Linear Collider Collaboration?* http://www.linearcollider.org/about. Accessed online on July 2018.

[298] Alain Blondel, Alex Chao, Weiren Chou, Daniel Schulte, Jie Gao, and Kaoru Yokoya. "ICFA Beam Dynamics Workshop Report - Accelerators for a Higgs Factory: Linear vs. Circular (HF2012)." In: *ICFA Beam Dyn. Newslett.* 60 (2013), pp. 113–157.

[299] Michelangelo Mangano et al. *Future Circular Collider*. Tech. rep. CERN-ACC-2018-0056. Submitted for publication to Eur. Phys. J. C. Geneva: CERN, 2018. URL: https://cds.cern.ch/record/2651294.

[300] Chris Adolphsen, Maura Barone, Barry Barish, Karsten Buesser, Philip Burrows, John Carwardine, Jeffrey Clark, Hélène Mainaud Durand, Gerry Dugan, Eckhard Elsen, et al. "The International Linear Collider Technical Design Report - Volume 3.II: Accelerator Baseline Design." In: (2013). arXiv: 1306.6328 [physics.acc-ph].

[301] M. Mangano. *FCC ee/hh and High Energy LHC*. https://indico.cern.ch/event/517784/contributions/2550640/attachments/1462710/2259814/Mangano-FCC-landscape.pdf. Conference talk at The Fifth Annual Large Hadron Collider Physics conference (LHCP2017), accessed online on July 2018. 2017.

[302] James E. Brau, T. Barklow, J. Brau, K. Fujii, J. Gao, J. List, N. Walker, and K. Yokoya. "500 GeV ILC Operating Scenarios." In: *Proceedings, Meeting of the APS Division of Particles and Fields (DPF 2015): Ann Arbor, Michigan, USA, 4-8 Aug 2015*. 2015. arXiv: 1510.05739 [hep-ex].

[303] Howard Baer, Tim Barklow, Keisuke Fujii, Yuanning Gao, Andre Hoang, Shinya Kanemura, Jenny List, Heather E. Logan, Andrei Nomerotski, Maxim Perelstein, et al. "The International Linear Collider Technical Design Report - Volume 2: Physics." In: (2013). arXiv: 1306.6352 [hep-ph].

[304] Tim M. P. Tait. "Collider signal I: Resonance." In: *Proceedings of Theoretical Advanced Study Institute in Elementary Particle Physics on The dawn of the LHC era (TASI 2008): Boulder, USA, June 2-27, 2008*. 2010, pp. 181–210. DOI: 10.1142/9789812838360_0004.

[305] D. Berdine, N. Kauer, and D. Rainwater. "Breakdown of the Narrow Width Approximation for New Physics." In: *Phys. Rev. Lett.* 99 (2007), p. 111601. DOI: 10.1103/PhysRevLett.99.111601. arXiv: hep-ph/0703058 [hep-ph].

[306] C. F. Uhlemann and N. Kauer. "Narrow-width approximation accuracy." In: *Nucl. Phys.* B814 (2009), pp. 195–211. DOI: 10.1016/j.nuclphysb.2009.01.022. arXiv: 0807.4112 [hep-ph].

[307] Ian Hinchliffe, Ashutosh Kotwal, Michelangelo L. Mangano, Chris Quigg, and Lian-Tao Wang. "Luminosity goals for a 100-TeV pp collider." In: *Int. J. Mod. Phys.* A30.23 (2015), p. 1544002. DOI: 10.1142/S0217751X15440029. arXiv: 1504.06108 [hep-ph].

[308] P. S. Bhupal Dev, Apostolos Pilaftsis, and Un-ki Yang. "New Production Mechanism for Heavy Neutrinos at the LHC." In: *Phys. Rev. Lett.* 112.8 (2014), p. 081801. DOI: 10.1103/PhysRevLett.112.081801. arXiv: 1308.2209 [hep-ph].

[309] Daniel Alva, Tao Han, and Richard Ruiz. "Heavy Majorana neutrinos from $W\gamma$ fusion at hadron colliders." In: *JHEP* 02 (2015), p. 072. DOI: 10.1007/JHEP02(2015)072. arXiv: 1411.7305 [hep-ph].

[310] Richard Ruiz, Michael Spannowsky, and Philip Waite. "Heavy neutrinos from gluon fusion." In: *Phys. Rev.* D96.5 (2017), p. 055042. DOI: 10.1103/PhysRevD.96.055042. arXiv: 1706.02298 [hep-ph].

[311] Max Klein. "The Large Hadron Electron Collider Project." In: *Proceedings, 17th International Workshop on Deep-Inelastic Scattering and Related Subjects (DIS 2009): Madrid, Spain, April 26-30, 2009*. 2009, p. 236. arXiv: 0908.2877 [hep-ex].

[312] Max Klein. "Deep inelastic scattering at the energy frontier." In: *Annalen Phys.* 528 (2016), pp. 138–144. DOI: 10.1002/andp.201500252.

[313] Oliver Bruening and Max Klein. "The Large Hadron Electron Collider." In: *Mod. Phys. Lett.* A28.16 (2013), p. 1330011. DOI: 10.1142/S0217732313300115. arXiv: 1305.2090 [physics.acc-ph].

[314] Davison E. Soper. "Basics of QCD perturbation theory." In: *The Strong interaction, from hadrons to partons: Proceedings, 24th SLAC Summer Institute on Particle Physics (SSI 96), Stanford, Calif., 19-30 Aug 1996*. 1996, pp. 15–42. arXiv: hep-ph/9702203 [hep-ph]. URL: http://www.slac.stanford.edu/pubs/confproc/ssi96/ssi96-002.html.

[315] Lorenzo Basso. "Resonant mono Higgs at the LHC." In: *JHEP* 04 (2016), p. 087. DOI: 10.1007/JHEP04(2016)087. arXiv: 1512.06381 [hep-ph].

[316] Higgs Cross Section Working Group. *Higgs cross sections for HL-LHC and HE-LHC*. https://twiki.cern.ch/twiki/bin/view/LHCPhysics/HiggsEuropeanStrategy. Accessed online on July 2018.

[317] Uta Klein. *FCC-eh as a Higgs Facility*. https://indico.cern.ch/event/656491/contributions/2947252/attachments/1631779/2602870/FCC_Amsterdam_12.04.2018.pdf. Conference talk at the FCC Week 2018, Amsterdam, accessed online on July 2018. 2017.

[318] Roberto Tenchini. "Precision Electroweak Measurements at FCC-ee." In: *Nucl. Part. Phys. Proc.* 273-275 (2016), pp. 2244–2248. DOI: 10.1016/j.nuclphysbps.2015.09.365. arXiv: 1412.2928 [hep-ex].

[319] W Kilian, M Kramer, and P. M. Zerwas. "Higgsstrahlung and W W fusion in e+ e- collisions." In: *Phys. Lett.* B373 (1996), pp. 135–140. DOI: 10.1016/0370-2693(96)00100-1. arXiv: hep-ph/9512355 [hep-ph].

[320] Hiroaki Ono and Akiya Miyamoto. "A study of measurement precision of the Higgs boson branching ratios at the International Linear Collider." In: *Eur. Phys. J.* C73.3 (2013), p. 2343. DOI: 10.1140/epjc/s10052-013-2343-8. arXiv: 1207.0300 [hep-ex].

[321] D. de Florian et al. "Handbook of LHC Higgs Cross Sections: 4. Deciphering the Nature of the Higgs Sector." In: (2016). DOI: 10.23731/CYRM-2017-002. arXiv: 1610.07922 [hep-ph].

[322] C. T. Potter, James E. Brau, and M. Iwasaki. "Standard model Higgs boson branching ratio measurements at a linear collider." In: *eConf* C010630 (2001), P118.

[323] David J. Jackson. "A Topological vertex reconstruction algorithm for hadronic jets." In: *Nucl. Instrum. Meth.* A388 (1997), pp. 247–253. DOI: 10.1016/S0168-9002(97)00341-0.

[324] Eder Izaguirre and Brian Shuve. "Multilepton and Lepton Jet Probes of Sub-Weak-Scale Right-Handed Neutrinos." In: *Phys. Rev.* D91.9 (2015), p. 093010. DOI: 10.1103/PhysRevD.91.093010. arXiv: 1504.02470 [hep-ph].

[325] Georges Aad et al. "Search for massive, long-lived particles using multitrack displaced vertices or displaced lepton pairs in pp collisions at $\sqrt{s}$ = 8 TeV with the ATLAS detector." In: *Phys. Rev.* D92.7 (2015), p. 072004. DOI: 10.1103/PhysRevD.92.072004. arXiv: 1504.05162 [hep-ex].

[326] Morad Aaboud et al. "Search for long-lived, massive particles in events with displaced vertices and missing transverse momentum in $\sqrt{s}$ = 13 TeV pp collisions with the ATLAS detector." In: *Phys. Rev.* D97.5 (2018), p. 052012. DOI: 10.1103/PhysRevD.97.052012. arXiv: 1710.04901 [hep-ex].

[327] Morad Aaboud et al. "Search for long-lived particles in final states with displaced dimuon vertices in pp collisions at $\sqrt{s}$ = 13 TeV with the ATLAS detector." In: (2018). arXiv: 1808.03057 [hep-ex].

[328] Albert M Sirunyan et al. "Search for long-lived particles with displaced vertices in multijet events in proton-proton collisions at $\sqrt{s}$ =13 TeV." In: (2018). arXiv: 1808.03078 [hep-ex].

[329] Georges Aad et al. "Search for heavy Majorana neutrinos with the ATLAS detector in pp collisions at $\sqrt{s}$ = 8 TeV." In: *JHEP* 07 (2015), p. 162. DOI: 10.1007/JHEP07(2015)162. arXiv: 1506.06020 [hep-ex].

[330] Vardan Khachatryan et al. "Search for heavy Majorana neutrinos in $\mu^{\pm}\mu^{\pm}$+ jets events in proton-proton collisions at $\sqrt{s}$ = 8 TeV." In: *Phys. Lett.* B748 (2015), pp. 144–166. DOI: 10.1016/j.physletb.2015.06.070. arXiv: 1501.05566 [hep-ex].

[331] Michael L. Graesser. "Broadening the Higgs boson with right-handed neutrinos and a higher dimension operator at the electroweak scale." In: *Phys. Rev.* D76 (2007), p. 075006. DOI: 10.1103/PhysRevD.76.075006. arXiv: 0704.0438 [hep-ph].

[332] Michael L. Graesser. "Experimental Constraints on Higgs Boson Decays to TeV-scale Right-Handed Neutrinos." In: (2007). arXiv: 0705.2190 [hep-ph].

[333] Miha Nemevsek, Fabrizio Nesti, Goran Senjanovic, and Yue Zhang. "First Limits on Left-Right Symmetry Scale from LHC Data." In: *Phys. Rev.* D83 (2011), p. 115014. DOI: 10.1103/PhysRevD.83.115014. arXiv: 1103.1627 [hep-ph].

[334] Alessio Maiezza, Miha Nemevšek, and Fabrizio Nesti. "Lepton Number Violation in Higgs Decay at LHC." In: *Phys. Rev. Lett.* 115 (2015), p. 081802. DOI: 10.1103/PhysRevLett.115.081802. arXiv: 1503.06834 [hep-ph].

[335] Juan C. Helo, Martin Hirsch, and Sergey Kovalenko. "Heavy neutrino searches at the LHC with displaced vertices." In: *Phys. Rev.* D89 (2014). [Erratum: Phys. Rev.D93,no.9,099902(2016)], p. 073005. DOI: 10.1103/PhysRevD.89.073005,10.1103/PhysRevD.93.099902. arXiv: 1312.2900 [hep-ph].

[336] David G. Cerdeño, Victor Martín-Lozano, and Osamu Seto. "Displaced vertices and long-lived charged particles in the NMSSM with right-handed sneutrinos." In: *JHEP* 05 (2014), p. 035. DOI: 10.1007/JHEP05(2014)035. arXiv: 1311.7260 [hep-ph].

[337] Alberto M. Gago, Pilar Hernández, Joel Jones-Pérez, Marta Losada, and Alexander Moreno Briceño. "Probing the Type I Seesaw Mechanism with Displaced Vertices at the LHC." In: *Eur. Phys. J.* C75.10 (2015), p. 470. DOI: 10.1140/epjc/s10052-015-3693-1. arXiv: 1505.05880 [hep-ph].

[338] Bidyut Prava Nayak and M. K. Parida. "Dilepton events with displaced vertices, double beta decay, and resonant leptogenesis with Type-II seesaw dominance, TeV scale Z′ and heavy neutrinos." In: (2015). arXiv: 1509.06192 [hep-ph].

[339] Claudio O. Dib, C. S. Kim, Nicolás A. Neill, and Xing-Bo Yuan. "Search for sterile neutrinos decaying into pions at the LHC." In: *Phys. Rev.* D97.3 (2018), p. 035022. DOI: 10.1103/PhysRevD.97.035022. arXiv: 1801.03624 [hep-ph].

[340] Giovanna Cottin, Juan Carlos Helo, and Martin Hirsch. "Searches for light sterile neutrinos with multitrack displaced vertices." In: *Phys. Rev.* D97.5 (2018), p. 055025. DOI: 10.1103/PhysRevD.97.055025. arXiv: 1801.02734 [hep-ph].

[341] Giovanna Cottin, Juan Carlos Helo, and Martin Hirsch. "Displaced vertices as probes of sterile neutrino mixing at the LHC." In: *Phys. Rev.* D98.3 (2018), p. 035012. DOI: 10.1103/PhysRevD.98.035012. arXiv: 1806.05191 [hep-ph].

[342] Asmaa Abada, Nicolás Bernal, Marta Losada, and Xabier Marcano. "Inclusive Displaced Vertex Searches for Heavy Neutral Leptons at the LHC." In: (2018). arXiv: 1807.10024 [hep-ph].

[343] Frank F. Deppisch, Wei Liu, and Manimala Mitra. "Long-lived Heavy Neutrinos from Higgs Decays." In: *JHEP* 08 (2018), p. 181. DOI: 10.1007/JHEP08(2018)181. arXiv: 1804.04075 [hep-ph].

[344] Vladimir V. Gligorov, Simon Knapen, Michele Papucci, and Dean J. Robinson. "Searching for Long-lived Particles: A Compact Detector for Exotics at LHCb." In: *Phys. Rev.* D97.1 (2018), p. 015023. DOI: 10.1103/PhysRevD.97.015023. arXiv: 1708.09395 [hep-ph].

[345] Juan Carlos Helo, Martin Hirsch, and Zeren Simon Wang. "Heavy neutral fermions at the high-luminosity LHC." In: *JHEP* 07 (2018), p. 056. DOI: 10.1007/JHEP07(2018)056. arXiv: 1803.02212 [hep-ph].

[346] Sudip Jana, Nobuchika Okada, and Digesh Raut. "Displaced vertex signature of type-I seesaw model." In: *Phys. Rev.* D98.3 (2018), p. 035023. DOI: 10.1103/PhysRevD.98.035023. arXiv: 1804.06828 [hep-ph].

[347] H. Aihara, P. Burrows, M. Oreglia, E. L. Berger, V. Guarino, J. Repond, H. Weerts, L. Xia, J. Zhang, Q. Zhang, et al. "SiD Letter of Intent." In: (2009). arXiv: 0911.0006 [physics.ins-det].

[348] Halina Abramowicz et al. "The International Linear Collider Technical Design Report - Volume 4: Detectors." In: (2013). Ed. by Ties Behnke, James E. Brau, Philip N. Burrows, Juan Fuster, Michael Peskin, Marcel Stanitzki, Yasuhiro Sugimoto, Sakue Yamada, and Hitoshi Yamamoto. arXiv: 1306.6329 [physics.ins-det].

[349] Mike Koratzinos. "FCC-ee accelerator parameters, performance and limitations." In: *Nucl. Part. Phys. Proc.* 273-275 (2016), pp. 2326–2328. DOI: 10.1016/j.nuclphysbps.2015.09.380. arXiv: 1411.2819 [physics.acc-ph].

[350] Silicon Detector Design Study. *Detector for the ILC - SiD "Silicon Detector"*. https://pages.uoregon.edu/silicondetector/. Accessed online on August 2018.

[351] C. Alpigiani et al. "A Letter of Intent for MATHUSLA: a dedicated displaced vertex detector above ATLAS or CMS." In: (2018).

[352] David Curtin et al. "Long-Lived Particles at the Energy Frontier: The MATHUSLA Physics Case." In: (2018). arXiv: 1806.07396 [hep-ph].

[353] David Curtin, Kaustubh Deshpande, Oliver Fischer, and José Zurita. "New Physics Opportunities for Long-Lived Particles at Electron-Proton Colliders." In: *JHEP* 07 (2018), p. 024. DOI: 10.1007/JHEP07(2018)024. arXiv: 1712.07135 [hep-ph].

[354] Roel Aaij et al. "Search for massive long-lived particles decaying semileptonically in the LHCb detector." In: *Eur. Phys. J.* C77.4 (2017), p. 224. DOI: 10.1140/epjc/s10052-017-4744-6. arXiv: 1612.00945 [hep-ex].

[355] R. Aaij et al. "Performance of the LHCb Vertex Locator." In: *JINST* 9 (2014), P09007. DOI: 10.1088/1748-0221/9/09/P09007. arXiv: 1405.7808 [physics.ins-det].

[356] D. Liventsev et al. "Search for heavy neutrinos at Belle." In: *Phys. Rev.* D87.7 (2013). [Erratum: Phys. Rev.D95,no.9,099903(2017)], p. 071102. DOI: 10.1103/PhysRevD.95.099903, 10.1103/PhysRevD.87.071102. arXiv: 1301.1105 [hep-ex].

[357] Roel Aaij et al. "Search for Majorana neutrinos in $B^- \to \pi^+\mu^-\mu^-$ decays." In: *Phys. Rev. Lett.* 112.13 (2014), p. 131802. DOI: 10.1103/PhysRevLett.112.131802. arXiv: 1401.5361 [hep-ex].

[358] Brian Shuve and Michael E. Peskin. "Revision of the LHCb Limit on Majorana Neutrinos." In: *Phys. Rev.* D94.11 (2016), p. 113007. DOI: 10.1103/PhysRevD.94.113007. arXiv: 1607.04258 [hep-ph].

[359] Andrew Kobach. "Baryon Number, Lepton Number, and Operator Dimension in the Standard Model." In: *Phys. Lett.* B758 (2016), pp. 455–457. DOI: 10.1016/j.physletb.2016.05.050. arXiv: 1604.05726 [hep-ph].

[360] Gerard 't Hooft. "Computation of the Quantum Effects Due to a Four-Dimensional Pseudoparticle." In: *Phys. Rev.* D14 (1976). [,70(1976)], pp. 3432–3450. DOI: 10.1103/PhysRevD.18.2199.3, 10.1103/PhysRevD.14.3432.

[361] Savas Dimopoulos and Leonard Susskind. "On the Baryon Number of the Universe." In: *Phys. Rev.* D18 (1978), pp. 4500–4509. DOI: 10.1103/PhysRevD.18.4500.

[362] N. S. Manton. "Topology in the Weinberg-Salam Theory." In: *Phys. Rev.* D28 (1983), p. 2019. DOI: 10.1103/PhysRevD.28.2019.

[363] Frans R. Klinkhamer and N. S. Manton. "A Saddle Point Solution in the Weinberg-Salam Theory." In: *Phys. Rev.* D30 (1984), p. 2212. DOI: 10.1103/PhysRevD.30.2212.

[364] Vardan Khachatryan et al. "Search for heavy Majorana neutrinos in $e^{\S}e^{\S}$+ jets and $e^{\S}$ $\mu^{\S}$+ jets events in proton-proton collisions at $\sqrt{s} = 8$ TeV." In: *JHEP* 04 (2016), p. 169. DOI: 10.1007/JHEP04(2016)169. arXiv: 1603.02248 [hep-ex].

[365] F. del Aguila, J. A. Aguilar-Saavedra, and R. Pittau. "Neutrino physics at large colliders." In: *J. Phys. Conf. Ser.* 53 (2006), pp. 506–527. DOI: 10.1088/1742-6596/53/1/032. arXiv: hep-ph/0606198 [hep-ph].

[366] Tao Han and Bin Zhang. "Signatures for Majorana neutrinos at hadron colliders." In: *Phys. Rev. Lett.* 97 (2006), p. 171804. DOI: 10.1103/PhysRevLett.97.171804. arXiv: hep-ph/0604064 [hep-ph].

[367] F. del Aguila, J. A. Aguilar-Saavedra, and R. Pittau. "Heavy neutrino signals at large hadron colliders." In: *JHEP* 10 (2007), p. 047. DOI: 10.1088/1126-6708/2007/10/047. arXiv: hep-ph/0703261 [hep-ph].

[368] F. del Aguila and J. A. Aguilar-Saavedra. "Distinguishing seesaw models at LHC with multi-lepton signals." In: *Nucl. Phys.* B813 (2009), pp. 22–90. DOI: 10.1016/j.nuclphysb.2008.12.029. arXiv: 0808.2468 [hep-ph].

[369] F. del Aguila and J. A. Aguilar-Saavedra. "Electroweak scale seesaw and heavy Dirac neutrino signals at LHC." In: *Phys. Lett.* B672 (2009), pp. 158–165. DOI: 10.1016/j.physletb.2009.01.010. arXiv: 0809.2096 [hep-ph].

[370] Wei Chao, Zong-guo Si, Ya-juan Zheng, and Shun Zhou. "Testing the Realistic Seesaw Model with Two Heavy Majorana Neutrinos at the CERN Large Hadron Collider." In: *Phys. Lett.* B683 (2010), pp. 26–32. DOI: 10.1016/j.physletb.2009.11.059. arXiv: 0907.0935 [hep-ph].

[371] Arindam Das and Nobuchika Okada. "Inverse seesaw neutrino signatures at the LHC and ILC." In: *Phys. Rev.* D88 (2013), p. 113001. DOI: 10.1103/PhysRevD.88.113001. arXiv: 1207.3734 [hep-ph].

[372] Arindam Das, Partha Konar, and Swapan Majhi. "Production of Heavy neutrino in next-to-leading order QCD at the LHC and beyond." In: *JHEP* 06 (2016), p. 019. DOI: 10.1007/JHEP06(2016)019. arXiv: 1604.00608 [hep-ph].

[373] Simon Bray, Jae Sik Lee, and Apostolos Pilaftsis. "Resonant CP violation due to heavy neutrinos at the LHC." In: *Nucl. Phys.* B786 (2007), pp. 95–118. DOI: 10.1016/j.nuclphysb.2007.07.002. arXiv: hep-ph/0702294 [HEP-PH].

[374] F. del Aguila, J. A. Aguilar-Saavedra, and J. de Blas. "Trilepton signals: the golden channel for seesaw searches at LHC." In: *Acta Phys. Polon.* B40 (2009), pp. 2901–2911. arXiv: 0910.2720 [hep-ph].

[375] Albert M Sirunyan et al. "Search for heavy neutral leptons in events with three charged leptons in proton-proton collisions at $\sqrt{s} = 13$ TeV." In: *Phys. Rev. Lett.* 120.22 (2018), p. 221801. DOI: 10.1103/PhysRevLett.120.221801. arXiv: 1802.02965 [hep-ex].

[376] Claudio O. Dib, C. S. Kim, Kechen Wang, and Jue Zhang. "Distinguishing Dirac/Majorana Sterile Neutrinos at the LHC." In: *Phys. Rev.* D94.1 (2016), p. 013005. DOI: 10.1103/PhysRevD.94.013005. arXiv: 1605.01123 [hep-ph].

[377] Han Liang, Xiao-Gang He, Wen-Gan Ma, Shao-Ming Wang, and Ren-You Zhang. "Seesaw Type I and III at the LHeC." In: *JHEP* 09 (2010), p. 023. DOI: 10.1007/JHEP09(2010)023. arXiv: 1006.5534 [hep-ph].

[378] Carl Blaksley, Mattias Blennow, Florian Bonnet, Pilar Coloma, and Enrique Fernandez-Martinez. "Heavy Neutrinos and Lepton Number Violation in lp Colliders." In: *Nucl. Phys.* B852 (2011), pp. 353–365. DOI: 10.1016/j.nuclphysb.2011.06.021. arXiv: 1105.0308 [hep-ph].

[379] Subhadeep Mondal and Santosh Kumar Rai. "Probing the Heavy Neutrinos of Inverse Seesaw Model at the LHeC." In: *Phys. Rev.* D94.3 (2016), p. 033008. DOI: 10.1103/PhysRevD.94.033008. arXiv: 1605.04508 [hep-ph].

[380] Lucía Duarte, Gabriel A. González-Sprinberg, and Oscar Alfredo Sampayo. "Majorana neutrinos production at LHeC in an effective approach." In: *Phys. Rev.* D91.5 (2015), p. 053007. DOI: 10.1103/PhysRevD.91.053007. arXiv: 1412.1433 [hep-ph].

[381] Subhadeep Mondal and Santosh Kumar Rai. "Polarized window for left-right symmetry and a right-handed neutrino at the Large Hadron-Electron Collider." In: *Phys. Rev.* D93.1 (2016), p. 011702. DOI: 10.1103/PhysRevD.93.011702. arXiv: 1510.08632 [hep-ph].

[382] Manfred Lindner, Farinaldo S. Queiroz, Werner Rodejohann, and Carlos E. Yaguna. "Left-Right Symmetry and Lepton Number Violation at the Large Hadron Electron Collider." In: *JHEP* 06 (2016), p. 140. DOI: 10.1007/JHEP06(2016)140. arXiv: 1604.08596 [hep-ph].

[383] Yosef Nir. "CP violation." In: *Conf. Proc.* C9207131 (1992). [,81(1992)], pp. 81–136.

[384] Janusz Gluza and Tomasz Jeliński. "Heavy neutrinos and the pp→lljj CMS data." In: *Phys. Lett.* B748 (2015), pp. 125–131. DOI: 10.1016/j.physletb.2015.06.077. arXiv: 1504.05568 [hep-ph].

[385] G. Anamiati, M. Hirsch, and E. Nardi. "Quasi-Dirac neutrinos at the LHC." In: *JHEP* 10 (2016), p. 010. DOI: 10.1007/JHEP10(2016)010. arXiv: 1607.05641 [hep-ph].

[386] Arindam Das, P. S. Bhupal Dev, and Rabindra N. Mohapatra. "Same Sign versus Opposite Sign Dileptons as a Probe of Low Scale Seesaw Mechanisms." In: *Phys. Rev.* D97.1 (2018), p. 015018. DOI: 10.1103/PhysRevD.97.015018. arXiv: 1709.06553 [hep-ph].

[387] Gorazd Cvetič, Arindam Das, and Jilberto Zamora-Saá. "Probing heavy neutrino oscillations in rare W boson decays." In: (2018). arXiv: 1805.00070 [hep-ph].

[388] E. Arganda, M. J. Herrero, X. Marcano, and C. Weiland. "Exotic μτjj events from heavy ISS neutrinos at the LHC." In: *Phys. Lett.* B752 (2016), pp. 46–50. DOI: 10.1016/j.physletb.2015.11.013. arXiv: 1508.05074 [hep-ph].

[389] Ernesto Arganda, Ana M. Curiel, Maria J. Herrero, and David Temes. "Lepton flavor violating Higgs boson decays from massive seesaw neutrinos." In: *Phys. Rev.* D71 (2005), p. 035011. DOI: 10.1103/PhysRevD.71.035011. arXiv: hep-ph/0407302 [hep-ph].

[390] E. Arganda, M. J. Herrero, X. Marcano, and C. Weiland. "Imprints of massive inverse seesaw model neutrinos in lepton flavor violating Higgs boson decays." In: *Phys. Rev.* D91.1 (2015), p. 015001. DOI: 10.1103/PhysRevD.91.015001. arXiv: 1405.4300 [hep-ph].

[391] A. Abada, V. De Romeri, S. Monteil, J. Orloff, and A. M. Teixeira. "Indirect searches for sterile neutrinos at a high-luminosity Z-factory." In: *JHEP* 04 (2015), p. 051. DOI: 10.1007/JHEP04(2015)051. arXiv: 1412.6322 [hep-ph].

[392] Asmaa Abada, Damir Bečirević, Michele Lucente, and Olcyr Sumensari. "Lepton flavor violating decays of vector quarkonia and of the Z boson." In: *Phys. Rev.* D91.11 (2015), p. 113013. DOI: 10.1103/PhysRevD.91.113013. arXiv: 1503.04159 [hep-ph].

[393] Shankha Banerjee, Biplob Bhattacherjee, Manimala Mitra, and Michael Spannowsky. "The Lepton Flavour Violating Higgs Decays at the HL-LHC and the ILC." In: *JHEP* 07 (2016), p. 059. DOI: 10.1007/JHEP07(2016)059. arXiv: 1603.05952 [hep-ph].

[394] Juan Herrero-Garcia, Nuria Rius, and Arcadi Santamaria. "Higgs lepton flavour violation: UV completions and connection to neutrino masses." In: *JHEP* 11 (2016), p. 084. DOI: 10.1007/JHEP11(2016)084. arXiv: 1605.06091 [hep-ph].

[395] V. De Romeri, M. J. Herrero, X. Marcano, and F. Scarcella. "Lepton flavor violating Z decays: A promising window to low scale seesaw neutrinos." In: *Phys. Rev.* D95.7 (2017), p. 075028. DOI: 10.1103/PhysRevD.95.075028. arXiv: 1607.05257 [hep-ph].

[396] Xabier Marcano Imaz. "Lepton flavor violation from low scale seesaw neutrinos with masses reachable at the LHC." PhD thesis. Cham: U. Autonoma, Madrid (main), 2017-06. arXiv: 1710.08032 [hep-ph]. URL: https://repositorio.uam.es/handle/10486/681399.

[397] Arindam Das, Partha Konar, and Arun Thalapillil. "Jet substructure shedding light on heavy Majorana neutrinos at the LHC." In: *JHEP* 02 (2018), p. 083. DOI: 10.1007/JHEP02(2018)083. arXiv: 1709.09712 [hep-ph].

[398] Akanksha Bhardwaj, Arindam Das, Partha Konar, and Arun Thalapillil. "Looking for Minimal Inverse Seesaw scenarios at the LHC with Jet Substructure Techniques." In: (2018). arXiv: 1801.00797 [hep-ph].

[399] MadGraph5_aMC@NLO Wiki. *Introduction to jet-parton matching in MG/ME*. https://cp3.irmp.ucl.ac.be/projects/madgraph/wiki/IntroMatching. Accessed online on August 2018.

[400] Evgeny Kh. Akhmedov. "Do charged leptons oscillate?" In: *JHEP* 09 (2007), p. 116. DOI: 10.1088/1126-6708/2007/09/116. arXiv: 0706.1216 [hep-ph].

[401] Eduardo Cortina Gil et al. "Search for heavy neutral lepton production in K^+ decays." In: *Phys. Lett.* B778 (2018), pp. 137–145. DOI: 10.1016/j.physletb.2018.01.031. arXiv: 1712.00297 [hep-ex].

[402] Marco Drewes, Jan Hajer, Juraj Klaric, and Gaia Lanfranchi. "NA62 sensitivity to heavy neutral leptons in the low scale seesaw model." In: *JHEP* 07 (2018), p. 105. DOI: 10.1007/JHEP07(2018)105. arXiv: 1801.04207 [hep-ph].

[403] S. Eijima, M. Shaposhnikov, and I. Timiryasov. "Parameter space of baryogenesis in the νMSM." In: (2018). arXiv: 1808.10833 [hep-ph].

[404] Elena Graverini, Nicola Serra, and Barbara Storaci. "Search for New Physics in SHiP and at future colliders." In: *JINST* 10.07 (2015), p. C07007. DOI: 10.1088/1748-0221/10/07/C07007. arXiv: 1503.08624 [hep-ex].

[405] Elena Graverini. "SHiP sensitivity to Heavy Neutral Leptons." In: (2016). URL: https://cds.cern.ch/record/2214085.

[406] Laurent Canetti and Mikhail Shaposhnikov. "Baryon Asymmetry of the Universe in the NuMSM." In: *JCAP* 1009 (2010), p. 001. DOI: 10.1088/1475-7516/2010/09/001. arXiv: 1006.0133 [hep-ph].

[407] Laurent Canetti, Marco Drewes, and Mikhail Shaposhnikov. "Sterile Neutrinos as the Origin of Dark and Baryonic Matter." In: *Phys. Rev. Lett.* 110.6 (2013), p. 061801. DOI: 10.1103/PhysRevLett.110.061801. arXiv: 1204.3902 [hep-ph].

[408] Laurent Canetti, Marco Drewes, Tibor Frossard, and Mikhail Shaposhnikov. "Dark Matter, Baryogenesis and Neutrino Oscillations from Right Handed Neutrinos." In: *Phys. Rev.* D87 (2013), p. 093006. DOI: 10.1103/PhysRevD.87.093006. arXiv: 1208.4607 [hep-ph].

[409] Laurent Canetti, Marco Drewes, and Björn Garbrecht. "Probing leptogenesis with GeV-scale sterile neutrinos at LHCb and Belle II." In: *Phys. Rev.* D90.12 (2014), p. 125005. DOI: 10.1103/PhysRevD.90.125005. arXiv: 1404.7114 [hep-ph].

[410] P. Hernández, M. Kekic, J. López-Pavón, J. Racker, and N. Rius. "Leptogenesis in GeV scale seesaw models." In: *JHEP* 10 (2015), p. 067. DOI: 10.1007/JHEP10(2015)067. arXiv: 1508.03676 [hep-ph].

[411] Asmaa Abada, Giorgio Arcadi, Valerie Domcke, and Michele Lucente. "Lepton number violation as a key to low-scale leptogenesis." In: *JCAP* 1511.11 (2015), p. 041. DOI: 10.1088/1475-7516/2015/11/041. arXiv: 1507.06215 [hep-ph].

[412] P. Hernández, M. Kekic, J. López-Pavón, J. Racker, and J. Salvado. "Testable Baryogenesis in Seesaw Models." In: *JHEP* 08 (2016), p. 157. DOI: 10.1007/JHEP08(2016)157. arXiv: 1606.06719 [hep-ph].

[413] Asmaa Abada, Giorgio Arcadi, Valerie Domcke, and Michele Lucente. "Neutrino masses, leptogenesis and dark matter from small lepton number violation?" In: *JCAP* 1712.12 (2017), p. 024. DOI: 10.1088/1475-7516/2017/12/024. arXiv: 1709.00415 [hep-ph].

[414] Thomas Hambye and Daniele Teresi. "Baryogenesis from L-violating Higgs-doublet decay in the density-matrix formalism." In: *Phys. Rev.* D96.1 (2017), p. 015031. DOI: 10.1103/PhysRevD.96.015031. arXiv: 1705.00016 [hep-ph].

[415] Takehiko Asaka and Takanao Tsuyuki. "Seesaw mechanism at electron-electron colliders." In: *Phys. Rev.* D92.9 (2015), p. 094012. DOI: 10.1103/PhysRevD.92.094012. arXiv: 1508.04937 [hep-ph].

[416] The CEPC-SPPC Study Group. *CEPC-SPPC - Preliminary Conceptual Design Report*. Tech. rep. IHEP-CEPC-DR-2015-01. IHEP, 2015. URL: http://cepc.ihep.ac.cn/preCDR/main_preCDR.pdf.

[417] J. S. Marshall and M. A. Thomson. "Pandora Particle Flow Algorithm." In: *Proceedings, International Conference on Calorimetry for the High Energy Frontier (CHEF 2013): Paris, France, April 22-25, 2013*. 2013, pp. 305–315. arXiv: 1308.4537 [physics.ins-det].

[418] S. I. Bityukov and N. V. Krasnikov. "Uncertainties and discovery potential in planned experiments." In: *Advanced Statistical Techniques in Particle Physics. Proceedings, Conference, Durham, UK, March 18-22, 2002*. 2002, pp. 77–80. arXiv: hep-ph/0204326 [hep-ph]. URL: http://www.ippp.dur.ac.uk/Workshops/02/statistics/proceedings//bityoukov.pdf.

[419] S. I. Bityukov. "Signal significance in the presence of systematic and statistical uncertainties." In: *JHEP* 09 (2002). [Nucl. Instrum. Meth.A502,795(2003)], p. 060. DOI: 10.1088/1126-6708/2002/09/060, 10.1016/S0168-9002(03)00586-2. arXiv: hep-ph/0207130 [hep-ph].

[420] Pekka K. Sinervo. "Signal significance in particle physics." In: *Advanced Statistical Techniques in Particle Physics. Proceedings, Conference, Durham, UK, March 18-22, 2002*. 2002, pp. 64–76. arXiv: hep-ex/0208005 [hep-ex]. URL: http://www.ippp.dur.ac.uk/Workshops/02/statistics/proceedings//sinervo.pdf.

[421] Yong-Sheng Zhu. "On Statistical Significance of Signal." In: *HEPNP* 30 (2006), pp. 331–334. arXiv: 0812.2708 [physics.data-an].

[422] Gary J. Feldman and Robert D. Cousins. "A Unified approach to the classical statistical analysis of small signals." In: *Phys. Rev.* D57 (1998), pp. 3873–3889. DOI: 10.1103/PhysRevD.57.3873. arXiv: physics/9711021 [physics.data-an].

[423] Andreas Hocker et al. "TMVA - Toolkit for Multivariate Data Analysis." In: (2007). arXiv: physics/0703039 [physics.data-an].